N7622200

BLADE ROW DYNAMIC DIGITAL COMPRESSOR PROGRAM. VOLUME 1: J85 CLEAN INLET FLOW AND PARALLEL COMPRESSOR MODELS

GENERAL ELECTRIC CO., CINCINNATI, OHIO.
AIRCRAFT ENGINE GROUP

MAR 1976

1. Report No.	2. Government Accession No.	3. Recipient's Catalog No.
NASA CR-134978		
4. Title and Subtitle Blade Row Dynamic Digital Compression Program Volume I J85 Clean Inlet Flow and Parallel Compressor Models		5. Report Date March 1976
		6. Performing Organization Code
7. Author(s) W. A. Tesch W. G. Steenken		8. Performing Organization Report No. R75AEG406
9. Performing Organization Name and Address General Electric Company Aircraft Engine Group Cincinnati, Ohio 45215		10. Work Unit No.
		11. Contract or Grant No. NAS3-18526
12. Sponsoring Agency Name and Address National Aeronautics and Space Administration Washington, D.C. 20546		13. Type of Report and Period Covered Contractor Report
		14. Sponsoring Agency Code
15. Supplementary Notes Project Monitors: D.G. Evans and E.J. Graber, Jr. NASA-Lewis Research Center, Cleveland, Ohio 44135		
16. Abstract		

1. Report No.	2. Government Accession No.	3. Recipient's Catalog No.
NASA CR-134978		

4. Title and Subtitle Blade Row Dynamic Digital Compression Program Volume I J85 Clean Inlet Flow and Parallel Compressor Models	5. Report Date March 1976
	6. Performing Organization Code
7. Author(s) W. A. Tesch W. G. Steenken	8. Performing Organization Report No. R75AEG406
	10. Work Unit No.
9. Performing Organization Name and Address General Electric Company Aircraft Engine Group Cincinnati, Ohio 45215	11. Contract or Grant No. NAS3-18526
	13. Type of Report and Period Covered Contractor Report
12. Sponsoring Agency Name and Address National Aeronautics and Space Administration Washington, D.C. 20546	14. Sponsoring Agency Code

15. Supplementary Notes

Project Monitors: D.G. Evans and E.J. Graber, Jr.

NASA-Lewis Research Center, Cleveland, Ohio 44135

16. Abstract

This report presents the results of a one-dimensional dynamic digital blade row compressor model study of a J85-13 engine operating with uniform and with circumferentially distorted inlet flow. Details of the geometry and the derived blade row characteristics used to simulate the clean inlet performance are given. A stability criterion based upon the self developing unsteady internal flows near surge provided an accurate determination of the clean inlet surge line. The basic model was modified to include an arbitrary extent multi-sector parallel compressor configuration for investigating 180° 1/rev total-pressure, total-temperature, and combined total-pressure and total-temperature distortions. The combined distortions included opposed, coincident, and 90° overlapped patterns. The predicted losses in surge pressure ratio matched the measured data trends at all speeds and gave accurate predictions at high corrected speeds where the slope of the speed lines approached the vertical.

17. Key Words (Suggested by Author(s))	18. Distribution Statement
Compressor Stability Blade Row Model Parallel Compressor Model	

19. Security Classif. (of this report)	20. Security Classif. (of this page)	21. No. of Pages	22.
Unclassified	Unclassified	200	

NASA-C-168 (Rev. 6-71)

FOREWORD

The program described in this report was conducted by the Aircraft Engine Group of the General Electric Company, Cincinnati, Ohio for the NASA Lewis Research Center, National Aeronautics and Space Administration under Contract NAS3-18526.

The program was carried out under the technical cognizance of Mr. D.G. Evans and Mr. E.J. Graber, Jr. of the NASA Lewis Research Center Engine Research Branch.

The contract effort was conducted at the Evendale Plant of the Aircraft Engine Group, Cincinnati, Ohio under the technical direction of Dr. W.G. Steenken with Mr. W.A. Tesch being the prime technical contributor. Support was provided by Mrs. V.M. Haywood of the Lynn Plant, Aircraft Engine Group, Lynn, Massachusetts in deriving the clean-inlet-flow compressor stage characteristics and by Mrs. P. Gibson in preparing this report for publication.

TABLE OF CONTENTS

TABLE OF CONTENTS (concluded)

LIST OF ILLUSTRATIONS

LIST OF ILLUSTRATIONS (Continued)

LIST OF ILLUSTRATIONS (Continued)

LIST OF ILLUSTRATIONS (Continued)

LIST OF ILLUSTRATIONS (Continued)

LIST OF ILLUSTRATIONS (Continued)

LIST OF ILLUSTRATIONS (Concluded)

LIST OF TABLES

LIST OF TABLES (concluded)

NOMENCLATURE*

A	-	Area
C	-	Absolute Velocity
C_i	-	Coefficients for Relative Total-Pressure Loss Coefficient Polynominals
C_Z	-	Axial Velocity
C_U	-	Absolute Tangential Velocity
D	-	Diffusion Factor

Rotor $$D=1-\frac{W'_{i+1}}{W'_i}+\frac{r_{i+1}\,C_{U_{i+1}}-r_i C_{U_i}}{(r_i+r_{i+1})\,\sigma\,W'_i}$$

Stator $$D=1-\frac{C_{i+1}}{C_i}+\frac{r_i\,C_{U_i}-r_{i+1}\,C_{U_{i+1}}}{(r_i+r_{i+1})\,\sigma\,C_i}$$

D_i	-	Coefficients for Deviation Angle Polynominals
EX	-	Polytropic Exponent
F_B	-	Blade Force
F_D	-	Drag Force in Direction of Blade Mean Camber
F_{DZ}	-	Axial Component of Drag Force
F_L	-	Blade Lift Force
F_T	-	Blade Tangential Force
FV	-	Scale Factor
IAA	-	Inlet Air Angle
IGV	-	Inlet Guide Vane
L	-	Volume Length
M	-	Mach Number
M	-	Number of Screen Mesh Per Unit Dimension
N	-	Rotor Speed in Revolutions per Minute
OGV	-	Outlet Guide Vane
P	-	Static Pressure
P_d	-	Dynamic Pressure (P_T - P)

*The Nomenclature for computer tabulations in Appendices C and D are given in Tables 24 and 26, respectively.

NOMENCLATURE (Continued)

P_M	-	Mean Static Pressure
P_n	-	Polynominal of Degree n
P_T	-	Total Pressure
R	-	Specific Gas Constant
S	-	Entropy
S_F	-	Entropy Production Term
SS	-	Stator Setting
T_T	-	Total Temperature
U	-	Pitch Line Wheel Speed
V	-	Volume
W	-	Flow Rate
W'	-	Relative Velocity
a_T	-	Stagnation Velocity of Sound
c	-	Blade Chord
g_o	-	Gravitational Constant
i	-	Incidence Angle
m	-	Slope of Linearized Characteristic
n	-	Stage Number
q	-	Kinetic Pressure $1/2\ \rho\ (W')^2$
r	-	Pitch-line Radius
t	-	Time
α, β	-	Blade Inlet Air Angles
α^*, β^*	-	Blade Inlet Metal Angles
β_c	-	Lift Direction Vector Correction Angle
β_∞	-	Lift Direction Vector
ε	-	Small Quantity
γ	-	Ratio of Specific Heats
δ	-	Deviation Angle
θ	-	T_T/T_{STD}
ξ	-	Dummy Variable
ρ	-	Density

NOMENCLATURE (Concluded)

σ	-	Solidity
ϕ	-	Flow Coefficient $\left(\frac{C_{z_i}}{2\pi N r_i} \right)$
Ψ_m	-	Work Coefficient $\frac{\frac{\gamma}{\gamma - 1} g_o R \, (T_{T_{i+1}} - T_{T_i})}{[2\pi N(r_i)]^2/2}$
ψ'_m	-	Pressure Coefficient $\frac{\frac{\gamma}{\gamma - 1} g_o R \, T_{T_i}\left[\left(\frac{P_{T_{i+1}}}{P_{T_i}}\right)^{(\gamma-1)/\gamma} - 1\right]}{[2\pi N(r_i)]^2/2}$
$\bar{\omega}'_n$	-	Relative Total-Pressure Loss Coefficient
ω^*	-	Reduced Frequency $(2\pi fc/W')$

SUBSCRIPTS

2	-	Compressor Entrance Station
3	-	Compressor Discharge Station
M	-	Mean
T	-	Total
i	-	i-th Station
k	-	K-th Volume
m	-	M-th Stage
n	-	N-th Blade Row

SUPERSCRIPTS

$\overline{\quad}$	-	Volume Average (Clean or Distorted Sector)
$'$	-	Relative Frame of Reference

1.0 SUMMARY

The objectives of the Blade Row Dynamic Digital Compressor Program were twofold. Firstly, the General Electric developed pitch-line, blade row, time marching, digital compression component stability model was adapted to the J85-13 engine configuration. In particular, the J85-13 compressor, including the combustor volume to the turbine diaphragm, was modeled taking into account the variable IGV geometry and the third, fourth, and fifth stage bleeds. The clean inlet performance of the compressor component was reproduced for two engines including dynamic indication of the surge line. This prediction for surge was accomplished by developing a stability criterion based upon the derivative of flow rate within the blade rows as compared to the derivative of the flow imposed by the throttling process boundary condition. Secondly, the clean inlet flow compressor model was modified to a parallel compressor configuration to permit imposing total-pressure, total-temperature, and combined total-pressure and total-temperature distorted upstream boundary conditions. The flow split between the sectors was determined by a method which simultaneously satisfied the inlet boundary conditions and the parallel-compressor uniform-static-pressure assumption imposed at the entrance to the combustor volume. It was anticipated that static-pressure gradients should be minimal at this location due to the low Mach number of the flow. Since the input to this model is the clean-inlet-flow blade row characteristics (relative total-pressure loss coefficients and deviation angles) as functions of incidence angle and corrected speed, it was necessary to develop a procedure for defining blade row characteristics at corrected speeds other than those for which clean-inlet-flow data existed. In this manner good simulations with total-temperature distorted inlet flow boundary conditions could be obtained. This procedure makes use of spline curve fits of the blade characteristic data as a function of corrected speed within the data range. This permits interpolations to be carried out inside the range of data, while outside the data range, the blade characteristics are obtained from linear extrapolations of the spline at its end points.

Simulations of 25 180-degree 1/rev circumferential distortions were carried out for the following types of distortion patterns and the indicated speed range:

A. Pure Total Pressure (80%-100% $N/\sqrt{\theta}$)

B. Pure Total Temperature (87%-100% $N/\sqrt{\theta}$)

C. Combined Total Pressure and Total Temperature

180° Opposed (87%-100% $N/\sqrt{\theta}$)

180° Coincident (87%-100% $N/\sqrt{\theta}$)

90° Overlapped (87%-100% $N/\sqrt{\theta}$)

The loss in surge pressure ratio trends were correctly predicted at all speeds. However, the model exhibits characteristics similar to other parallel

compressor models, that is, it predicts the loss in surge pressure ratio accurately when the compressor speed line is near vertical and over predicts the loss in surge pressure ratio when the compressor speed line has a low slope. This deficiency is being studied and attempts to rectify it, while still maintaining the major concepts of the classical parallel-compressor model, are being carried out in a continuing study.

2.0 INTRODUCTION

Engine inlet total-pressure and total-temperature distortions lead to well-documented losses of surge pressure ratio in the compression systems of turbofan and turbojet engines. One approach to obtaining a more detailed understanding of the internal flow mechanisms which cause this loss in surge pressure ratio is to develop computer simulations of the compression systems that will not only permit studying the effects of steady-state spatial distortions, but provide the means for rapidly and efficiently screening the effects of many types of distortion. Such simulations are also useful for determining the potential effects of design modifications on compression system stability.

However, if such models are to achieve their ultimate capability as a design and evaluation tool, it is necessary to develop and validate the capability of the models against existing bodies of test data. This step establishes confidence in the model, helps to define its range of validity, and insures that it is understood. Toward this goal, this report presents the results of an analytical investigation in which an existing generalized compression component computer model was modified to simulate the performance characteristics of the J85-13 compressor system operating without inlet distortion. The model was then modified to predict the effects of inlet distortion on the stability and internal flow characteristics of the compressor system. The resulting predictions were compared to the measured effects.

An existing one-dimensional pitch-line, dynamic digital model for compression components, developed by the Aircraft Engine Group of the General Electric Company, was used as the basis for the investigation. Because the breakdown of flow in a compression system is an inherently unsteady aerodynamic phenomena which typically manifests itself as a rotating stall or surge, it was postulated that a time-dependent model would offer a unique approach for studying the factors affecting compression system stability. Certainly, one could question the value of a one-dimensional pitch-line model for investigating stability problems since it is known that rotating stall and surge are multi-dimensional events which generally initiate and propagate in the hub or tip regions of the blading. However, for aerodynamic stability studies it is not necessary to be able to detail the propagation velocity, number of cells, size, etc., of a rotating stall or the spatial distribution of the wave front of the surge pulse as long as the conditions under which the aerodynamic instability would occur can be determined. A properly constructed one-dimensional model should have the ability to predict the circumstances under which a disturbance will change from being attenuated to being propagated. Examination of a stability criterion derived by Jansen (Reference 1) supports this contention.

Another way to convey the same information is to examine the eigenvalues of the characteristic equation derived from the Jacobian matrix of equations describing the aerodynamic performance of the compression system. This approach is currently under investigation in a parallel study (Contract No. NAS3-19854). In it, a change from negative to positive real eigenvalues will lead to the propagation of disturbances - a problem akin to the problem of acoustic propagation in wave guides. The use of this method has been discussed by Daniele, Blaha, and Seldner (Reference 2).

Confidence in the basic approach used in the present study had been established in a study documented by Ruegg (Reference 3). In it, the propagation velocity of waves in a duct were studied using the basic equations of the model and the calculational technique. The results were compared with method of characteristics results. Analysis showed that the model produced accurate predictions of wave speed, thermodynamic properties, and flow parameters. Resonances in ducts were also studied and the resonant frequencies compared well with those predicted by acoustic theory. Proper location of nodal points with frequency was noticed as well as proper qualitative changes in wave amplitude with frequency.

In another study, both a two-stage fan and a nine-stage compressor were simulated with clean inlet conditions. The clean inlet maps were accurately reproduced and the surge lines predicted. Time dependent inlet and exit boundary conditions were imposed without creating numerical instabilities, and the results indicated proper qualitative response.

With this background, it was felt that the generalized model which had demonstrated the ability to properly calculate the state of the fluid in ducts and blade rows, was in a sufficient state of development to adapt it to the "real world" stability problems encountered in compression systems. The compressor model was divided into volumes, one blade row per volume, except for free volumes whose lengths were chosen to be commensurate with the longest axial length blade row. The equations of change (conservation of mass, momentum, and energy) integrated once over the volume to give the macrobalances were written in a form that permitted the determination of time derivatives of density, physical flow, and the product of density times entropy as functions of space variables. Time-dependent solution was accomplished by substituting the time derivatives in a Taylor series to give an estimate of the three above mentioned state variables at the next increment in time. This was continued until the solution had settled out if the boundary conditions were not time dependent, or until stationary behavior was reached if periodic boundary conditions were imposed, or for any portion of a transient for boundary conditions not previously stated.

It is important to note that the momentum and energy macrobalance equations from which the time derivatives of flow and density-entropy product are determined contain a blade force term and an entropy production term, respectively. The blade force was obtained from resolving the forces that act on a blade including the tangential force obtained from the Euler turbine equation, and the blade drag force which was related to the losses within a blade row. The entropy production term was also related to the losses that develop within a blade row. In this generalized model, it is the presence of these terms which determine that a volume is treated as a blade row volume. The absence of the blade force and entropy production terms indicates a free volume indicative of lossless duct flow. Hence, it was through the blade force and entropy production terms that the clean inlet performance of the compressor was input. The input of the performance was accomplished through the relative total-pressure loss coefficient and the deviation angle as a function of incidence angle at each corrected speed for each rotor. The stators were assumed to be lossless although a constant deviation angle was assigned to them. The relative total-pressure loss coefficient and the rotor deviation angle were determined from the steady-state stage characteristics. Because the method completely specifies the flow condition, program output includes the total temperatures and total pressures of individual stages, stage characteristics, velocity diagram information at both the inlet and exit of each blade row, and diffusion factors.

The present investigation was divided into two parts - (1) Clean Inlet Model and (2) Distorted Inlet Model. For the clean inlet model, the existing General Electric Dynamic Digital Blade Row Compression Component Stability Model was modified to represent the NASA-Lewis Research Center J85-13 compressor configurations and stage performance characteristics for undistorted inlet flow conditions. The resulting model accounted for the scheduled changes of variable IGV angle and variable third, fourth, and fifth stage bleed flow with changes in corrected speed. The performance characteristics of each blade row were determined from stage stacking procedures and expressed in terms of incidence angle, deviation angles, and loss coefficient variations for each blade row. These values were determined from compressor interstage data furnished by the Lewis Research Center which consisted of a hub, mean and tip radius total-temperature, total-pressure and tip wall-static-pressure measurements for the pressure ratio and flow ranges of each speed line. The resulting model also incorporated an improved stability criterion, based on the self developing unsteady internal flows generated near surge.

Two clean inlet compressor maps were generated using the computer model. The maps consisted of four speed lines (80, 87, 94, and 100 percent corrected speed) for the first, or "Moss" engine (Reference 4), three speed lines (87, 94 and 100 percent corrected speed) for the second, or "Mehalic" engine (Reference 5), and the predicted surge points for each speed line. Verification of the computer model was made based on the comparisons achieved between the predicted maps and the corresponding experimental maps presented in the references. These comparisons were based on the accuracy of predicting the pressure ratio flow characteristics, and the surge point for each speed investigated. Following this verification, the predicted stage velocity diagrams, blade and stator incidence angles, diffusion factors, and loss coefficients at surge and at two points below surge for each corrected speed line were analytically determined.

The computer model was then modified to a multi-sector parallel compressor configuration to accept circumferentially distorted inlet flow conditions. This modification was accomplished by dividing the inlet annulus into sectors, the number of which depended on the manner in which the state properties varied circumferentially at the compressor inlet. The maximum number of sectors was limited to 12, and the minimum number was limited to two. The variable IGV and bleed schedules, and the stage performance characteristics used for each distorted sector were the same as those used for the corresponding compressor with undistorted inlet flow. As the rotor blades moved from one sector to the next, it was assumed that both the rotor inlet and exit velocity diagrams shifted instantaneously to a new equilibrium condition representative of the next sector. No account was made of the possible effects of the rotor blade unsteady response characteristics. This approach was deemed appropriate for the J85 compressor operating with 180 degree extent distortion, where the broad extent of the distorted sector coupled with the short chorded rotor blades resulted in low values of rotor reduced frequency ($\omega^* < 0.17$). The analysis of Schorr and Reddy (Reference 6) indicates the essentially steady-state response characteristics of cascades of blades operating at this level of reduced frequency. Also, it was assumed that no crossflows or mixing occurs between sectors, which according to Reid (Reference 7) may be a good assumption for circumferential distortion patterns and according to Plourde and Stenning (Reference 8) may be a good assumption for compressors with low gap-to-radius ratios. Finally provisions were made to determine the circumferential displacement of a streamtube for each sector of distorted flow through the compressor and the displacement of the streamtube was assumed to be equal to the circumferential displacement of the sector.

Compressor maps and the associated inter-stage flow characteristics for distorted inlet flow conditions representative of the distortion tests conducted on the two J85-13 engines at the Lewis Research Center were then generated. The total number of corrected speed lines generated with inlet distortion was twenty five and the circumferential extent of the distortions considered was limited to 180°. The types of inlet distortion simulated corresponded to the total-pressure distortion imposed on the "Moss" engine, and the total-temperature distortion and a combination of the two with the distorted temperature region circumferentially opposed to, coincident with, and 90° overlapped with the distorted pressure region imposed on the "Mehalic" engine.

The computer model predictions were once again verified based upon the comparisons achieved between the predicted maps and the corresponding experimental maps noted in References 4 and 5. Specifically, verification was based upon the accuracy of predicting the flow-pressure ratio characteristics for each speed, and the surge lines. Following this verification, the predicted stage velocity diagrams, blade and stator incidence angles, diffusion factors, and loss coefficients at surge and at two points below surge for each corrected speed were analytically determined.

Included in this report are: (1) The loss in surge pressure ratio at constant corrected speed and at constant corrected flow; (2) The amplitude of total-pressure, static-pressure, and total-temperature distortion at the inlet, at each stage, and at the compressor exit; (3) The rotation (circumferential displacement) of the distorted sectors across each stage; and (4) The velocity diagrams, pressures and temperatures, and blade and stator diffusion factors for each stage for at least two sectors, depending on the type of distortion and its circumferential profile. Only the tables and figures which serve to substantiate a point or which summarizes final results are included in the text. All documentation of model input and other additional information is relegated to the appendix.

The results are presented in the International System of Units. The dimensions of the compressor system which was designed using U.S. customary units are presented in both systems of units.

3.0 BLADE ROW DYNAMIC MODEL

In this section is described the manner in which the Dynamic Digital Blade Row Compression Component Stability Model is applied to the compressor of the J85-13 turbojet engine, the determination of the blade row characteristics, and the solution of the governing differential equations using a time-marching technique based on a Taylor series expansion. In addition, a steady-state model option is described which is used for determining some model input parameters and for initialization of the dynamic program. Also, the details of the parallel compressor option of the program are discussed.

3.1 GENERAL DESCRIPTION OF ENGINE AND MODEL

3.1.1 J85-13 Compressor

The compressor of a J85-13 engine has eight stages with a variable camber IGV and variable third, fourth, and fifth stage bleeds located in each stator channel at the casing wall. The IGV trailing edge flaps and the bleeds are ganged together and are scheduled as a function of corrected speed biased by compressor-face total temperature. The geometry of the J85-13 engine in the compressor and combustor regions is shown in Figure 1. The nomonal IGV and bleed schedules are given in Figure 2.

It is appropriate to discuss the two engines modeled in this study. The pure total-pressure distortion patterns that were simulated during this study were obtained during testing of a J85-13 engine known as the "Moss" engine (Reference 4). This engine was run in support of the NASA casing treatment program. The clean inlet and distortion data utilized in this model were obtained from the untreated configuration with solid compressor-case inserts. The pure total-temperature distortion patterns and the combined total-pressure and total-temperature distortion patterns that were simulated were obtained during testing of a J85-13 engine known as the "Mehalic" engine (Reference 5).

The "Moss" engine was instrumented at the engine face with a 60 probe array (5 rings/12 rakes) to measure the total-pressure distortion patterns generated during testing. It was from these data supplied by the NASA Lewis Research Center that the patterns used in conducting the parallel compressor efforts of this program were selected. Further details concerning the instrumentation can be found in Reference 4. The "Mehalic" engine was instrumented at the engine face with a 60 probe array (5 rings/12 rakes), for measuring total-temperature distortion and with an 8-probe array for monitoring the gross levels of total-pressure distortion. Further details can be found in Reference 5.

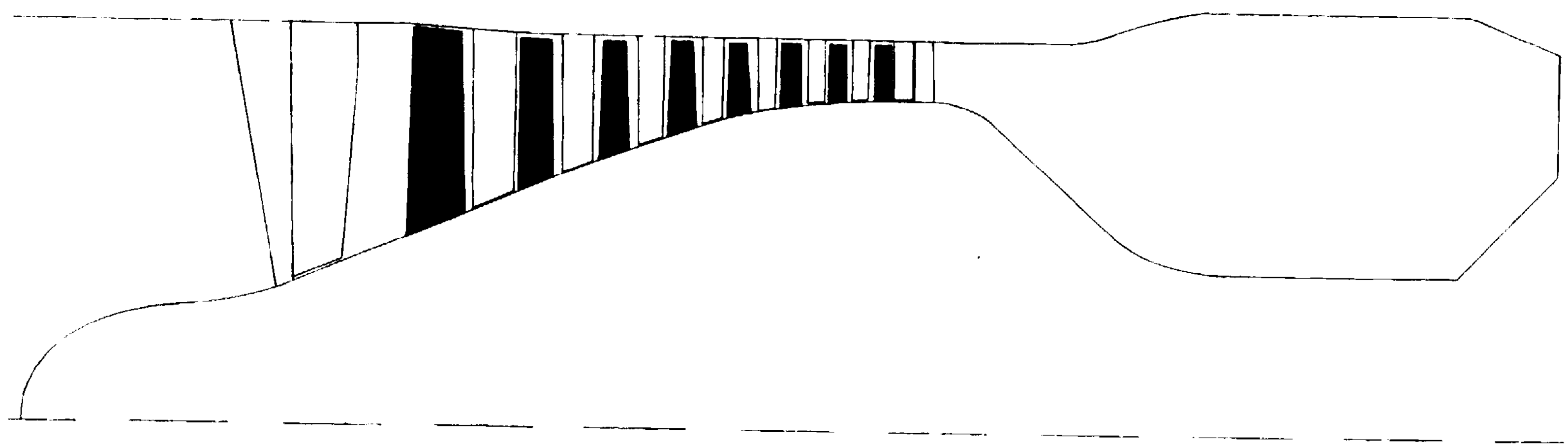

Figure 1. Section View of J85-13 Compressor.

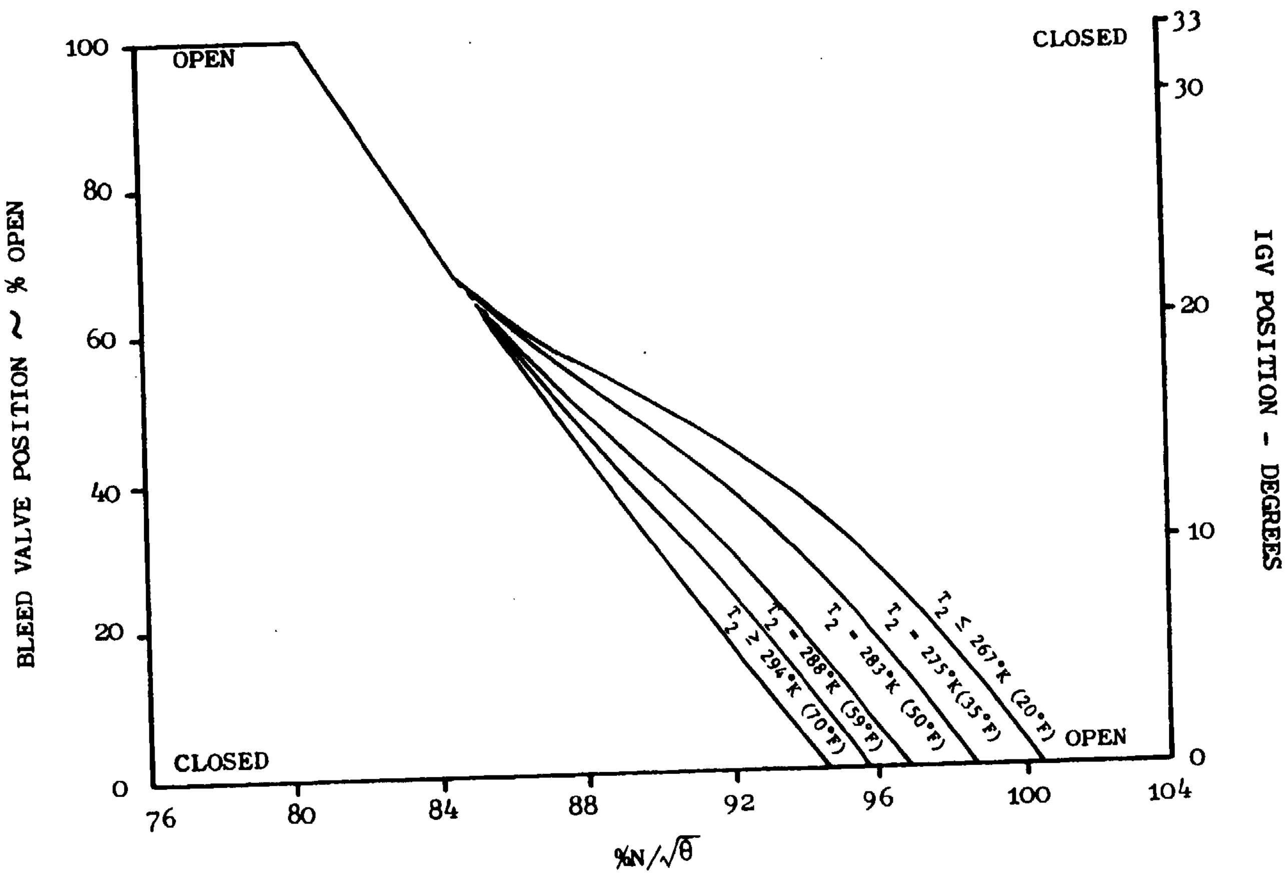

Figure 2. Nominal IGV and Bleed Valve Schedule For Bill of Material Engine.

3.1.2 Compressor Model

For the purposes of this study, the compressor model includes volumes upstream of the IGV to the distortion measurement plane and downstream of the OGV continuing to a choke plane located at the turbine nozzle diaphragm (A_4). The purpose of including these extra volumes is to insure that realistic boundary conditions can be imposed.

The compressor model consists of twenty-nine volumes. There are 18 bladed volumes (one blade row per volume) consisting of the IGV, rotors 1-8, stators 1-8, and the OGV and 11 free volumes. These free volumes consist of two volumes between the instrumentation plane and the leading edge of the IGV, a volume between the trailing edge of the IGV and the leading edge of rotor 1, and eight volumes between the trailing edge of the OGV and the turbine diaphragm. The axial lengths of the free volumes are chosen to be commensurate with the length of the longest blade chord axial projection, as it is this length which will control the upper bound of the frequency response of the model. This configuration is shown schematically in Figure 3. It should be noted that the length of a rotor blade row extends from the trailing edge of the upstream stator to the leading edge of the downstream stator and includes the axial inter-blade row gaps while the length of a stator blade row extends from the leading edge of the stator to the trailing edge of the stator.

The geometry used in the model as well as the boundary layer blockage and blade solidities is given in Table 1. The α_1* and the α_2* parameters are the blade leading edge and trailing edge metal angles, respectively. The given α_2 values are stator absolute exit air angles. The difference between the exit air angle and the metal angle is the deviation angle which for stators is assumed to be constant independent of incidence angle or corrected speed. This assumption is based upon cascade tests which show a small variation in deviation angle over a wide range of incidence angle for stators operating at Mach numbers less than 0.7. This is the case for the operating ranges encountered by the J85-13 compressors in this study.

The blade work on the fluid is accomplished in a distributed, but unspecified, manner across a rotor volume length. All losses are assumed to take place in rotors, that is, no losses are accounted for in blade free volumes or stator blade volumes, although this is not a restriction of the model. The rotor deviation angles vary as functions of the incidence angle. The rotor 1 absolute inlet air angle (IAA) is tabulated below for both the "Moss" and "Mehalic" engines as a function of IGV Stator Setting (SS).

	"Moss"		"Mehalic"	
$\%N\sqrt{\theta}$	SS	IAA	SS	IAA
80	33.0°	16.73°	---	---
87	16.5	9.27	6.7°	3.98°
94	1.0	.61	0.0	0.0
100	0.0	0.0	0.0	0.0

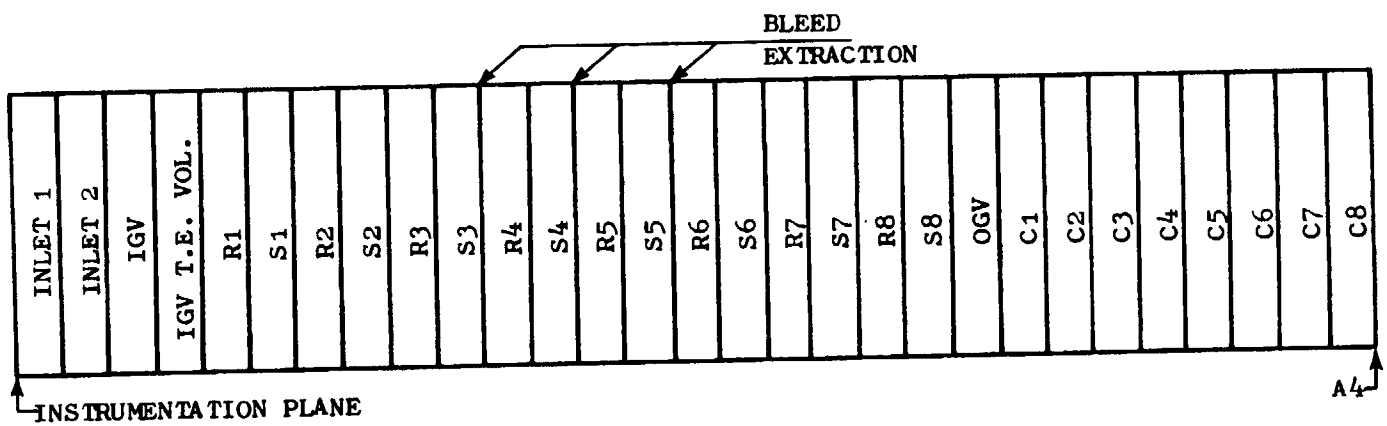

Figure 3. Schematic of Model Volumes.

Table 1. J85-13 Compressor Geometry.

Volume Description	Station Number	R_T (cm)	R_T (in.)	R_H (cm)	R_H (in.)	A (cm^2)	A (in.^{2})	R_P (cm)	R_P (in.)	Blockage	Volume Number	α_1^* (deg)	α_2^* (deg)	α_2 (deg)	Volume Length (cm)	Volume Length (in.)	Solidity
Inlet 1	1	20.447	8.050	5.791	2.280	1208.08	187.252	--	--	1.00	1	--	--	--	3.175	1.250	--
Inlet 2	2	20.447	8.050	5.791	2.280	1208.08	187.252	--	--	1.00	2	--	--	--	3.175	1.250	--
IGV	3	20.447	8.050	5.817	2.290	1207.15	187.108	15.030	5.918	1.00	3	0	Scheduled	--	6.375	2.510	--
IGV Trailing Volume	4	20.333	8.005	8.573	3.375	1067.93	165.529	15.735	6.195	0.97	4	--	--	--	2.337	0.920	--
R1	5	20.193	7.950	9.622	3.788	990.18	153.478	15.931	6.272	0.97	5	51.50	37.50	--	3.012	1.186	1.143
S1	6	19.980	7.866	10.914	4.297	879.84	136.376	16.256	6.400	0.97	6	34.84	-2.86	5.40	2.644	1.041	1.057
R2	7	19.802	7.796	11.994	4.722	779.93	120.890	16.520	6.504	0.97	7	50.20	30.20	---	2.004	0.789	1.204
S2	8	19.685	7.750	12.835	5.053	699.86	108.478	16.764	6.600	0.97	8	40.58	2.98	12.10	2.154	0.848	1.208
R3	9	19.685	7.750	13.630	5.366	633.76	98.233	17.048	6.712	0.97	9	51.05	26.49	--	1.521	0.599	1.326
S3	10	19.685	7.750	14.206	5.593	583.34	90.418	17.252	6.792	0.97	10	45.68	6.96	14.80	1.880	0.740	1.350
R4	11	19.685	7.750	14.867	5.853	523.02	81.068	17.516	6.896	0.97	11	50.81	25.83	--	1.313	0.517	1.384
S4	12	19.685	7.750	15.276	6.014	484.30	75.066	16.993	6.690	0.97	12	46.40	10.00	19.40	1.664	0.655	1.390
R5	13	19.685	7.750	15.773	6.210	435.73	67.539	17.861	7.032	0.97	13	55.95	28.35	--	1.092	0.430	1.432
S5	14	19.685	7.750	16.038	6.314	409.33	63.447	17.983	7.080	0.97	14	46.03	12.43	23.20	1.567	0.617	1.436
R6	15	19.685	7.750	16.358	6.440	376.77	58.399	18.105	7.128	0.97	15	54.80	34.10	--	0.922	0.363	1.306
S6	16	19.685	7.750	16.505	6.498	361.55	56.041	18.166	7.152	0.97	16	44.90	15.16	22.20	1.483	0.584	1.311
R7	17	19.685	7.750	16.678	6.566	343.55	53.250	18.247	7.184	0.97	17	55.11	40.37	--	0.846	0.333	1.318
S7	18	19.685	7.750	16.726	6.585	338.48	52.465	18.268	7.192	0.97	18	43.79	17.03	21.60	1.516	0.597	1.322
R8	19	19.685	7.750	16.782	6.607	332.61	51.554	18.288	7.200	0.97	19	52.94	44.82	--	0.770	0.303	1.326
S8	20	19.685	7.750	16.815	6.620	329.12	51.013	18.308	7.208	0.97	20	42.10	9.58	9.58	1.184	0.466	1.209
OGV	21	19.685	7.750	16.815	6.620	329.12	51.013	18.301	7.205	0.97	21	9.58	0	0	1.059	0.417	1.209
Combustor 1	22	19.685	7.750	16.815	6.620	329.12	51.013	18.301	7.205	0.97	22	--	--	--	2.540	1.000	--
Combustor 2	23	19.685	7.750	15.926	6.270	420.56	65.187	--	--	1.00	23	--	--	--	5.080	2.000	--
Combustor 3	24	19.812	7.800	11.684	4.600	804.24	124.658	--	--	1.00	24	--	--	--	5.080	2.000	--
Combustor 4	25	21.107	8.310	8.407	3.310	1177.59	182.527	--	--	1.00	25	--	--	--	5.080	2.000	--
Combustor 5	26	21.336	8.400	8.179	3.220	1219.98	189.097	--	--	1.00	26	--	--	--	5.080	2.000	--
Combustor 6	27	21.336	8.400	8.179	3.220	1219.98	189.097	--	--	1.00	27	--	--	--	5.080	2.000	--
Combustor 7	28	21.209	8.350	8.382	3.300	1192.44	184.828	--	--	1.00	28	--	--	--	3.810	1.500	--
Turbine Inlet	29	19.304	7.600	13.335	5.250	612.05	94.868	--	--	1.00	29	--	--	--	2.540	1.000	--
	30	19.380	7.630	13.208	5.200	631.90	97.945	--	--	1.00							

The reason that the above schedules are not functions of T_{T2} as in Figure 2 is that the T_{T2} bias was subverted during NASA engine testing in a manner that controlled the IGV and blade schedules to the 294.3°K (70° F) or higher temperature curve. The "Mehalic" engine had a modified schedule. The actual schedules used during this study are given in Figure 4.

At this point, it is worth mentioning that because a blade row formulation is being used, stage characteristics information was used in the form of a relative total-pressure loss coefficient and deviation angle rather than the more often used non-dimensional work and pressure coefficient as a function of flow coefficient. This approach tends to de-couple the inlet and exit stations of a blade row in a dynamic analysis since volume storage of mass, momentum, and energy are permitted within the work producing volume. Further, splitting a stage volume into two blade row volumes will potentially double the frequency capabilities of a dynamic compression component model.

The third, fourth, and fifth stage bleed flows in the model are removed at the exit of the stator while holding exit air angle constant. The percentage of inlet flow that is removed from each stage is given in Table 2.

Table 2. Bleed Removal Schedule (Percent of Inlet Physical Flow).

Engine	Corrected Speed	Stage 3	Stage 4	Stage 5
Moss	80	3.95%	4.90%	5.78%
Moss	87	2.28	2.83	3.33
Moss	94	0	0	0
Moss	100	0	0	0
Mehalic	87	1.20	1.49	1.76
Mehalic	94	0	0	0
Mehalic	100	0	0	0

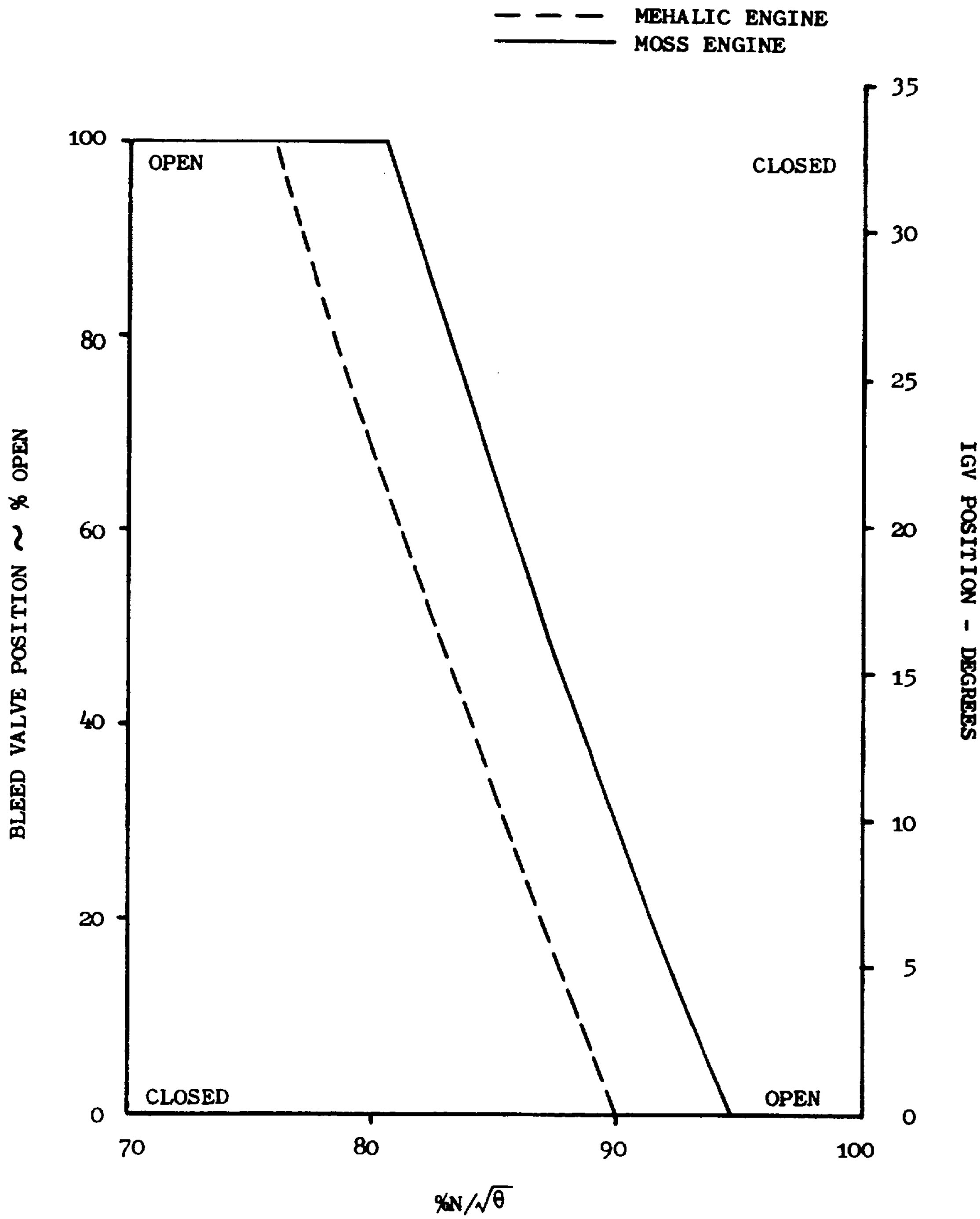

Figure 4. IGV and Bleed Valve Schedules Used in Model.

The boundary conditions imposed upon the model consists of specifying the total pressure and total temperature entering volume 1 and specifying the value of the exit flow function ($W\sqrt{T_S}/P_S$) at the exit of the last volume and its time rate of change. Throttling along all speed lines was accomplished by decreasing the flow function at a rate of 7.5 units per second. This rate was established by throttling at a number of rates and selecting one which would not cause the throttled speed line to deviate from the speed line obtained from steady-state solutions. This rate is unique to the J85-13 model and would have to be determined for each new compression component that is modeled.

3.2 BLADE ROW CHARACTERISTICS DETERMINATION

As in any inter-blade-row compressor analysis, the performance of each blade-row or stage is described by a set of relations known as characteristics, which describe the manner in which work is input and losses are generated as a function of inlet conditions. As part of this program, it was necessary to generate a set of characteristics for both the "Moss" and "Mehalic" J85-13 engines. The data used for obtaining the characteristics resulted from NASA tests of these two engines and were supplied by NASA. Generation of the non-dimensional characteristcs (flow, work and pressure coefficient) was accomplished by compressor design personnel familiar in detail with the aerodynamic design of the J85-13 compressor using the General Electric Stage Characteristics and Stage Stacking computer programs. These programs provided a number of tecniques for determining stage characteristics from test data and calculated overall performance from a stage stacking of such characteristics. The techniques employed in this program for characteristics determination are discussed in the following paragraphs. Assumptions made in the analyses, as noted previously, include associating all the stage losses with the rotor and specifying the stator deviation angle to be constant over the whole compressor map.

In the case of the "Moss" engine, instrumentation provided total-temperature and total-pressure test data at the leading edge plane of each stator blade row at three radial immersions. Based upon radially area averaged test data (20% hub, 60% midspan, and 20% tip), initial non-dimensional stage characteristics calculations indicated certain inconsistencies in the data. These inconsistencies appeared in the form of calculated negative loss coefficients and efficiencies greater than one. In order to determine the possible sources of error, radial and axial distributions of total pressure and total temperature were plotted for each speed for at least the lowest and highest operating pressure ratios. Wall static pressures were also plotted as a check on the tip total-pressure levels.

Two obvious problem areas were revealed by these plots. At 100 percent corrected speed, the stage 2 radial profile of total pressure was inconsistent with the profiles of adjacent stages and other speeds; that is, the pitchline value was considerably lower than hub and tip values. The tip and hub values were held constant and a curve was forced through them. Based on the shapes of the stages 1 and 3 radial profiles, a new mass-weighted average pressure was calculated for rotor 2 only as all other pressures were left unchanged.

The temperature measurements appeared inconsistent in several stages, particularly 2, 6, and 7. These data presented a dilemma since only two options were available in the current data reduction program - one uses measured temperatures at every stage and the other which uses no measured internal temperatures. Since the discharge pressures and temperatures were consistent with data from other J85 tests, the latter option was used.

This option calculates an overall polytropic exponent based on compressor inlet - and discharge - total pressures and total temperatures according to the equation:

$$EX = \ln (T_{T_3}/T_{T_2}) / \ \ln (P_{T_3}/P_{T_2}) \qquad (3\text{-}1)$$

where $EX = \frac{\gamma-1}{\gamma} \ \frac{1}{\eta_{Poly}}$

and η_{Poly} is the polytropic efficiency. This exponent was then used in conjunction with the average interstage total pressures to calculate the interstage total temperature according to the equation:

$$\frac{T_{T_n}}{T_{T_2}} = \left(\frac{P_{T_n}}{P_{T_2}} \right)^{EX} \qquad (3\text{-}2)$$

The advantage of maintaining a constant exponent rather than a constant polytropic efficiency is that an iteration on $\gamma = f(T)$ is avoided. However, a variable γ is used in the remaining calculations.

Upon performing a constant-speed stage-stack analysis it was observed that the non-dimensional stage characteristics did not adequately reproduce the speed line indicated by the test data. Consequently, adjustments were made to the characteristics in order to correct obvious stage mismatches and in the process to obtain a better match with the test data. Figures 5 and 6 indicate the data points and the final non-dimensional stage characteristics used for the 100% corrected speed line of the "Moss" engine. Stage 2 data were modified as previously discussed and this forced changes in the Stage 3 characteristics. These changes represent the worst case in terms of amount of adjustment needed. The complete sets of non-dimensional stage characteristics for the "Moss" engine are documented in Appendix A.

The implied relative total-pressure loss coefficients and deviation angles were calculated along each speed line from the final set of nondimensional characteristics. The relative total-pressure loss coefficient and deviation angle distributions for each rotor on each speed line were then curve fit with a least-squares polynominal in order to provide explicit analytical expressions

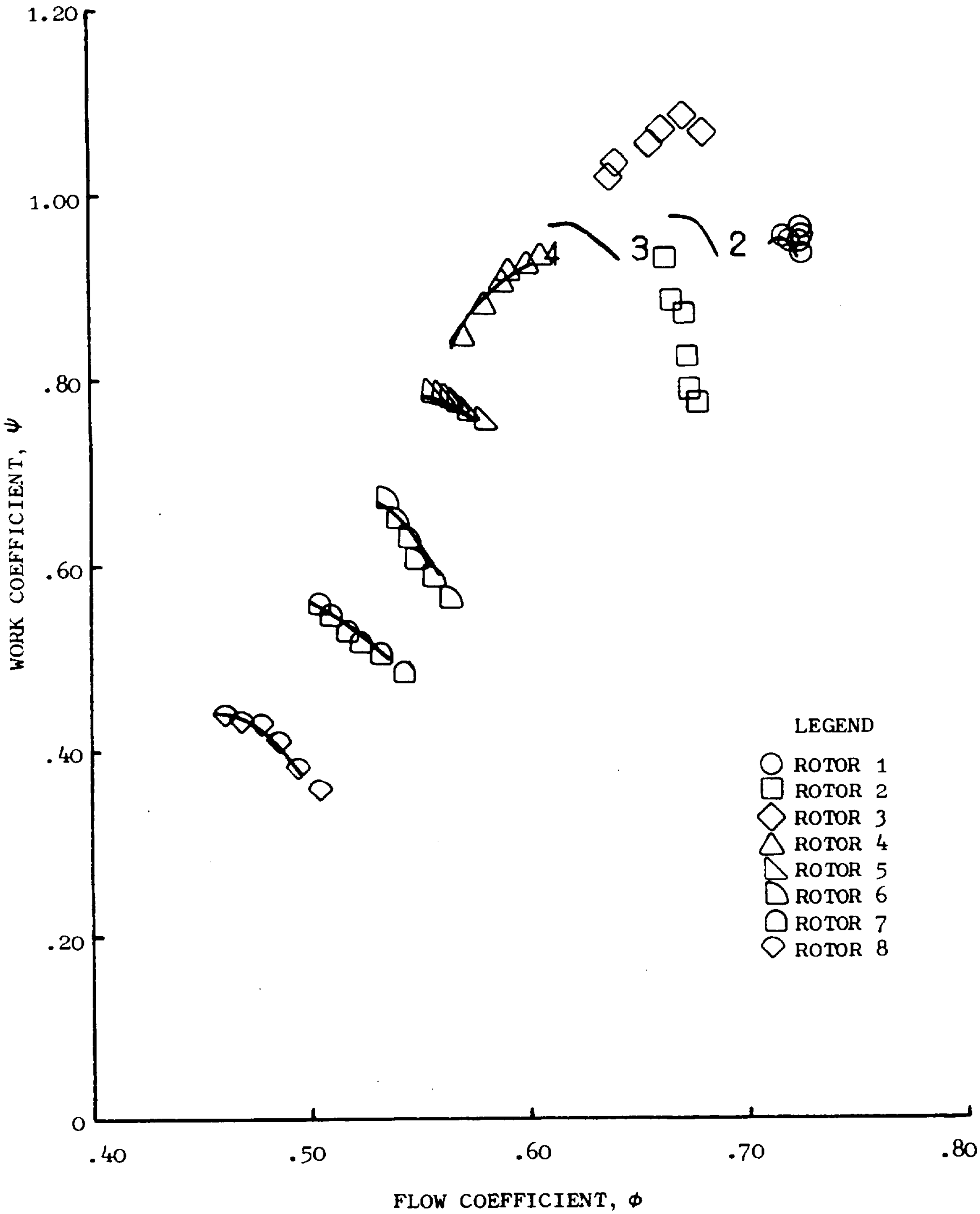

Figure 5. Preliminary and Final Work Coefficients, "Moss" Engine 100% $N/\sqrt{\theta}$.

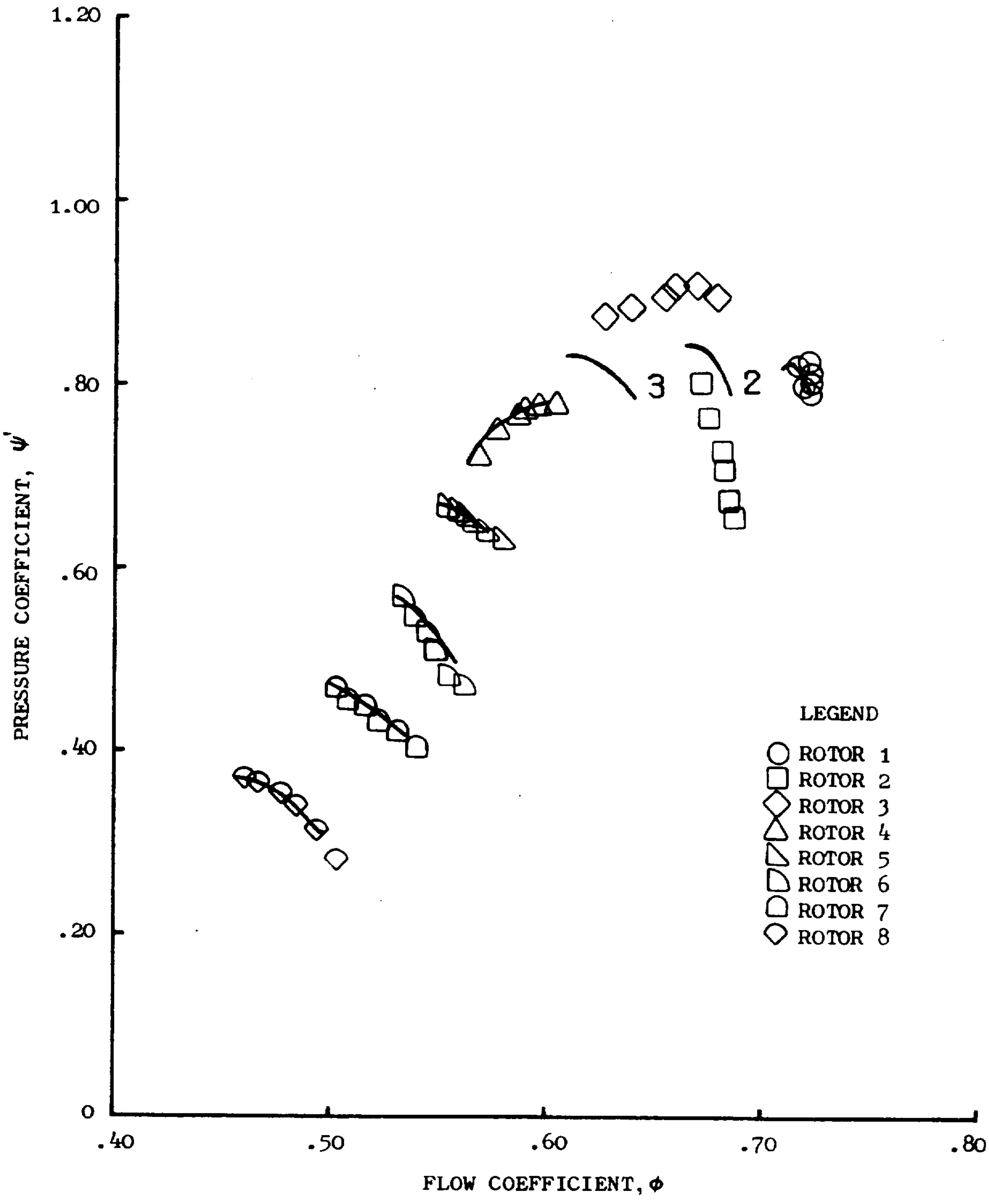

Figure 6. Preliminary and Final Pressure Coefficients, "Moss" Engine 100% $N/\sqrt{\theta}$.

and avoid inefficient interpolation schemes in the dynamic model. Each characteristic was represented by a second, third or fourth order polynomial, whichever gave the best fit of the data points. In general, characteristics between the last data point and to some arbitrary point beyond the surge line were provided by extrapolation of the polynomial beyond which linear extrapolation was used as illustrated in Figure 7. Figures 8 and 9 illustrate the resultant distributions of relative total-pressure loss coefficient and deviation angle used for the "Moss" engine 100% corrected speed line. Curves for the remaining speeds are given in Appendix A.

The nondimensional characteristics for the "Mehalic" engine were derived in a manner similar to that previously discussed. However, the "Mehalic" engine instrumentation provided casing static pressures as the only source of interstage data. This constraint necessitated the use of the constant polytropic exponent method of calculation in conjunction with casing static pressures in order to determine the stage performance and characteristics. These characteristics are documented in Appendix A. Further, Appendix A provides a compilation of the relative total-pressure-loss coefficient and deviation-angle distributions used for all speeds investigated plus tabular listings of the coefficients of the polynomial representations.

3.3 ANALYTICAL TECHNIQUE

3.3.1 Equations of Change

The complete set of non-linear partial differential equations which describe the transfer and storage of mass, momentum, and energy within a fluid are called the equations of change (Reference 9). These equations have been integrated once over an arbitrary volume of the flow system to obtain the macroscopic balances for quasi one-dimensional flow without heat transfer and are reproduced below in the form in which they are used in the dynamic compression component model.

$$\frac{\partial \bar{\rho}_k}{\partial t} = \frac{1}{V} (W_i - W_{i+1}) \tag{3-3}$$

$$\frac{\partial \bar{W}_k}{\partial t} = \frac{g_o}{L} \left[\frac{W_i C_{z_i}}{g_o} - \frac{W_{i+1} C_{z\,i+1}}{g_o} + P_i A_i - P_{i+1} A_{i+1} - P_M (A_i - A_{i+1}) + F_B \right] \tag{3-4}$$

$$\frac{\partial \overline{\rho S}_k}{\partial t} = \frac{1}{V} [W_i S_i - W_{i+1} S_{i+1} + S_F] \tag{3-5}$$

CURVE FIT - FOURTH ORDER POLYNOMIAL (OR LOWER) IN TAN i
FOR DATA RANGE

EXTRAPOLATED REGIONS - STRAIGHT LINE WITH SLOPE MATCHING
SLOPE OF POLYNOMIAL AT MATCH POINT

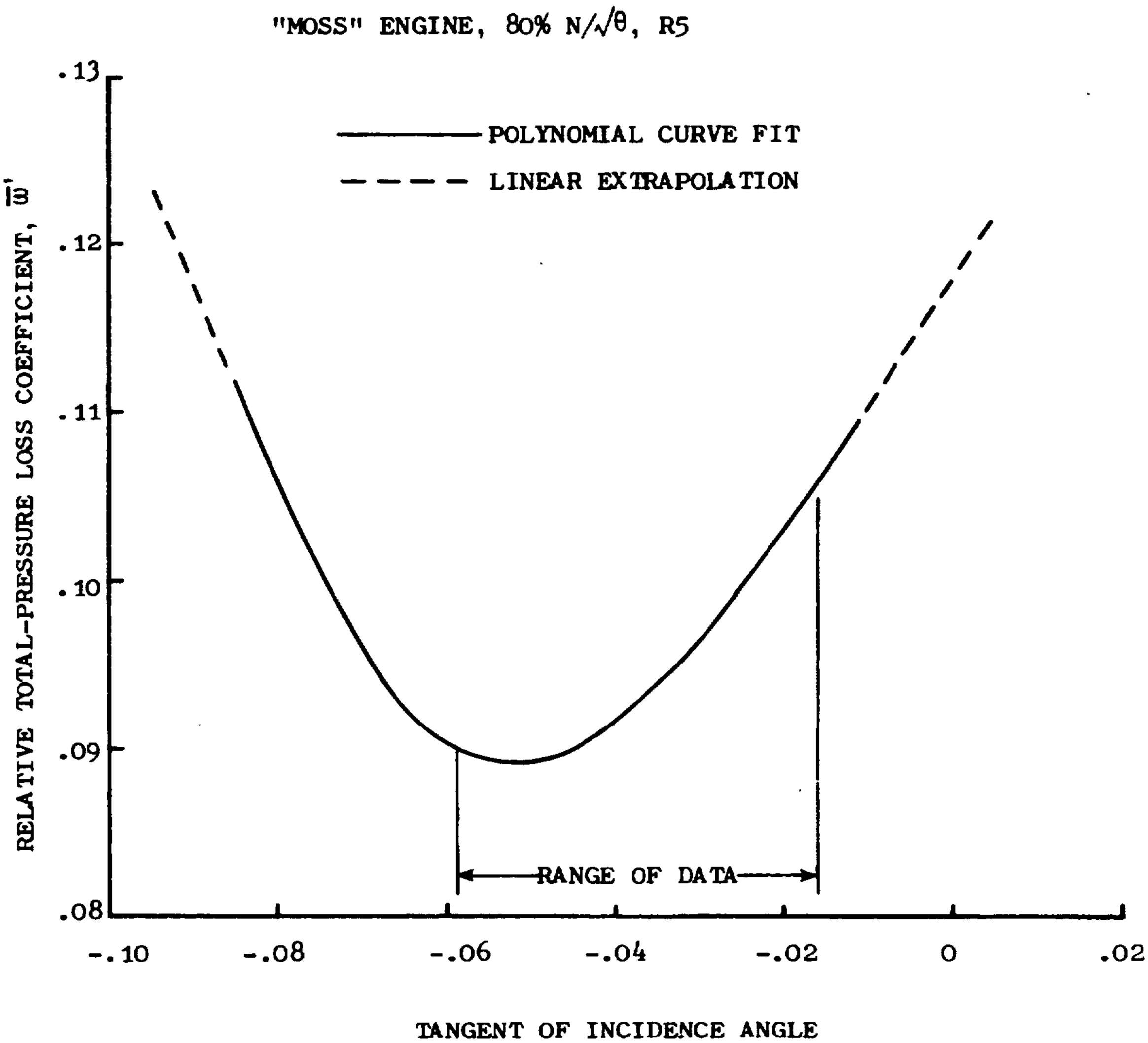

Figure 7. Loss Coefficient Polynomial Representation.

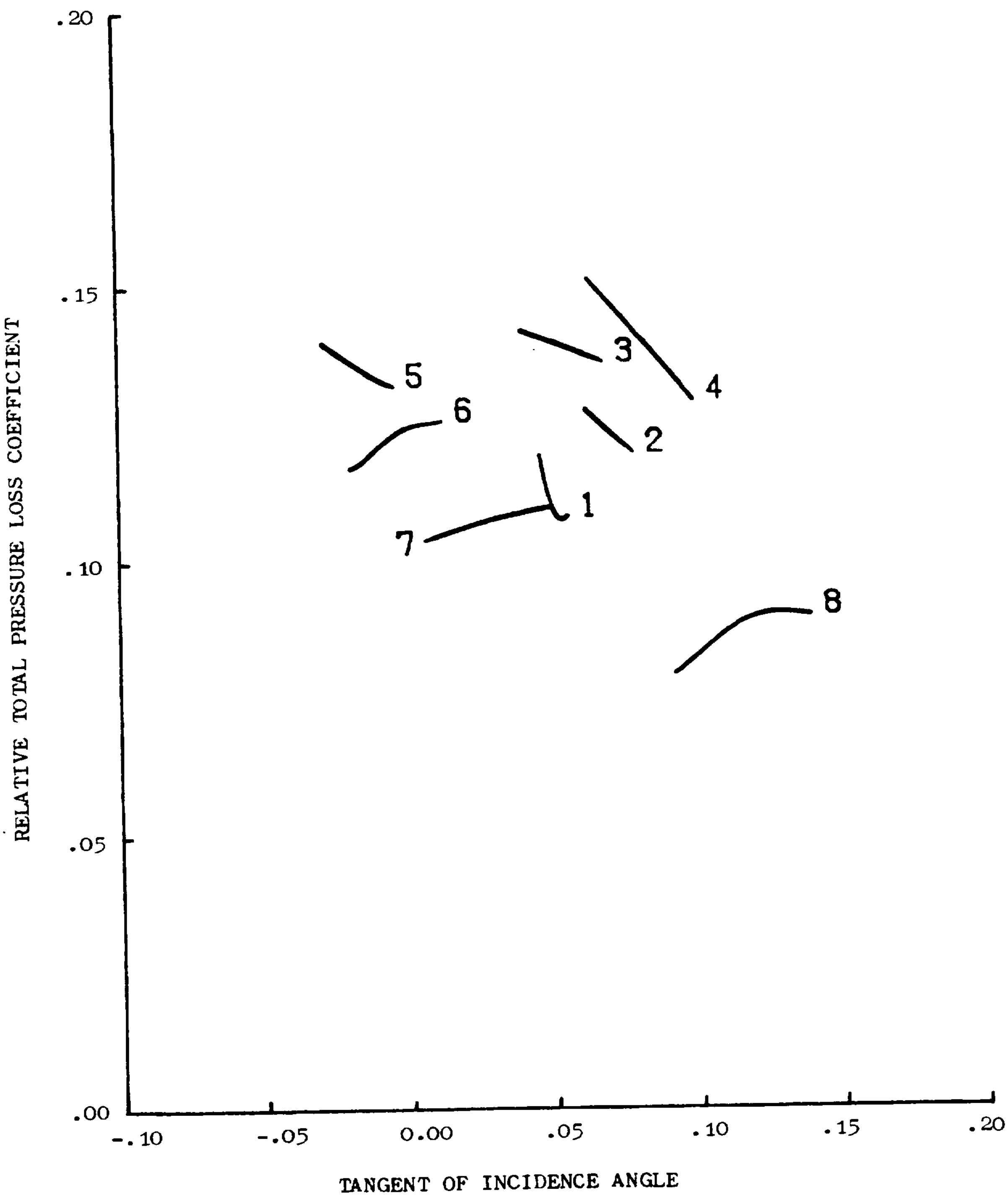

Figure 8. Rotor Total-Pressure Loss Coefficient, "Moss" Engine 100% $N/\sqrt{\theta}$.

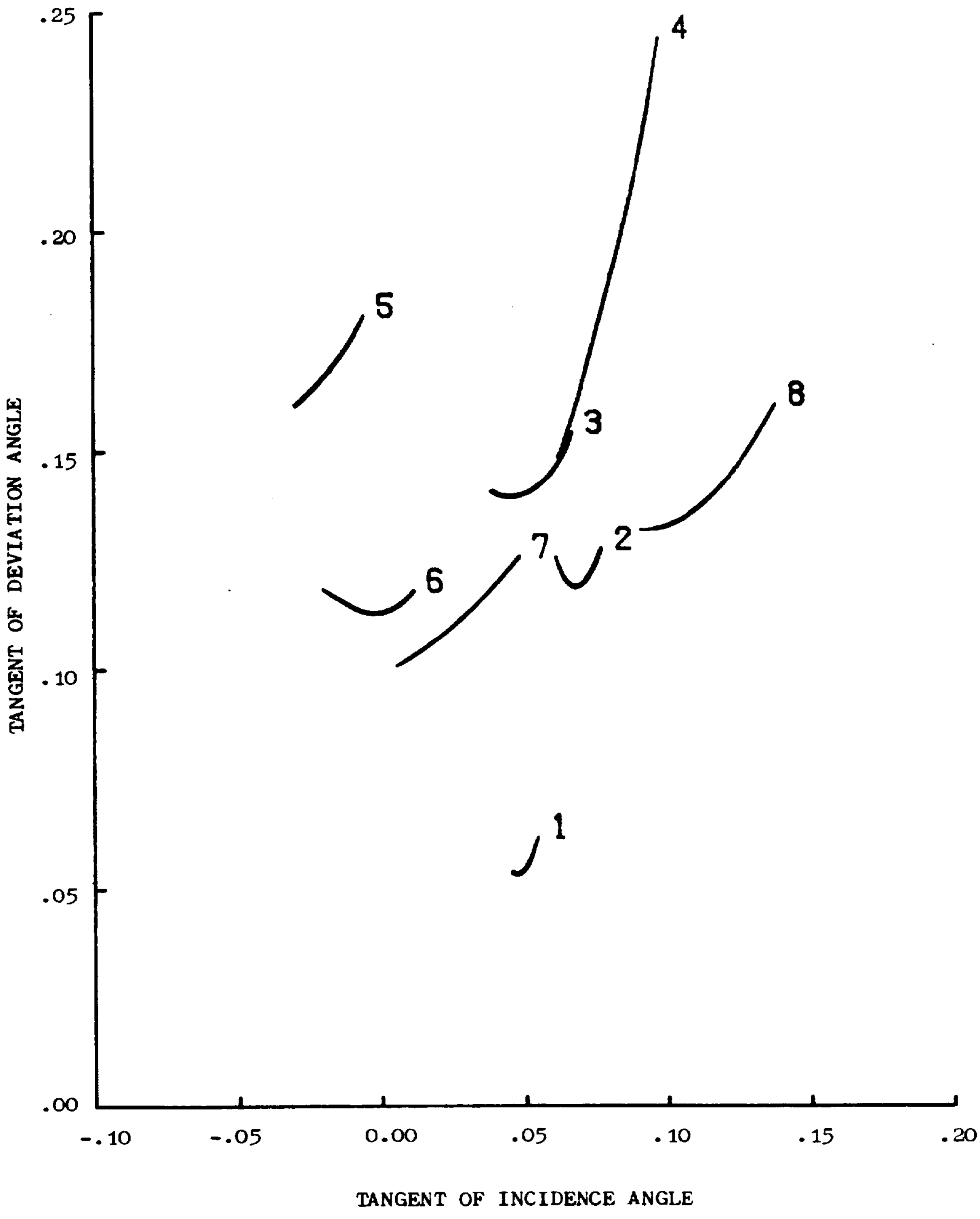

Figure 9. Rotor Deviation Angle, "Moss" Engine 100% $N/\sqrt{\theta}$.

The subscripted variables on the right-hand side of the equations refer to quantities at the inlet and exit of the control volume. Variables on the left-hand side refer to volume averaged quantities, i.e., in generalized form

$$\bar{\xi} = \frac{\int \bar{\xi}\, dV}{\int dV} \tag{3-6}$$

The energy equation (Equation 3-5) was derived by combining the equation of change for energy and one of the thermodynamic TdS relationships.

3.3.2 Force, Pressure and Entropy Production Terms

This set of equations (other than being applicable to quasi one-dimensional flows without heat transfer and a finite, but small volume) properly and exactly describes the state of a fluid in motion. In order for a solution to be obtained, it is necessary to supply the caloric and thermal equations of state and expressions for F_B, P_M, and S_F.

F_B (Equation 3-4) represents the blade force acting upon the fluid. The blade force can be determined through reference to the following sketch:

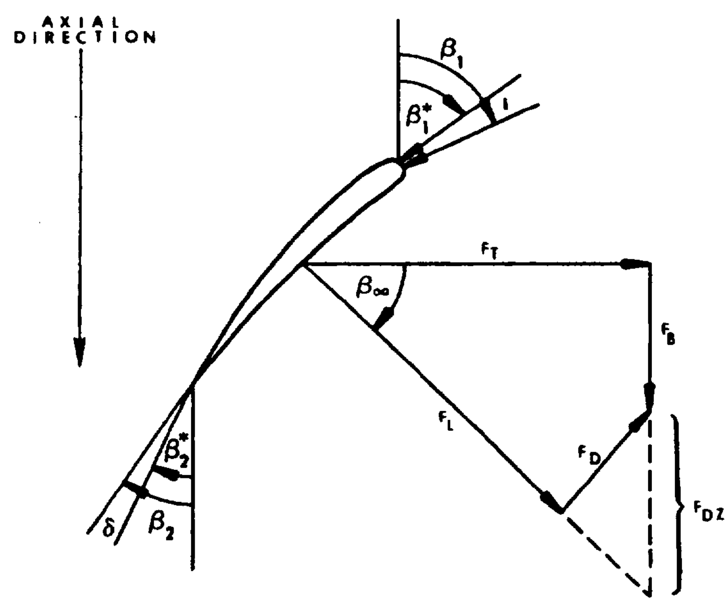

$$F_B = F_T \tan \beta_\infty - F_{DZ} \tag{3-7}$$

where

$$F_T = \frac{2}{g_o} \left(\frac{r_2 W_2 C_{U_2} - r_1 W_1 C_{U_1}}{r_1 + r_2} \right) \tag{3-8}$$

and is derived from the Euler Turbine Equation. The direction of the lift vector is assumed to be

$$\beta_\infty = \frac{1}{2} \ (\beta_1 + \beta_2) \tag{3-9}$$

The drag force (F_D) is obtained from the following equation

$$F_D = \bar{\omega}' \ \frac{P_1'}{P_{T_1}'} \ \frac{P_{d_1}'}{q_1'} \ \ (A_{1\beta} \cdot q_1') \tag{3-10}$$

which is based upon an analogy with the drag coefficient for duct flows. The term F_{DZ} in Equation 3-7 is then obtained from the relation $F_{DZ} = F_D/\cos \beta_\infty$.

The prime (′) symbol indicates the value of the parameters with respect to the relative velocity frame of reference and $A_{1\beta}$ is the flow area perpendicular to the direction of the entrance relative velocity vector. It should be noted that in steady flow a momentum balance, in general, will not give the same total-pressure rise per stage as does an energy balance. The reason for this difference is that the direction of the blade lift vector is not exactly the arithmetic average (Equation 3-9) of the flow angles. Comparison of the steady-state momentum and energy balance solutions permits the determination of a small "correction angle" which can then be added to β_∞ to give the proper lift direction. It should be noted that the more familiar expression for the lift direction given by

$$\tan \beta_\infty = 1/2 \ (\tan \beta_1 + \tan \beta_2) \tag{3-11}$$

also required use of a correction angle. Hence, Equation 3-9 is used in this formulation since it results in simple analytical relationships without introducing any compromises to accuracy or frequency response. Appendix B provides documentation of the correction angle relations used in this program.

P_M (Equation 3-4) represents the mean pressure over the lateral surface area of the volume element as sketched below:

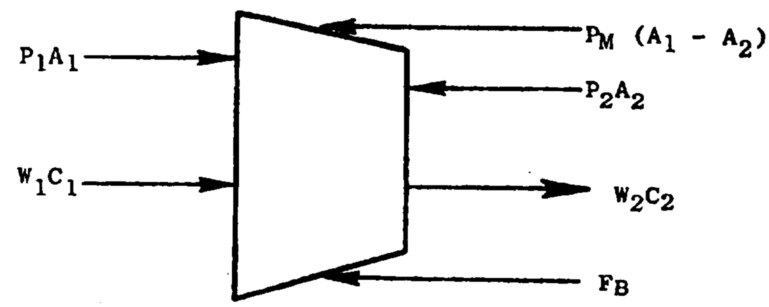

where $P_M = \int PdA / \int dA$. Although an analytical expression for the mean pressure acting on lossless, blade free volumes in steady flow can be derived, it leads to redundancy in the system of equations describing unsteady flow. Therefore, based upon steady-state momentum-balance analyses, an approximate linear expression for calculating blade-free volume mean pressure as a function of area convergence and inlet and exit pressures has been established for the J85-13 compressor model. Figure 10 illustrates the correlation developed in terms of a scale factor (FV) for zero-swirl free volumes; its form is given by the following equation:

$$P_M = P_1 + FV\ (P_2)\ /\ (1 + FV) \qquad (3\text{-}12)$$

Similarly, an additional correlation was established for the non-zero swirl free volume between the IGV and the first rotor. As shown in Figure 11, this correlation is a function of IGV exit air angle. It should be noted that the correlations presented in Figures 10 and 11 are unique to this formulation and the J85-13 compressor; they are probably valid only for other compressors with similar Mach numbers and area changes.

For blade-row volumes, investigations have revealed that a good approximation for the mean pressure is two-thirds the higher of the inlet or exit static pressures plus one third the lower pressure. Deviations from this approximation are accounted for in the lift direction correction angle.

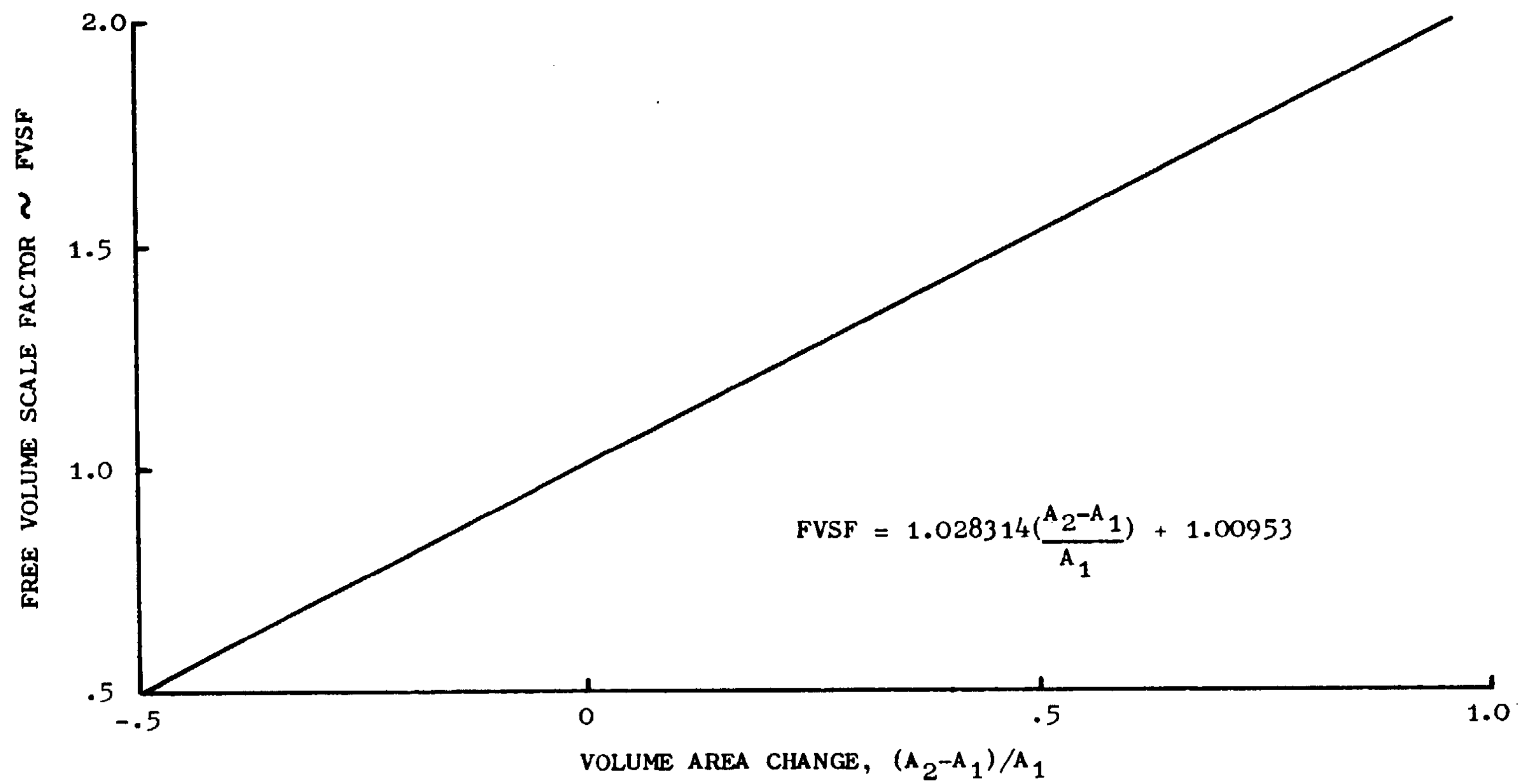

Figure 10. Mean Pressure Correlation For Swirl-Free Volumes.

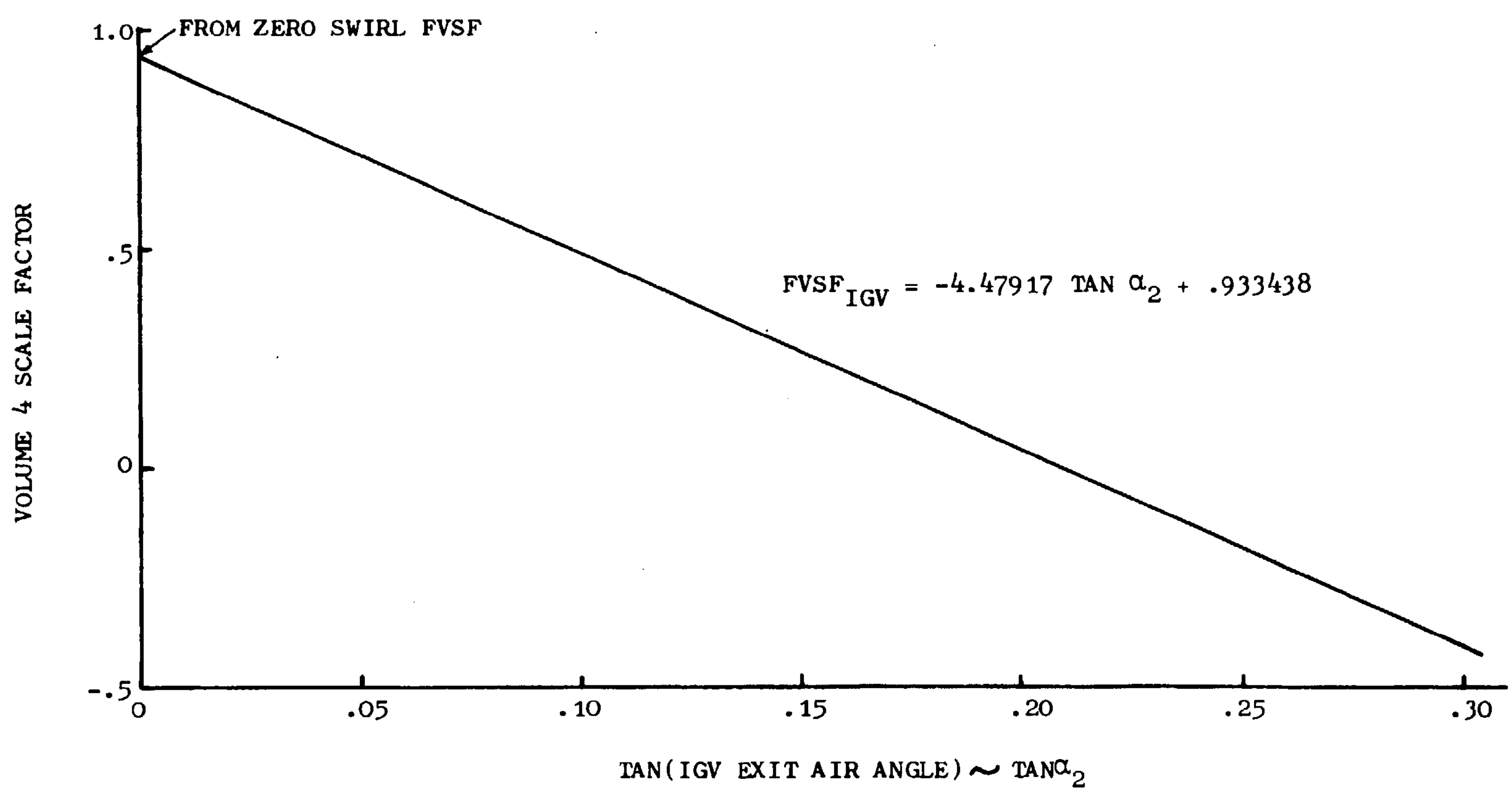

Figure 11. Mean Pressure Correlation For IGV Trailing Edge Volume.

S_F (Equation 3-5) is the term which represents the total rate of irreversible conversion of mechanical to internal energy and, in the case of this model, represents the entropy production due to blade row losses. It can be obtained from the expression:

$$S_F = \bar{W}R \ln \frac{\left.P'_{T_2}/P'_{T_1}\right)_{ideal}}{\left.P'_{T_2}/P'_{T_1}\right)_{actual}} \tag{3-13}$$

where the ideal relative total-pressure ratio which accounts for the change in pitch line radius (Reference 10) from the entrance of a rotor blade row to its exit is written as

$$\left.\frac{P'_{T_2}}{P'_{T_1}}\right)_{ideal} = \left\{1 + \frac{\gamma - 1}{2} M_T^2 \left[1 - \left(\frac{r_1}{r_2}\right)^2\right]\right\}^{\gamma/(\gamma - 1)} \tag{3-14}$$

M_T is equal to the ratio of the blade row exit pitch line wheel speed to the inlet relative stagnation velocity of sound $(2\pi N r_2/a'_{T_1})$. In the case of a stator, the ideal relative total-pressure ratio is equal to one. The actual relative total-pressure ratio requires knowledge of the relative total-pressure loss coefficient which is defined as

$$\bar{\omega}' = \frac{\left.P'_{T_2}\right)_{ideal} - \left.P'_{T_2}\right)_{actual}}{P'_{T_1} - P_1} \tag{3-15}$$

Equation 3-15 can be rewritten in the form

$$\left.\frac{P'_{T_2}}{P'_{T_1}}\right)_{actual} = \left.\frac{P'_{T_2}}{P'_{T_1}}\right)_{ideal} - \bar{\omega}' \left\{1 - \left[\frac{1}{1 + \frac{\gamma - 1}{2} (M'_1)^2}\right]\right\}^{\gamma/(\gamma - 1)} \tag{3-16}$$

Hence, Equations 3-14 and 3-16 when substituted into Equation 3-13 provide complete definition of the entropy production term.

As might be expected, the input to the program, in addition to physical speed, inlet conditions and compressor geometry, requires the relative total-pressure loss coefficient ($\bar{\omega}'$) for the rotors, the tangent of the deviation angle (δ) for the rotors, and the tangent of the correction angle (β_c) for both the rotors and stators. The relative total-pressure loss coefficient and the deviation angle are derived from stage stacking results based upon clean inlet flow test data obtained by throttling at constant speed. The correction angle is obtained by comparing steady flow force and energy balance solutions on a blade row basis. These parameters can be represented as functions of incidence angle and are input to the program in this manner. These parameters, in conjunction with the velocity triangles and other ancillary relations, permit the determination of the thermodynamics of the fluid at each station. Blade-free volumes are treated as lossless volumes with no imposed blade force; hence, the F_B and S_F terms of Equations 3-4 and 3-5 are identically zero.

3.3.3 Calculation Technique

Time dependent solution of the system of equations (Equations 3-3 through 3-5 and the relations for F_B, P_M, and S_F) that comprise the dynamic digital compression component model is effected through a Taylor series which establishes the values of the three independent volume-averaged variables at the next increment in time. In the case of this model and with reference to the left hand side of Equations 3-3, 3-4, and 3-5, the variables $\bar{\rho}$, $\bar{W}$, and ρS are the ones for which a solution is sought. Solution is now straightforward and will be illustrated for one variable - the volume-averaged density. Considering that this method is applicable to any volume, the subscript "k", indicating the k-th volume will be dropped. The Taylor series for volume-averaged density correct to second order can be written as:

$$\bar{\rho}(t+\Delta t) = \bar{\rho}(t) + \frac{\partial\bar{\rho}(t)}{\partial t}\Delta t + \frac{\partial^2\bar{\rho}(t)}{\partial t^2}\frac{(\Delta t^2)}{2} \quad (3\text{-}17)$$

where:

$\bar{\rho}(t)$ is established by the initial conditions or from the previous time step.

$$\frac{\partial\bar{\rho}(t)}{\partial t} = \frac{1}{V}(W_i - W_{i+1}) \text{ from Equation 3-3 and differentiating}$$

Equation 3-3 with respect to time yields:

$$\frac{\partial^2\bar{\rho}(t)}{\partial t^2} = \frac{1}{V}\left(\frac{\partial W_i}{\partial t} - \frac{\partial W_{i+1}}{\partial t}\right) \quad (3\text{-}18)$$

Examination of Equation 3-18 reveals that the right-hand side is composed of derivatives of station values of flow with respect to time. Since Equation 3-4 will supply only the derivatives of the volume-averaged flow with respect to time, use of an interpolation scheme for obtaining station values from volume-averaged values will permit Equation 3-18 to be solved for the second partial derivative of volume-averaged density with respect to time. Equations 3-3 and 3-18 then can be substituted into Equation 3-17 to obtain the estimate of the volume averaged density correct to second order at the next increment in time. Equation 3-18 implies that first derivatives with respect to time of a large number of terms (e.g. F_B, P_M, and S_F) will be required. Although these expansions are lengthy, they can be derived in a straightforward manner and will not be reproduced here due to lack of space. Similarly, this technique can be used for the remaining two variables ($\bar{W}$ and ρS) and can be continued from one time step to the next for the desired number of time steps.

This calculational scheme is numerically stable, and (to date) anomalous behavior has occurred only when a physical aerodynamic instability in the flow would be expected to occur.

Now the calculational technique utilized in the Dynamic Digital Blade Row Compression Component Stability Model can be discussed and is illustrated in Figure 12 in block diagram format. The use of the blade row building block concept allowed construction of a generalized model which is independent of the particular compression component being simulated.

Block I is a statement of the required dependent variable information, that is, volume-averaged density, flow, and entropy which are available from either a steady-state (SS) initialization or a previous time step of a time dependent (TD) analysis.

Block II presents the macrobalances in the form they are used in the analysis. The variables on the right-hand-side of the equations are station-value properties. Knowledge of these parameters allows the first time derivatives of the volume averaged properties to be calculated. However, as stated in Block I, only volume-averaged quantities are available at the beginning of each time step. Therefore, Block II illustrates that it is necessary to interpolate between volume-averaged parameters in order to obtain station-value properties.

In the case of blade-free volumes, where no blade forces or entropy production takes place, it is only necessary to calculate station axial velocity in order to evaluate the equations of change. As shown in the lower branch of Block IV, the assumption of constant absolute flow angle across the volume is made. Total pressure, total temperature and other desirable parameters are also calculated at this point. A special case of the blade free-volume calculations is the imposition of the boundary conditions. At the model inlet, constant total pressure and total temperature as well as constant entropy are maintained. At the exit of a model of a turbojet compressor and burner, a specified exit flow function boundary condition is imposed. This

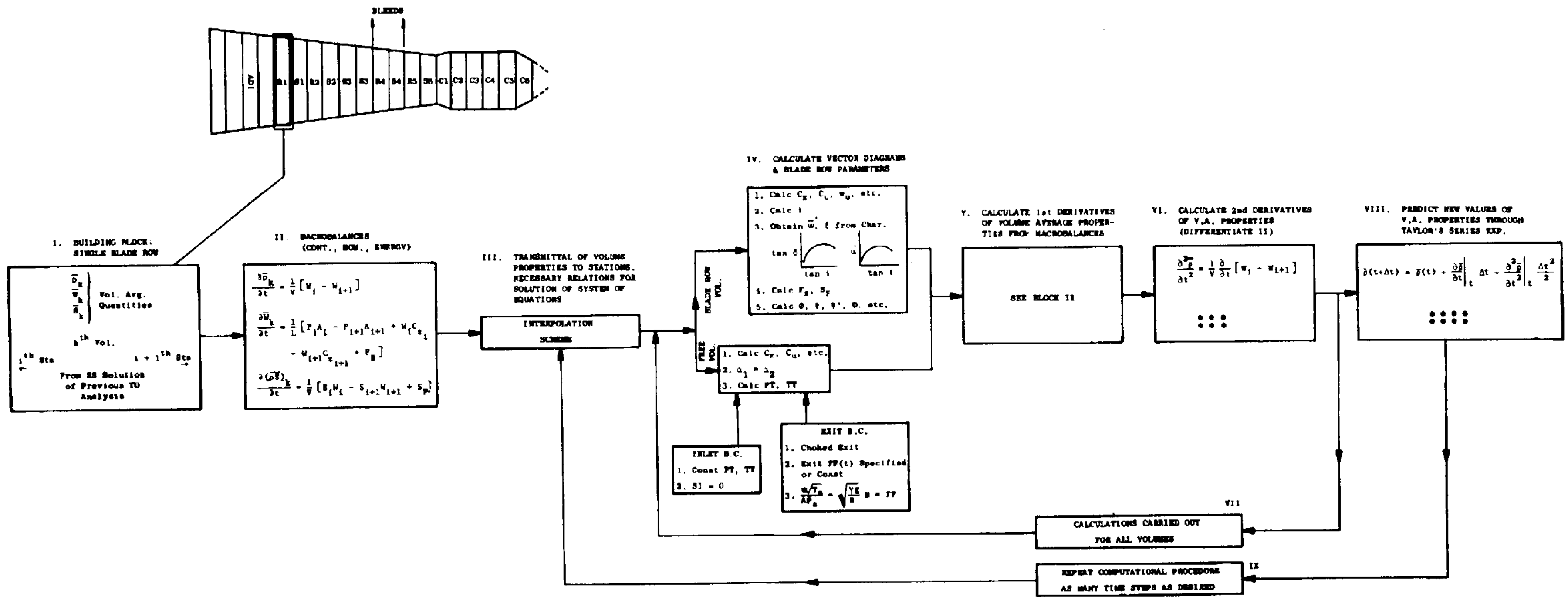

Figure 12. Dynamic Model Block Diagram.

boundary condition was derived from the assumption that a fictitious, zero-length choked nozzle existed at the burner exit. The fictitious, zero-length choked exit condition implies the upstream flow function at the burner exit is specified and can be either held constant or changed at some rate to simulate a constant-speed throttling process.

As indicated in the upper branch of Block IV, the presence of a bladed volume requires the net axial blade force, entropy production, and station axial velocities to be calculated. Calculation of the net axial force and entropy production terms require knowledge of the loss coefficient and deviation angle. This information is available as polynomial representations which are functions of incidence angle. Stationary blade rows are assumed to be lossless with constant deviation angles.

Once the flow conditions at the stations are completely described, various quantities of interest can be calculated such as stage coefficients, diffusion factors, etc. With all the necessary quantities on the right hand side of the macrobalances available, the first time derivatives of the volume averaged properties can be calculated as indicated in Block V using the macrobalances of Block II.

Expressions for the second time derivatives of the volume averaged quantities are obtained from differentiating the macrobalances with respect to time. Analytical expressions for the time derivatives of the station properties can be evaluated by interpolating between volumes and through use of the macrobalances. Thus, as indicated in Block VI, the second time derivatives of volume averaged properties can be calculated.

This procedure for calculating station properties and evaluating first and second time derivatives of the volume averaged properties can be carried out for any number and types of volumes (Block VII) and is not dependent on the particular geometry being modeled. Once these calculations are carried out for all the volumes, the solution can be advanced to the next time step through use of the second-order Taylor's series approximations, Block VIII. As specified in Block IX, the technique can be repeated for as many time steps as required by the event being simulated.

3.4 STEADY-STATE OPTION - INITIALIZATION

Although the dynamic compression system model is of prime interest in this study, many of the preliminary tasks required the use of steady-state analyses. In addition, all explicit time-dependent calculation schemes require initial conditions with which to start the solution procedure. Therefore, an optional steady-state solution technique was included as an integral part of the computer program which can be used to supply initial conditions to a transient solution or to perform separate steady-state analyses. The steady-state option was made compatible with the equations of change of Section 3.3 in that the time derivatives are set to zero and the downstream conditions at each volume are solved by satisfying the steady-state continuity and momentum equations rather than the more often used energy equation. Compatibility between the steady-state and dynamic portions of the program was further maintained through the use of identical techniques for including the loss coefficients, deviation angles, lift direction correction angles (β_C), and the mean pressures (P_M).

3.5 PARALLEL COMPRESSOR

As it was the primary purpose of this program to analyze circumferential distortion, the macrobalances and the calculation technique were formulated in a manner such that a dynamic parallel-compressor analysis, constrained by the well-known parallel-compressor boundary conditions, could be performed. That is, it was assumed that the compressor was made up of several sectors, acting as independent compressors operating with different inlet total-pressure and/or total-temperature conditions. Each sector operated on its clean inlet characteristics and exited to a common static pressure downstream of the compressor discharge diffuser. This exit point provided the only location where inter-communication between sectors was allowed; downstream of this point the flow was assumed to be completely mixed and was modeled as a single duct flow which terminated in a choke plane at the turbine diaphragm (A4). The model developed during this study was unique in that the overall physical inlet flow was specified and the flow split to the various sectors was determined as a function of the imposed distortion levels and the calculated compressor diffuser-discharge uniform static-pressure boundary condition.

When simulating a temperature distortion, the model incorporated an interpolation technique to determine blade-row characteristics for corrected speeds for which data were not available. The technique is illustrated in Figure 13. For each blade row at each corrected speed for which data were supplied, values of the characteristic at intervals of constant percent tan(i) of the data range were established. The sets of characteristic data at constant percent intervals were then curve fit with a cubic spline to establish the blade-row characteristic as a function of corrected speed. Interpolating the spline-fit data at each constant percent interval for a particular corrected speed supplied a set of characteristic data as a function of tan(i). These data were then fit with a least-squares polynomial to provide an analytical expression for the blade-row characteristic. Beyond the range of available data, the spline-fit curve fits were linearly extrapolated.

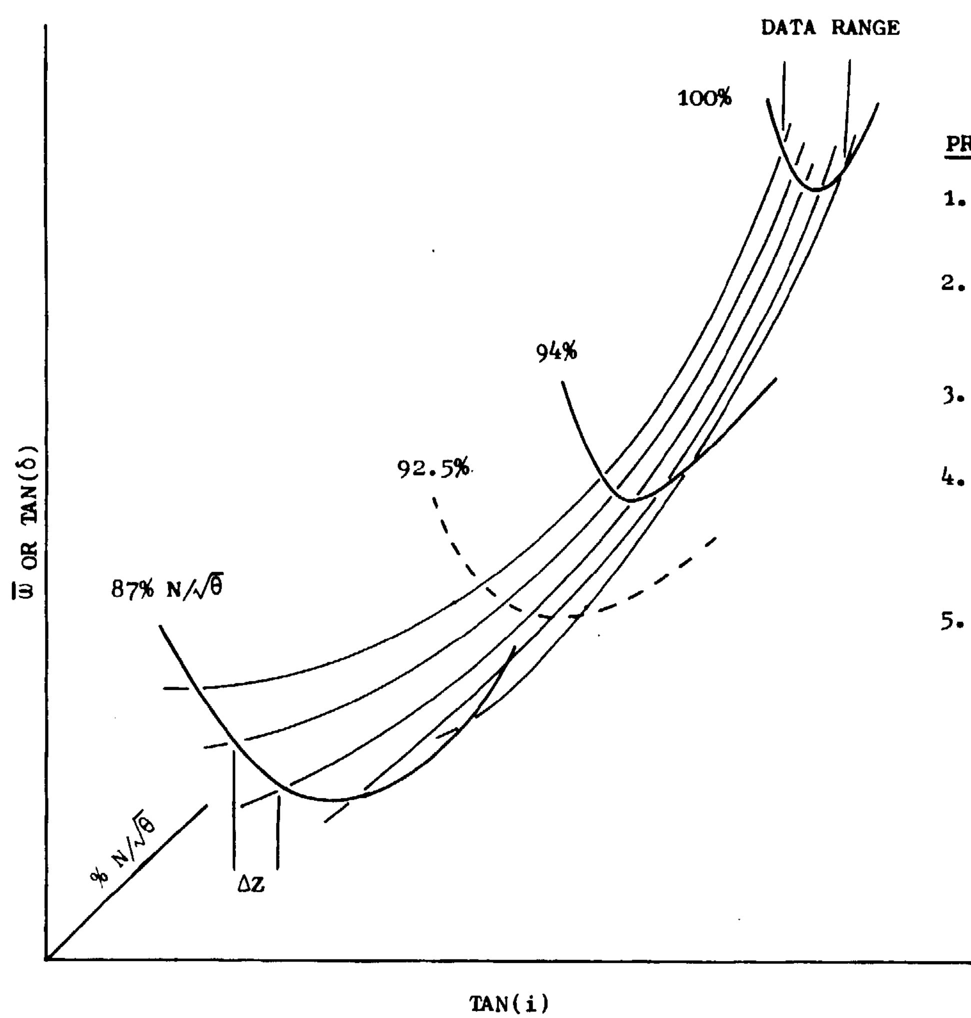

PROCEDURE:

1. ΔZ = CONSTANT PERCENT ΔTAN i OF DATA RANGE
2. ESTABLISH LINES OF $\bar{\omega}$ VS. % N_C ALONG LINES OF CONSTANT ΔZ USING A CUBIC SPLINE FIT TECHNIQUE
3. INTERPOLATE FOR VALUES OF $\bar{\omega}$ AT DESIRED % N_C
4. LEAST-SQUARE CURVE FIT INTERPOLATED DATA TO ESTABLISH POLYNOMIAL REPRESENTATION OF $\bar{\omega}$ VS. TAN i FOR DESIRED % N_C
5. FOR DESIRED % N_C BEYOND RANGE OF CLEAN INLET SPEED LINES, SPLINE FITS ARE LINEARLY EXTRAPOLATED

Figure 13. Speed Line Interpolation For Blade Row Characteristics.

4.0 RESULTS

Apart from determining suitable blade row characteristics for both of the J85-13 engines considered in this program, the objective of this study was to establish the validity and capabilities of the computer model. This involved verification of the ability of the pitch-line analysis technique to accurately represent the performance of the compressor and the demonstration of the ability to predict the stability limit of the compressor for clean inlet flows. Once the capability of the model was established, the stability limit of the compressor was predicted when subjected to circumferential, 180° 1/rev total-pressure, total-temperature, and combined total-pressure and total-temperature distortions. Combined inlet distortion conditions included configurations where the total-pressure distortion was opposed, coincident, and 90° over-lapped with the total-temperature distortion.

4.1 CLEAN INLET ANALYSES

Clean inlet compressor maps for both versions of the J85-13 considered are presented in Figures 14 and 15. It should be noted that the "Moss" engine clean inlet data (Reference 4) used in this study were taken from NASA data readings 521-543 which were obtained after the distortion tests had been run. The "Mehalic" engine clean inlet data (Reference 5) were taken from NASA data readings 13-38. As can be seen, there is excellent agreement between the NASA test data and the speed lines generated from the previously determined blade-row characteristics. Included on the figures are the stability limits obtained for each speed line by dynamic throttling simulations. The throttling simulations were accomplished by specifying the decrease in the flow function at the exit of the model as a linear function of time. The choked exit boundary condition was never explicity calculated, but rather was handled by assuming a zero length choked exit nozzle existed. As such, a change in the exit area of a choke plane would impress a change in upstream flow function. The rate of change of the flow function with time was chosen low enough such that the dynamic solution did not deviate from the steady-state speed line. It was the intent of this portion of the study to illustrate that the stability limit of a compressor could be determined from the dynamic response of a quasi-steady-state representation of the speed line. Figure 16 provides a more detailed view of the throttling process for the 94% $N/\sqrt{\theta}$ "Moss" engine speed line. It should be noticed that up to time step 5000 the decrease in flow is well behaved, that is, the flow change per each 1000 time-step increment is roughly the same. However, in the region of the experimentally determined surge line, the flow decreased about twice as much in 700 time steps as it did in the previous 1000 time steps even though the throttling rate was maintained at the same value as used throughout the throttling process. This behavior is typical once the stable operating region is exceeded. Special note should be taken of time step 5400 as further discussion will be undertaken later in this section.

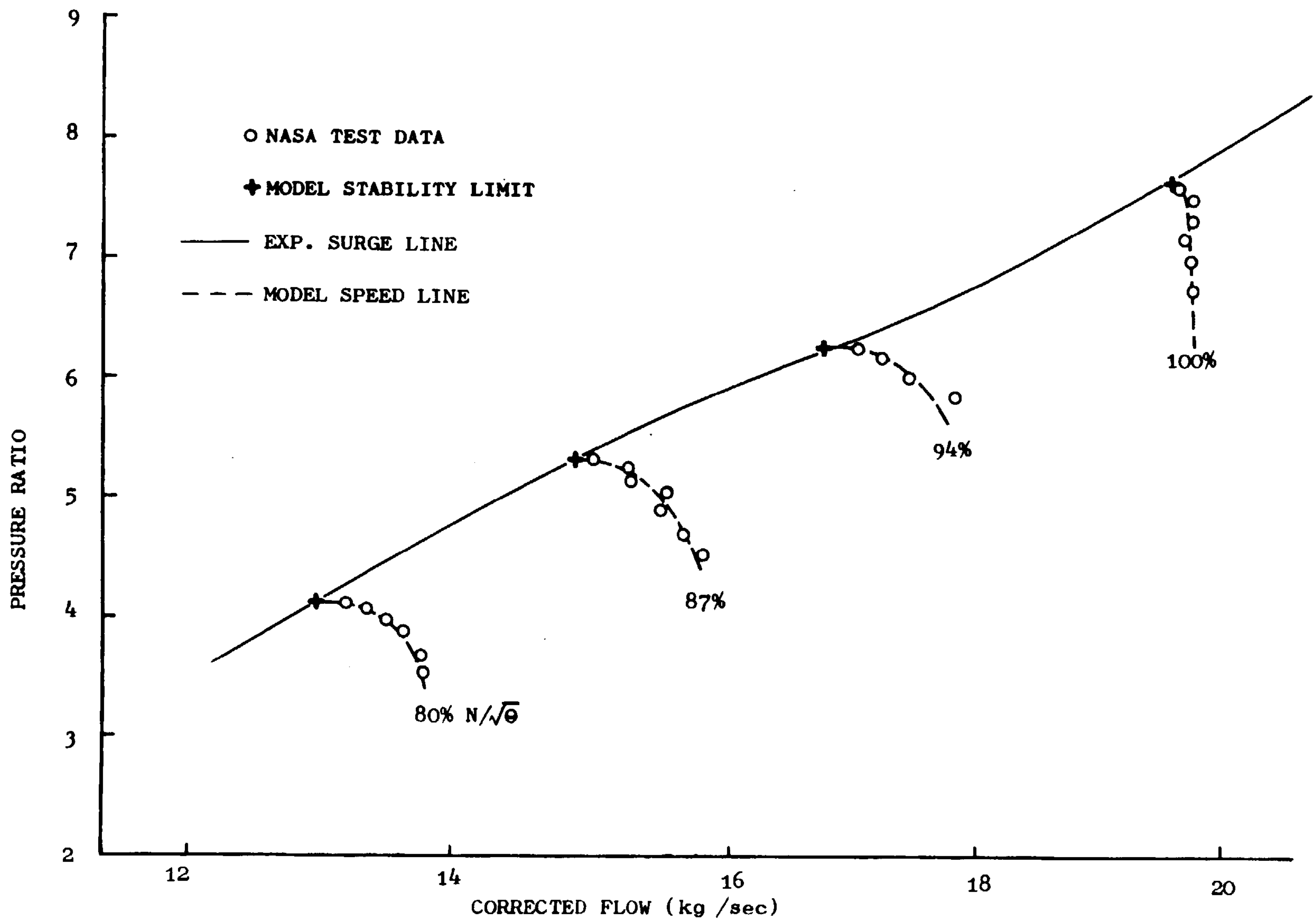

Figure 14. Clean Inlet Flow Compressor Map, "Moss" Engine.

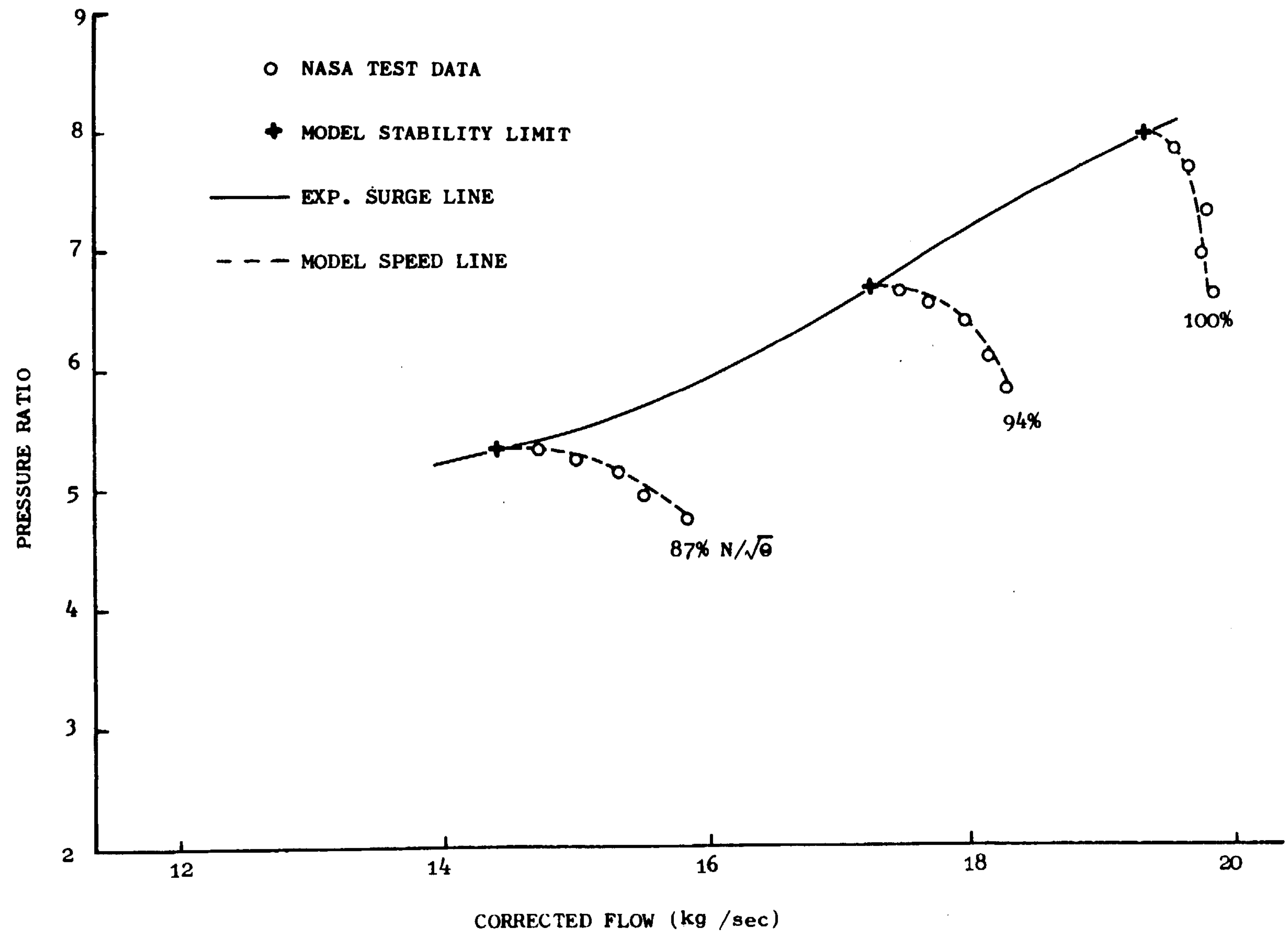

Figure 15. Clean Inlet Flow Compressor Map, "Mehalic" Engine.

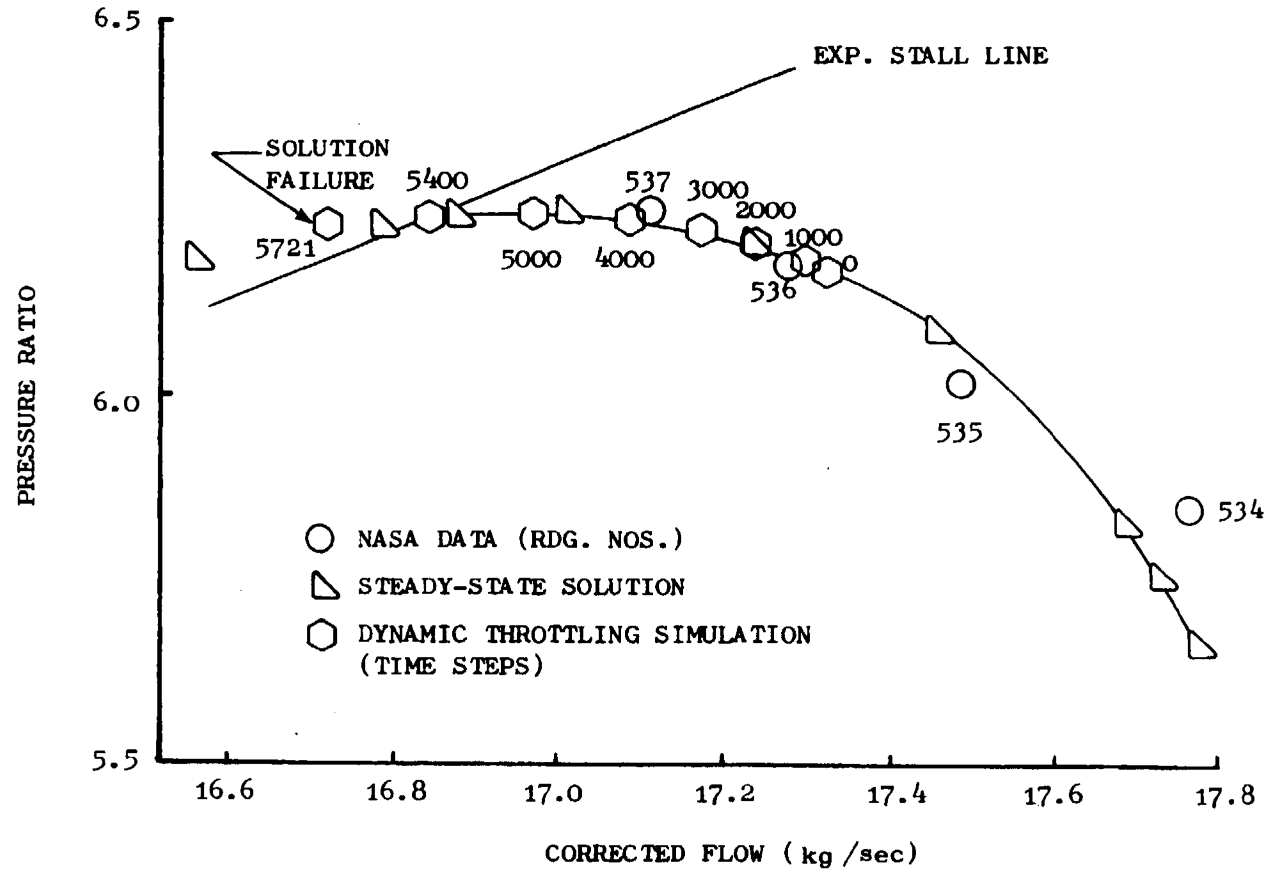

Figure 16. Detailed Throttling Representation of "Moss" Engine at 94% $N/\sqrt{\theta}$.

In an effort to establish stability criteria, many of the traditional compressor performance parameters were investigated for indications of anomalous behavior during the throttling simulation, particularly in the experimentally determined surge region. Figures 17 to 26 present the time history plots of several variables for the "Mehalic" engine, 100% corrected speed line near the surge point. These plots show the time histories of:

Overall Compressor Total-Pressure and Total-Temperature Ratio,

Tangent of Incidence Angle at Entrance to Rotors,

Rotor Diffusion Factors,

Stage Total-Pressure Ratio,

Rotor Axial Velocity Ratio,

Stage Total-Temperature Ratio,

Rotor Flow Coefficients,

Rotor Work Coefficients, and

Rotor Pressure Coefficients, respectively.

As can be seen, none of these parameters exhibit anomalous behavior as the solution progresses through the region of the experimentally determined surge point, that is, the time when the model pressure ratio and corrected flow equal the values at the experimentally determined surge line. As a result, the performance of several of the dynamic variables of the throttling simulation was investigated. Figure 27 presents the time history response of the ratio of the rotor-volume-flow time derivative to exit-volume-flow time derivative. As the compressor is throttled, the parameter exhibits either a constant value of one or a monotonicly increasing value in the region of the experimentally determined instability. Since the level of the exit flow derivative is constrained by the imposed exit boundary condition, the behavior of the flow derivative ratio indicates that internal perturbations are amplified significantly as the model nears the surge point. It was observed that once large amplifications had been encountered, the failure of the dynamic solution was imminent as it would predict impossible values of flow variables such as density being less than zero. In an attempt to determine the level of flow derivative ratio associated with instability, several test cases were run in which the compressor model was throttled to various levels of flow derivative ratio. The throttling process was then terminated in order to let the solution stabilize. It was discovered that once the flow derivative ratio had reached a level greater than 2 in all the rotor volumes, the solution was unstable and termination of the throttling process would not prevent the solution from progressing into the post-surge region and failing. Therefore, this stability criterion was adopted and used throughout the program. It was noted that, in all cases, this criterion resulted in surge occurring in the region where the speed line slope approached zero.

Discussion is redirected to Figure 16. The dynamic solution data point indicated by time step 5400 is the point where the flow derivative ratio attained the value of two or greater, in all blade rows, and is also the point where the slope of the speed line goes through zero.

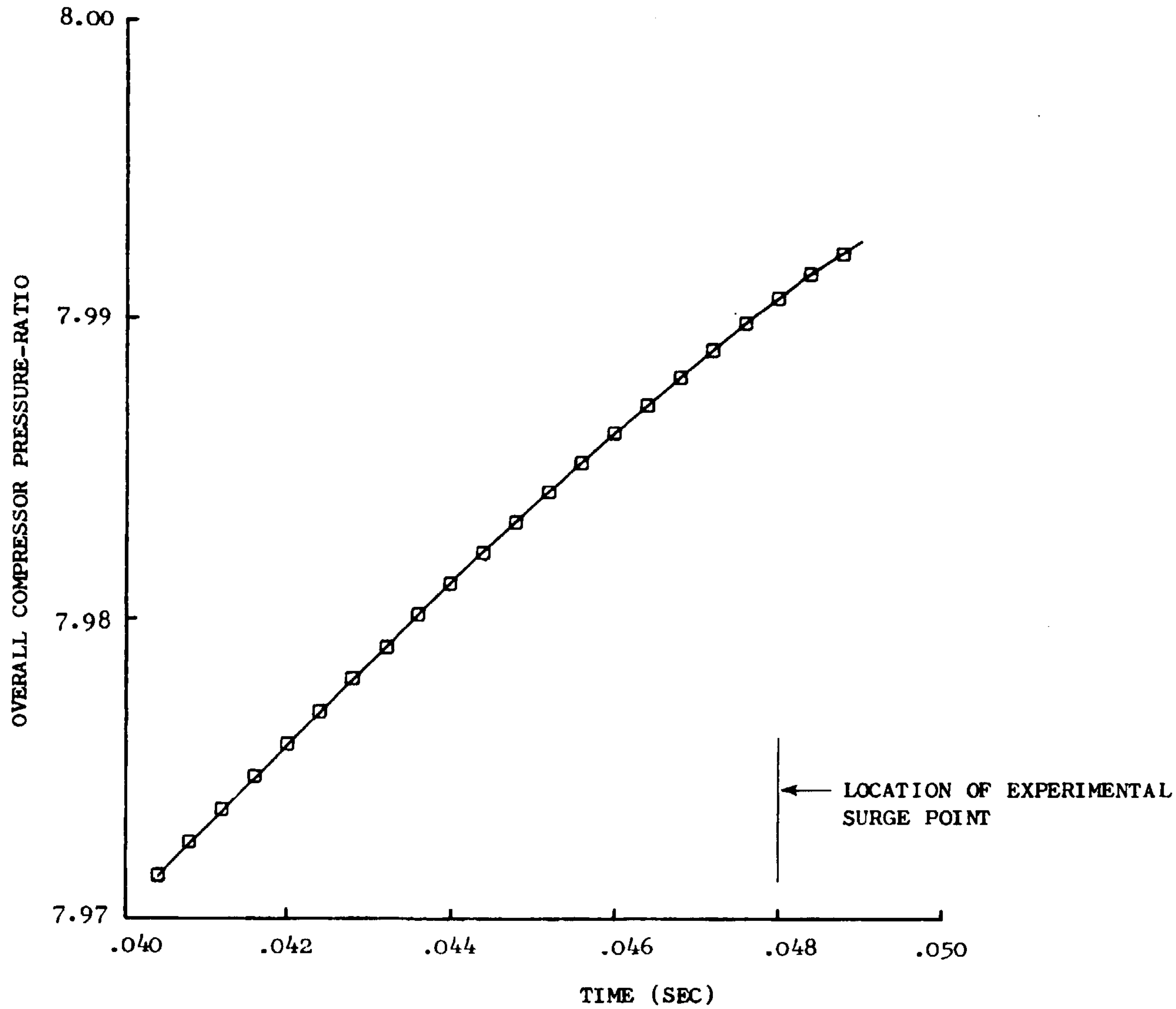

Figure 17. Stability Criterion Investigation - Overall Compressor Total-Pressure Ratio Versus Time.

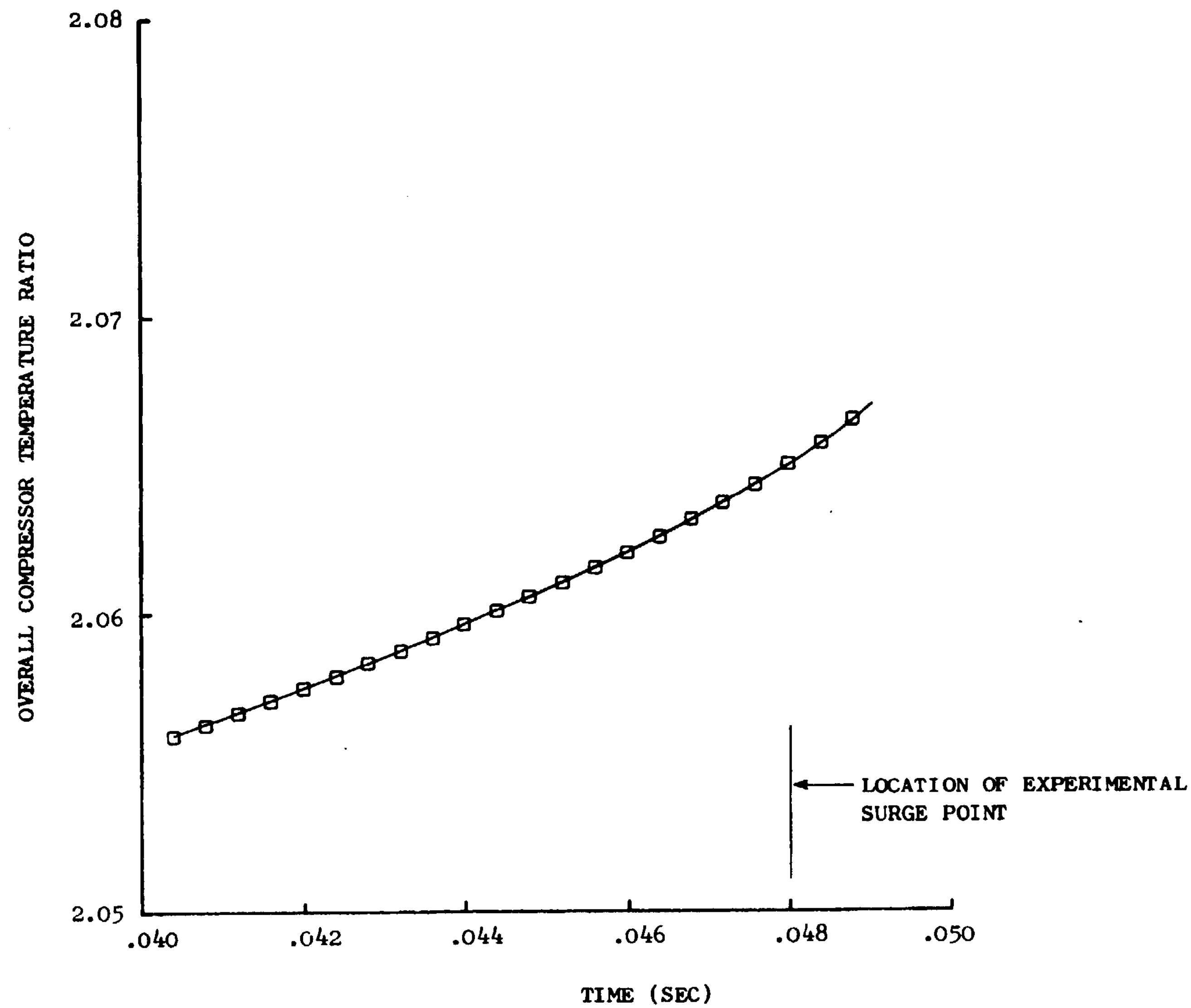

Figure 18. Stability Criterion Investigation - Overall Compressor Total-Temperature Ratio Versus Time.

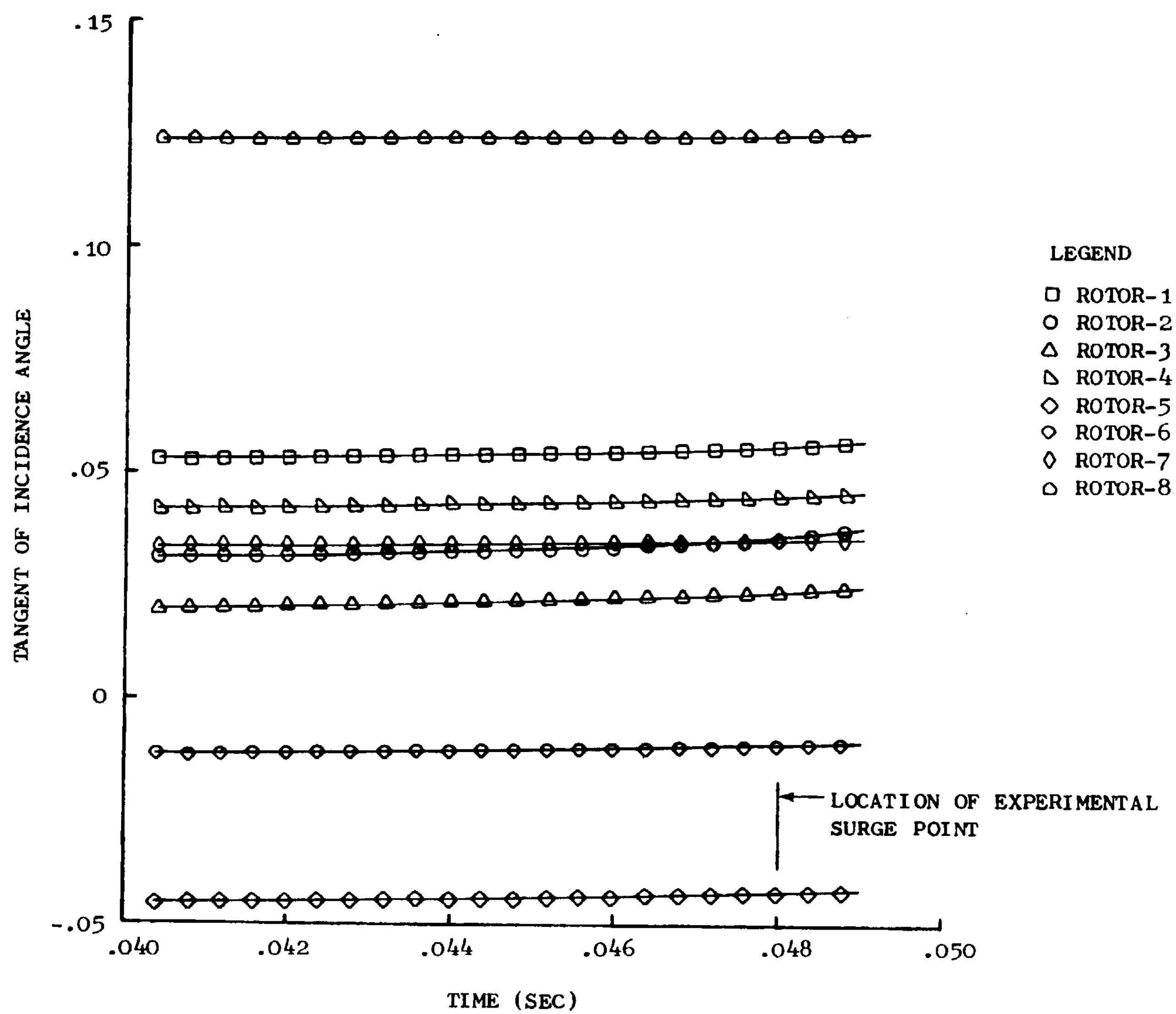

Figure 19. Stability Criterion Investigation - Tangent of Incidence Angle at Entrance to Rotors Versus Time.

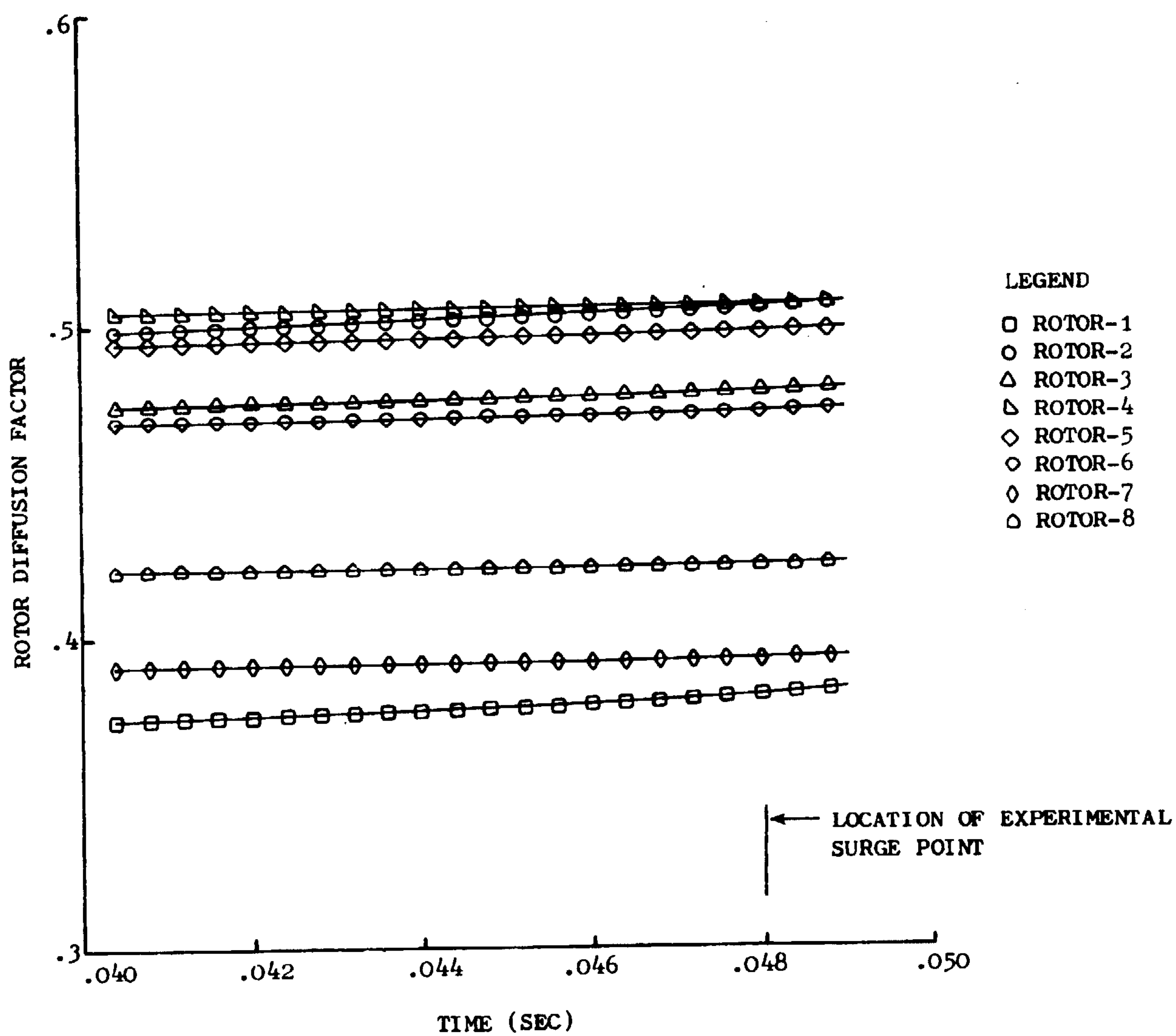

Figure 20. Stability Criterion Investigation - Rotor Diffusion Factors Versus Time.

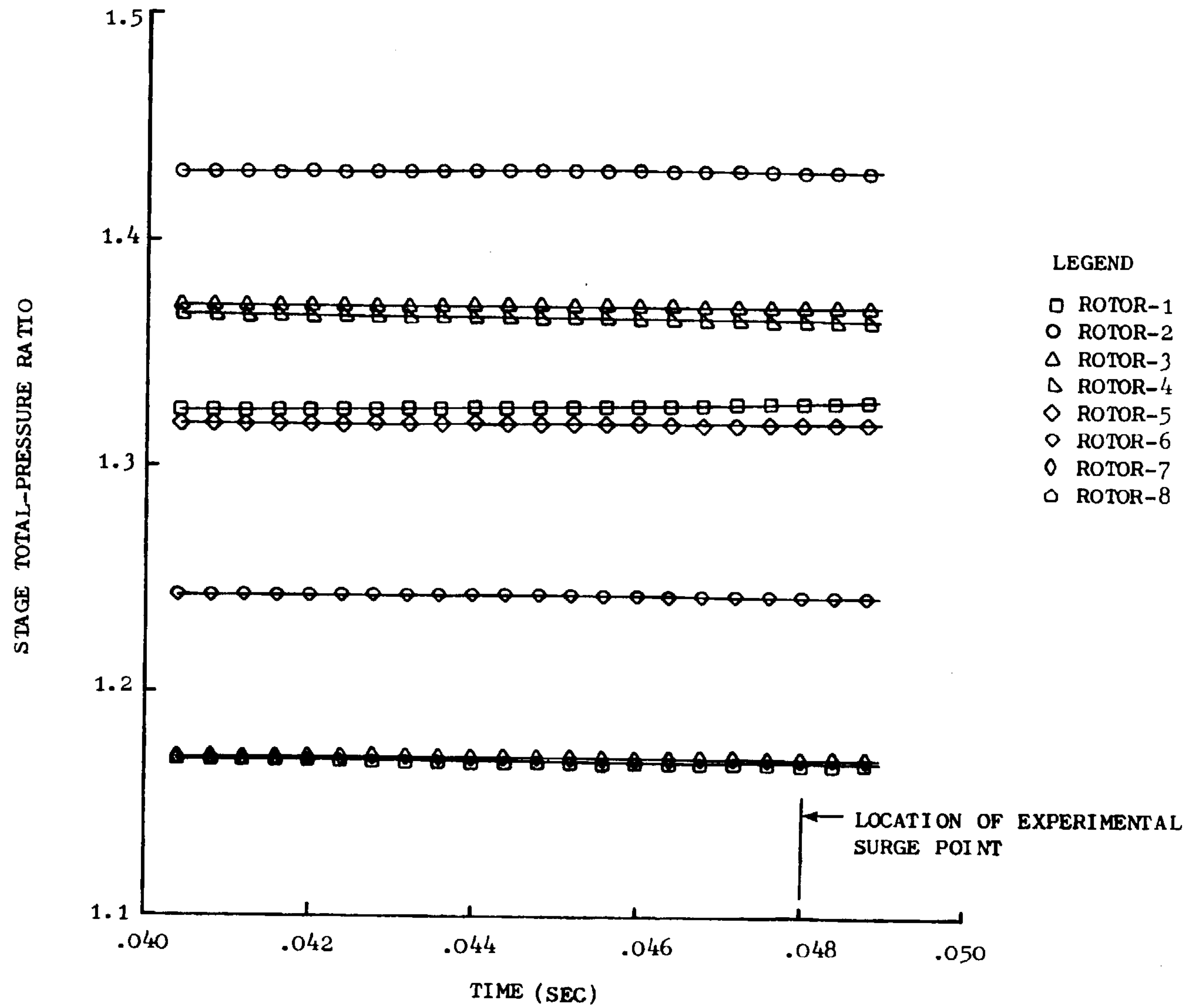

Figure 21. Stability Criterion Investigation - Stage Total-Pressure Ratio Versus Time.

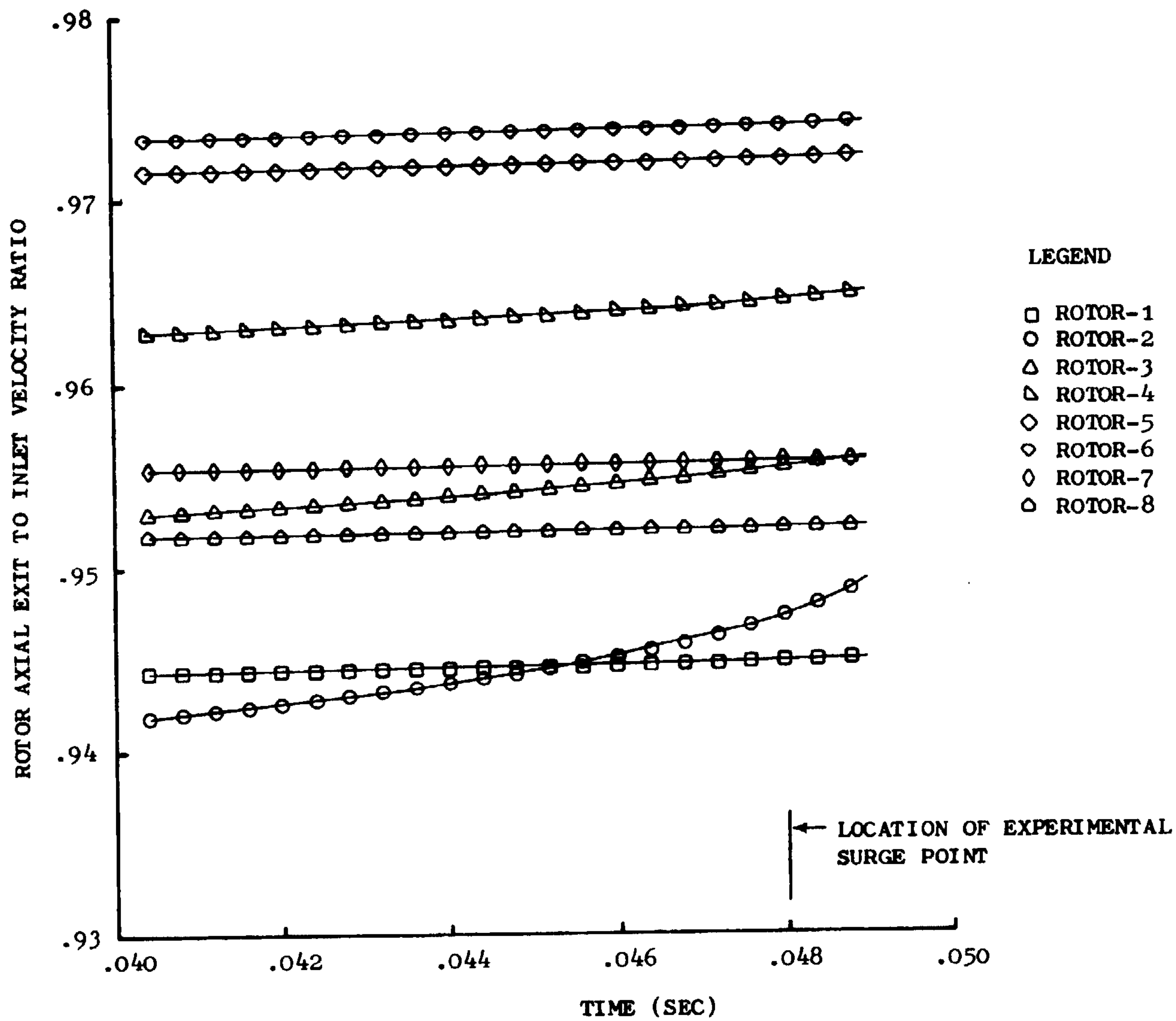

Figure 22. Stability Criterion Investigation - Rotor Axial Velocity Ratio Versus Time.

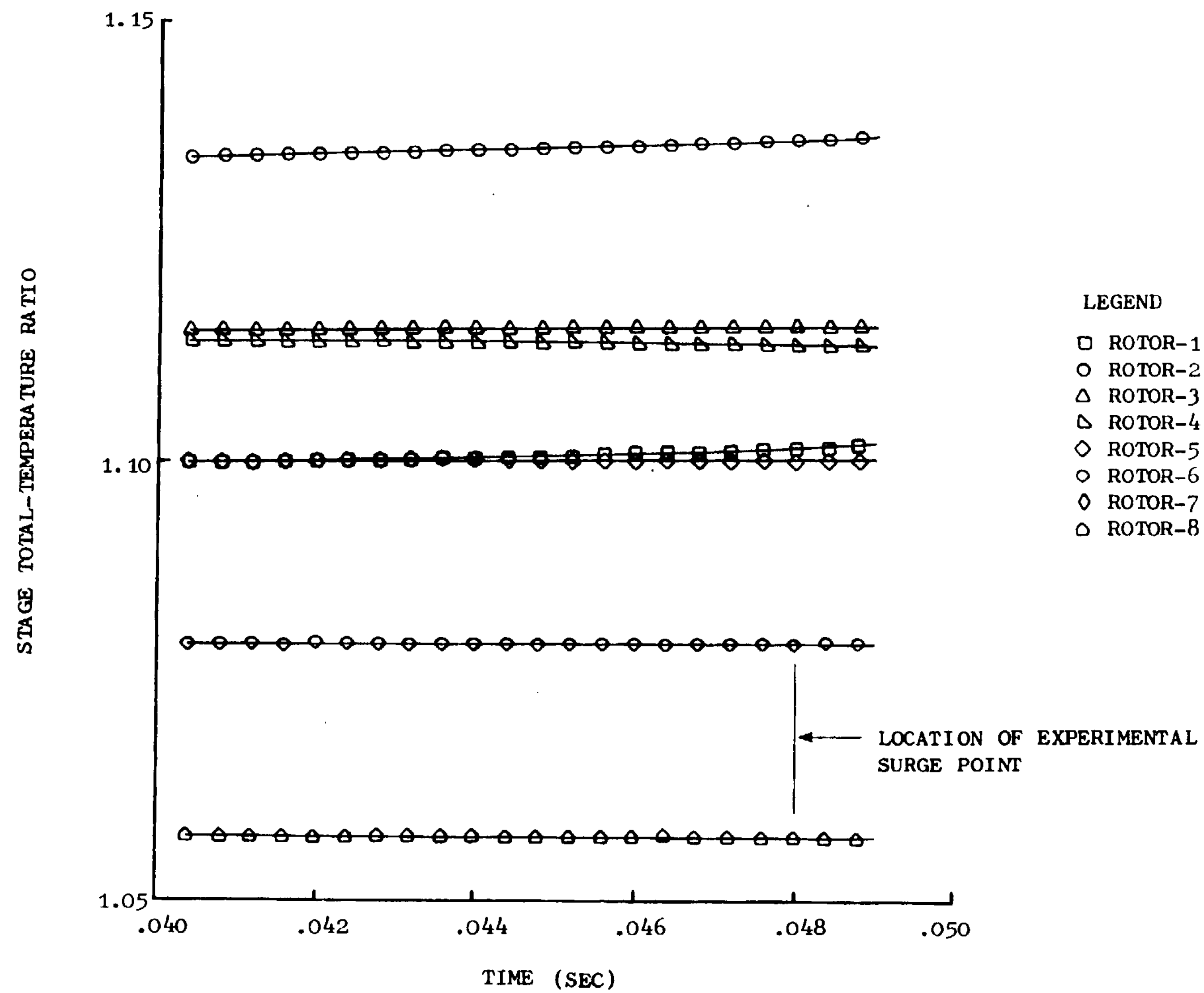

Figure 23. Stability Criterion Investigation - Stage Total-Temperature Ratio Versus Time.

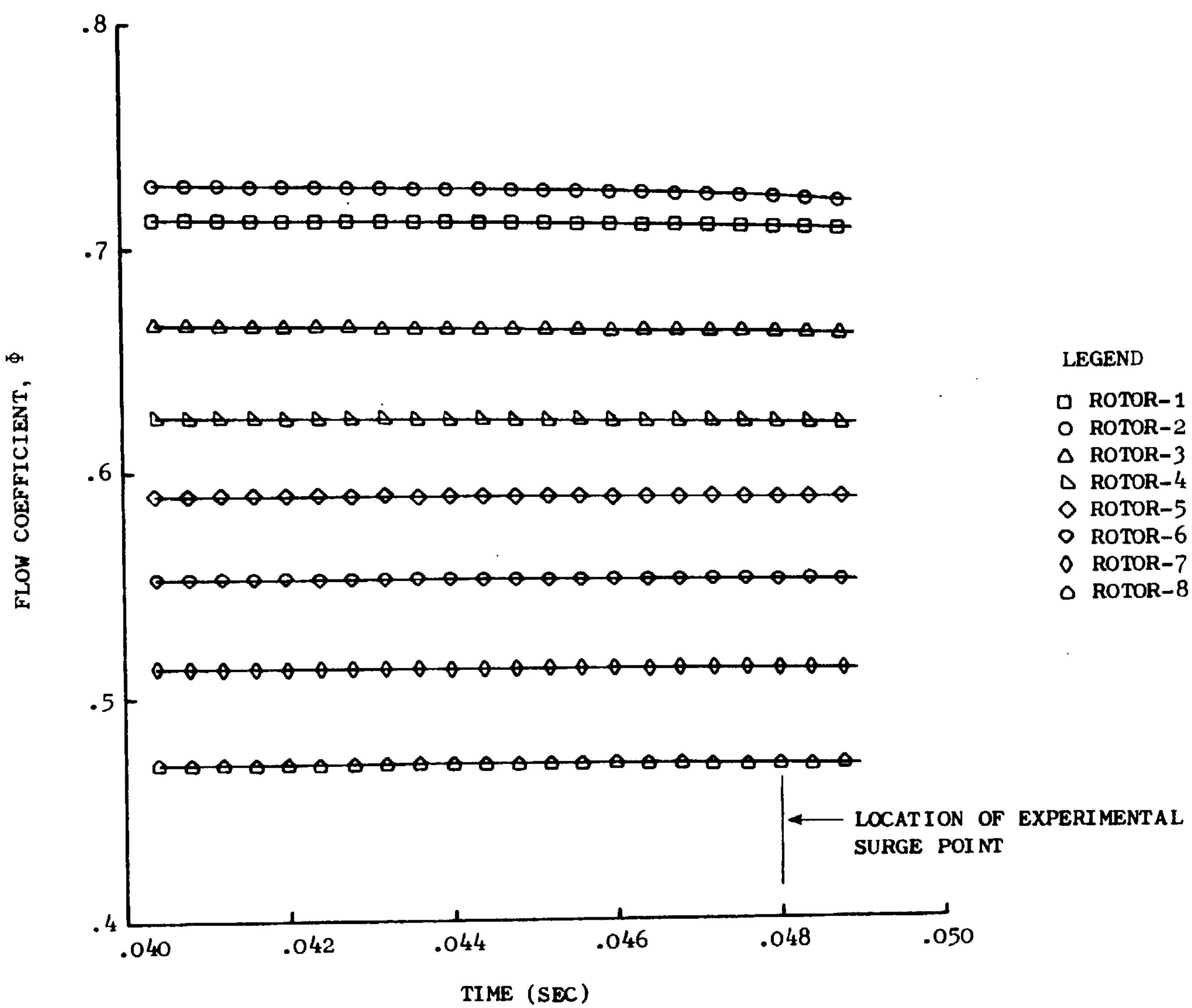

Figure 24. Stability Criterion Investigation - Rotor Flow Coefficients Versus Time.

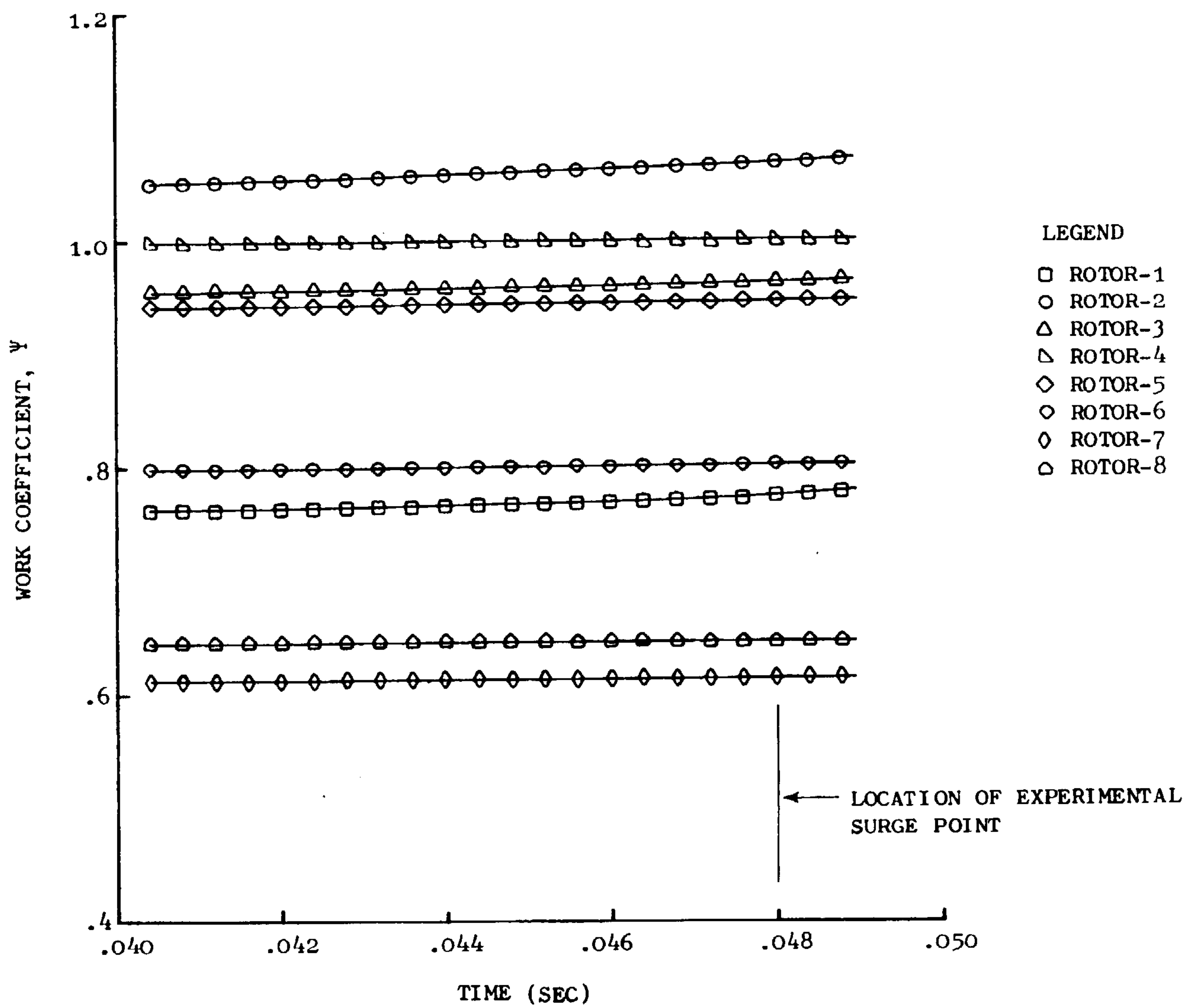

Figure 25. Stability Criterion Investigation - Rotor Work Coefficients Versus Time.

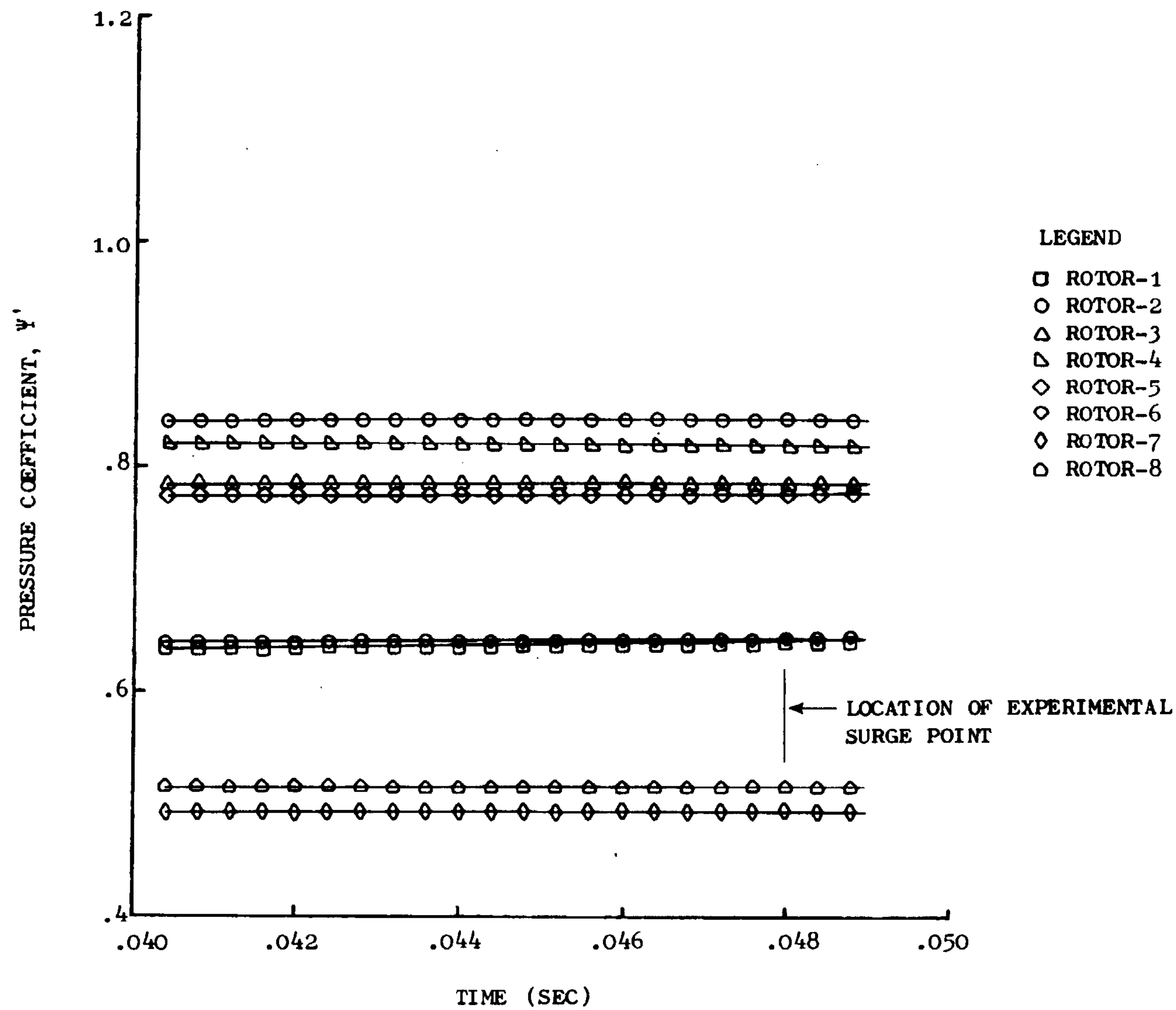

Figure 26. Stability Criterion Investigation - Rotor Pressure Coefficients Versus Time.

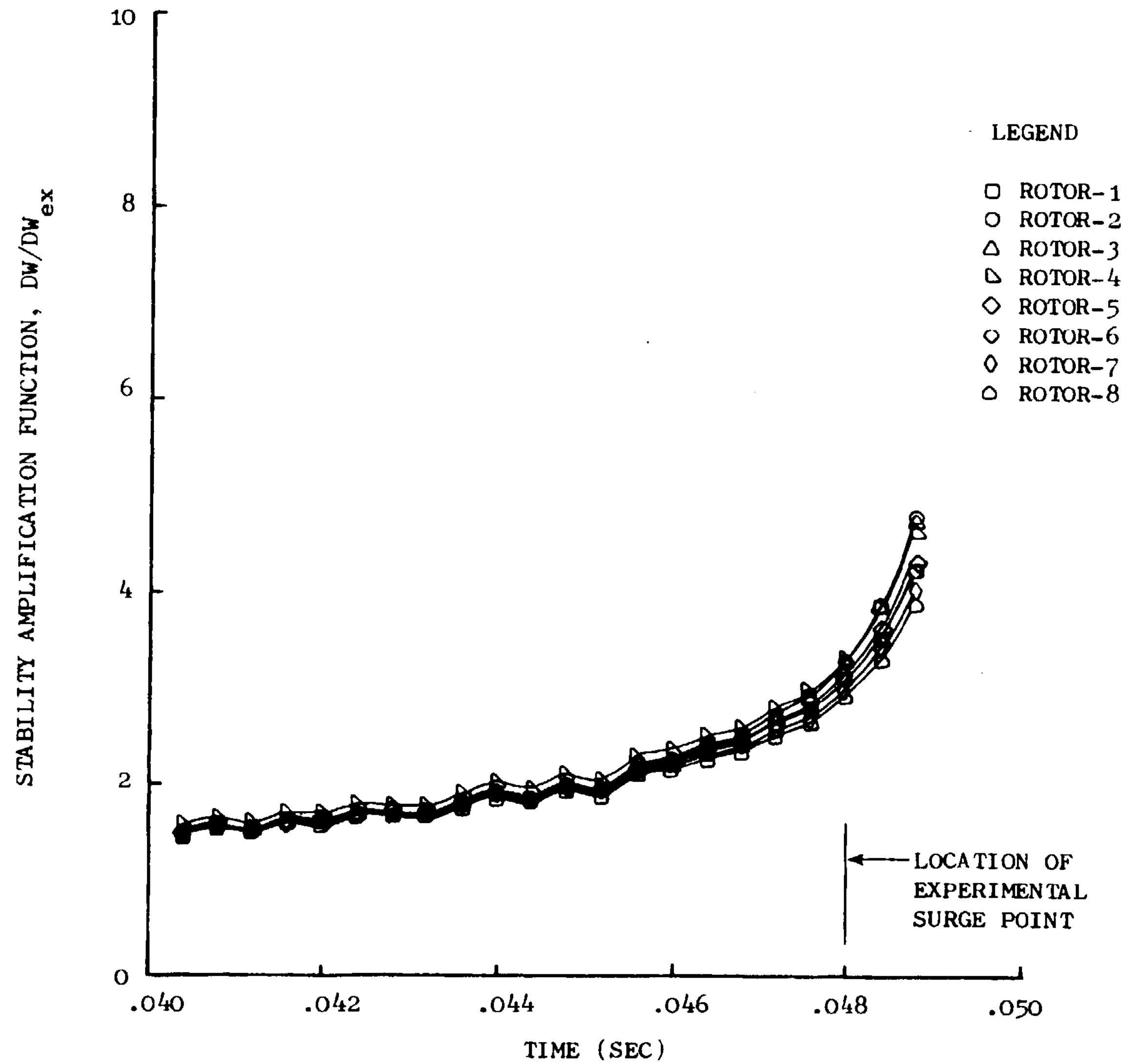

Figure 27. Stability Criterion Investigation - Stability Amplification Function Versus Time.

At this point, it was appropriate to question whether this stability criterion represented a limitation of the model or did it in fact represent the actual behavior of the J85-13 compressor in the region of the clean inlet surge line. Discussion of the speed-line zero-slope phenomena at surge with compressor designers indicated that they had not seen any data which would dispute the fact, although in general, data sufficiently close to the surge line to define the slope going to zero are not usually obtained, especially, at high speeds (steep speed lines). However, one instance of high speed data was recalled where much data was obtained and a number of surges were incurred while investigating the near surge behavior of a near vertical high-speed, speed line. The data showed that the slope of the speed line did go toward zero in a small region near the surge line with small changes (decreases) in flow.

It has been pointed out that the slope of the speed line must go to zero at the surge line in the presence of a choked exit boundary condition (choked turbine diaphragm) which is representative of compressor operation in the speed ranges studied in this program. Goethert et al, (Reference 11) have proposed a stability criterion that explains this behavior. The criterion was derived by application of the continuity equation to the stage volume and using a linearized representation of the stage characteristic in the region of interest. For a single stage followed by a choked nozzle, the requirement for stability can be expressed as

$$\frac{\partial W_{i+2}}{\partial P_{T_{i+2}}} - \frac{\partial W_i}{\partial P_{T_{i+2}}} > 0 \qquad (4\text{-}1)$$

The first term represents the characteristic of the nozzle in terms of the manner in which the exit flow rate responds to a change in stage exit total pressure. The second term represents the stage characteristic in terms of the manner in which the stage inlet flow responds to a change in compressor exit total pressure. Equation 4-1 can be written in an equivalent form as

$$\frac{0.532\ A_{i+2}}{\sqrt{T_{T_{i+2}}}} - \frac{A_i}{m_i\sqrt{T_{T_i}}} > 0 \qquad (4\text{-}2)$$

where the subscript "$_i$" indicates the stage entrance conditions, the subscript "$_{i+2}$" indicates the choked nozzle throat conditions, and m_i is the slope of the stage characteristic at the point under consideration. The first term is clearly positive and bounded. As one progresses along the speed line from high flow to low flow, the sign and magnitude of the second term is governed by the local slope m_i. The slope is initially negative, goes to zero, and then becomes positive. In the region of zero slope, this term exhibits a discontinuous behavior as it goes from indeterminately large negative values to indeterminately large positive values for small changes in flow on the order of ε. It is at this point that the model will exhibit the characteristics of incipient instability since the sign of Equation (4-2) changes from a positive to a negative value. Hence, it was for this reason that it is expected that the speed line should exhibit zero slope at the surge line considering that a choked turbine diaphragm boundary condition has been imposed. Therefore, it was possible to draw the inference that the more sophisticated solution of the flow aerodynamics represented by the subject Dynamic Digital Blade Row Compression Component Stability Model supports the stability criterion based upon a simplified, linearized model of the flow proposed by Goethert et al.

Figure 28 presents the ratio of exit-to inlet-flow for the rotor volumes as a function of time. As the compressor is throttled toward instability, the data illustrate that the rotors exhibit flow storage and flow evacuation, that is, more fluid enters rotors 1 and 2 than leaves and more fluid leaves rotors 3-8 than enters near the region of instability. If it is assumed that surge or overall compressor instability is associated with flow blockage, then this parameter could be useful in identifying the stage where the surge event is initiated.

Sample documentation of the clean-inlet compressor performance is contained in Table 25 of Appendix C.

4.2 TOTAL-PRESSURE DISTORTION ANALYSES

The dynamic parallel-compressor model was used to analyze the response of the "Moss" J85-13 engine to 180°, 1/rev circumferential total-pressure distortions. Three different distortion-screen porosities were tested on the engine and the effects of total-pressure distortion produced by the screens were simulated by the model. Table 3 provides a tabulation of the speed lines investigated and the distortion levels imposed for the NASA data readings recorded nearest to surge. The total-pressure distortions were modeled as two, 180° sectors with $\Delta P_T/\overline{P_T}$ levels ((max-min)/avg) which ranged from 1.9% to 13.7%. Maximum and minimum values were established by averaging all probe readings in the high- and low-pressure regions respectively, disregarding probe readings which were determined to be erroneous through examination of distortion profile plots. Sample plots of the radial and circumferential profiles of the distortion data analyzed are given in Appendix D (Figures 80 through 82).

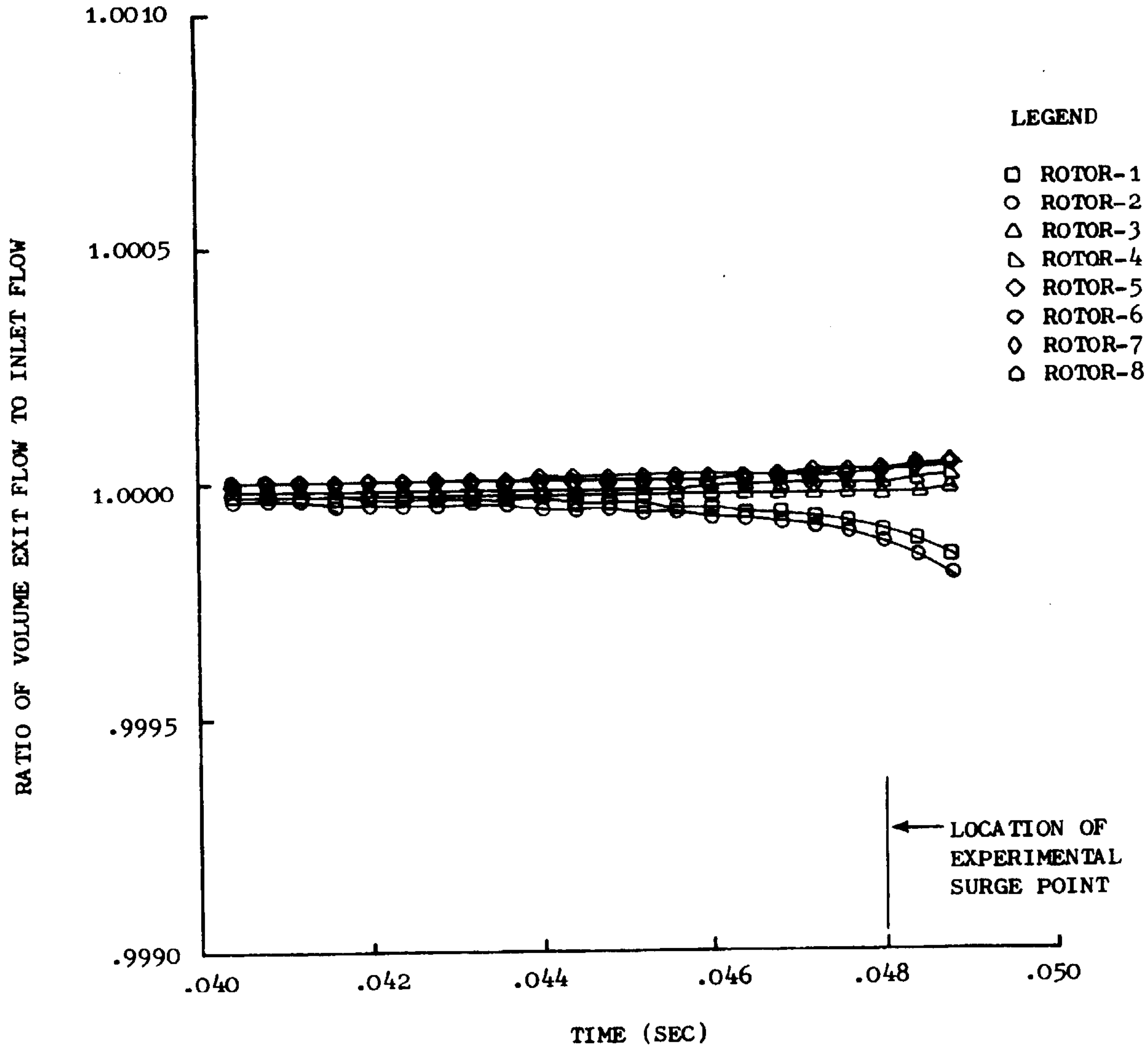

Figure 28. Stability Criterion Investigation - Ratio of Volume Exit Flow to Inlet Flow.

Table 3. 180°, 1/Rev Total-Pressure Distortion Cases.

$\%N/\sqrt{\theta}$	Screen*	Near Surge Reading	$\Delta P_T/\bar{P}_T$**
80	4M	490	0.0187
80	9M	126	0.0475
87	4M	485	0.0281
87	7-1/2M	379	0.0554
87	9M	90	0.0677
94	4M	481	0.0362
94	7-1/2M	381	0.0751
94	9M	94	0.0967
100	4M	478	0.0524
100	7-1/2M	384	0.1119
100	9M	99	0.1367

* Percent Open Area

4M - 74.0

7-1/2M - 57.8

9M - 50.7

** $\Delta P_T/\bar{P}_T = (\overline{P_{T\ Max}} - \overline{P_{T\ Min}})/P_{T\ Avg}$

Figures 29, 30, and 31 present the performance of the parallel-compressor model in the form of compressor maps for the three distortion screens - 4M, 7 1/2M, 9M (see Table 3). Shown on the figures are the NASA test data, experimental distortion surge line, experimental clean-inlet surge line, the parallel-compressor model speed-lines, and the stability limit predicted by the model. Regions on the figures where the distortion surge line exceeds the clean-inlet surge line were felt to be the result of using clean inlet data obtained at the end of the engine test and as such represents the performance of a degraded engine. In all cases, the distortion was simulated as two, 180° sectors with the distortion levels determined from the near-surge data and

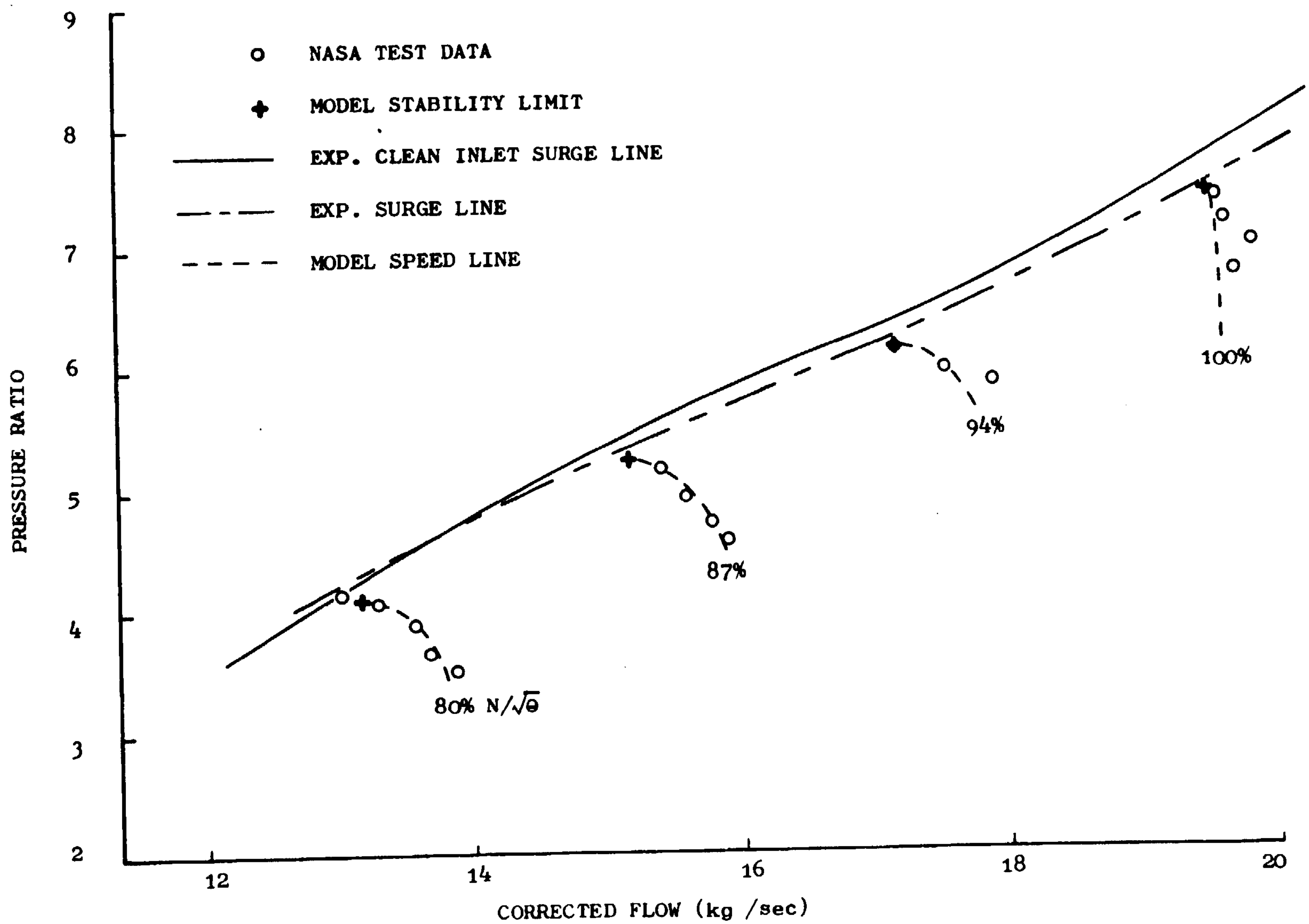

Figure 29. Effect of 180°, 1/Rev Total-Pressure Distortion (4M Screen) on Surge Line of "Moss" Engine.

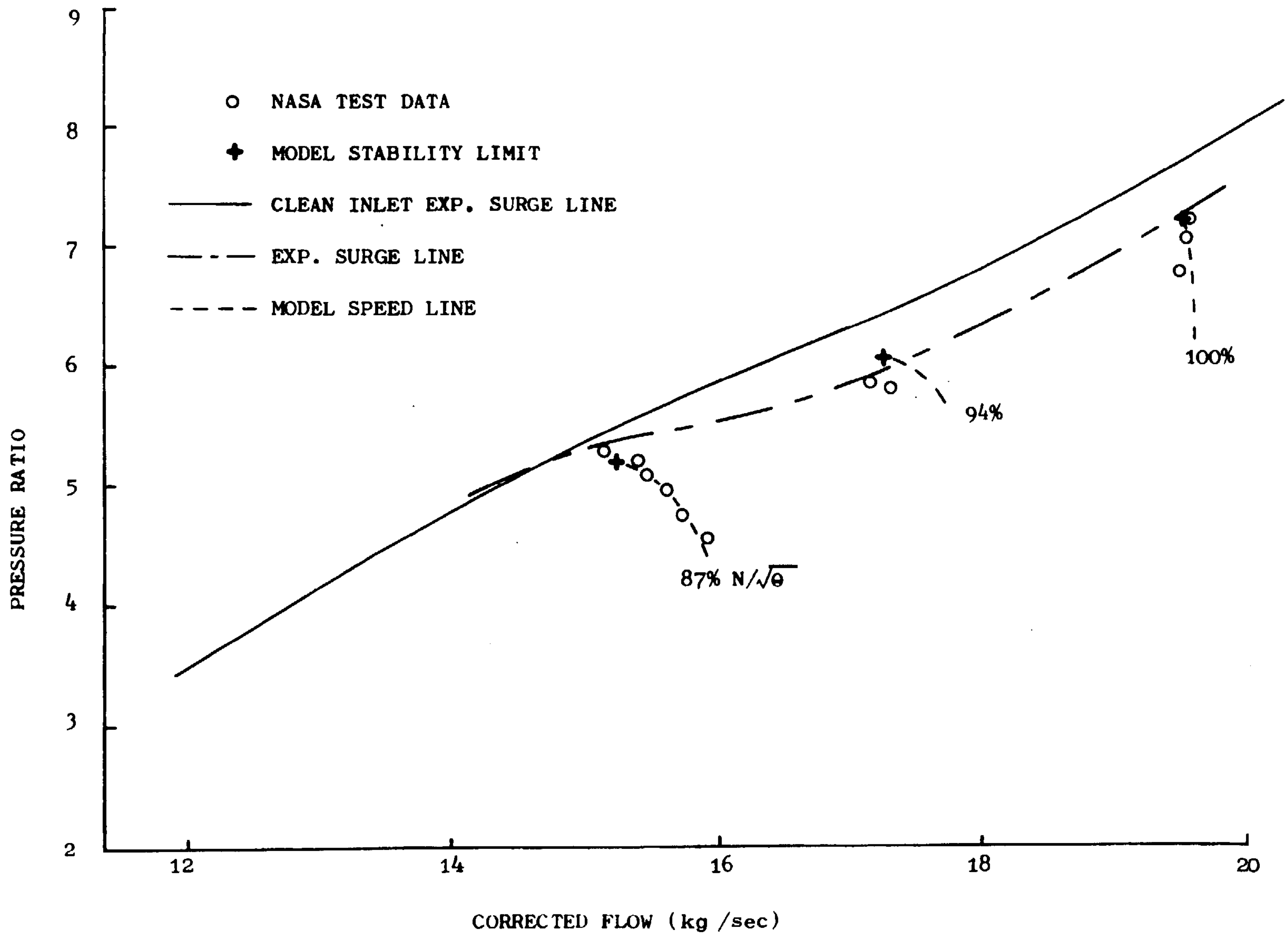

Figure 30. Effect of 180°, 1/Rev Total-Pressure Distortion (7½M Screen) on Surge Line "Moss" Engine.

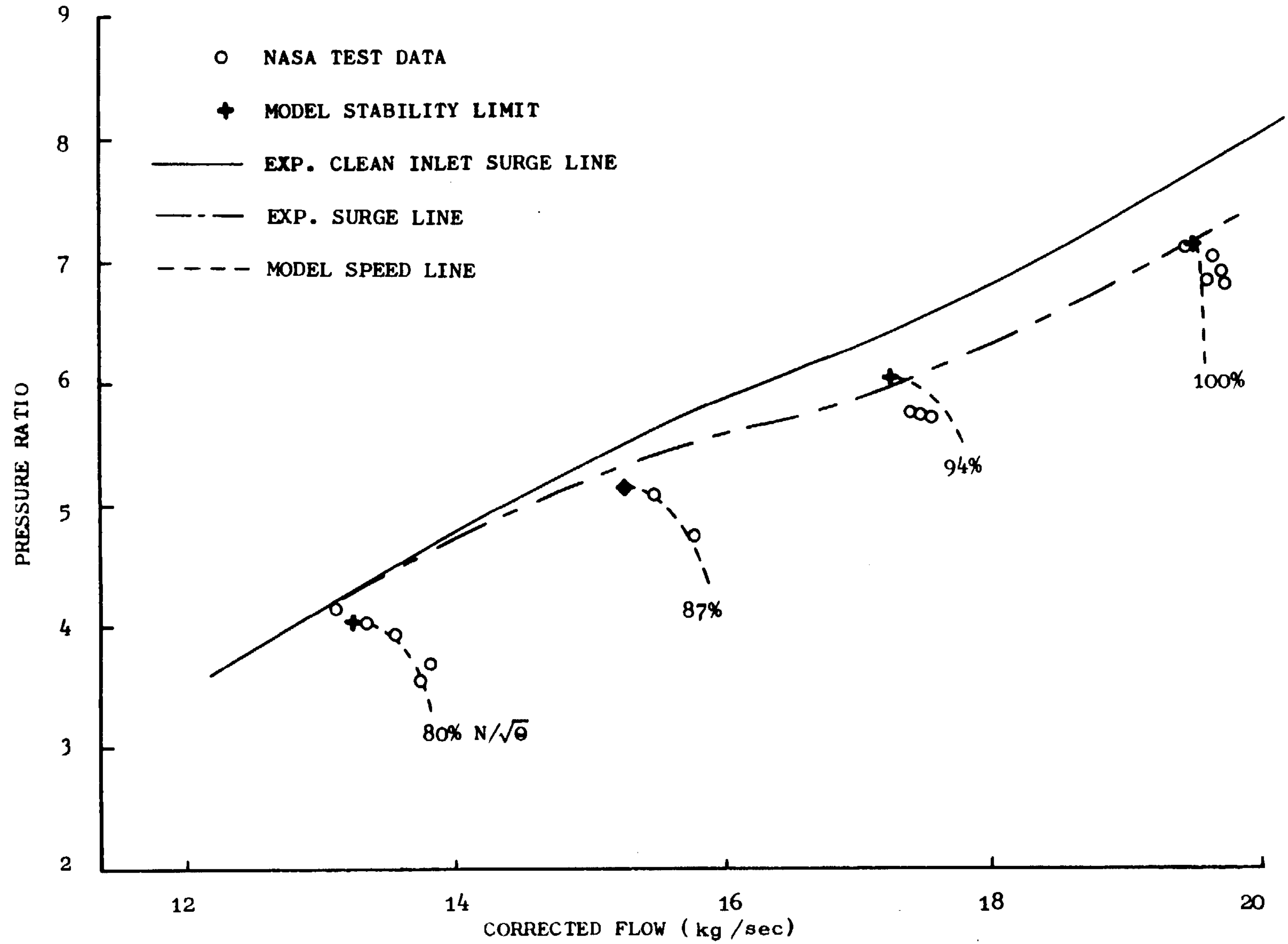

Figure 31. Effect of 180°, 1/Rev Total-Pressure Distortion (9M Screen) on Surge Line of "Moss" Engine.

held constant over the entire speed line. The stability limit of the overall compressor was established as that point where the previously determined stability criterion was exceeded by any of the parallel-compressor sectors. For all distortion levels, the model exhibited the ability to predict the experimental surge point quite well at 100% corrected speed. Conversely, at the lower speeds, the model predicts a more conservative loss in surge pressure-ratio than demonstrated experimentally. This result was expected as even with small distortions, the parallel-compressor concept maintains the integrity of each sector and prevents any mixing or redistribution of flow. Further discussion of this result is reserved for Paragraph 4.5.1. The apparent inability of the model to match the test data at 94% corrected speed for the higher distortion levels was not resolved. Since it was possible to match the test data at other speeds, erroneous test instrumentation was not felt to be a probable cause. A significant factor might possibly be the proximity of the 94% corrected speed to the break-point on the IGV and bleed schedules for the "Moss" engine (Figure 4) and the possibility of the distorted-flow compressor not reacting to the clean-inlet-flow IGV and bleed schedules as expected.

Sample documentation of the total-pressure distortion parallel-compressor analyses is given in Table 27. The predicted operating points for the individual parallel compressor sectors on the compressor maps are shown in Figures 83 through 85 of Appendix D.

4.3 TOTAL-TEMPERATURE DDISTORTION ANALYSES

A total of three 180°, 1/rev, circumferential total-temperature distortion patterns were analyzed for the "Mehalic" J85-13 engine. Distortion levels of $\Delta T_T/T_T$ ((max-min)/avg) from 3.6% to 15.6% were investigated. Table 4 provides a compilation of the distortion levels simulated, the NASA test reading for the points recorded near surge from which the data were obtained, and the nominal corrected speed of the speed lines simulated. As shown in Figure 86 of Appendix E, the profile plot of the circumferential total-temperature distortion distribution does not exhibit a very "square" profile. In addition, the radial profile plot indicates the existence of substantial radial distortion as well. The procedure for modeling the temperature distortion as two, 180° sectors was to radially and circumferentially average the probe readings from the center four rakes in the high- and low-temperature regions and the resultant temperatures were then assumed to extend over their respective 180° sectors. Any differences in corrected speed and total-temperature distortion levels noted between the results presented in this report and the results presented in Reference 5 are the result of the above manner of averaging probes in the high and low temperature regions to obtain the maximum and minimum values to calculate the $\Delta T_T/T_T$ parameter. Preliminary 4-sector modeling efforts which provided for sectors of intermediate temperature between the high and low regions yielded near-identical overall-average temperatures as the two-sector model. Thus both simulations would indicate the same corrected speed, and overall performance, but the 4-sector analysis would require twice the computational time by requiring the consideration of two additional, non-critical sectors. Bleed and IGV schedules were specified as a function of the average inlet total temperature.

Table 4. 180°, 1/Rev Total-Temperature Distortion Cases.

$\%N/\sqrt{\theta}$	Near Surge Reading	$\Delta T_T/\bar{T}_T$*
86.8	568	0.1557
93.4	154	0.0466
99.6	138	0.0363

$$*\Delta T_T/\bar{T}_T = (\overline{T_{T\ Max}} - \overline{T_{T\ Min}})/T_{T\ Avg}$$

Figure 32 illustrates the results of the total-temperature distortion, parallel-compressor analyses of the Mehalic engine. The compressor map illustrates the NASA test data, the experimental surge line, and the throttling simulation stability limits. A detailed view of the performance of the individual parallel compressor sectors is provided in Figure 87 of Appendix E. The experimental distortion surge line is shown disconnected as this indicates two levels of distortion amplitude (Table 4). A comparison of the test data and the model-generated speed lines indicates the validity of interpolating blade-row characteristics to determine speed lines not established by engine tests. The deviation of the model speed line at 86.8 percent corrected speed was due primarily to the large extrapolation necessary to provide characteristics data for the high total-temperature sector operating at 83.6% corrected speed; an extrapolation equivalent to 15% of the data range beyond the lowest speed data available. As in the case of total-pressure distortion, the total-temperature distortion results indicate the model predictions correlate quite well with experimental results at high corrected speed, but are conservative at the lower corrected speeds. At 93.4% corrected speed, the parallel-compressor results indicate that the associated sector at 92.3% corrected speed (See Figure 87 of Appendix E) did not experience instability until beyond the experimental clean inlet surge line. This was a result of only using data at 87, 94 and 100% corrected speeds for the basis of interpolation; the inclusion of characteristic data at additional speeds would undoubtedly improve the ability of the sector to better match the experimental clean inlet flow surge line. In all the temperature distortion cases investigated, the low corrected speed sector (high T_T) was limiting and experienced the instability. Sample documentation of the total-temperature distortion analyses is contained in Table 28 of Appendix E.

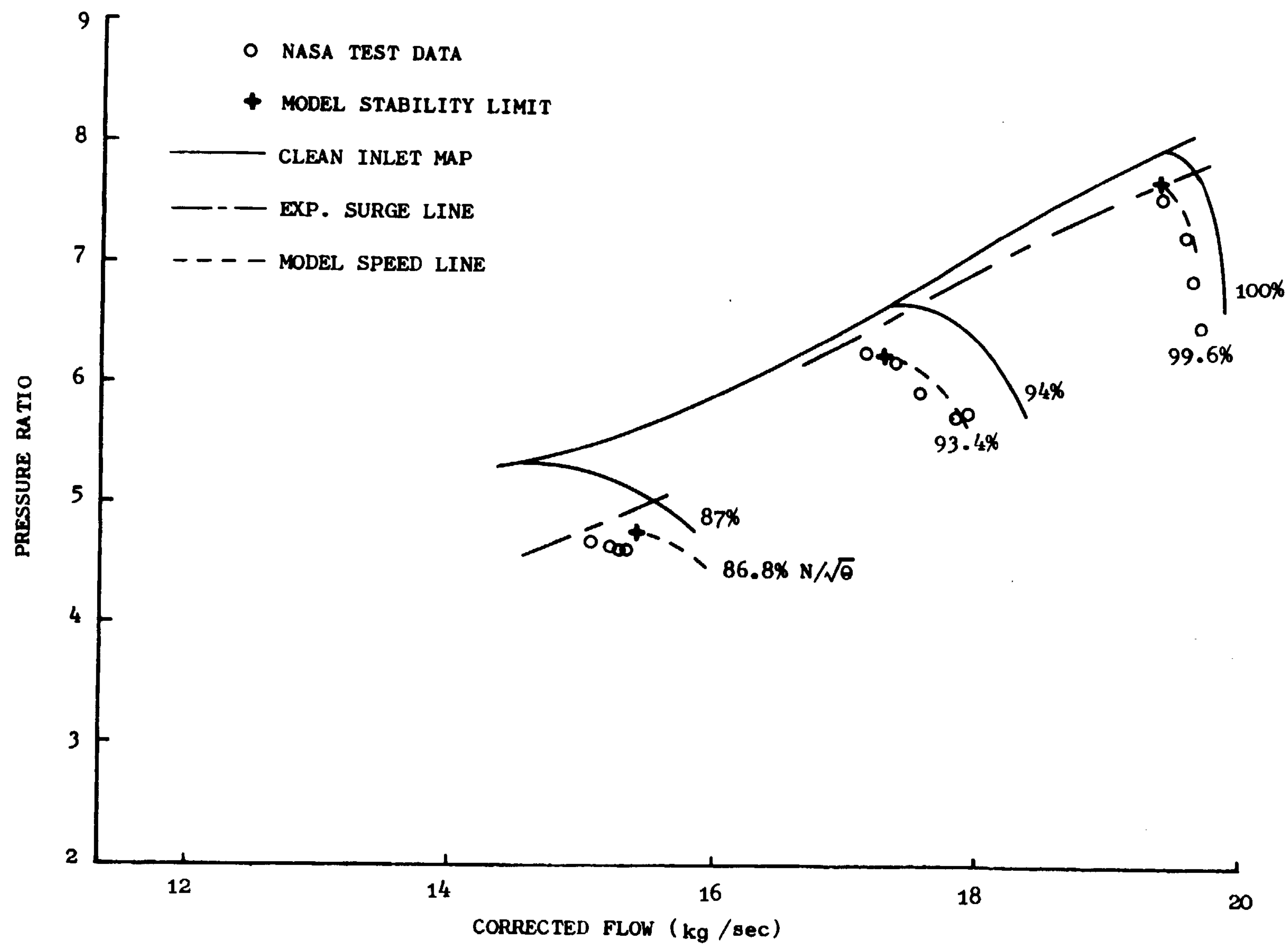

Figure 32. Effect of 180°, 1/Rev Total-Temperature Distortion on Surge Line of "Mehalic" Engine.

4.4 COMBINED TOTAL-PRESSURE AND TOTAL-TEMPERATURE DISTORTION ANALYSES

In addition to total-pressure and total-temperature distortion analyses alone, analyses of the "Mehalic" J85-13 engine were performed for combined total-pressure and total-temperature distortions of 180° in extent. Three orientations of the distortions were considered: opposed, coincident, and 90° overlapped. The "opposed pattern" term refers to the low P_T sector being opposed to the high T_T sector, while the "coincident pattern" term refers to the low P_T sector overlapping the high T_T sector. With the exception of the 90° overlapped configuration, the temperature distributions imposed on the model were determined in the same manner as discussed in the previous section. Total-pressure instrumentation at the upstream distortion instrumentation plane consisted of only eight probes (four rakes with probes at two immersions) as indicated in Reference 5. A square wave circumferential total-pressure profile was assumed. Examination of the limited test data indicated no significant radial total-pressure gradients and as such, the distortion levels imposed on the model were obtained from averages of the probe readings in the high- and low-pressure regions. In the case of combined distortions any differences in corrected speed and total-temperature distortion levels noted between the results presented in this report and the results presented in Reference 5 are the result of averaging the total-temperature probe readings as for the case of the pure total-temperature distortion patterns (Paragraph 4.3). The differences between the total-pressure distortion levels reported in Reference 5 and herein are due to the difference in the distortion parameter $(P_{T_{avg}} - P_{T_{min}})/P_{T_{avg}}$ used in Reference 5 versus the distortion parameter $(P_{T_{max}} - P_{T_{min}})/P_{T_{avg}}$ used in this report. Further, differences will arise due to the averaging of the total-pressure probe readings as noted above. Figures 88 through 90 of Appendix F contain sample plots of the circumferential and radial profiles of the distortion patterns considered.

4.4.1 Opposed Orientation

Table 5 presents a listing of the opposed combined-distortion analyses performed, the distortion levels imposed, and the corresponding NASA data reading numbers. Since the distortions were opposed, it was possible to use a two, 180° sector parallel compressor model. Figures 33 and 34 present the results of the parallel-compressor modeling and the predicted stability limits for the cases of low- and moderate-temperature distortions, respectively. The stability-limit throttling simulations correctly predicted the qualitative change in the surge line with the different imposed distortion patterns. In addition, a comparison between the low-speed simulations of both figures indicated the model was able to predict the drop in the surge line as the level of temperature distortion was increased. As in the previous distortion cases, the model prediction of loss in surge pressure ratio corresponds quite well with experimental results at high speed but tends to over-predict losses at the lower speeds where the compressor speed lines are of lower slope. A comparison of the approximately 87% corrected-speed lines of Figures 33 and 34 indicates the effect of extrapolating blade-row characteristics. Figure 33 demonstrates the model does a very credible job of matching the test data with 4.9% temperature distortion while Figure 34 illustrates a greater

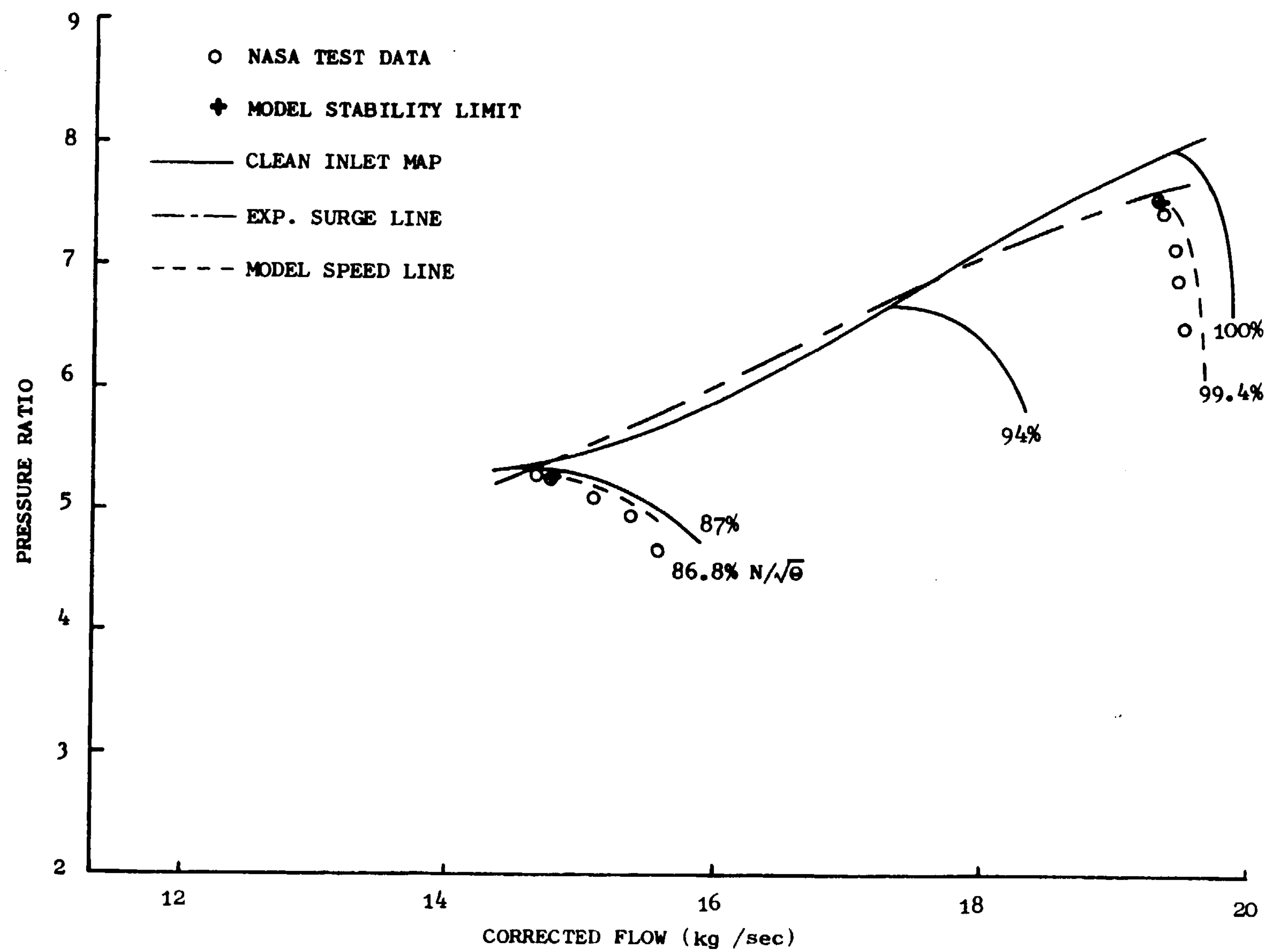

Figure 33. Effect of 180°, 1/Rev Combined Total-Pressure and Total-Temperature Distortion, Opposed Orientation Low Total-Temperature Distortion on Surge Line of "Mehalic" Engine.

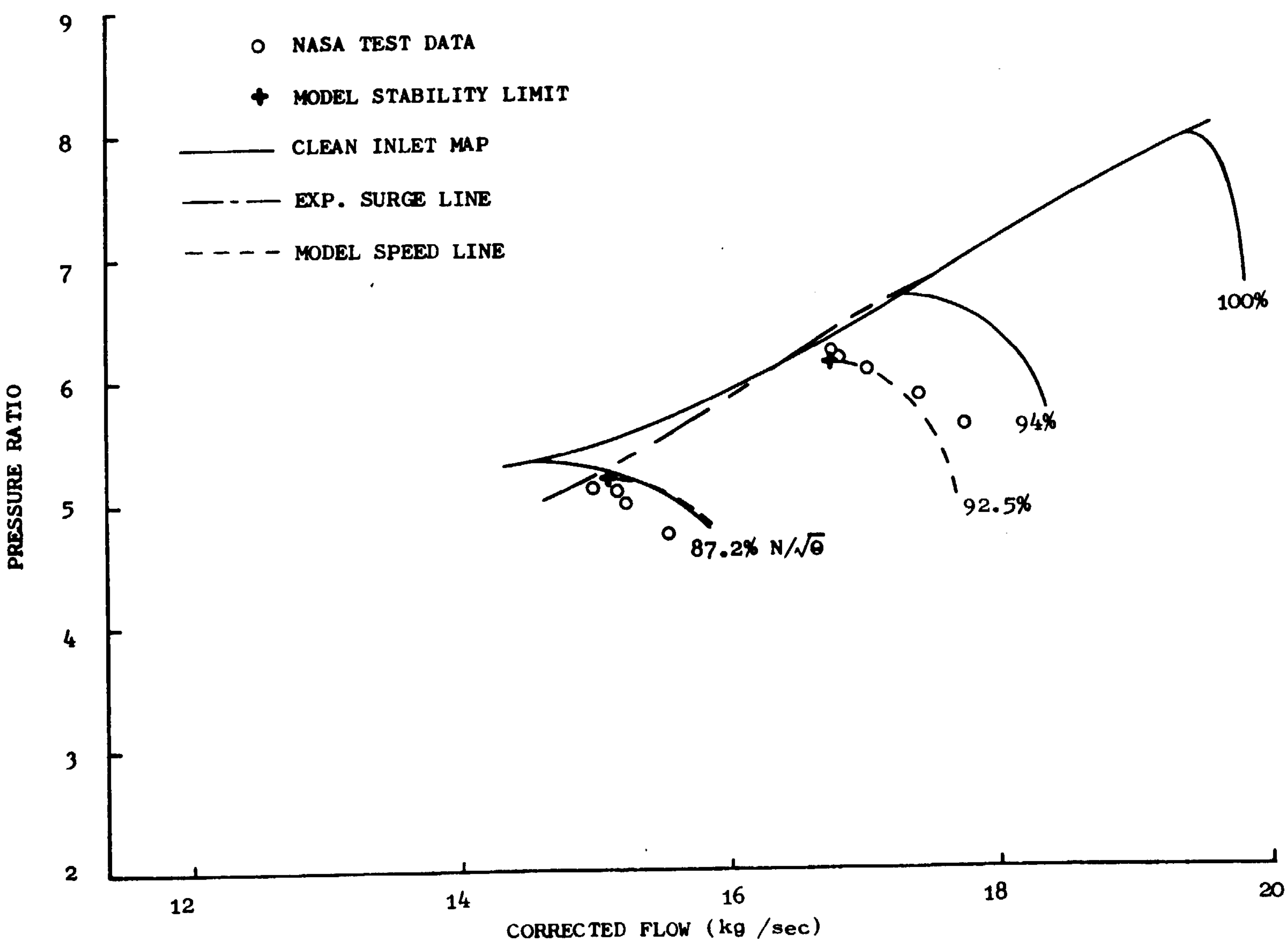

Figure 34. Effect of 180°, 1/Rev Combined Total-Pressure and Total-Temperature Distortion, Opposed Orientation Moderate Total-Temperature Distortion on Surge Line of "Mehalic" Engine.

deviation between the test data and model simulation with 9% total-temperature distortion. In both cases (87% corrected speed) the total-pressure distortion levels were equivalent.

Table 5. 180°, 1/Rev Combined Total-Pressure and Total-Temperature Distortion Cases Opposed Orientation.

$\%N/\sqrt{\theta}$	Near Surge Reading	$\Delta T_T/\overline{T}_T$*	$\Delta P_T/\overline{P}_T$**
87.2	494	0.0900	0.0648
92.5	479	0.0919	0.0870
86.8	441	0.0489	0.0612
99.4	416	0.0362	0.1262

$$* \quad \Delta T_T/\overline{T}_T = (\overline{T_{T\ Max}} - \overline{T_{T\ Min}})/T_{T\ Avg}$$

$$** \quad \Delta P_T/\overline{P}_T = (\overline{P_{T\ Max}} - \overline{P_{T\ Min}})/P_{T\ Avg}$$

The limiting sector, in all the cases but one, was the low corrected-speed sector; the total-pressure distortion for the 100% corrected speed event was sufficiently high (12.6%) to cause the high corrected-speed sector to experience the limiting instability. Appendix F contains detailed compressor maps illustrating the performance of the individual parallel compressor sectors (Figures 91 and 92). A comparison of the detailed maps for pure total-temperature distortion and the opposed combined distortions indicates the effect of total-pressure distortion in changing the operating points of the sectors.

4.4.2 Coincident Orientation

The second combined-distortion configuration considered was that where the total-pressure distortion (low P_T) and total-temperature (high T_T) are completely coincident (overlapped). The speed lines investigated, the distortions imposed, and the corresponding NASA readings are listed in Table 6.

Appendix F contains sample plots of the circumferential- and radial-profiles for one distortion case as obtained from the NASA data. Figure 35 illustrates the resultant compressor map including the test data, parallel-compressor speed lines and the throttling simulation predicted stability limits. The experimental stall line is shown disconnected and represents two different levels of temperature distortion. As can be seen, the 2-sector parallel-compressor modeling of the distortions correlated well with test data and predicted the increased drop in the surge line due to the overlapping of the distortions. The detailed compressor map (Figure 93) contained in Appendix F illustrates the fact that the drop in surge line can be attributed to the effect of the parallel-compressor uniform-exit-static-pressure boundary condition in forcing the distorted sector further up its speed line than if it were operating with one distortion only. A comparison of similar operating points for the coincident and opposed distortion illustrates that while both parallel compressor simulations exit to the same pressure, the pressure distortion sector in the coincident configuration must operate further up the speed line in order to produce sufficient pressure rise as it is operating at a lower corrected speed due to the superimposed temperature distortion. Again, it is apparent from Figure 35 that the model can provide an accurate estimate of loss in surge pressure in situations where speed lines are nearly vertical. At lower corrected speeds, where the lower slope speed lines require larger changes in flow for changes in pressure than at the higher speeds, the parallel compressor model forces the critical sector closer to surge than if the speed lines were more vertical, thus producing more pessimistic predictions of the surge point.

Table 6. 180°, 1/Rev Combined Total-Pressure and Total-Temperature Distortion Cases Coincident Orientation.

$\%N/\sqrt{\theta}$	Near Surge Reading	$\Delta T_T/\overline{T}_T$*	$\Delta P_T/\overline{P}_T$**
87.3	504	0.0873	0.0675
93.1	436	0.0371	0.0914
99.1	423	0.0402	0.1272

$$* \ \Delta T_T/\overline{T}_T = (\overline{T_{T\ Max}} - \overline{T_{T\ Min}})/T_{T\ Avg}$$

$$** \ \Delta P_T/\overline{P}_T \quad (\overline{P_{T\ Max}} - \overline{P_{T\ Min}})/P_{T\ Avg}$$

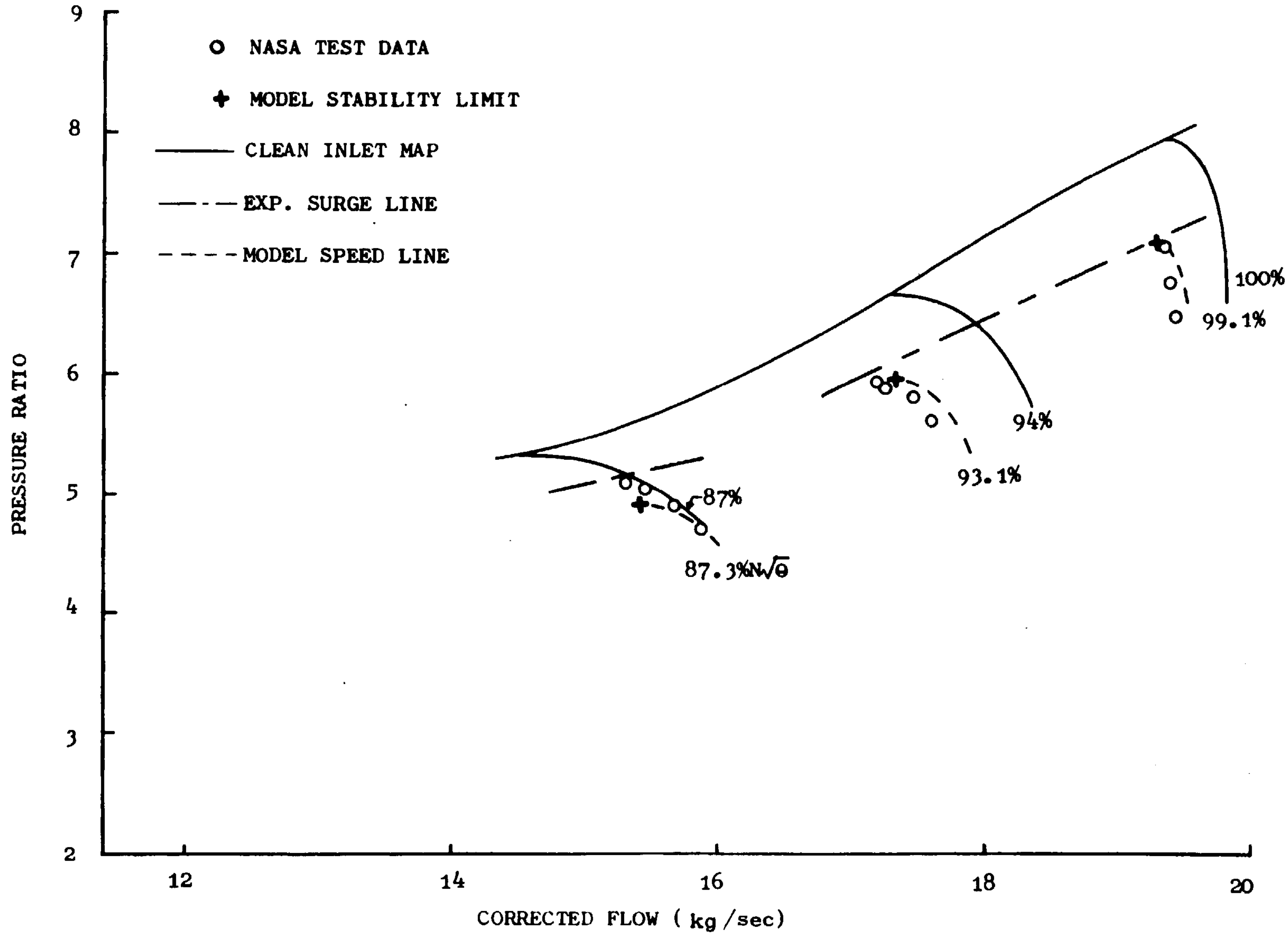

Figure 35. Effect of 180°, 1/Rev Combined Total-Pressure and Total-Temperature Distortion, Overlapped Orientation on Surge Line of "Mehalic" Engine.

4.4.3 90° Overlapped Orientation

The final combined-distortion configuration investigated consisted of the condition where 180° extent total-temperature and total-pressure distortions were overlapped by 90°. As presented in Table 7, total-temperature distortions ranged from 3.5 to 7.8 percent while total-pressure distortions ranged from 6.5 to 12.7 percent. The compressor response was analyzed using a four 90° sector, parallel-compressor model. Whereas total-pressure distortion levels were obtained as mentioned previously, total-temperature levels in each sector were obtained by averaging all inlet temperature probe data within the sector. Figures 36 and 37 present the results of the dynamic parallel-compressor modeling for low and moderate temperature distortions, respectively. Although the throttling simulations produce an accurate representation of the test data points and the qualitative changes in the surge line are duplicated, there is a greater deviation from the experimental surge line than with coincident distortions. This was due to the fact that the four-sector, 90° overlapped model (Figure 94 of Appendix F) had a higher exit static pressure than the coincident model (Figure 93 of Appendix F) and thus forced the critical sector further up the speed line producing a more pessimistic estimate of loss in surge pressure ratio. It is apparent that in order to make a reasonable analytical estimate of loss in surge pressure for small sector distortion, a more realistic model of the flow processes involved will have to be constructed.

Table 7. 180°, 1/Rev Combined Total-Pressure and Total-Temperature Distortion Cases 90° Overlapped Orientation.

$\%N/\sqrt{\theta}$	Near Surge Reading	$\Delta T_T/\overline{T}_T$**	$\Delta P_T/\overline{P}_T$**
86.8	445	0.0412	0.0651
93.0	432	0.0346	0.0888
99.0	420	0.0352	0.1272
87.2	499	0.0781	0.0672

* $\Delta T_T/\overline{T}_T = (\overline{T_{T\,Max}} - \overline{T_{T\,Min}})/T_{T\,Avg}$

** $\Delta P_T/\overline{P}_T = (\overline{P_{T\,Max}} - \overline{P_{T\,Min}})/P_{T\,Avg}$

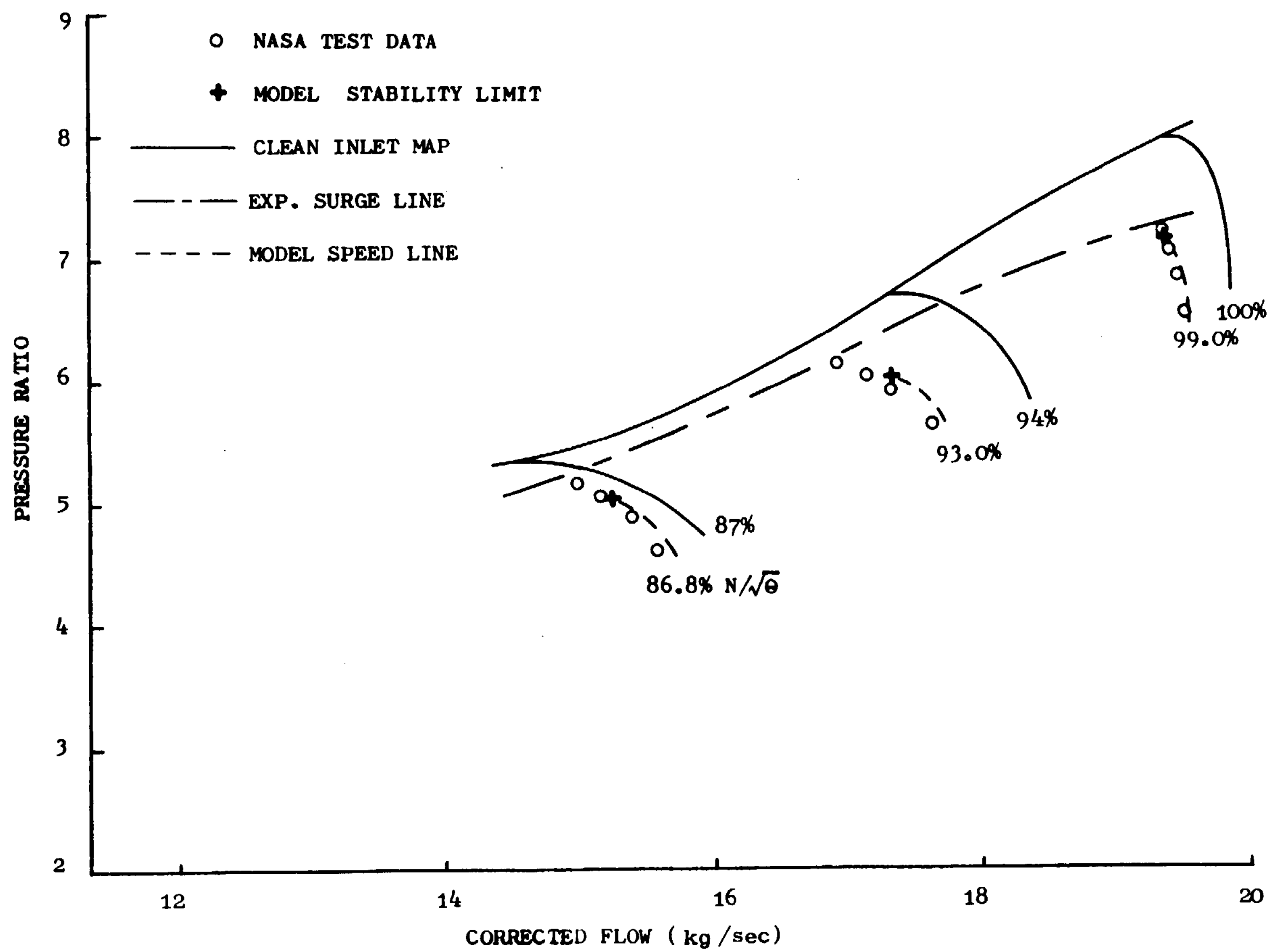

Figure 36. Effect of 180°, 1/Rev Combined Total-Pressure and Total-Temperature Distortion, 90° Overlapped Orientation Low Total-Temperature Distortion on Surge Line of "Mehalic" Engine.

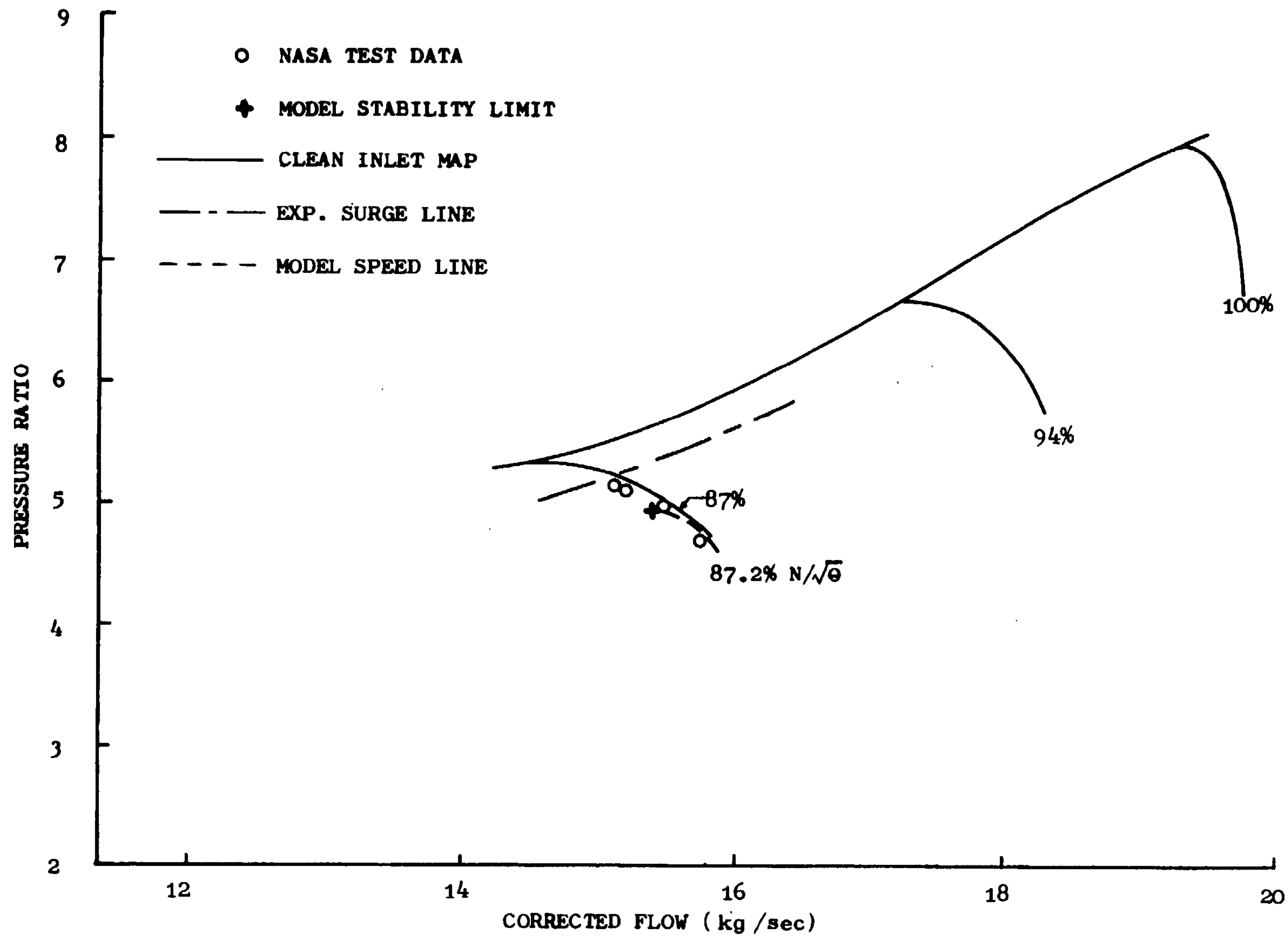

Figure 37. Effect of 180°, 1/Rev Combined Total-Pressure and Total-Temperature Distortion, 90° Overlapped Orientation Moderate Total-Temperature Distortion on Surge Line of "Mehalic" Engine.

Sample documentation for one 90° overlapped case is given by Table 29 of Appendix F. Also contained in Appendix F is the detailed compressor map (Figure 95) for moderate total-temperature distortion.

4.5 SUMMARY OF PARALLEL COMPRESSOR RESULTS

4.5.1 Distortion Sensitivity

One of the most common techniques for indicating the response of a compressor or engine to various inlet conditions is to compare the surge pressure ratio of the distorted inlet-flow compressor to the clean inlet-flow compressor. This loss in surge pressure ratio (ΔPRS) can be calculated on a constant speed or constant flow basis depending on the desired application of the results. As an aid in evaluating the overall ability of the dynamic parallel-compressor model to predict the degradation of the surge line when subjected to various inlet conditions, a comparison between the experimental- and predicted-loss in surge pressure ratios has been made. Figures 38 and 39 respectively present the loss in constant speed and constant flow surge pressure ratios predicted by the parallel-compressor model compared to the experimental losses in surge pressure ratio. At high corrected speeds, the parallel compressor model does a very credible job of predicting the actual loss in surge pressure ratio for 180 degree, 1/rev distortions. The data points on the figures which are scattered furthest from the perfect agreement line are indicative of results at lower corrected speeds and of the 90° overlapped distortions. It is felt the inability of the model to match the experimental performance is due largely to the parallel-compressor limitations which prevent any flow redistribution or communication between the sectors.

Due to the close proximity of the blade rows to one another, it is felt that the major redistribution events probably have to take part in the free volumes upstream of the inlet guide vane. This line of reasoning is supported by a number of studies. Plourde and Stenning (Reference 8) concluded that "for compressors with normal clearances, circumferential flow redistribution occurs ahead of the compressor, and very little crossflow occurs within the compressor." Spring (Reference 12) extended the analytical technique of Plourde and Stenning (Reference 8) to determine the effect of the compressor pumping characteristic on the flow field entering the compressor. He found that significant static-pressure distortions and tangential velocity components existed at the compressor face while none existed far upstream where a pure total-pressure distortion was being impressed. For a pure sinusoidal circumferential total-pressure distortion of ±5% far upstream of the compressor, it was found that at the compressor face, ±4% static pressure distortion was created with a concomitant tangential velocity distribution of ±37% of the mean axial velocity. However, the corrected flow distortion dropped from approximately ±35% to approximately ±5%. Adamczyk (Reference 13) also shows a flattening of axial velocity profile as the compressor face is approached from upstream.

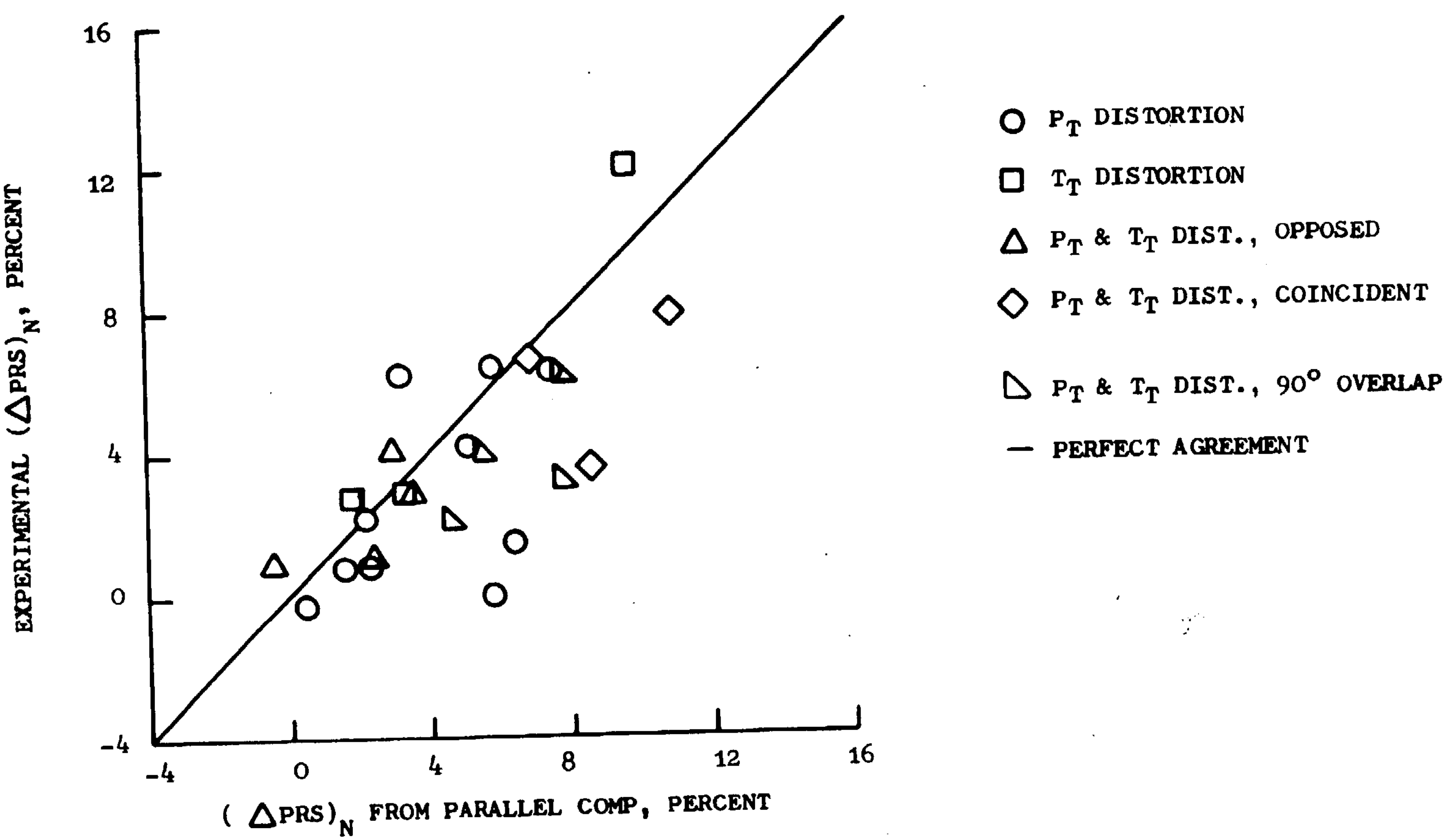

Figure 38. Comparison Between Actual and Predicted Loss In Surge Pressure Ratio at Constant Speed.

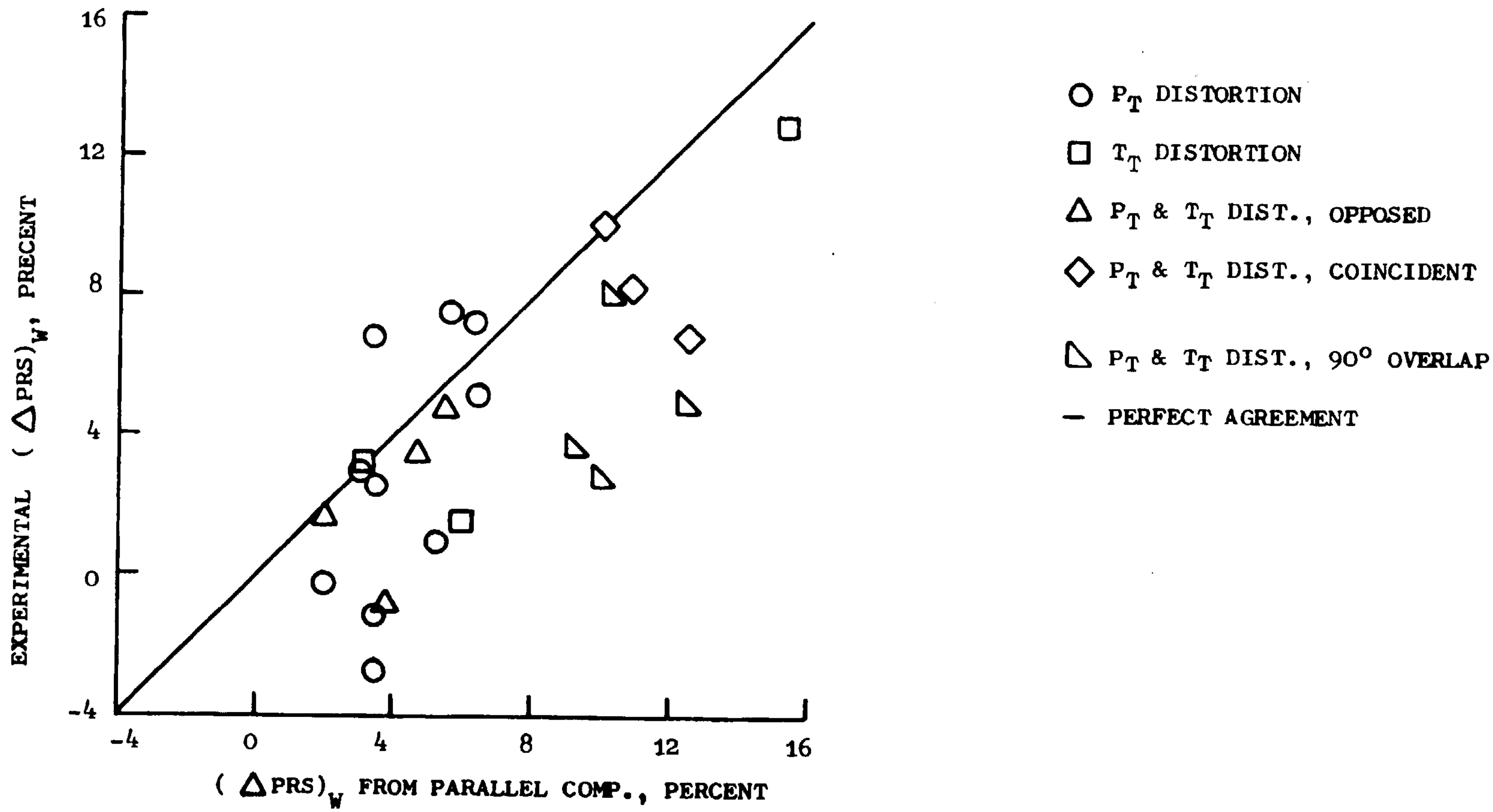

Figure 39. Comparison Between Actual and Predicted Loss In Surge Pressure Ratio at Constant Flow.

Braithwaite, Graber, and Mehalic (Reference 14) have derived a simplified parallel compressor model which yielded substantially the same results in terms of $\Delta PRS)_{Calculated}$ versus $\Delta PRS)_{Measured}$ correlation. Their analysis included all of the pure total-temperature and combined total-temperature and total-pressure distortion data points reported upon in this report. Further, it is noted that the Dynamic Blade Row Parallel Compressor model results also showed that opposed orientation total-pressure and total-temperature distortions can offset each other, thereby producing insignificant losses in surge pressure ratio. This is in agreement with the experimental data and the results of the simplified parallel compressor model proposed by Braithwaite, et al.

4.5.2 Transmission of Distortion

It is of interest to compressor design personnel to determine the contributions of individual stages to the attenuation or amplification of distortion. The normalized circumferential total-pressure, total-temperature, and static-pressure distortions at the exit of each rotor have been calculated. The distortion values were calculated as the difference between the highest and lowest circumferential values of the parameter normalized by the area weighted average of the parameter. As an example of the method of presentation, the results for inlet total-pressure distortion at high speeds (94 and 100% $N/\sqrt{\theta}$) are shown in Figures 40 through 42. Additional distortion amplification results are given in Figures 96 through 110 of Appendix G.

Examination of Figure 40 shows that the total-pressure distortion is amplified in rotors 3 and 4 at 94% $N/\sqrt{\theta}$ while it is amplified slightly or is transmitted with no change by rotor 4 at 100% $N/\sqrt{\theta}$. All other stages at both speeds attenuate the total-pressure distortion. Figure 41 shows that with an inlet total-pressure distortion at 94 and 100% $N/\sqrt{\theta}$, little temperature distortion is created or amplified until the pressure distortion reaches the rear stages (6, 7, and 8). The static-pressure distortion which accompanies the total-pressure distortion behaves in the same manner as the total-pressure distortion. In fact, this observation holds true for all the distortions simulated during this study.

It is interesting to note the behavior of the "Mehalic" engine when subjected to 180°, 1/rev total-temperature distortion (see Figures 99 through 101). Although there was no imposed total-pressure distortion, significant total-pressure distortion was generated as a result of the sectors operating at different corrected speeds. At 99.6% corrected speed, a small total-pressure distortion was created in rotor 1 and attenuated thereafter in the compressor. At lower corrected speeds, substantial total-pressure distortion was generated in rotors 2 through 4 although rotor 2 significantly attenuates this distortion at 93.4% $N/\sqrt{\theta}$. The magnitude of the imposed total-temperature distortion changes little throughout the compressor at the higher speeds with some slight attenuation taking place at the 86.8% corrected speed condition.

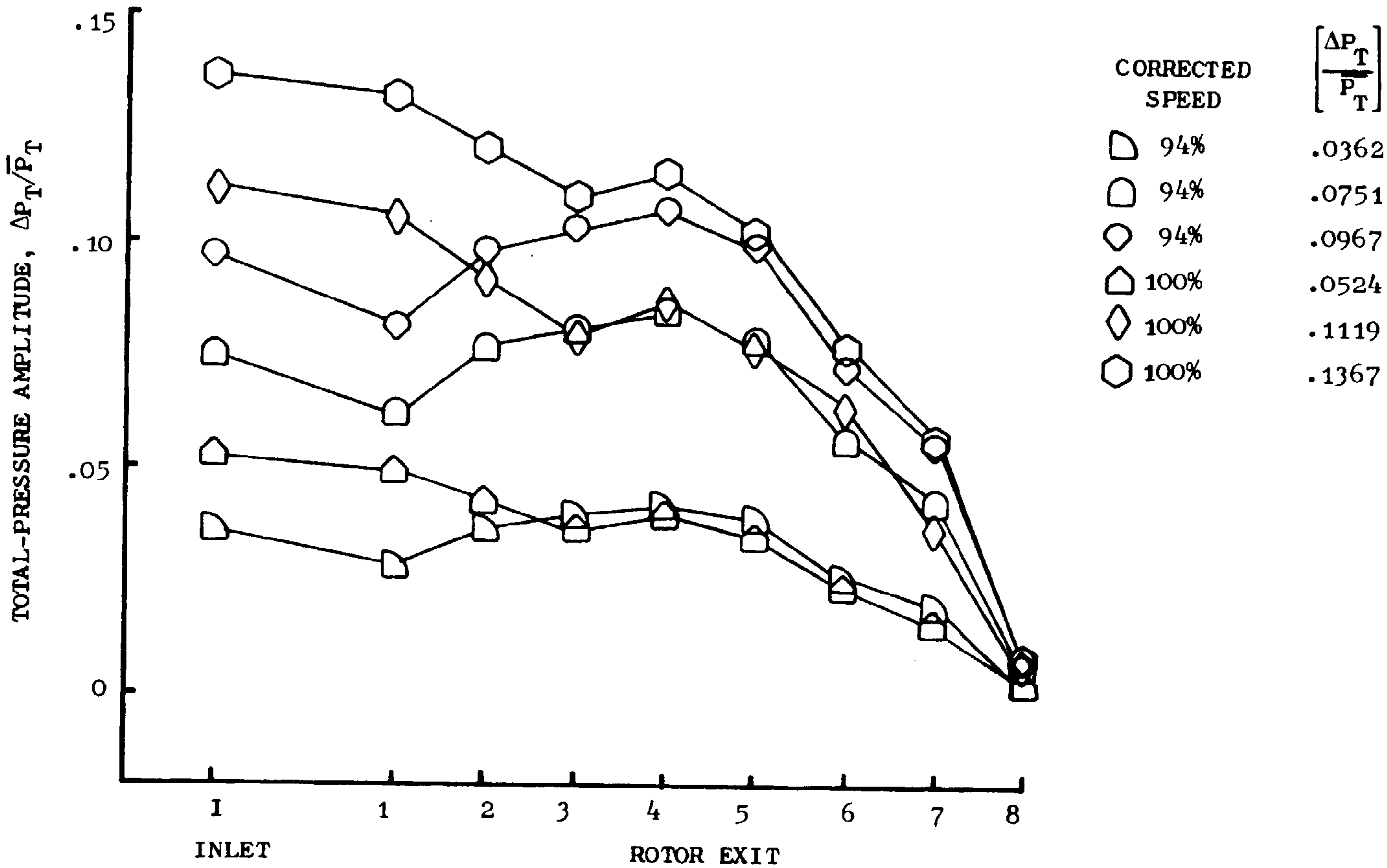

Figure 40. Predicted Total-Pressure Amplification For Inlet Total-Pressure Distortion at 94% and 100% $N/\sqrt{\theta}$.

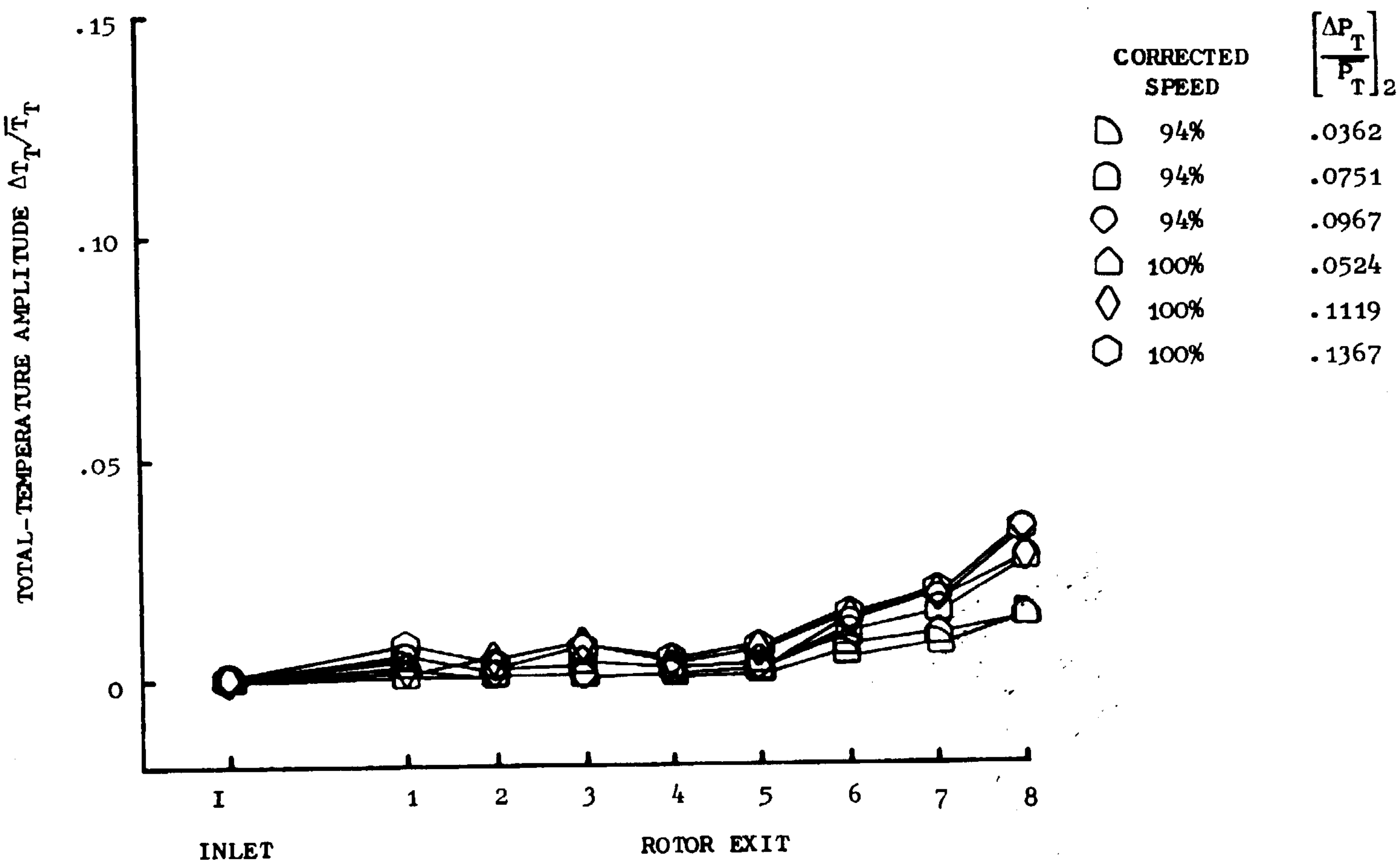

Figure 41. Predicted Total-Temperature Amplification For Inlet Total-Pressure Distortion at 94% and 100% $N/\sqrt{\theta}$.

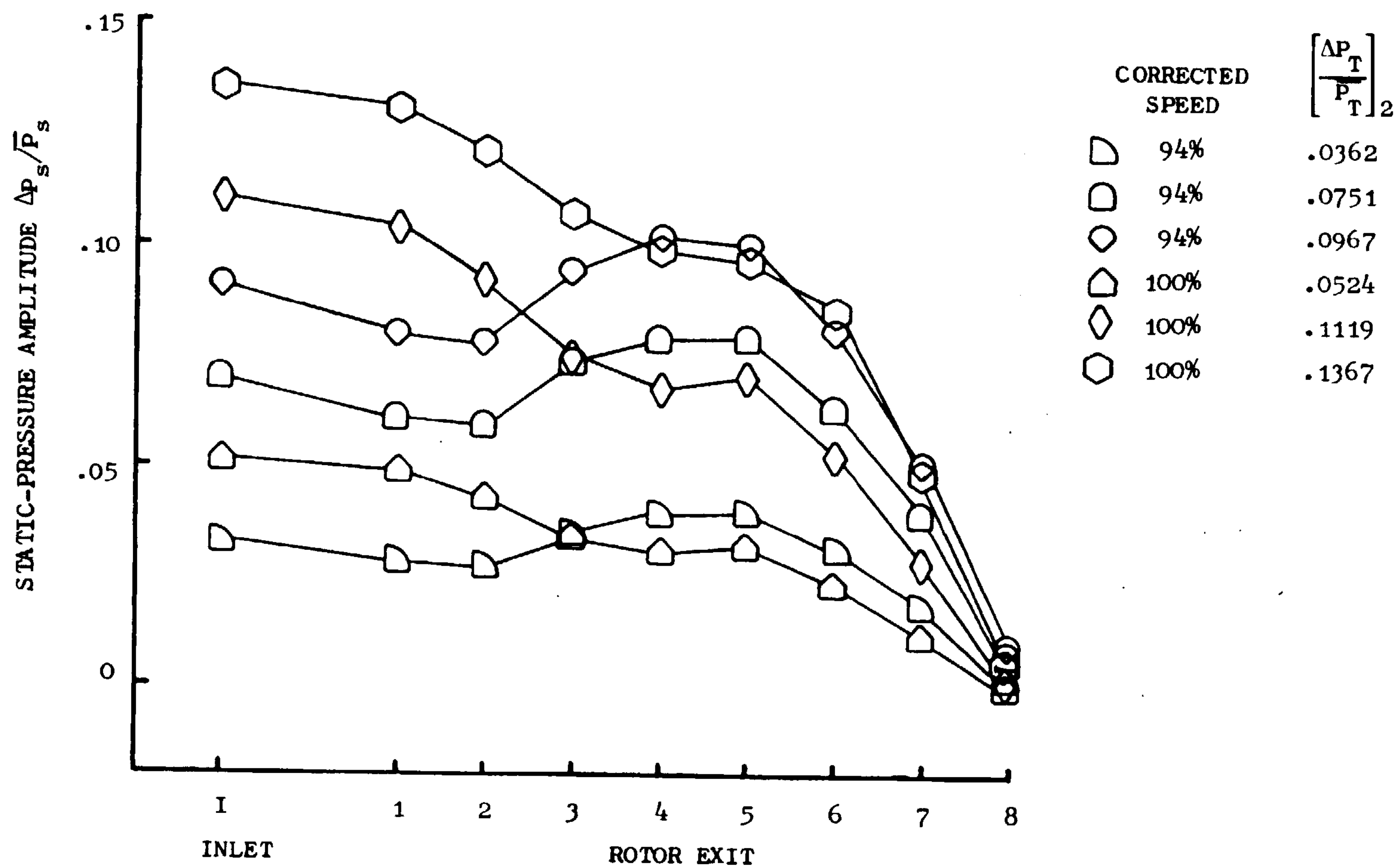

Figure 42. Predicted Static-Pressure Amplification For Inlet Total-Pressure Distortion at 94% and 100% $N/\sqrt{\theta}$.

An examination of the predicted amplifications for the combined total-pressure and total-temperature distortion, opposed orientation (Figures 102 through 104) reveals for all cases, that the imposed total-pressure distortion is attenuated through-out the compressor. Comparison of the two cases at the low corrected speed indicated that the higher total-temperature-distortion aided in attenuating the total-pressure distortion levels. In all cases there is a slight attenuation of the imposed total-temperature distortion.

The response of the compressor to combined total-pressure and total-temperature coincident distortion (Figures 105 through 107) is quite different from the opposed combined distortion. The imposed total-pressure distortion reacts in a manner similar to the "Moss" engine with pure total-pressure distortion. At the lower speeds, rotors 2 through 4 amplify the distortion while at 99.1 percent corrected speed, only rotor 4 causes amplification. In contrast to the opposed distortion pattern orientation, the coincident pattern net total-temperature distortion at the compressor exit was amplified somewhat.

The distortion level response to the combined total-pressure and total-temperature distortion 90° overlapped orientation (Figures 108 through 110) paralleled the coincident pattern distortion cases.

To further understanding and to improve predicting the response of a compressor to distortion, it would be desirable to have an estimate of the circumferential growth of a distorted sector as it passed through the compressor. In order to accurately predict such a phenomenon it would be necessary to calculate the flowfield in detail between blade rows, particularly in the region of the interface between the sectors. A task of this magnitude falls outside of the scope of parallel-compressor representations, but some estimates of the rotation of the sectors and their potential overlap as they travel through the compressor have been made. Based upon an average flow-angle technique, the parallel-compressor results indicated that the overlapping of sectors is probably not a powerful mixing force for this particular compressor since the sectors tend to overlap by less than 5° at most. This value is arrived at by comparing values of the parameter "ROT" given in the sector performance tables of Appendices E and F. It is recognized however, that this analysis has not taken into account the locally high values of induced swirl which can exist at the edges of a distortion pattern at the compressor face.

4.5.3 Diffusion Factor Analysis

The blade row model employed in this study provides sufficient information about the inlet and exit velocity diagrams of a blade row to make it possible to calculate one of the parameters useful to the compressor designer, the diffusion factor. As an example of this type of analysis, rotor diffusion factors are plotted for the "Moss" engines with clean inlet flow for 80 and 100 percent corrected speeds in Figures 43 and 44, respectively. At each speed, the diffusion factor is given for three flows - unthrottled, mid-range, and near surge. The largest difference between the two speeds occurs in rotor

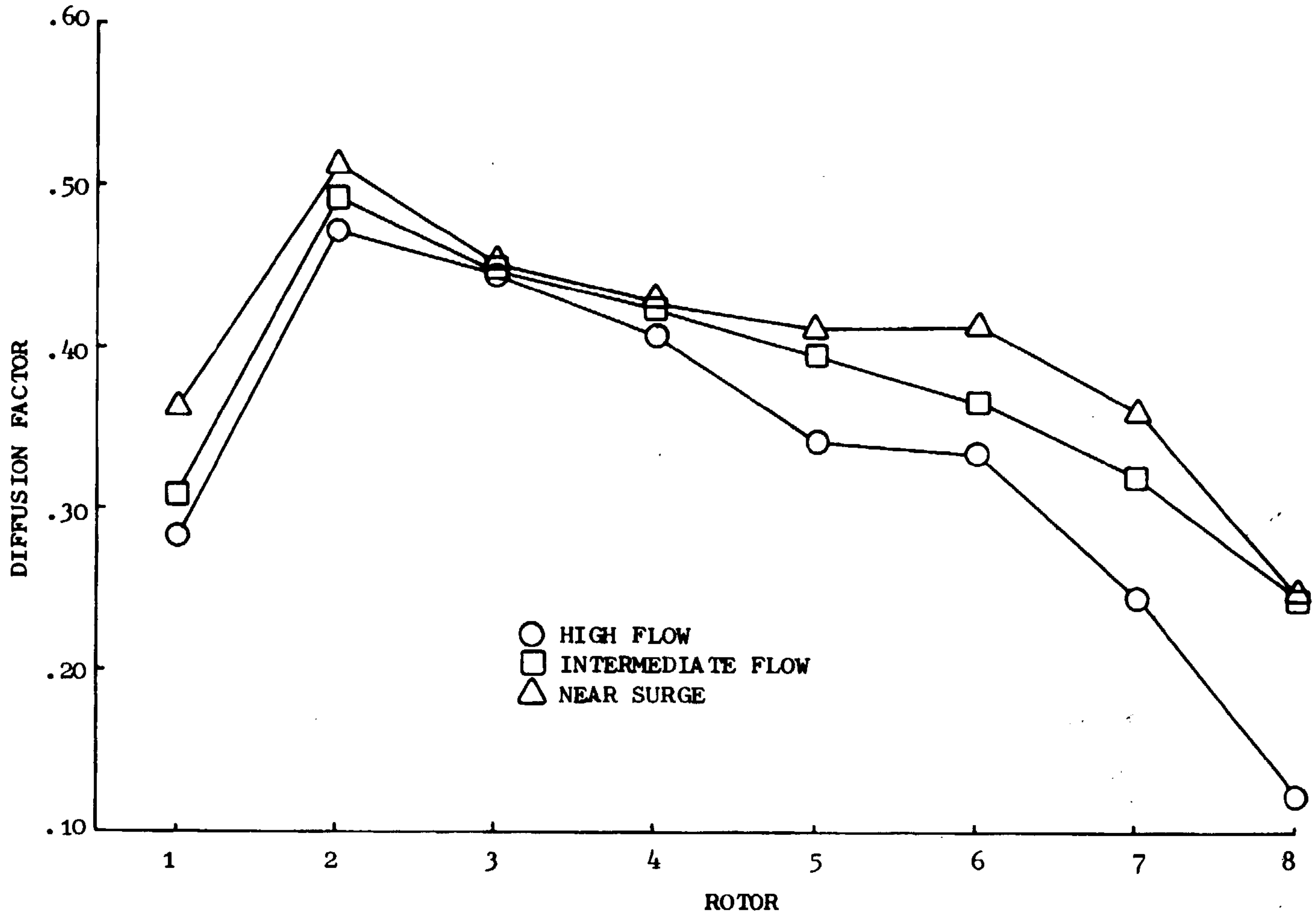

Figure 43. Rotor Diffusion Factors For "Moss" Engine Clean Inlet Flow at 80% $N/\sqrt{\theta}$.

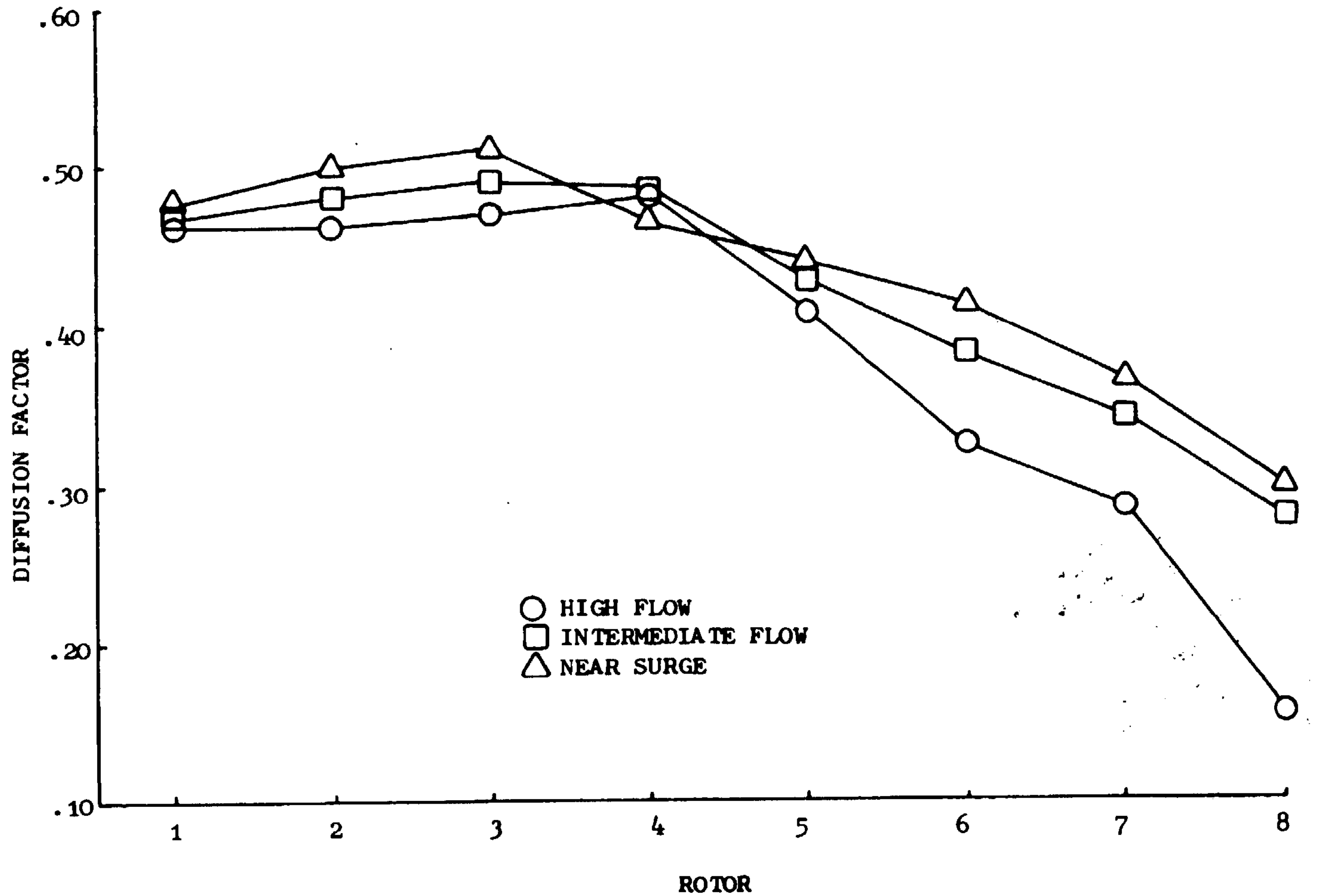

Figure 44. Rotor Diffusion Factors For "Moss" Engine Clean Inlet Flow at 100% $N/\sqrt{\theta}$.

1 where at 100 percent corrected speed, rotor 1 has a considerably higher level of loading. Both figures show that as surge is approached, the level of diffusion factor increases except in rotor 3 at 80 percent corrected speed, where it remains essentially constant and at 100 percent corrected speed where rotor 4 shows a small decrease in the diffusion factor as the near surge point is approached.

Analysis of the critical sector for the 180°, 1/rev total-pressure distortions shows that the value of the diffusion factor at surge is the same as that at surge for clean inlet flow. This result is expected since the parallel compressor sectors operate on their clean inlet characteristics. Investigation of the diffusion factor behavior when 180°, 1/rev total-temperature distortions were imposed was not conducted since the critical sector operated at a different corrected speed than the average corrected speed of all sectors, the only speed for which the clean inlet surge line diffusion factor data was available.

4.5.4 Critical Stage Analysis

In conjunction with the development of a stability criterion discussed in Paragraph 4.1, the use of the parameter W_{i+1}/W_i (the ratio of the physical flow leaving a volume to the physical flow entering a volume) as an indicator of the blade row location of the first aerodynamic instability initiation was presented.

Although it is felt that more experience concerning the behavior of this parameter must be gained before confidence in our ability to interpret its results is fully established, the parameter has been examined for the clean inlet flow and 180°, 1/rev inlet total-pressure distortion cases. The results of this analysis are given in Table 8. The indicated rotor is the one which shows W_{i+1}/W_i to drop first and also to give the lowest value of W_{i+1}/W_i at the time the stability criterion has a value of 2 or greater in all the blade rows. Examination of these clean inlet flow results show that the blade row characteristics derived for the "Moss" J85-13 engine imply that flow breakdown is initiated in the front of the compressor (stages 2 and 3) and does show a slight rearward movement with increasing corrected speed as would be expected. Since the blade rows in each sector of the parallel compressor are constrained to operate on blade characteristics determined from clean inlet flow data, it is anticipated that the critical sector blade row where flow breakdown is initiated with inlet total-pressure distortion would be the same as the clean inlet flow results. The parallel compressor results also shown in Table 8 substantiate this point of view.

Table 8. "Moss" Engine Stall Site Analysis.

Percent Corrected Speed	Clean Inlet Flow	180°, 1/Rev Total-Pressure Distortion		
		Low	Moderate	High
80	2*	2	--	2
87	2	2	2	2
94	2	2	2	2
100	3	3	3	3

* Stage where aerodynamic instability originates.

Wenzel, Moss, and Mehalic (Reference 5) have determined the location of the "stall sites", from an analysis of the high-response interstage static-pressure data obtained during testing of the "Moss" engine. The results shown below indicate that the "stall sites" are located in the rear half of the compressor for both clean inlet and distorted inlet flows.

$\% N/\sqrt{\theta}$	Stall Sites	
	Clean	180°, 1/rev P_T
80	5	?
87	–	5/6
94	6/8	6
100	7	6

The model results and the interpretation of the test data do not indicate the type of agreement one would like to see. However, this lack of agreement may not be due to model deficiencies. Before judgment can be rendered on the ability of the model to predict stall sites, it is necessary that a compression component which had extensive interstage instrumentation during testing be modeled and the latest techniques for analyzing and interpreting interstage data be applied. The problem of determining the location of hub stall sites, if they exist, must be remedied since it is unknown how long it takes for a hub stall pulse to propagate to the wall casing and be detected by wall static-pressure transducers.

It is felt that prediction of the blade row where flow breakdown is initiated can be accomplished by a model, but at the same time it is clear that this is an area which requires a lengthy study in itself if proper interpretation of the results are to be made with confidence.

4.5.5 Speed of Computation

An estimation of the speed of computation for any modeling effort of a compressor is dependent upon several variables: the number of volumes, the minimum size of the volume, the number of sectors specified for a parallel-compressor representation, and to a lesser extent upon the number of performance parameters calculated for each blade row and sector. In the case of the J85-13 model, the compressor and combustor were specified using 29 volumes and up to 12 circumferential sectors. The minimum volume length specified the maximum allowable time step in accord with the well known CFL (Courant, Friedrichs, and Lewy) criteria*, in this case, $1X10^{-5}$ sec. Under these constraints, typical run times on the GE/Honeywell 6000 computer were 167 time steps per minute for an undistorted-inlet model and 108 time steps per minute for a two-sector parallel compressor analyses. Quasi-steady-state throttling simulations were usually initiated on the upper-third of the speed line and averaged 3000-5000 time steps to reach surge depending on the speed line involved.

---

*Courant, R., Friedrichs, K.O., and Lewy, H., "Über die Partiellen Differenzengleichungen der Mathematischen Physik, Math. Ann., Vol. 100, 1928, pp 32-74.

In this classical work, it was observed that a necessary condition for the convergence of a difference scheme is that the rate of propagation of signals in the difference scheme should be at least as large as the true maximum signal speed.

5.0 CONCLUSIONS AND RECOMMENDATIONS

Accurate simulation of the clean-inlet-flow speed lines requires proper stacking of the individual stages of a compressor. In some instances, this requires modifying to varying degrees the level and/or the slope of the characteristics obtained from interstage test data. This type of modification requires the experience and judgement of the compressor designer to establish credible characteristics. It became apparent in the course of stacking the stages of the J85-13 compressor to obtain the overall compressor characteristics, that the pressure ratio-corrected flow speed lines passed through a maximum at the experimentally determined clean inlet surge line when the model reproduced the test surge line. In any region where the speed line slope was negative, the model was inherently stable. When the speed line slope became positive, the model was inherently unstable.

The stability criterion used throughout this effort was based upon the ratio of the time rate of change of flow within a blade row to the time rate of change of the flow at the exit imposed throttling boundary condition. Where this value exceeded two in all blade rows, the model could not recover to stable performance. In all cases of clean inlet flow for both the "Moss" and "Mehalic" engines, this criterion led to consistent results and the critical value occurred in a pressure ratio-corrected flow region where an experimental aerodynamic instability was observed. Further, this criterion produced consistent results throughout the distorted flow studies. For these reasons, it is assumed that the stability criterion is potentially an accurate predictor of compressor aerodynamic instability in a one-dimensional model for slow transients. Further studies using other compression components will be required to establish the generality of this stability criterion.

The search for a stability criterion led to another interesting result. Examination of the ratio of the exit flow from a blade-row volume to the entrance flow to that blade-row volume for each volume gives an indication of the location where the flow breakdown within the compressor is occurring. As a function of time, this parameter would indicate values less than one in the stages upstream of the stage where flow breakdown was occurring and a value greater than one downstream of the stage where flow breakdown was occurring. This character is associated with flow storage in a blade-row volume and flow emptying from a blade-row volume, respectively.

A dynamic blade row parallel compressor model with arbitrary extent sectors and with unspecified flow split was constructed. This model, using the clean inlet flow stability criterion applied to each sector, correctly predicted the trends of all the imposed 180°, 1/rev distortions - total-pressure, total-temperature and combined total-pressure and total-temperatue. The accuracy of the distortion predictions in terms of pressure ratio/corrected fflow coordinate differences between predicted and measured values was quite good at high speeds where the speed lines were steep. At low corrected speeds where the speed lines had a much lower slope, the dynamic blade-row parallel-compressor model over-predicted the loss in surge pressure ratio. Classical steady-state parallel compressor theory is also known to overpredict the loss in surge pressure ratio when the speed line has a low value of slope.

There are a number of factors to consider in discussing the differences between the distorted flow model predictions and the test data. First, the gap-to-radius ratios for the J85-13 compressor are quite small and thus, it is hard to imagine that significant inter-blade row flow redistribution is taking place. Secondly, since significant differences in the amount of rotation a streamtube associated with each sector experiences do not occur, it is assumed that the thermodynamics and velocity triangles are not major contributors to flow redistribution within the blade rows.

As previously discussed, probably the most important source contributing to this difference lies in the unrealistic boundary conditions which are imposed upon the flow at the compressor IGV. The analytical results of other investigations clearly indicate that the pumping characteristics of the compressor can substantially modify the flow field between the measurement plane and the engine face by reducing the flow differences in the sectors, by establishing a static-pressure distortion, and by establishing a swirl velocity component. Although static pressure differences between sectors (indicative of static pressure distortion) will be developed in this model upstream of the IGV's due to the flow split, none of the other effects are currently accounted for in the volumes between the measurement plane and the IGV's. Another possible source contributing to the difference between predicted and measured loss in surge pressure ratio may lie in the fact that the third, fourth, and fifth stage bleeds are manifolded in a manner that would allow bleed recirculation from the high-static-pressure distorted sector to the low-static-pressure distorted sector. This possibility has not been taken into account during this program, although a very crude and preliminary approximation indicates that it is probably a secondary effect. Further analysis is required to fully determine the magnitude of the effect of bleed flow manifold recirculation on the loss in surge pressure ratio.

The Dynamic Digital Blade Row Compression Component Stability Model is proving itself as a viable tool for use in stability studies because of its ability to provide insight into the dynamic events at the surge line, the effects of circumferential distortion, and the stage where an aerodynamic instability originates. It also provides the detailed row-by-row variations in the state properties and vector diagram conditions throughout the compressor as they vary with engine operating conditions and inlet distortion. Furthermore, this approach to distorted inlet modeling has the potential to demonstrate whether the circumferential distortion sensitivity of a compression system can be determined analytically from clean inlet stage data plus a minimal amount of distorted inlet testing to verify the validity of the model. This procedure would be in contrast to the current practice of running extensive distorted inlet tests, followed by extensive development and manipulation of distortion parameters to correlate the resulting loss in surge pressure ratios. However, its main strength lies in the general form and flexibility of the equations to handle more complicated flow situations without having to resort to a new model or unduly alter the present model.

For these reasons, it is recommended that the present Dynamic Digital Blade Row Compression Component Stability Model be modified to include tangential flow redistribution in a gross sense, while maintaining the essence of the parallel compressor concept. In this manner, the compressor will establish more realistic inlet flow conditions at the IGV as opposed to the artificially established boundary conditions imposed at the measurement plane and assumed to be valid back to the IGV. In addition, the effects of bleed flow redistribution within the bleed mainfolds should be investigated to determine the magnitude of this effect.

The present model lacks the ability to predict stator induced instabilities since stator loss coefficients are assumed to be zero and the deviation angles are constant. Important insight could be obtained if realistic stator loss coefficients were determined and the stages restacked to give new rotor loss coefficients and deviation angles. Clean-inlet-speed-line and distorted-speed-line throttling would provide results which could be compared with the results of this study, specifically as to the location of the stage where the instability is initiated and to determine if there are any differences in the manner in which flow breakdown occurs.

The ability of the model to handle distortions with extents different than 180° is partially handled by allowing for flow redistribution upstream of the IGV's but would also require that a method be developed for including unsteady flow effects in the loss coefficients and deviation angles, rather than assuming that the loss coefficients and deviation angles determined from steady-state data are always applicable.

APPENDIX A

STAGE CHARACTERISTICS

This appendix documents the J85-13 compressor stage characteristics utilized for this program. Characteristics for both the "Moss" and "Mehalic" versions of the engine are provided. Figures 45 through 58 illustrate the nondimensional characteristics in terms of work and pressure coefficients as a function of flow coefficients. It should be noted that the nondimensional characteristics presented herein are normalized by pitch line wheel speed. The corresponding loss coefficient and deviation angle characteristics are presented in Figures 59 through 72. Tables 9 through 15 provide a tabulation of the coefficients used in the fourth-order polynomial representation of the loss coefficient and deviation angle characteristics. In addition, the bounding values of tangent of incidence angle over which the polynomial representation is valid are indicated.

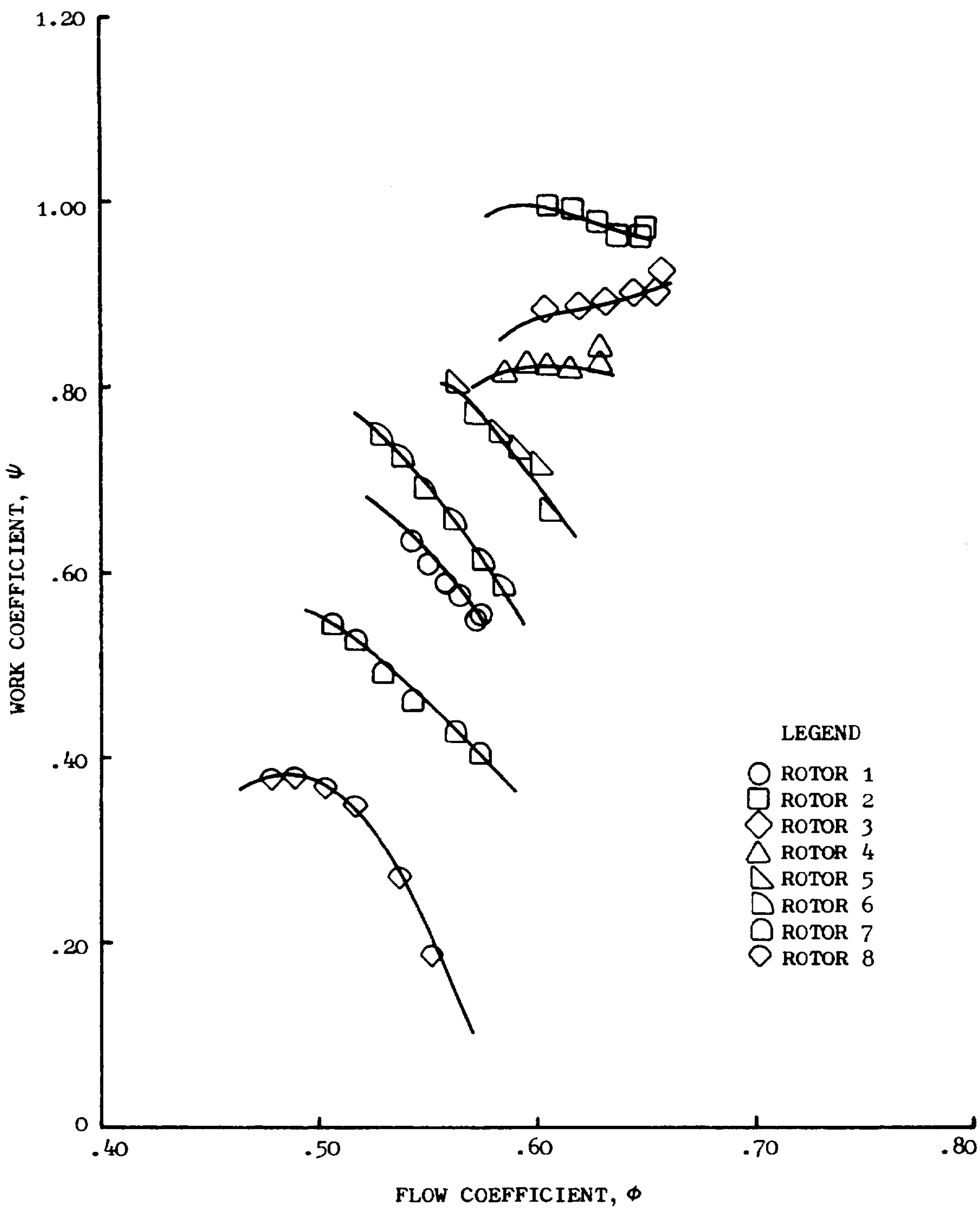

Figure 45. Preliminary and Final Work Coefficients, "Moss" Engine 80% $N/\sqrt{\theta}$.

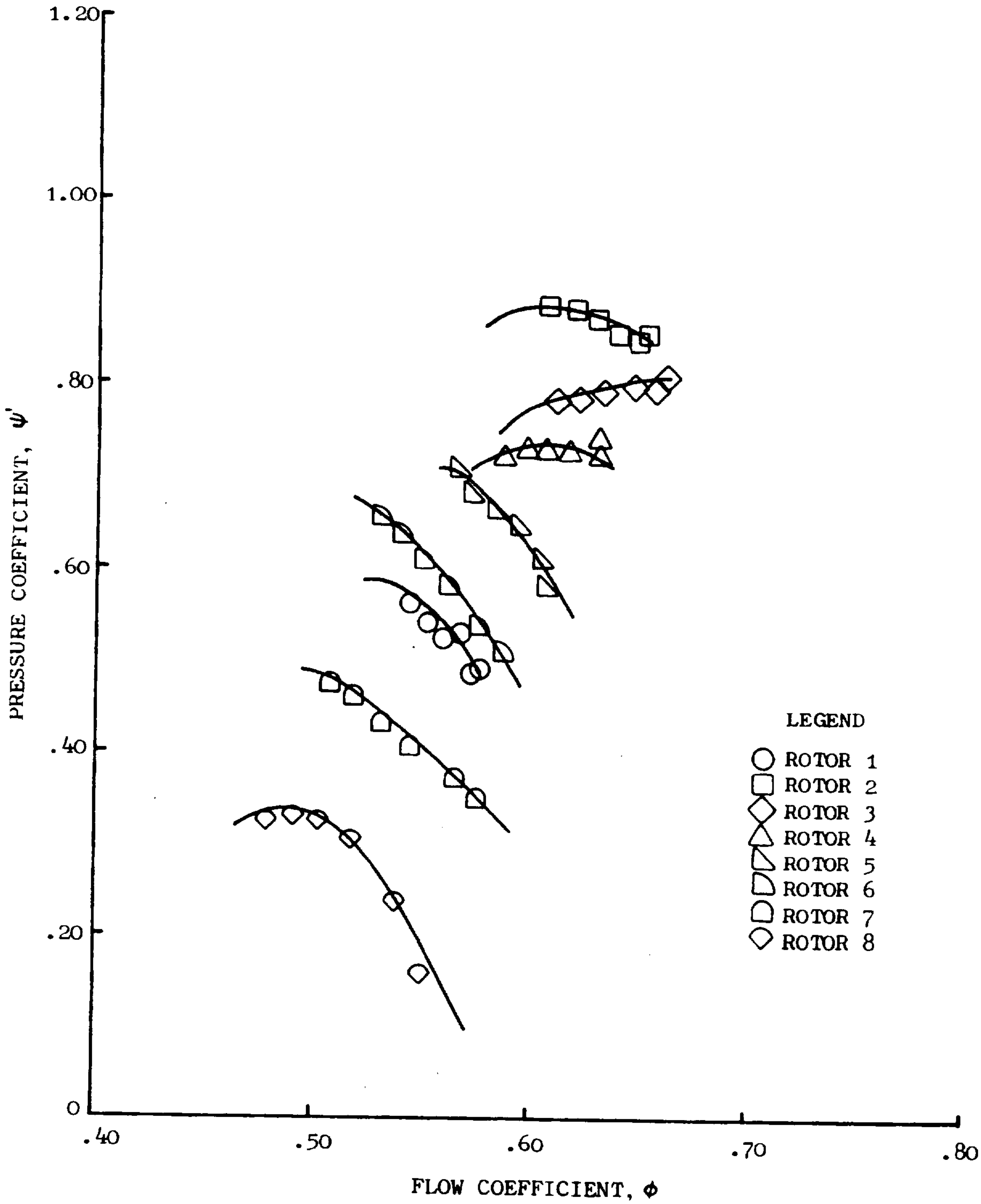

Figure 46. Preliminary and Final Pressure Coefficients, "Moss" Engine 80% $N/\sqrt{\theta}$.

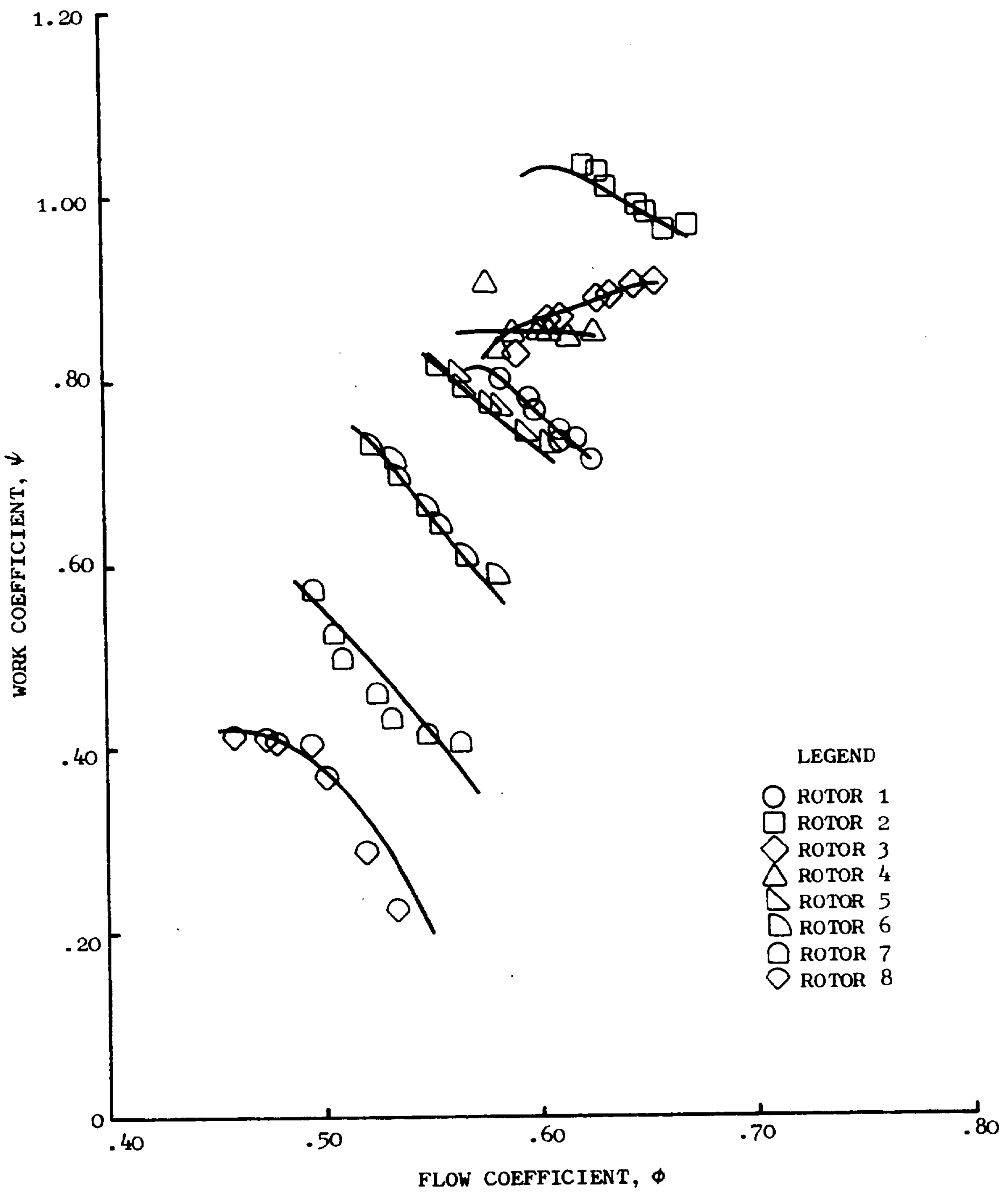

Figure 47. Preliminary and Final Work Coefficients, "Moss" Engine 87% $N/\sqrt{\theta}$.

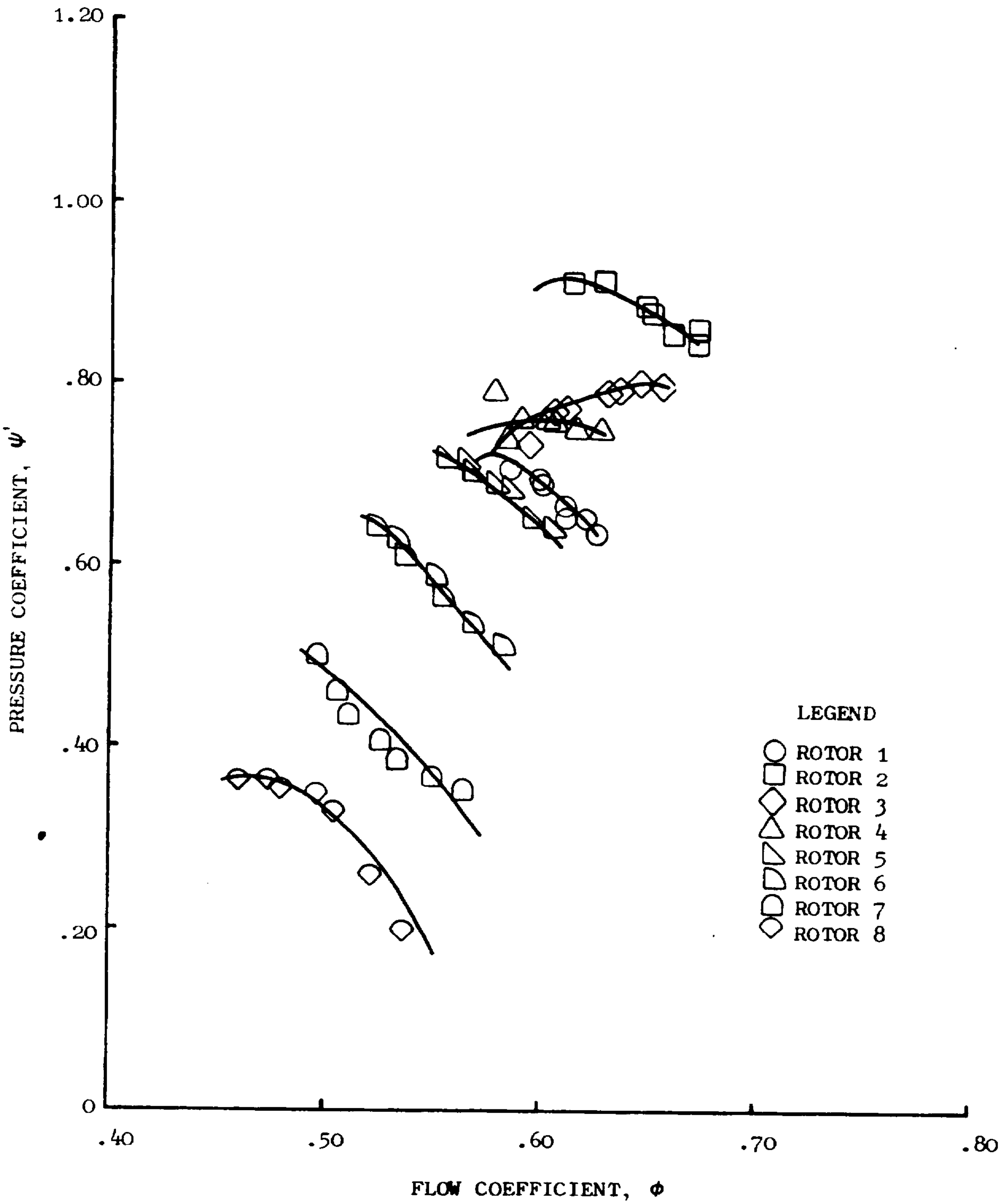

Figure 48. Preliminary and Final Pressure Coefficients, "Moss" Engine 87% $N/\sqrt{\theta}$.

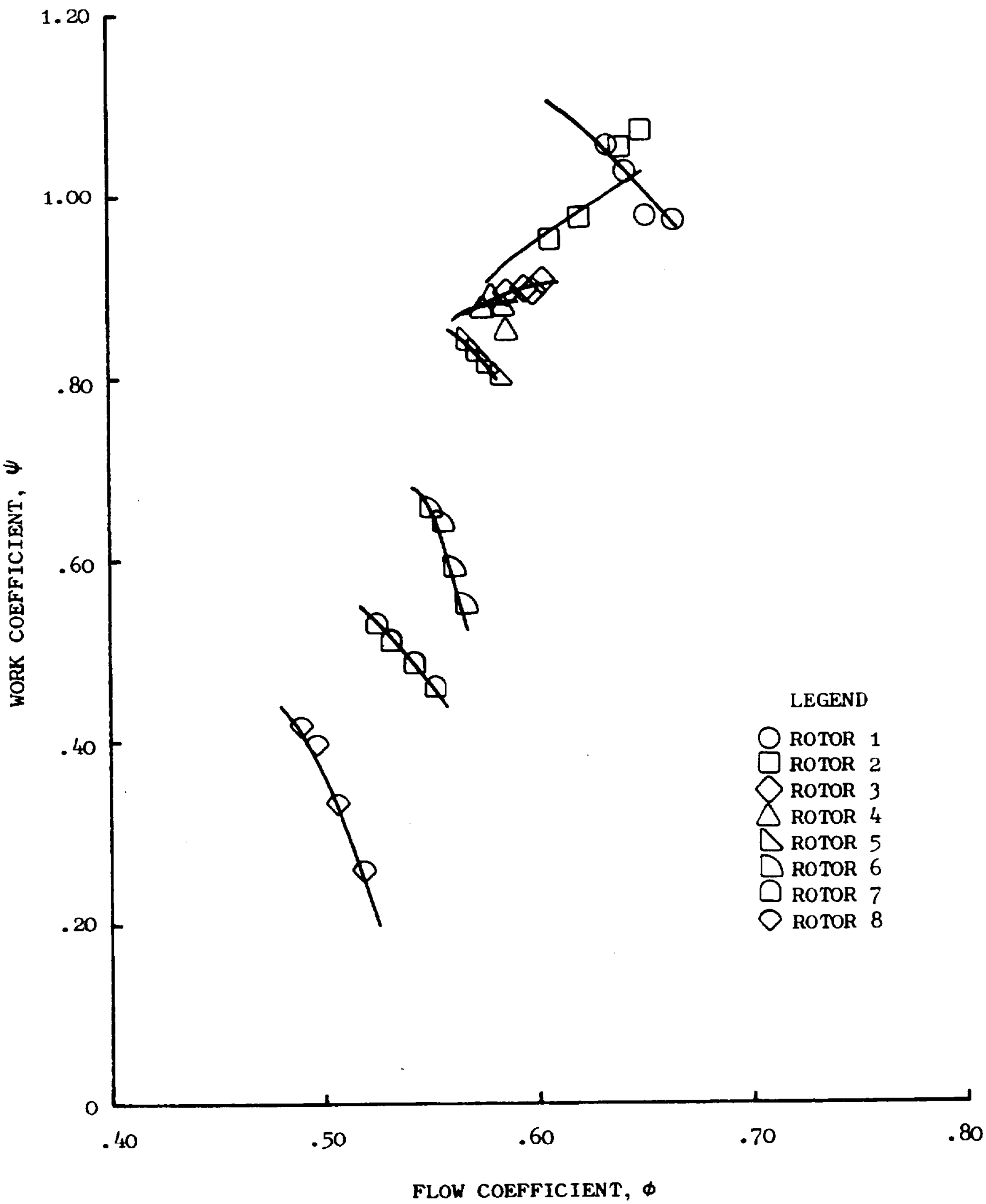

Figure 49. Preliminary and Final Work Coefficients, "Moss" Engine 94% $N/\sqrt{\theta}$.

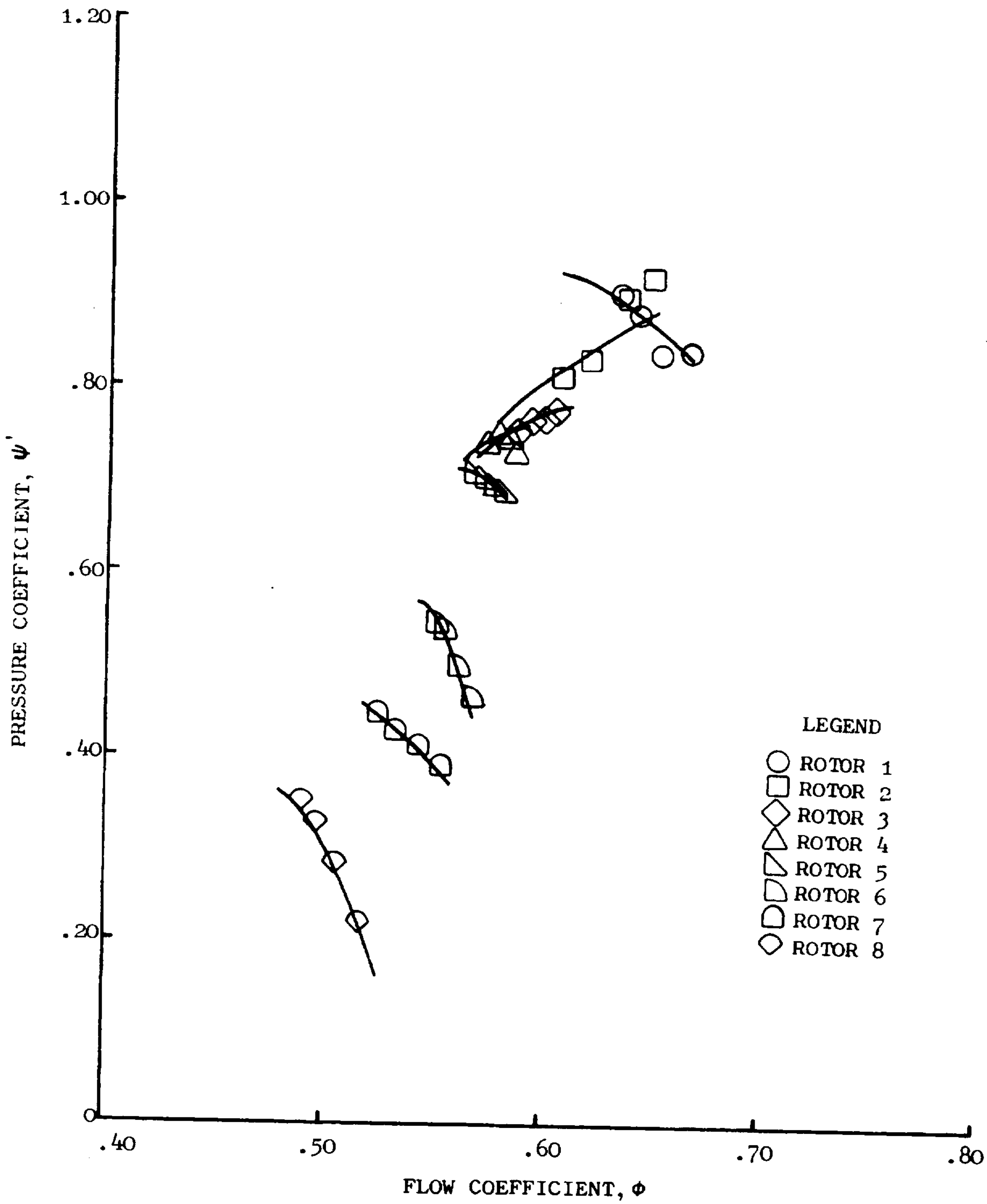

Figure 50. Preliminary and Final Pressure Coefficients, "Moss" Engine 94% $N/\sqrt{\theta}$.

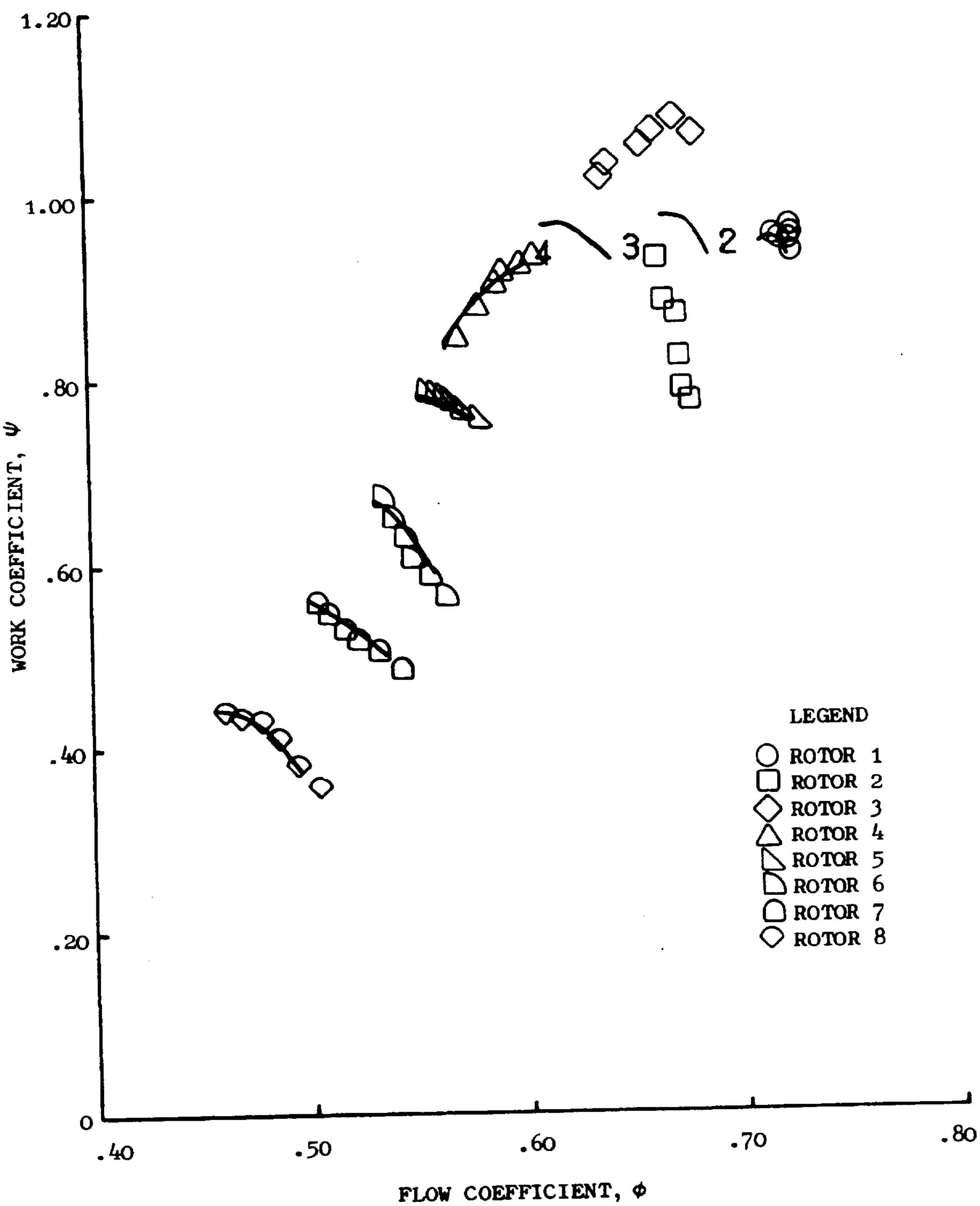

Figure 51. Preliminary and Final Work Coefficients, "Moss" Engine 100% $N/\sqrt{\theta}$.

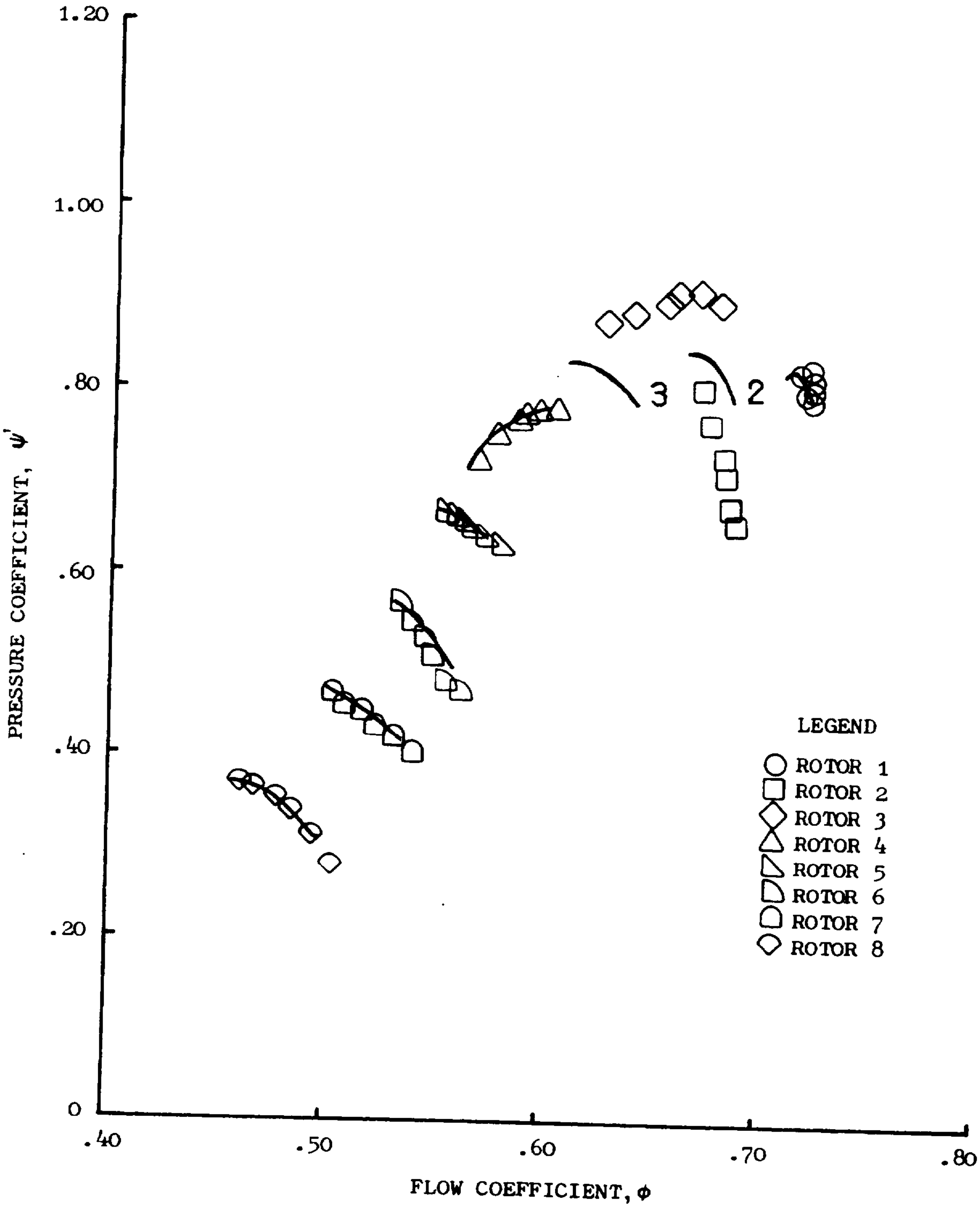

Figure 52. Preliminary and Final Pressure Coefficients, "Moss" Engine 100% $N/\sqrt{\theta}$.

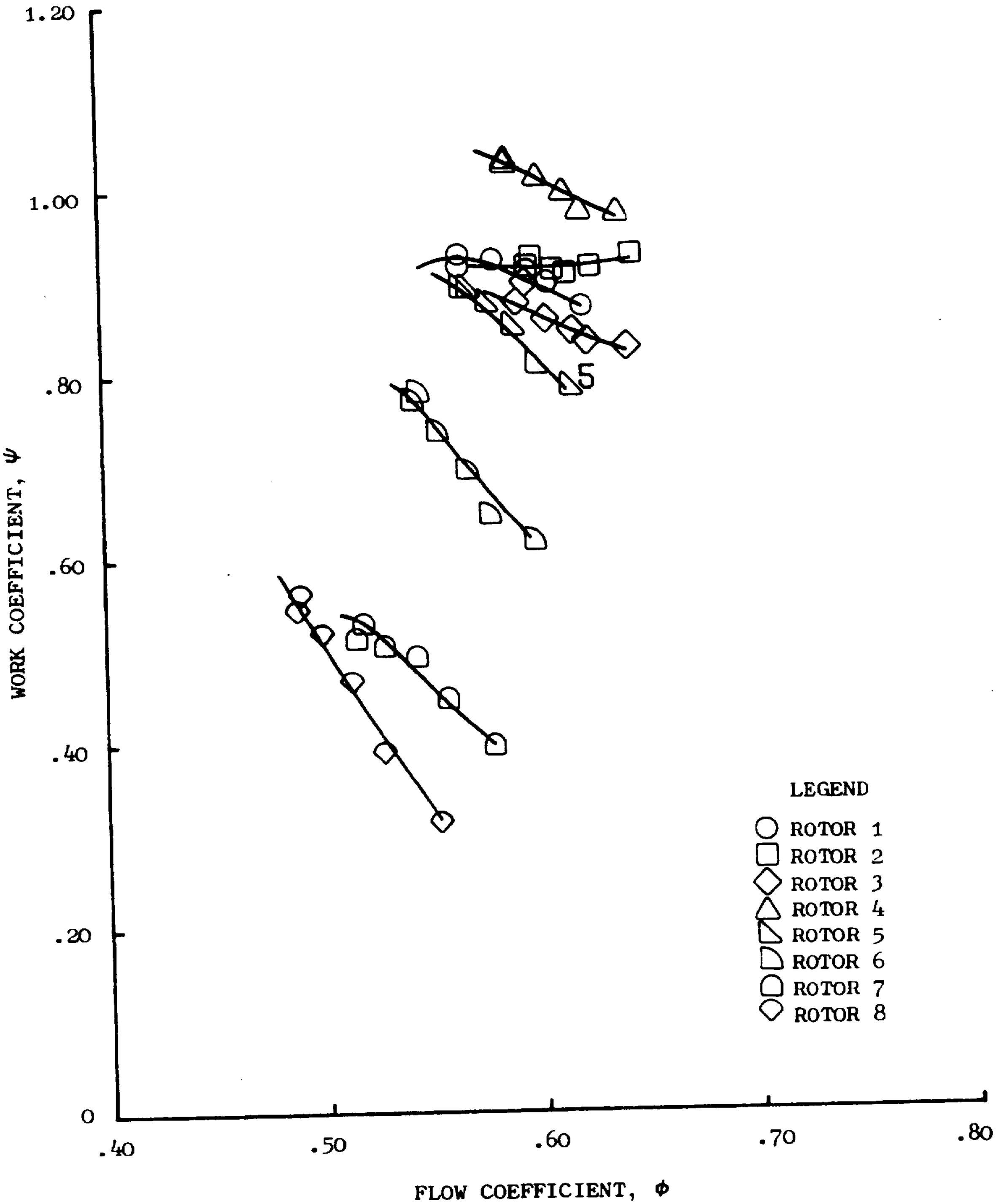

Figure 53. Preliminary and Final Work Coefficients, "Mehalic" Engine 87% N/√θ.

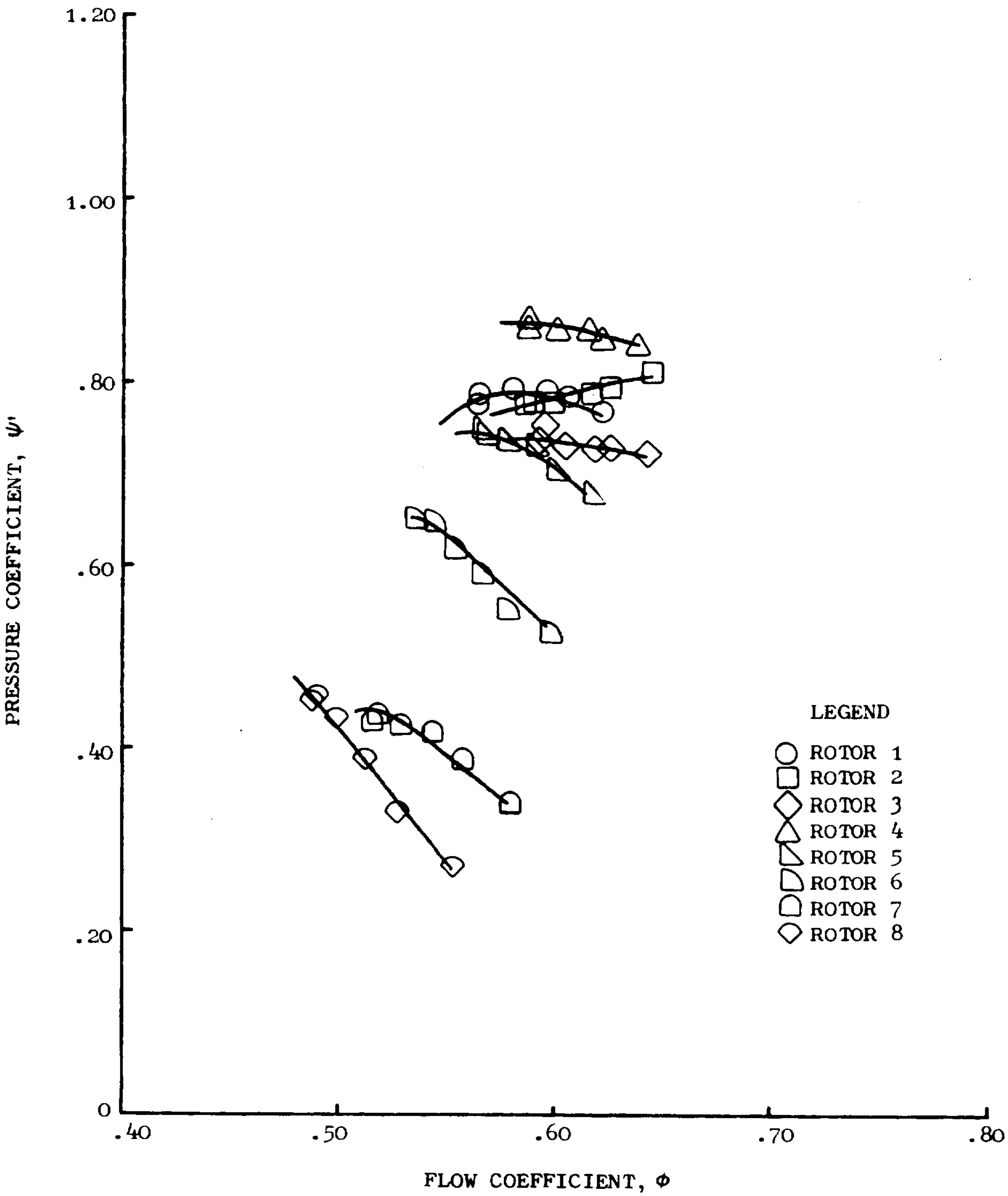

Figure 54. Preliminary and Final Pressure Coefficients, "Mehalic" Engine 87% $N/\sqrt{\theta}$.

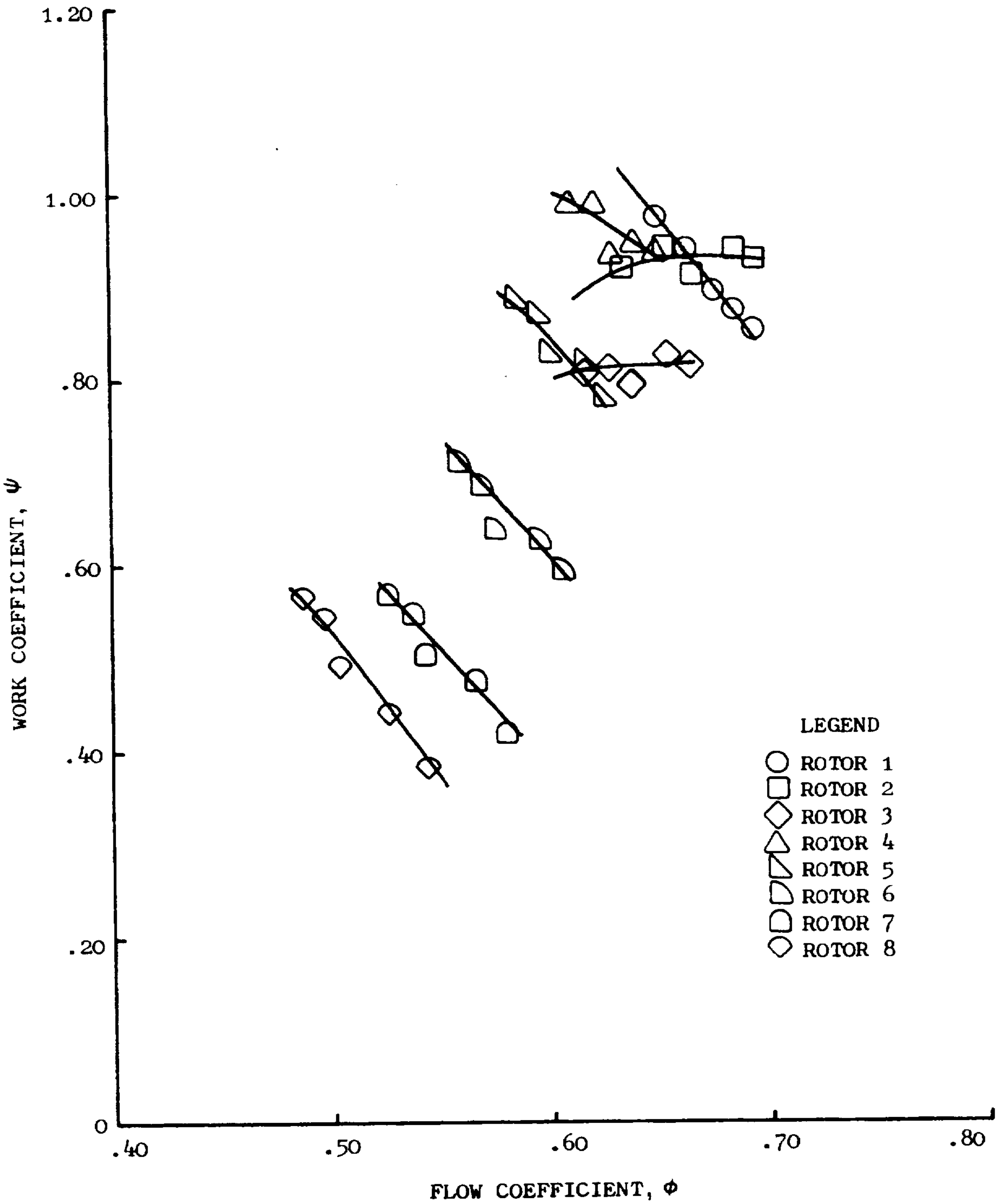

Figure 55. Preliminary and Final Work Coefficients, "Mehalic" Engine 94% $N/\sqrt{\theta}$.

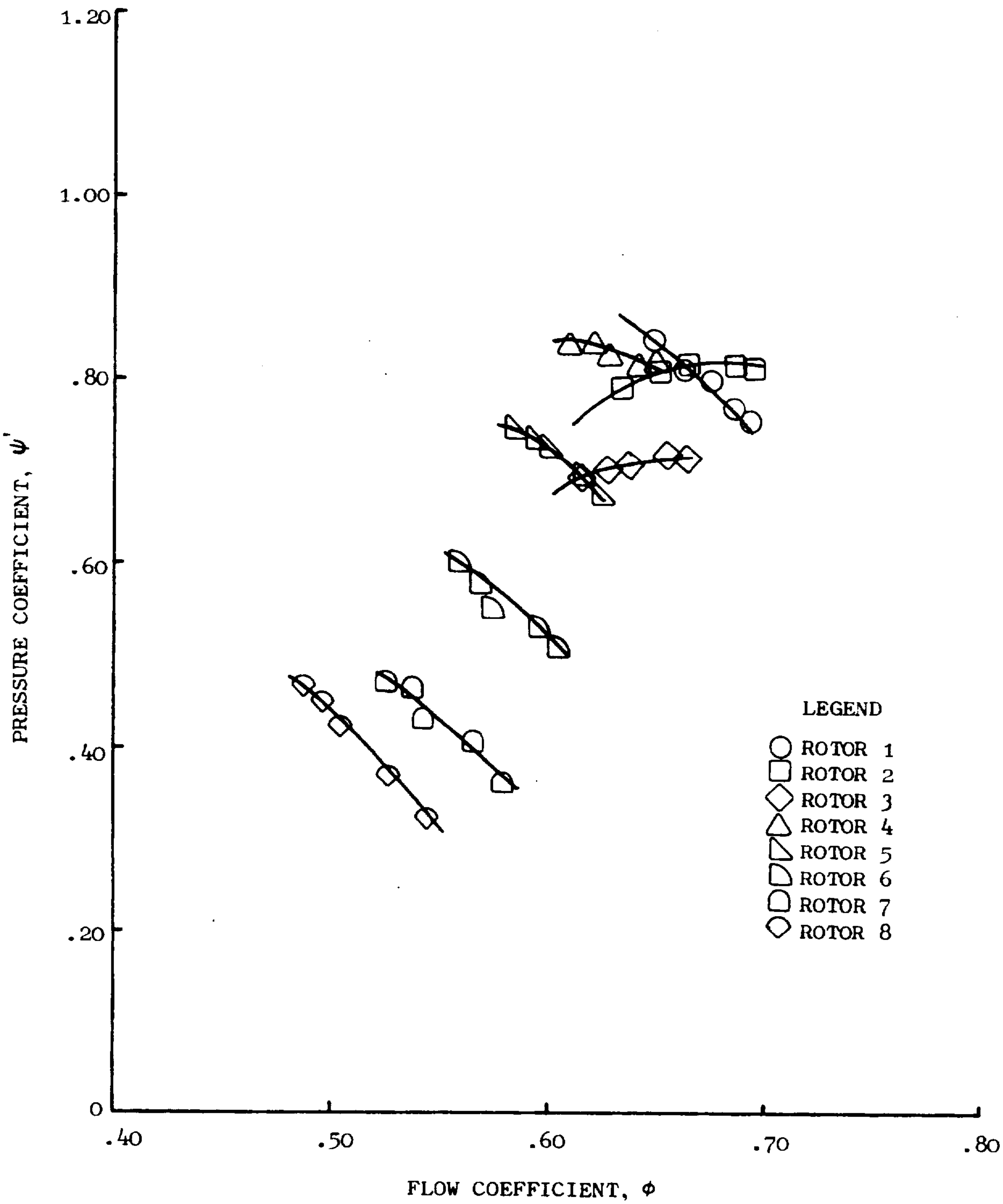

Figure 56. Preliminary and Final Pressure Coefficients, "Mehalic" Engine 94% $N/\sqrt{\theta}$.

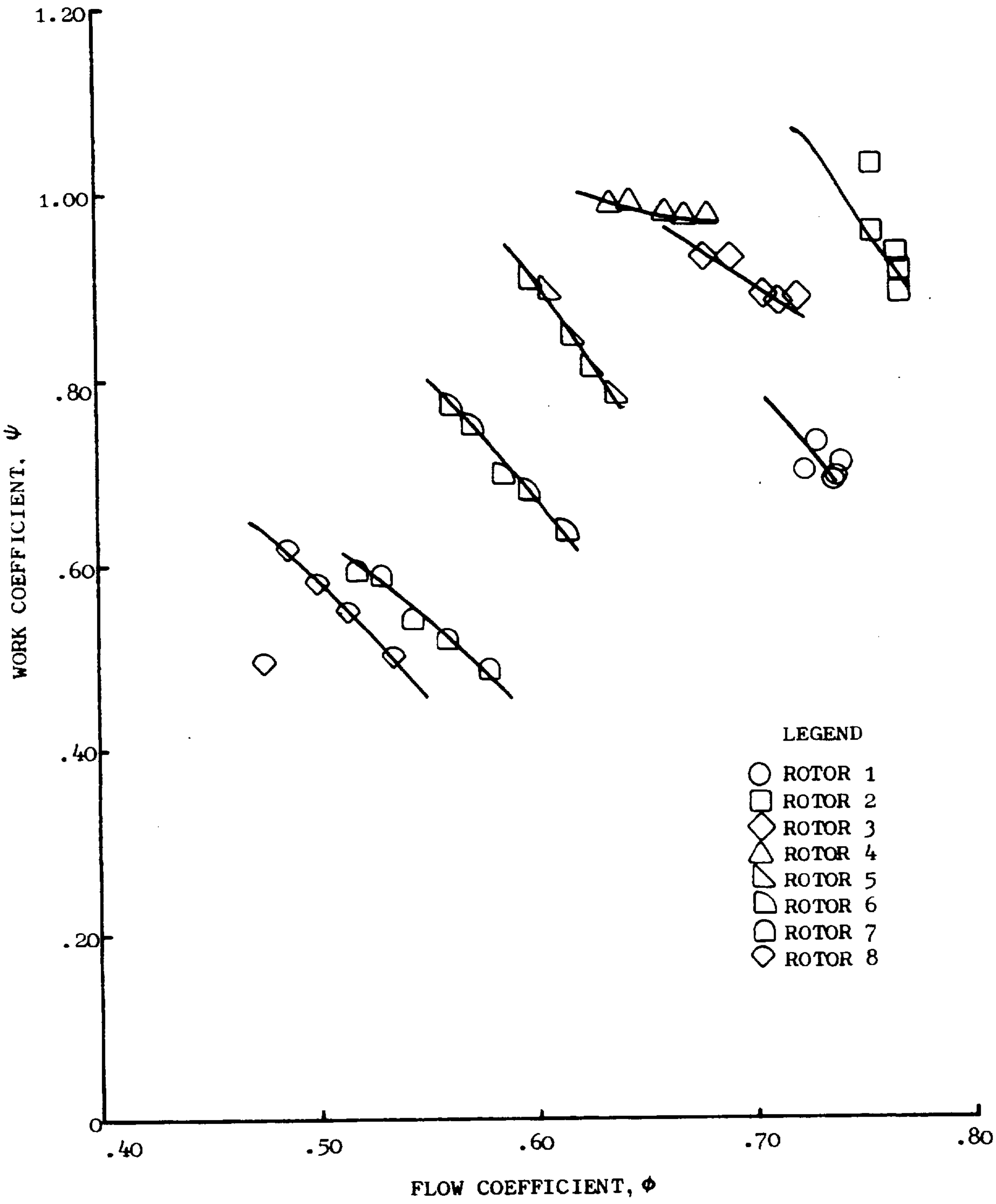

Figure 57. Preliminary and Final Work Coefficients, "Mehalic" Engine 100% $N/\sqrt{\theta}$.

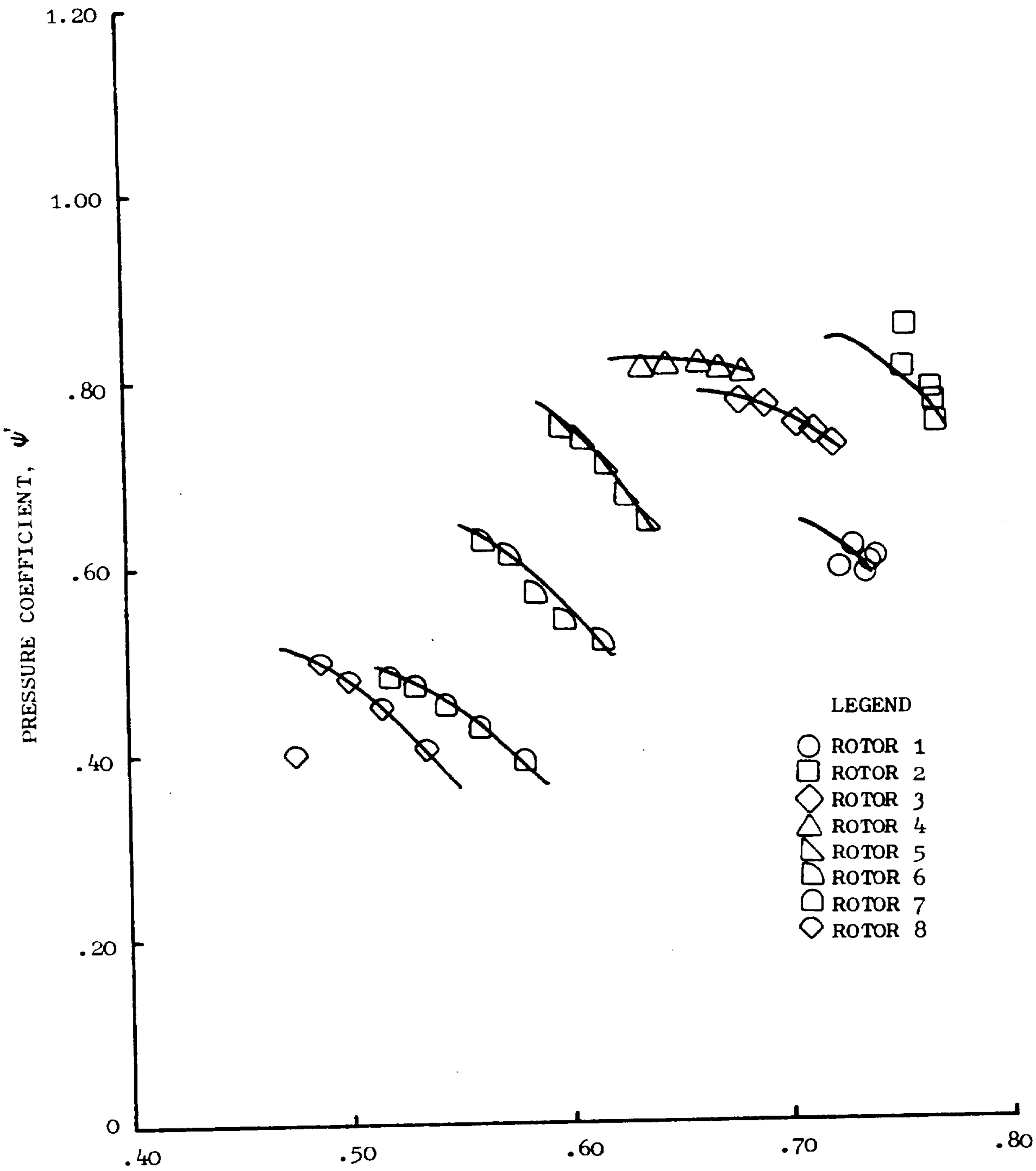

Figure 58. Preliminary and Final Pressure Coefficients, "Mehalic" Engine 100% $N/\sqrt{\theta}$.

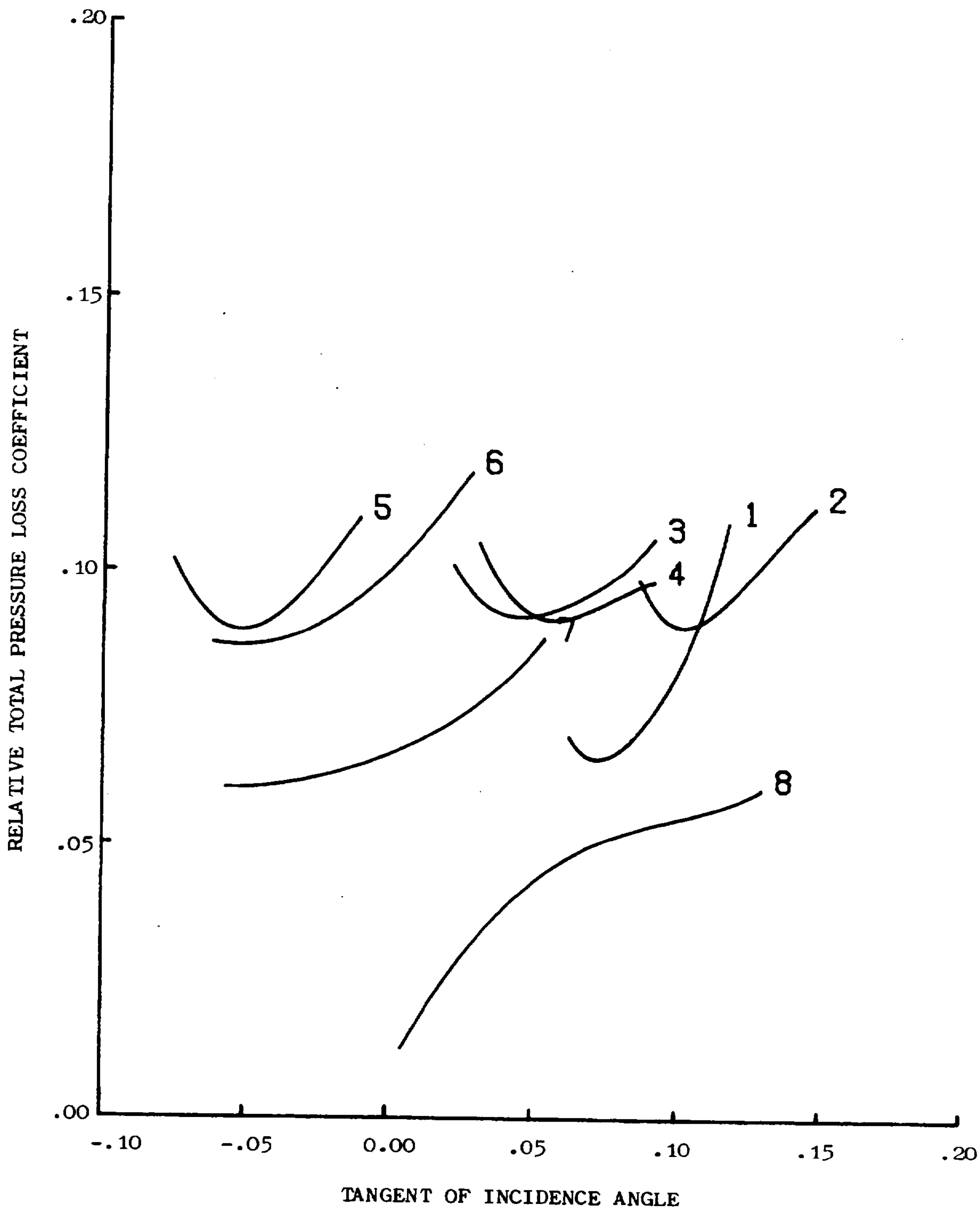

Figure 59. **Rotor Total-Pressure Loss Coefficients, "Moss" Engine 80% $N/\sqrt{\theta}$.**

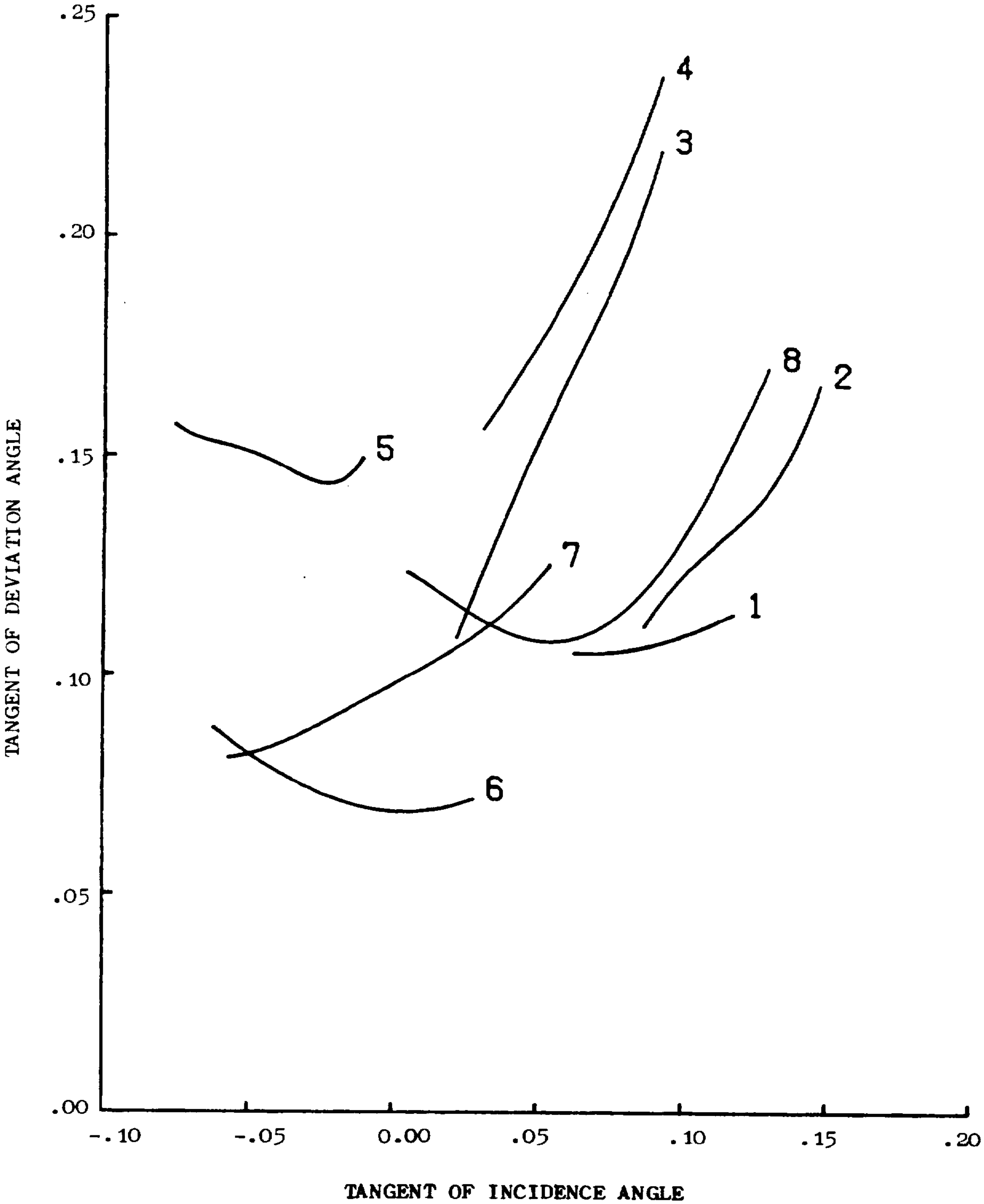

Figure 60. Rotor Deviation Angles, "Moss" Engine 80% $N/\sqrt{\theta}$.

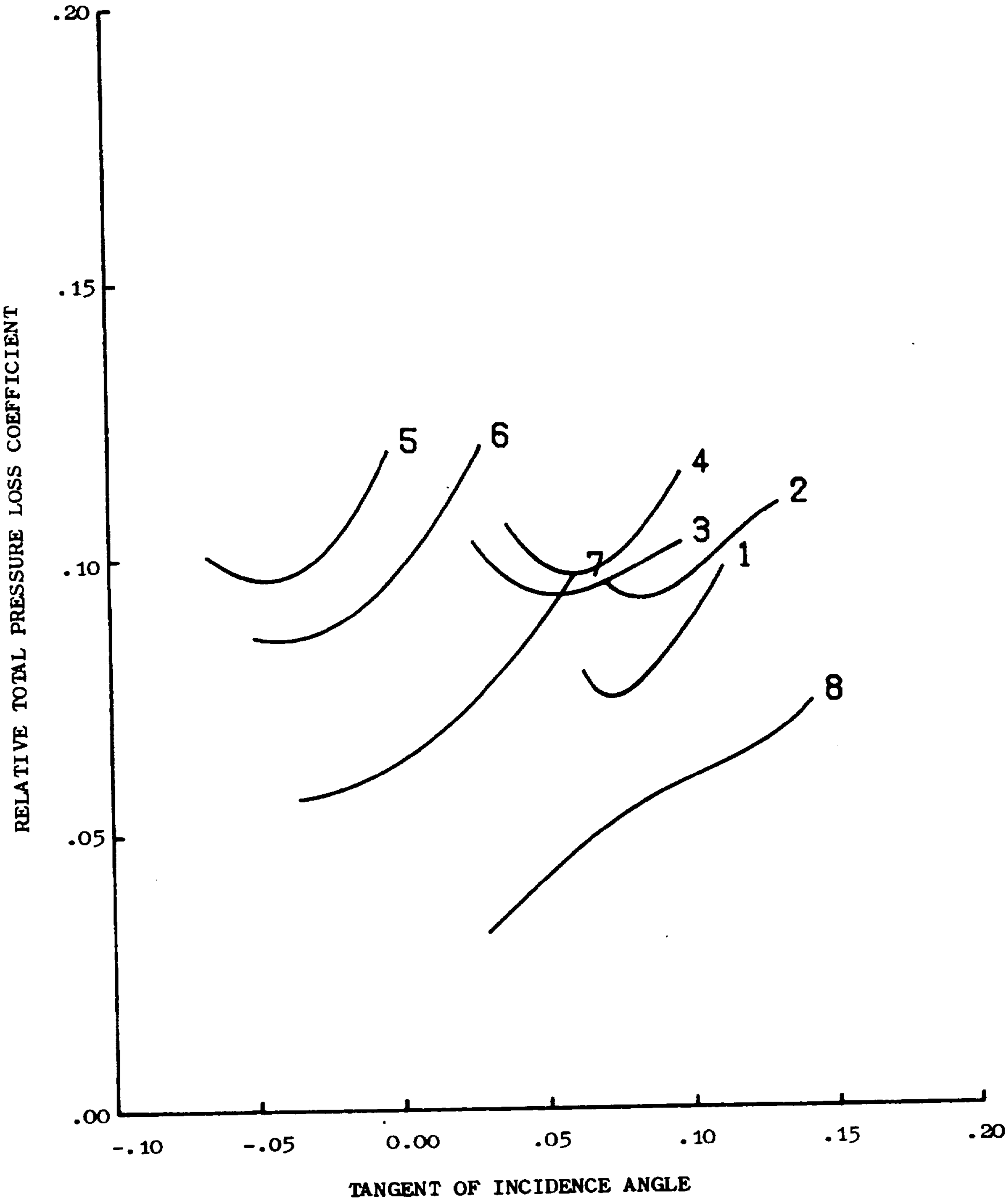

Figure 61. Rotor Total-Pressure Loss Coefficients, "Moss" Engine 87% $N/\sqrt{\theta}$.

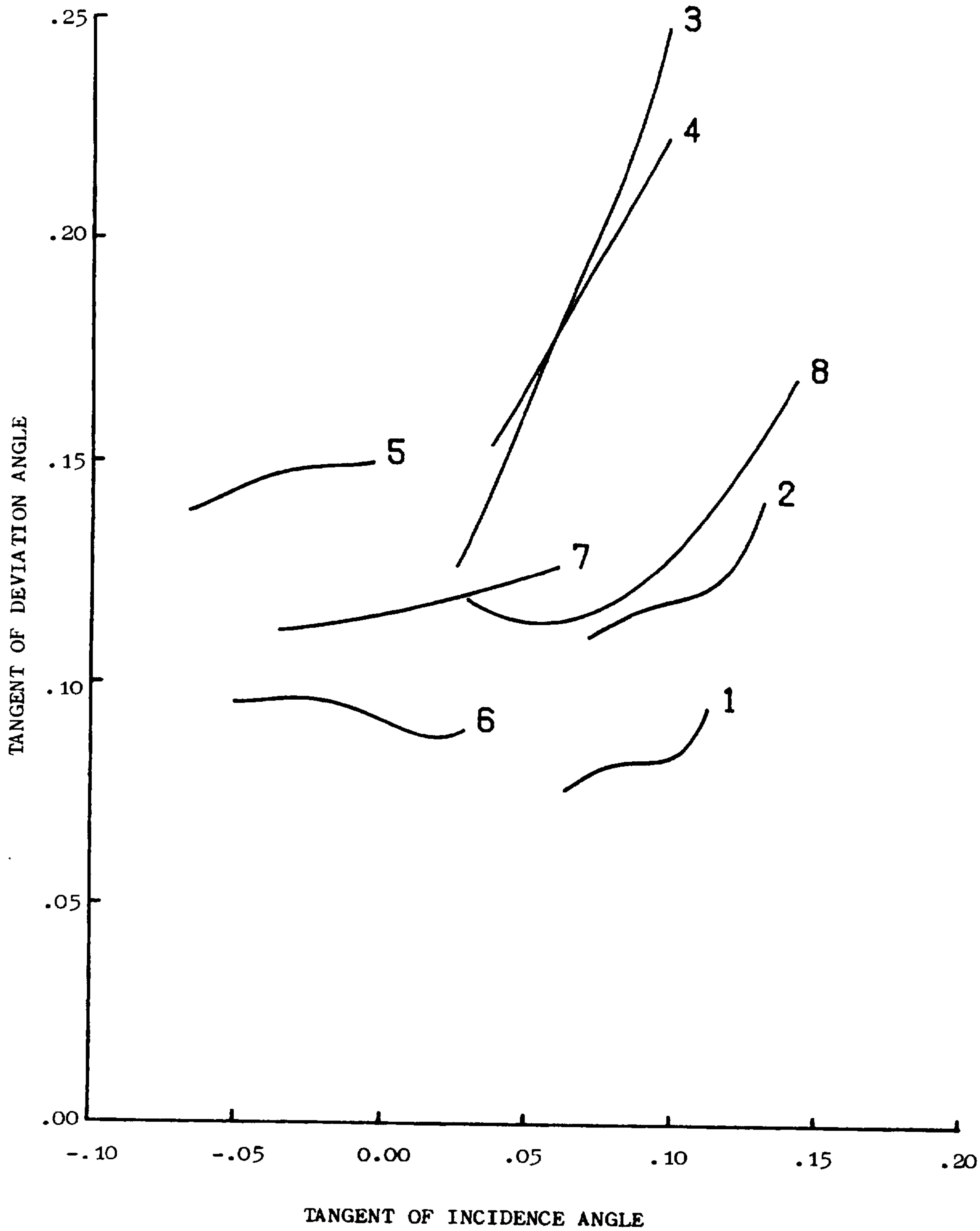

Figure 62. Rotor Deviation Angles, "Moss" Engine 87% $N/\sqrt{\theta}$.

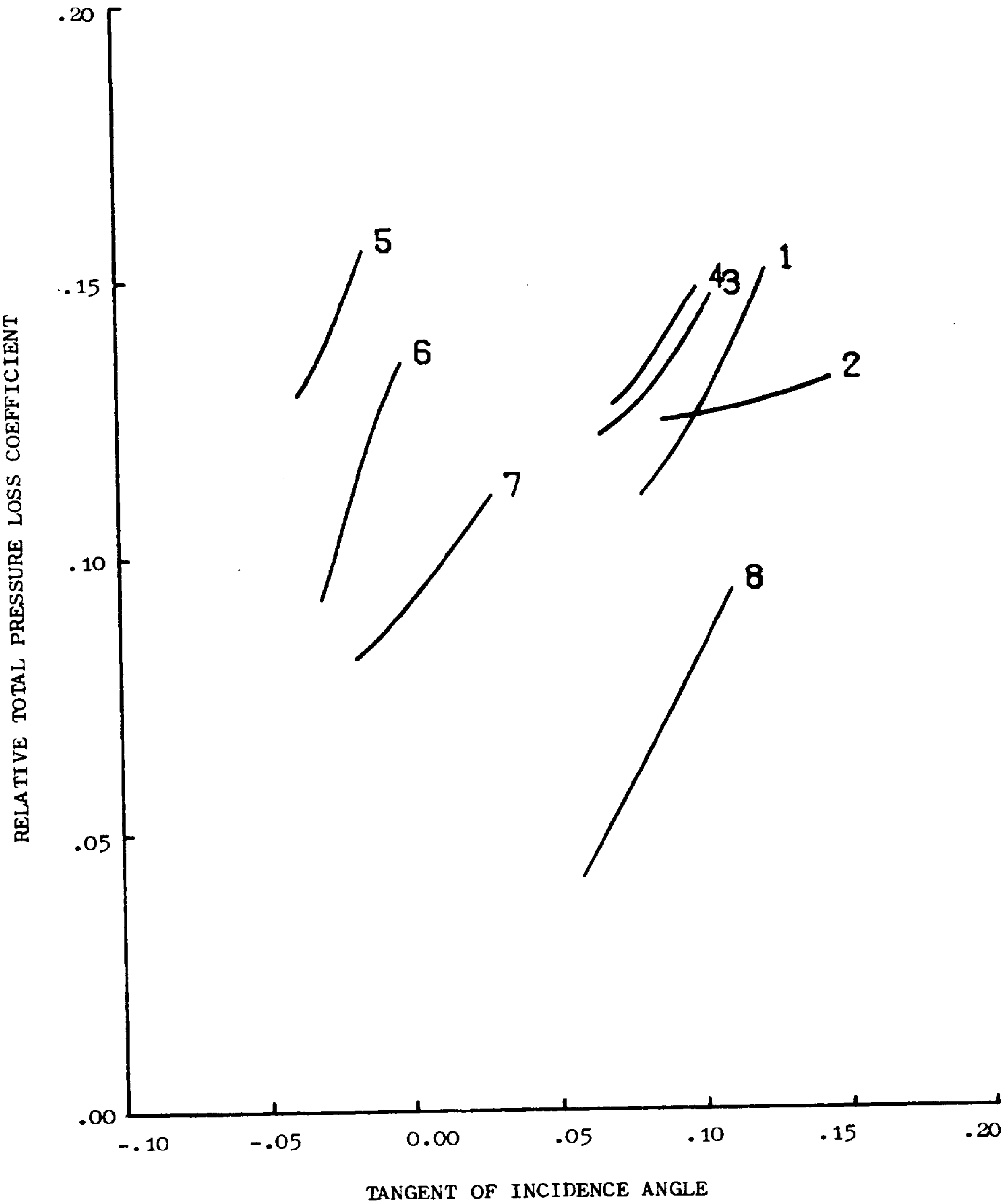

Figure 63. Rotor Total-Pressure Loss Coefficients, "Moss" Engine 94% $N/\sqrt{\theta}$.

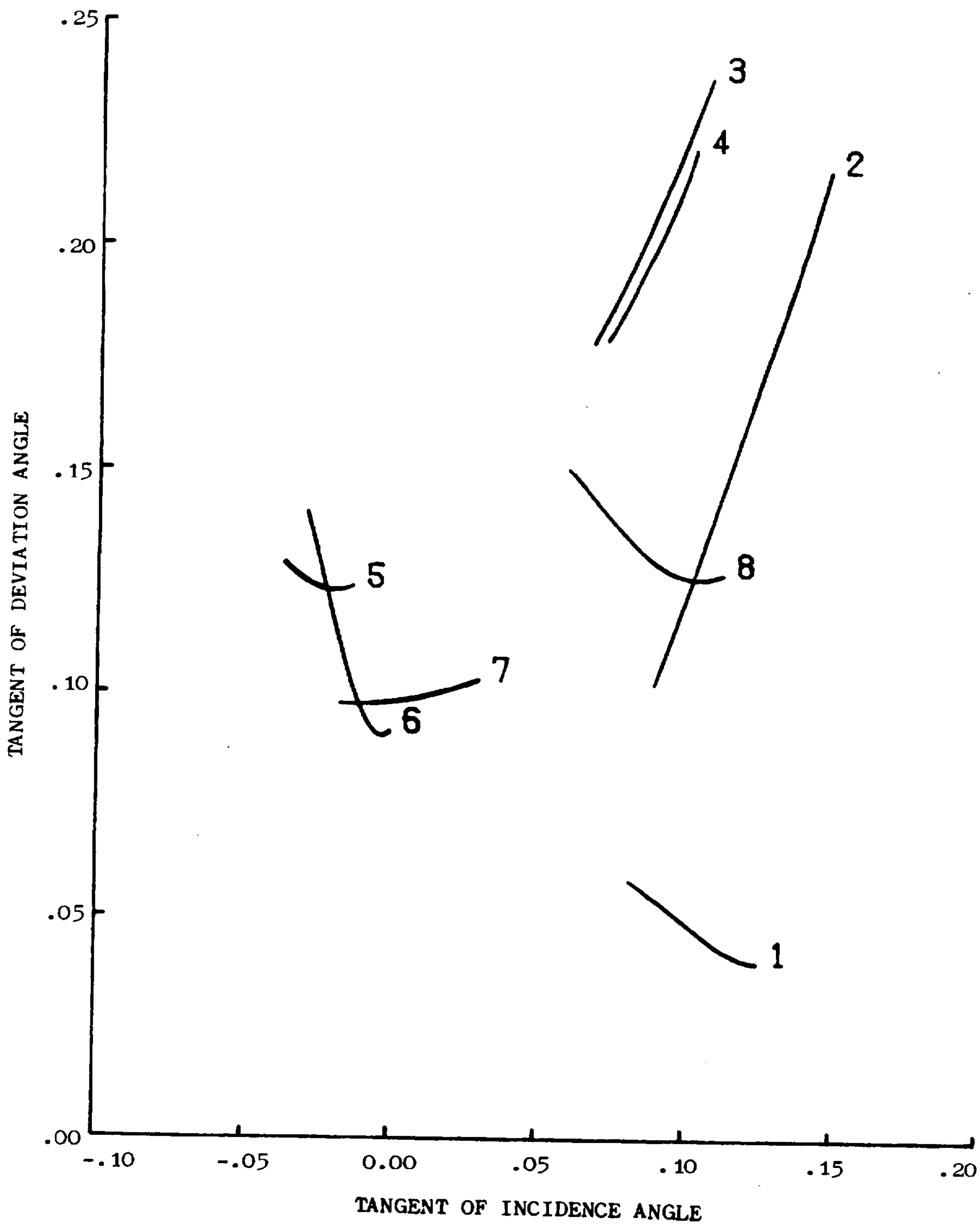

Figure 64. Rotor Deviation Angles, "Moss" Engine 94% $N/\sqrt{\theta}$.

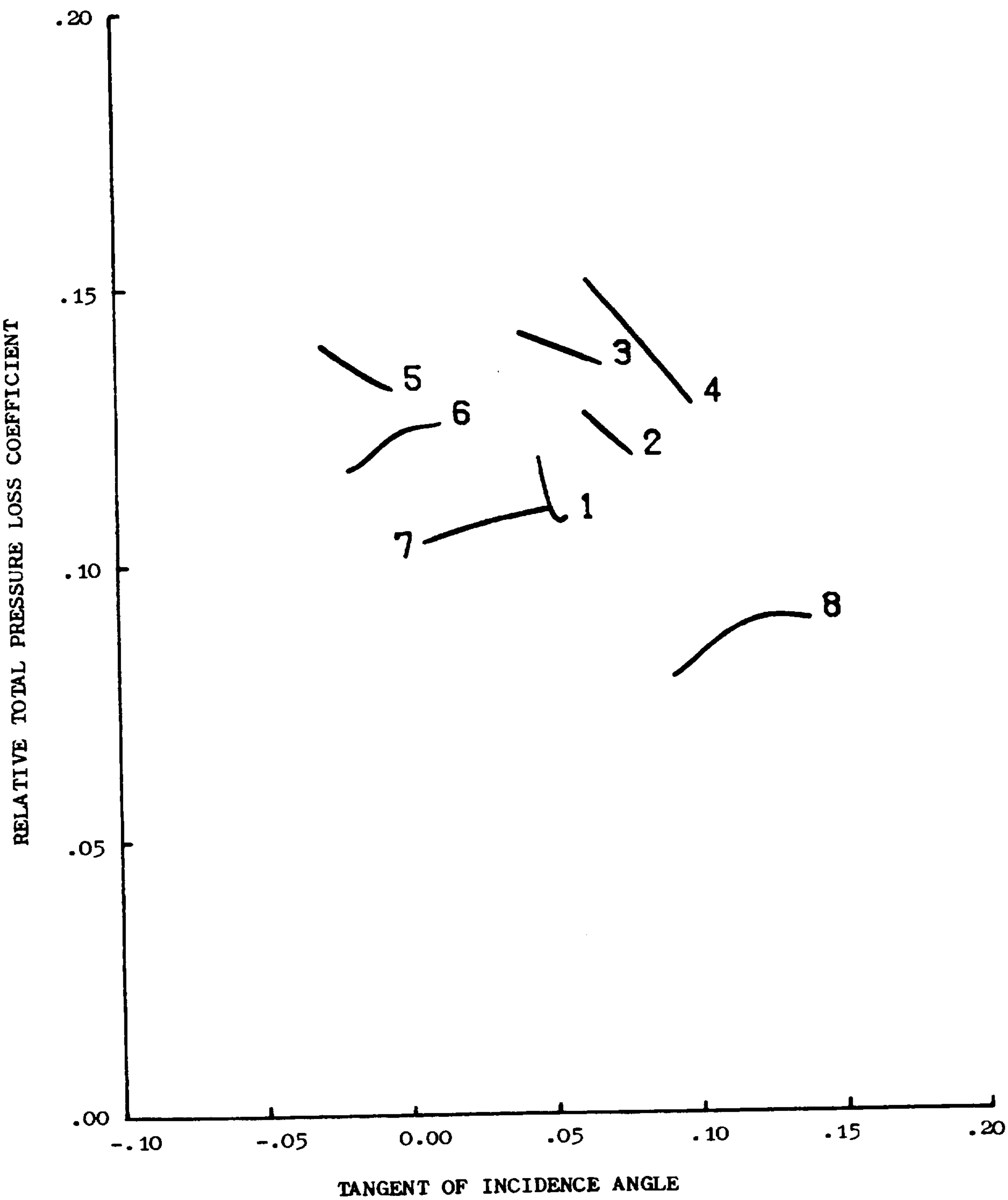

Figure 65. Rotor Total-Pressure Loss Coefficients, "Moss" Engine 100% $N/\sqrt{\theta}$.

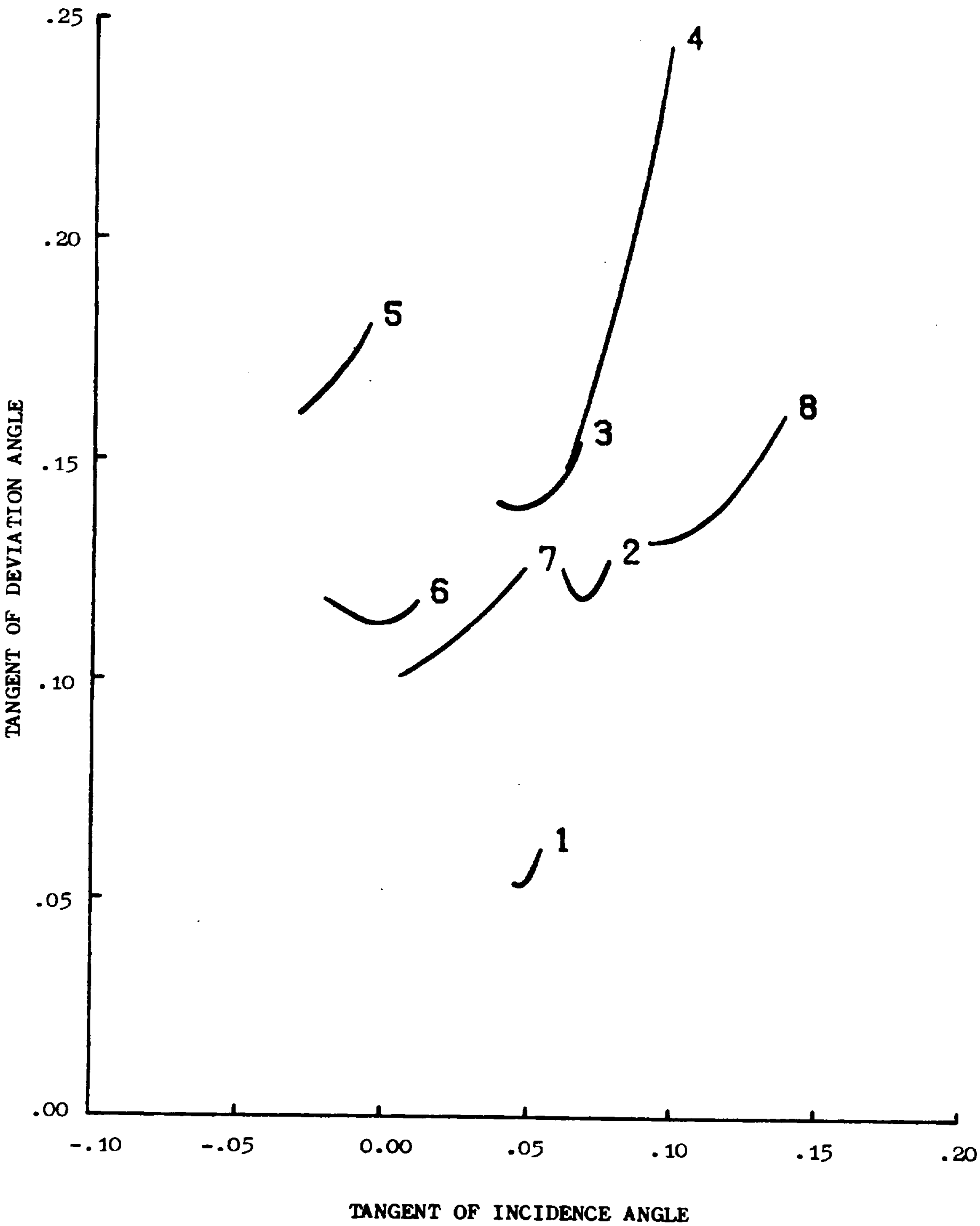

Figure 66. Rotor Deviation Angles, "Moss" Engine 100% $N/\sqrt{\theta}$.

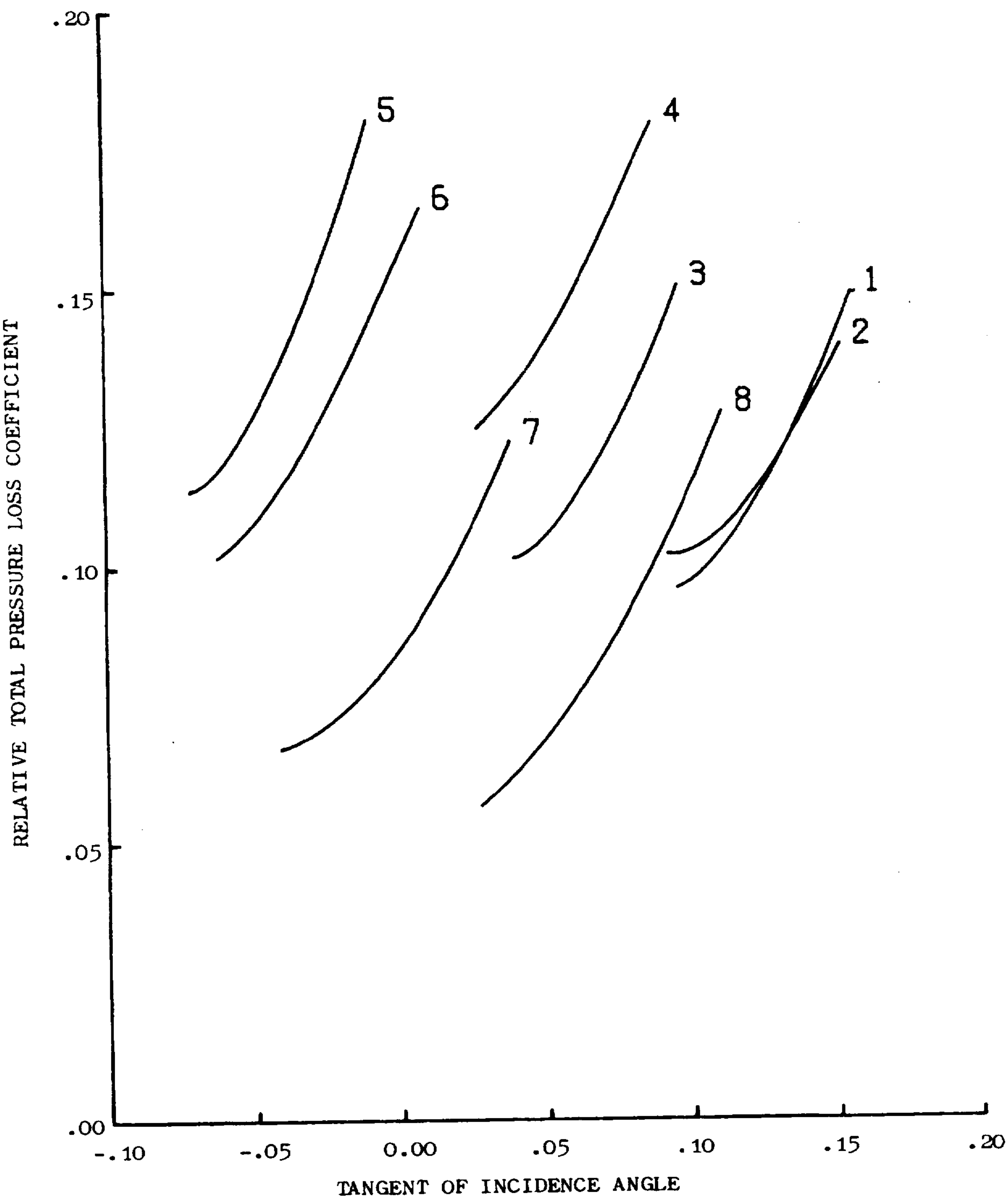

Figure 67. Rotor Total-Pressure Loss Coefficients, "Mehalic" Engine 87% $N/\sqrt{\theta}$.

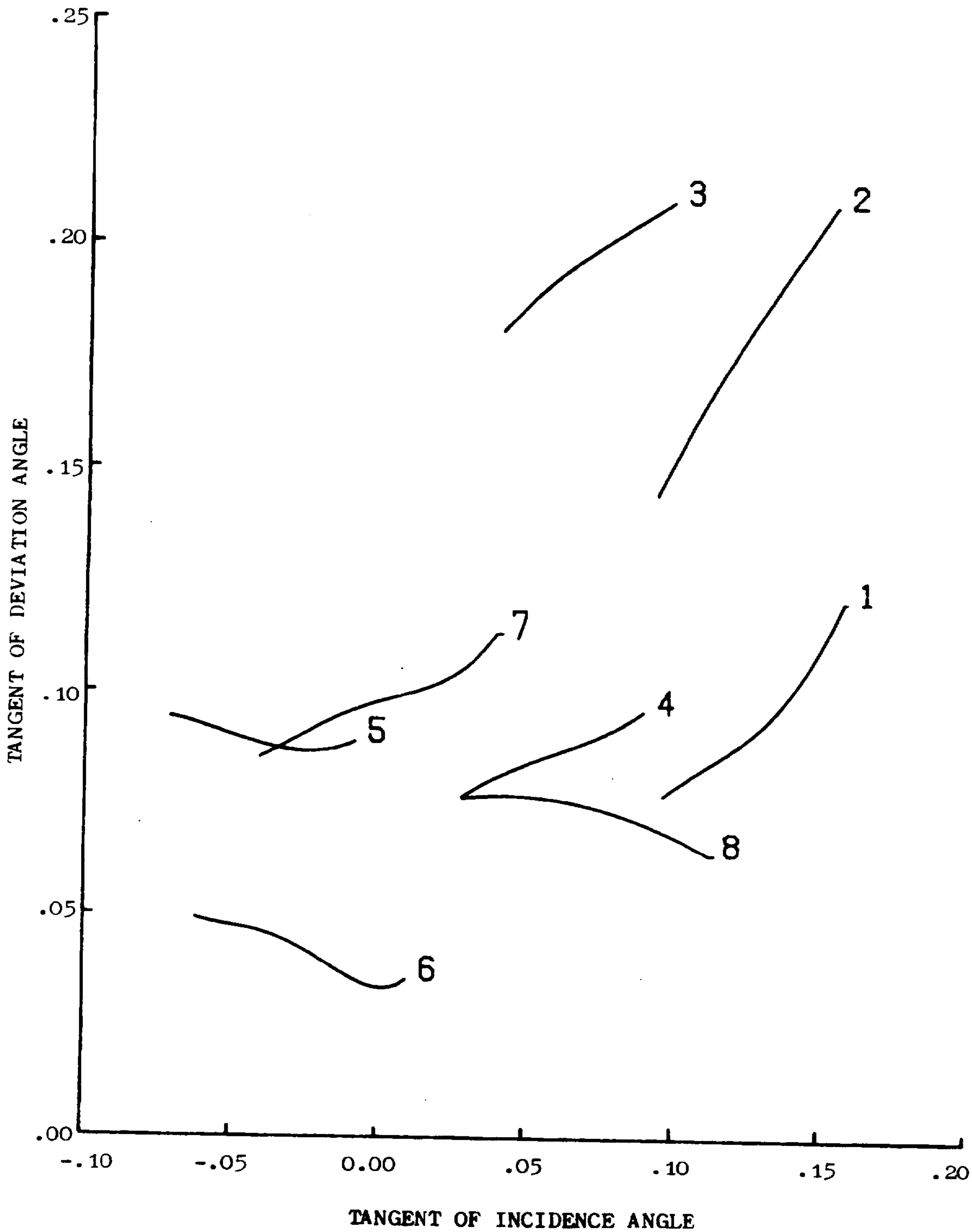

Figure 68. Rotor Deviation Angles, "Mehalic" Engine 87% $N/\sqrt{\theta}$.

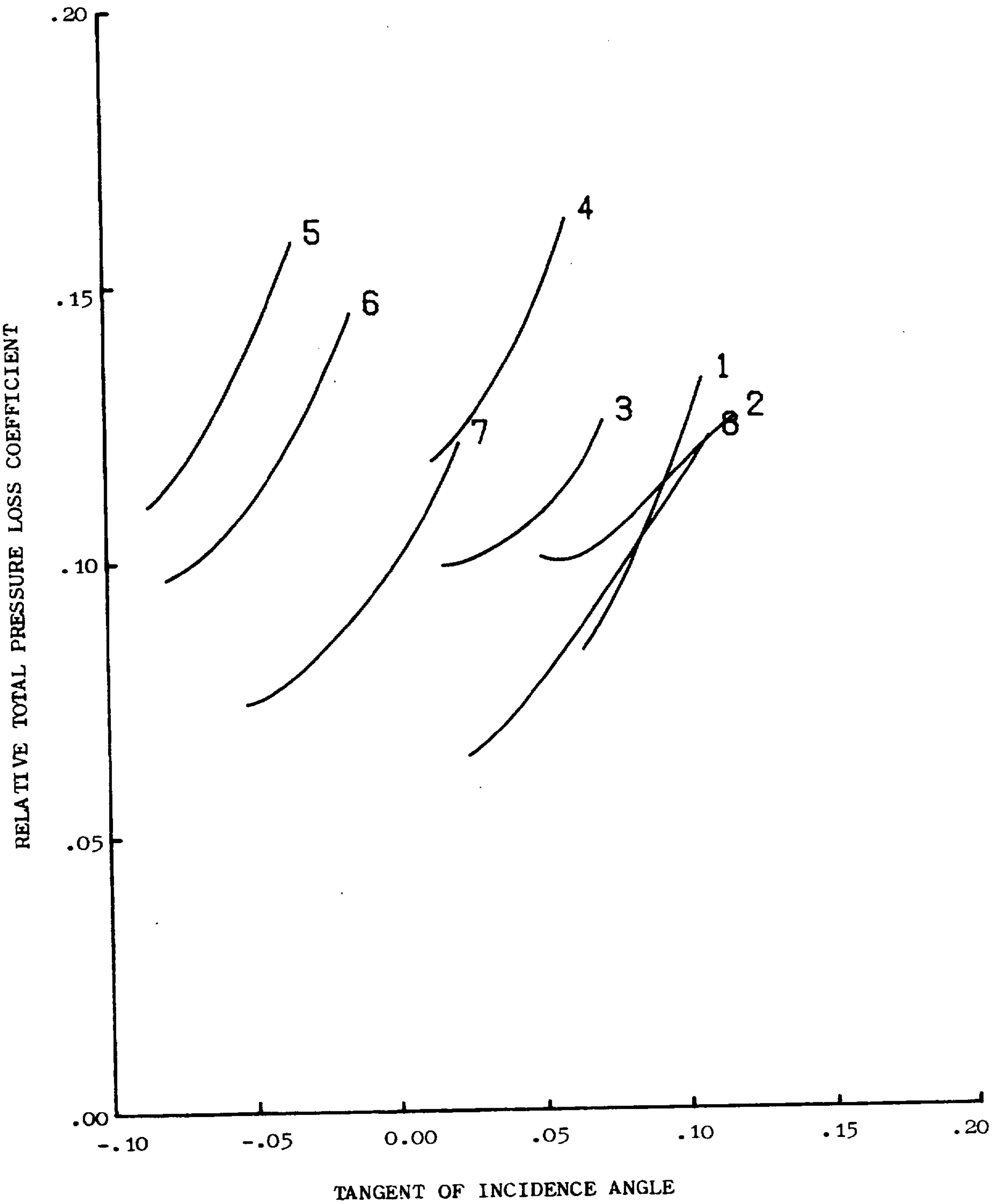

Figure 69. Rotor Total-Pressure Loss Coefficients, "Mehalic" Engine 94% $N/\sqrt{\theta}$.

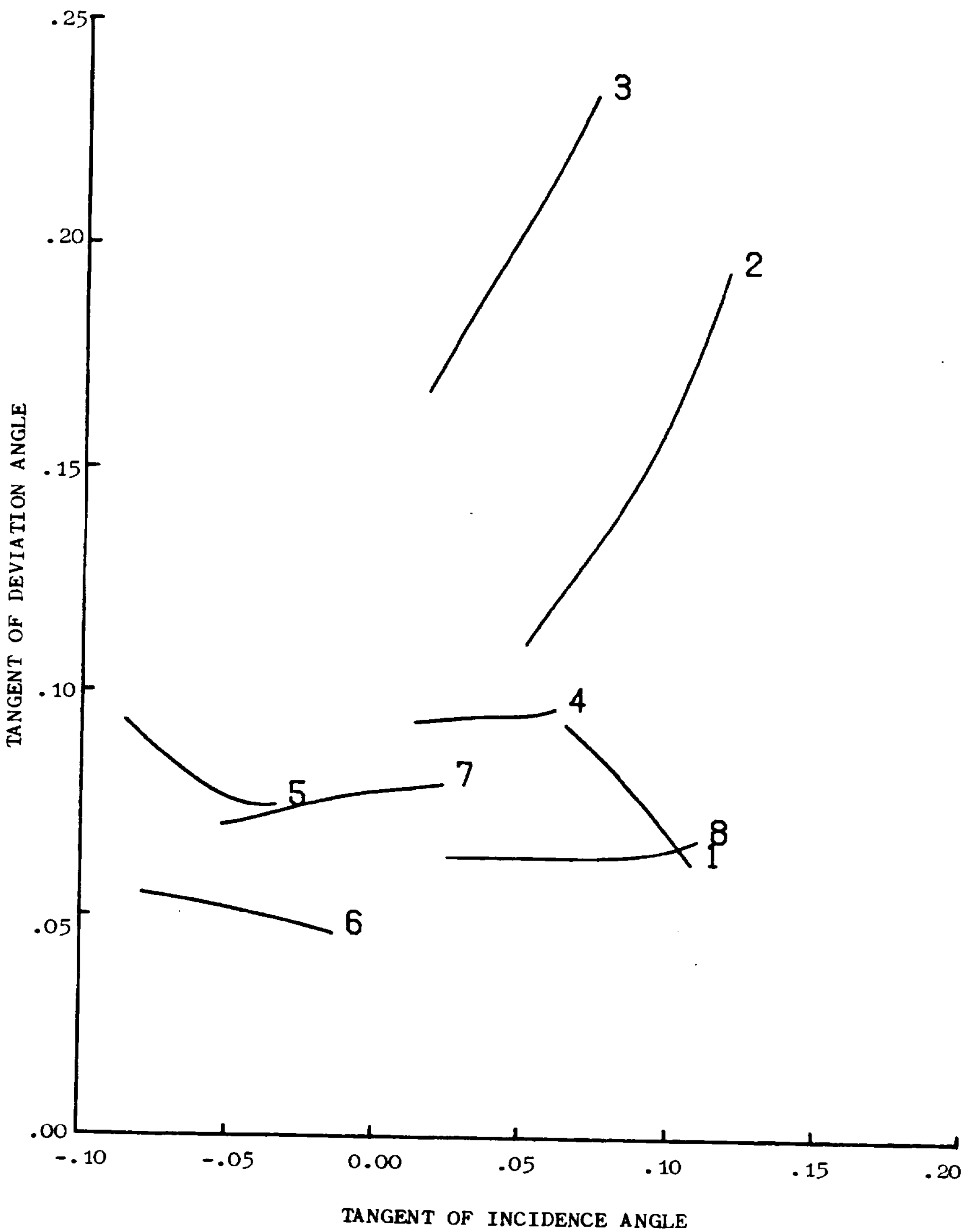

Figure 70. Rotor Deviation Angles, "Mehalic" Engine 94% $N/\sqrt{\theta}$.

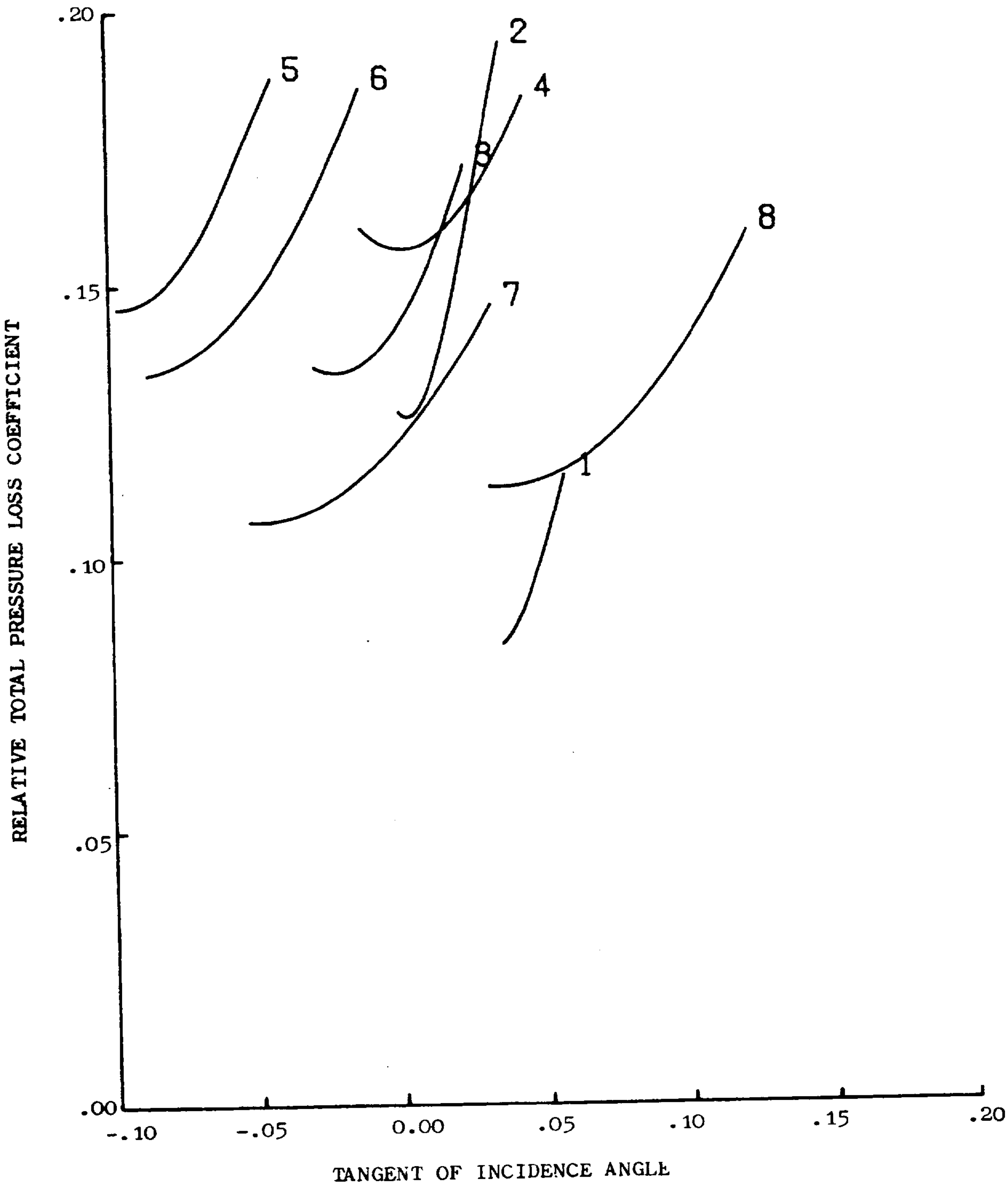

Figure 71. Rotor Total-Pressure Loss Coefficient, "Mehalic" Engine 100% $N/\sqrt{\theta}$.

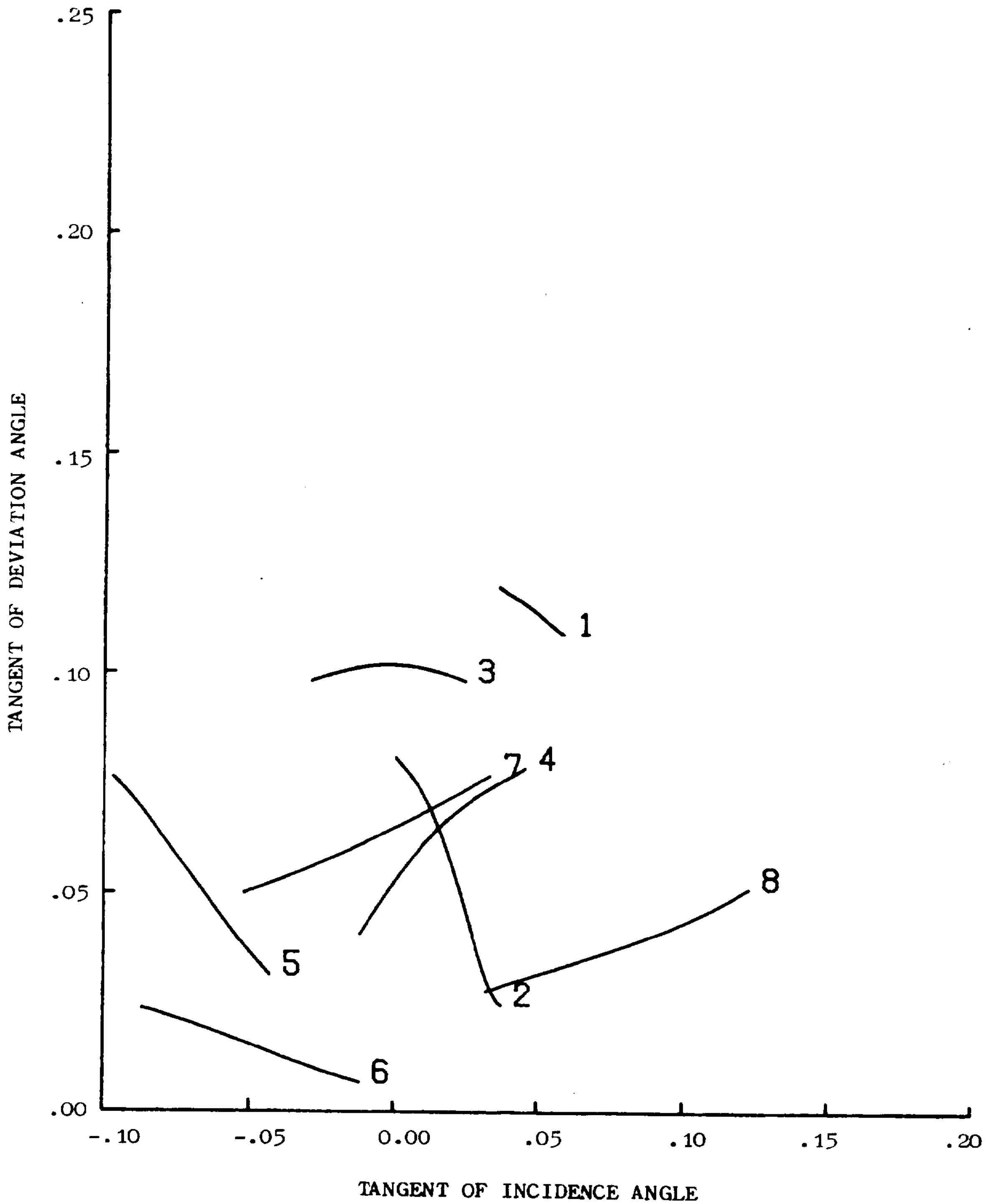

Figure 72. Rotor Deviation Angles, "Mehalic" Engine 100% $N/\sqrt{\theta}$.

Table 9. Polynomial Representation of Characteristics, "Moss" Engine, 80% $N/\sqrt{\theta}$.

A) RELATIVE TOTAL-PRESSURE LOSS COEFFICIENT, $\overline{\omega}' = P_n(\mathrm{TAN}(i))$

$$\overline{\omega}' = C_1 \mathrm{TAN}(i)^4 + C_2 \mathrm{TAN}(i)^3 + C_3 \mathrm{TAN}(i)^2 + C_4 \mathrm{TAN}(i) + C_5$$

ROTOR	TAN(i) DOMAIN		POLYNOMIAL COEFFICIENTS				
	MAX	MIN	C_1	C_2	C_3	C_4	C_5
1	.125	.05	10296.47	-3725.04	519.4211	-32.3017	.8125553
2	.155	.08	3138.456	-1777.74	375.2066	-34.4046	1.242685
3	.10	.02	2474.917	-649.511	68.53722	-3.14094	.1433927
4	.095	.025	476.4279	-345.946	63.55620	-4.23584	.1852950
5	-.005	-.085	55.26654	-143.067	-4.92062	.6828110	.1175013
6	.04	-.10	0.0	-1.40873	4.800277	.5172106	.1000674
7	.07	-.10	132.8065	13.14993	2.210511	.2179109	.06641416
8	.15	0.0	186.6458	-20.3605	-4.93896	.9791339	.0078742

B) TANGENT OF DEVIATION ANGLE, $\mathrm{TAN}(\delta) = P_n(\mathrm{TAN}(i))$

$$\mathrm{TAN}(\delta) = D_1 \mathrm{TAN}(i)^4 + D_2 \mathrm{TAN}(i)^3 + D_3 \mathrm{TAN}(i)^2 + D_4 \mathrm{TAN}(i) + D_5$$

ROTOR	TAN(i) DOMAIN		POLYNOMIAL COEFFICIENTS				
	MAX	MIN	D_1	D_2	D_3	D_4	D_5
1	.125	.05	0.0	-14.6956	7.337345	-.792069	.1297314
2	.155	.085	2153.873	-685.102	67.11727	-.767915	-.001947
3	.09	0.0	2710.453	-446.232	20.97019	1.336071	.0732273
4	.10	0.0	1101.343	-163.322	12.12245	.5626970	.1312668
5	-.005	-.085	8019.84	1577.664	110.2076	2.964105	.1708325
6	.04	-.09	0.0	11.78041	4.899814	-.045219	.0690769
7	.07	-.09	555.3677	15.65694	.3223334	.3663978	.0978986
8	.14	0.0	-519.723	163.2451	-7.17728	-.337419	.1256988

Table 10. Polynomial Representation of Characteristics, "Moss" Engine, 87% $N/\sqrt{\theta}$.

A) RELATIVE TOTAL-PRESSURE LOSS COEFFICIENT, $\overline{\omega}' = P_n(TAN(i))$

$$\overline{\omega}' = C_1 TAN(i)^4 + C_2 TAN(i)^3 + C_3 TAN(i)^2 + C_4 TAN(i) + C_5$$

ROTOR	TAN(i) DOMAIN		POLYNOMIAL COEFFICIENTS				
	MAX	MIN	C_1	C_2	C_3	C_4	C_5
1	.12	.055	9915.719	-3867.62	569.3342	-36.7901	.9491094
2	.1325	.06	0.0	-189.118	64.16281	-6.78050	.3214183
3	.10	.02	0.0	-89.4533	23.51807	-1.77353	.1344891
4	.105	.03	0.0	-64.463	27.43987	-2.62657	.1695358
5	.005	-.075	0.0	38.15494	16.47705	1.266251	.1232226
6	.04	-.09	0.0	0.0	7.049729	.5873602	.0974238
7	.07	-.08	0.0	0.0	3.781624	.3201148	.0629112
8	.16	-.02	481.2131	-141.206	12.46208	.0541908	.0224596

B) TANGENT OF DEVIATION ANGLE, $TAN(\delta) = P_n(TAN(i))$

$$TAN(\delta) = D_1 TAN(i)^4 + D_2 TAN(i)^3 + D_3 TAN(i)^2 + D_4 TAN(i) + D_5$$

ROTOR	TAN(i) DOMAIN		POLYNOMIAL COEFFICIENTS				
	MAX	MIN	D_1	D_2	D_3	D_4	D_5
1	.1175	.04	14032.75	-4379.77	499.8880	-24.4551	.5066225
2	.135	.04	6621.384	-2314.34	296.4176	-16.1789	.4250809
3	.11	0.0	6220.583	-1438.49	120.0122	-2.66769	.1375175
4	.12	0.0	2035.029	-544.69	53.15900	-1.08416	.1441326
5	.02	-.09	2446.596	338.8502	12.01995	.1958777	.1504018
6	.04	-.075	2617.987	198.7423	-.868978	-.287110	.0918752
7	.09	-.10	0.0	0.0	.7926447	.134846	.1157841
8	.16	0.0	0.0	-7.57951	9.093984	-.934917	.139405

Table 11. Polynomial Representation of Characteristics, "Moss" Engine, 94% $N/\sqrt{\theta}$.

A) RELATIVE TOTAL-PRESSURE LOSS COEFFICIENT, $\overline{\omega}' = P_n(TAN(i))$

$$\overline{\omega}' = C_1 TAN(i)^4 + C_2 TAN(i)^3 + C_3 TAN(i)^2 + C_4 TAN(i) + C_5$$

ROTOR	TAN(i) DOMAIN		POLYNOMIAL COEFFICIENTS				
	MAX	MIN	C_1	C_2	C_3	C_4	C_5
1	.13	.04	0.0	0.0	7.129519	-.543560	.1081784
2	.17	.02	0.0	-1.99551	1.742227	-.199135	.1298619
3	.115	.02	0.0	0.0	8.397373	-.813731	.1389918
4	.10	.045	0.0	-314.212	87.62617	-7.33003	.3184951
5	-.0125	-.065	0.0	-333.497	-11.9024	1.211618	.1739506
6	0.0	-.05	10888.61	-113.910	-36.4737	.7577479	.1360617
7	.04	-.07	0.0	-39.0041	3.952665	.6020591	.0912396
8	.13	.04	0.0	-6.74316	2.590046	.6832056	-.005907

B) TANGENT OF DEVIATION ANGLE, $TAN(\delta) = P_n(TAN(i))$

$$TAN(\delta) = D_1 TAN(i)^4 + D_2 TAN(i)^3 + D_3 TAN(i)^2 + D_4 TAN(i) + D_5$$

ROTOR	TAN(i) DOMAIN		POLYNOMIAL COEFFICIENTS				
	MAX	MIN	D_1	D_2	D_3	D_4	D_5
1	.145	.05	3398.148	-1208.91	159.2616	-9.69177	.2946683
2	.16	.03	2798.437	-1262.28	213.0223	-13.9984	.3751164
3	.12	.03	0.0	0.0	7.894496	.1606487	.1324595
4	.1075	.05	39001.74	-13015.8	1630.419	-89.5072	1.981923
5	0.0	-.04	0.0	284.6682	42.44993	1.346113	.1350251
6	.005	-.03	-24804.7	655.0748	124.1600	.8608806	.0921745
7	.05	-.05	0.0	0.0	3.114197	.845641	.0979034
8	.13	.06	-2383.20	990.6476	-137.480	7.178056	.0309516

Table 12. Polynomial Representation of Characteristics, "Moss" Engine, 100% $N/\sqrt{\theta}$.

A) RELATIVE TOTAL-PRESSURE LOSS COEFFICIENT, $\overline{\omega}' = P_n(\mathrm{TAN}(i))$

$$\overline{\omega}' = C_1 \mathrm{TAN}(i)^4 + C_2 \mathrm{TAN}(i)^3 + C_3 \mathrm{TAN}(i)^2 + C_4 \mathrm{TAN}(i) + C_5$$

ROTOR	TAN(i) DOMAIN		POLYNOMIAL COEFFICIENTS				
	MAX	MIN	C_1	C_2	C_3	C_4	C_5
1	.06	.04	0.0	0.0	215.8172	-23.0127	.7207863
2	.082	.056	0.0	0.0	2.034095	-.759529	.1662643
3	.075	.025	0.0	0.0	-.363236	-.166057	.1487989
4	.11	.05	0.0	0.0	-.648438	-.511238	.1857884
5	.02	-.055	4222.965	396.0822	15.54277	-.074075	.1309056
6	.025	-.03	32449.12	313.5944	-15.4741	.1838376	.1240465
7	.09	-.04	832.0635	-99.3475	2.912836	.1376405	.1027257
8	.16	.07	5484.248	-2612.16	455.7857	-34.2666	1.015377

B) TANGENT OF DEVIATION ANGLE, $\mathrm{TAN}(\delta) = P_n(\mathrm{TAN}(i))$

$$\mathrm{TAN}(\delta) = D_1 \mathrm{TAN}(i)^4 + D_2 \mathrm{TAN}(i)^3 + D_3 \mathrm{TAN}(i)^2 + D_4 \mathrm{TAN}(i) + D_5$$

ROTOR	TAN(i) DOMAIN		POLYNOMIAL COEFFICIENTS				
	MAX	MIN	D_1	D_2	D_3	D_4	D_5
1	.06	.038	0.0	0.0	148.4562	-14.1093	.3882548
2	.08	.06	0.0	-1843.99	503.7275	-43.1914	1.306363
3	.0775	.0225	35204.49	-7149.59	567.7469	-20.5501	.4214689
4	.105	.05	51524.39	-16195.9	1917.319	-98.8425	2.003651
5	0.0	-.06	12396.35	1279.547	56.98562	1.850652	.1888479
6	.02	-.01	0.0	144.509	25.5823	.0791817	.1128527
7	.07	-.06	0.0	0.0	5.027583	.2990132	.0986225
8	.16	.05	0.0	0.0	13.39909	-2.48155	.2463691

Table 13. Polynomial Representation of Characteristics, "Mehalic" Engine, 87% $N/\sqrt{\theta}$.

A) RELATIVE TOTAL-PRESSURE LOSS COEFFICIENT, $\bar{\omega}' = P_n(TAN(i))$

$$\bar{\omega}' = C_1 TAN(i)^4 + C_2 TAN(i)^3 + C_3 TAN(i)^2 + C_4 TAN(i) + C_5$$

ROTOR	TAN(i) DOMAIN		POLYNOMIAL COEFFICIENTS				
	MAX	MIN	C_1	C_2	C_3	C_4	C_5
1	.16	.07	1223.057	-673.875	145.4366	-13.4207	.5364305
2	.22	.05	0.0	-90.9595	41.98601	-5.48529	.3223603
3	.11	.015	3210.594	-930.548	107.2109	-4.81105	.1739071
4	.10	.01	-2329.58	493.3383	-30.3654	1.304443	.1032564
5	0.0	-.10	2855.604	408.6511	29.5338	2.260889	.1992862
6	.02	-.12	0.0	-57.2987	.9236123	1.132433	.1549713
7	.05	-.08	0.0	.9137445	6.686652	.7090976	.0850481
8	.13	-.02	2.082061	.2172444	4.926357	.1540027	.0486026

B) TANGENT OF DEVIATION ANGLE, $TAN(\delta) = P_n(TAN(i))$

$$TAN(\delta) = D_1 TAN(i)^4 + D_2 TAN(i)^3 + D_3 TAN(i)^2 + D_4 TAN(i) + D_5$$

ROTOR	TAN(i) DOMAIN		POLYNOMIAL COEFFICIENTS				
	MAX	MIN	D_1	D_2	D_3	D_4	D_5
1	.16	.09	74.75537	133.0319	-49.3825	6.054828	-.172610
2	.22	.065	864.1679	-384.924	59.63592	-2.59289	.115214
3	.13	-.04	910.8485	-190.641	9.851025	.6212142	.1504644
4	.09	-.01	0.0	73.4386	-12.8846	.9956342	.0577892
5	.01	-.075	0.0	94.01799	14.72459	.5541551	.09310201
6	.02	-.08	3918.553	545.4624	21.88857	-.050773	.0340064
7	.045	-.075	2056.583	103.7007	-2.00420	.1907098	.0981537
8	.13	-.02	0.0	2.627075	-3.21001	.2572847	.0720412

Table 14. Polynomial Representation of Characteristics, "Mehalic" Engine, 94% $N/\sqrt{\theta}$.

A) RELATIVE TOTAL-PRESSURE LOSS COEFFICIENT, $\overline{\omega}' = P_n(TAN(i))$

$$\overline{\omega}' = C_1 TAN(i)^4 + C_2 TAN(i)^3 + C_3 TAN(i)^2 + C_4 TAN(i) + C_5$$

ROTOR	TAN(i) DOMAIN		POLYNOMIAL COEFFICIENTS				
	MAX	MIN	C_1	C_2	C_3	C_4	C_5
1	.12	.035	0.0	-50.1735	21.89682	-1.49564	.1020144
2	.125	.03	664.1875	-353.044	64.25218	-4.38497	.1993741
3	.09	-.02	2740.146	-407.436	27.85772	-.634222	.1037031
4	.07	-.02	4304.548	-542.209	33.16342	-.242246	.1166197
5	-.02	-.12	1825.955	374.4205	34.43193	2.633864	.2201589
6	0.0	-.12	0.0	0.0	7.748663	1.459335	.1640660
7	.03	-.08	1766.0781	125.5993	6.367800	.7229095	.0994066
8	.15	-.02	795.0528	-241.583	27.60512	-.675066	.0675536

B) TANGENT OF DEVIATION ANGLE, $TAN(\delta) = P_n(TAN(i))$

$$TAN(\delta) = D_1 TAN(i)^4 + D_2 TAN(i)^3 + D_3 TAN(i)^2 + D_4 TAN(i) + D_5$$

ROTOR	TAN(i) DOMAIN		POLYNOMIAL COEFFICIENTS				
	MAX	MIN	D_1	D_2	D_3	D_4	D_5
1	.12	.05	381.9939	-125.325	11.81207	-.945612	.1321859
2	.125	.05	0.0	115.2502	-21.3997	2.235098	.0375340
3	.09	-.04	1288.390	-158.666	6.088931	1.075653	.1479905
4	.065	0.0	3717.266	-478.975	20.85731	-.305552	.0946924
5	0.0	-.09	0.0	90.67292	23.07326	1.358319	.0974262
6	.02	-.12	33.11539	5.302677	-.411678	-.193495	.0429261
7	.07	-.10	720.2954	31.11858	-1.48927	.0869565	.0774906
8	.15	-.03	358.2427	-70.2615	4.949831	-.146842	.0644381

Table 15. Polynomial Representation of Characteristics, "Mehalic" Engine, 100% $N/\sqrt{\theta}$.

A) RELATIVE TOTAL-PRESSURE LOSS COEFFICIENT, $\overline{\omega}' = P_n(\mathrm{TAN}(i))$

$$\overline{\omega}' = C_1 \mathrm{TAN}(i)^4 + C_2 \mathrm{TAN}(i)^3 + C_3 \mathrm{TAN}(i)^2 + C_4 \mathrm{TAN}(i) + C_5$$

ROTOR	TAN(i) DOMAIN		POLYNOMIAL COEFFICIENTS				
	MAX	MIN	C_1	C_2	C_3	C_4	C_5
1	.06	.02	0.0	-905.798	160.5883	-7.58402	.1910701
2	.04	-.01	0.0	-1368.523	119.5793	-.7384143	.1267253
3	.03	-.05	0.0	0.0	18.17642	.7811276	.1420771
4	.05	-.03	0.0	-61.5040	18.18450	-.081529	.1563241
5	-.06	-.14	0.0	42.93368	26.21303	3.884349	.3150148
6	-.01	-.13	0.0	0.0	8.281588	1.514769	.2026557
7	.04	-.08	0.0	-7.20423	5.454313	.5819092	.1210497
8	.13	0.0	0.0	0.0	6.105443	-.435468	.1204295

B) TANGENT OF DEVIATION ANGLE, $\mathrm{TAN}(\delta) = P_n(\mathrm{TAN}(i))$

$$\mathrm{TAN}(\delta) = D_1 \mathrm{TAN}(i)^4 + D_2 \mathrm{TAN}(i)^3 + D_3 \mathrm{TAN}(i)^2 + D_4 \mathrm{TAN}(i) + D_5$$

ROTOR	TAN(i) DOMAIN		POLYNOMIAL COEFFICIENTS				
	MAX	MIN	D_1	D_2	D_3	D_4	D_5
1	.07	.025	78135.81	-14606.7	1009.058	-31.0031	.4784627
2	.05	-.015	66410.15	-3616.78	23.49286	-.813796	.0811869
3	.09	-.08	794.8714	-4.16092	-6.00985	-.019592	.1019519
4	.075	-.06	2586.269	-134.166	-7.21418	.9417444	.0524781
5	0.0	-.1	0.0	134.3838	28.72648	1.115973	.0368576
6	.04	-.09	0.0	19.85554	2.869345	-.115185	.0048145
7	.05	-.08	0.0	-1.69849	.8652017	.3387322	.0648323
8	.13	-.01	0.0	16.42562	-2.87861	.3745065	.0179125

APPENDIX B

LIFT DIRECTION CORRECTIONS ANGLES

The figures and tables contained in this appendix document the lift-direction correction angles (β_c) used in this program. The distribution of the tangents of the correction angles for the rotors and stators along a speed line has been represented as a linear function of the tangent of the incidence angle. Figures 73 through 79 illustrate the final correction angle distribution as used in the dynamic model. Tables 16 through 22 provide a tabulation of the coefficients used in the straight-line representation of the correction angles. The inlet guide vane and outlet guide vanes were specified in the modeling effort as having constant incidence angle over a speed line and as such prevent presentation of the lift direction correction angle as a function of incidence angle. Therefore, the lift direction correction angles for the inlet and outlet guide vanes were chosen to be constants equal to the average of the calculated distribution of values. Table 23 documents the values used for both engines at each corrected speed.

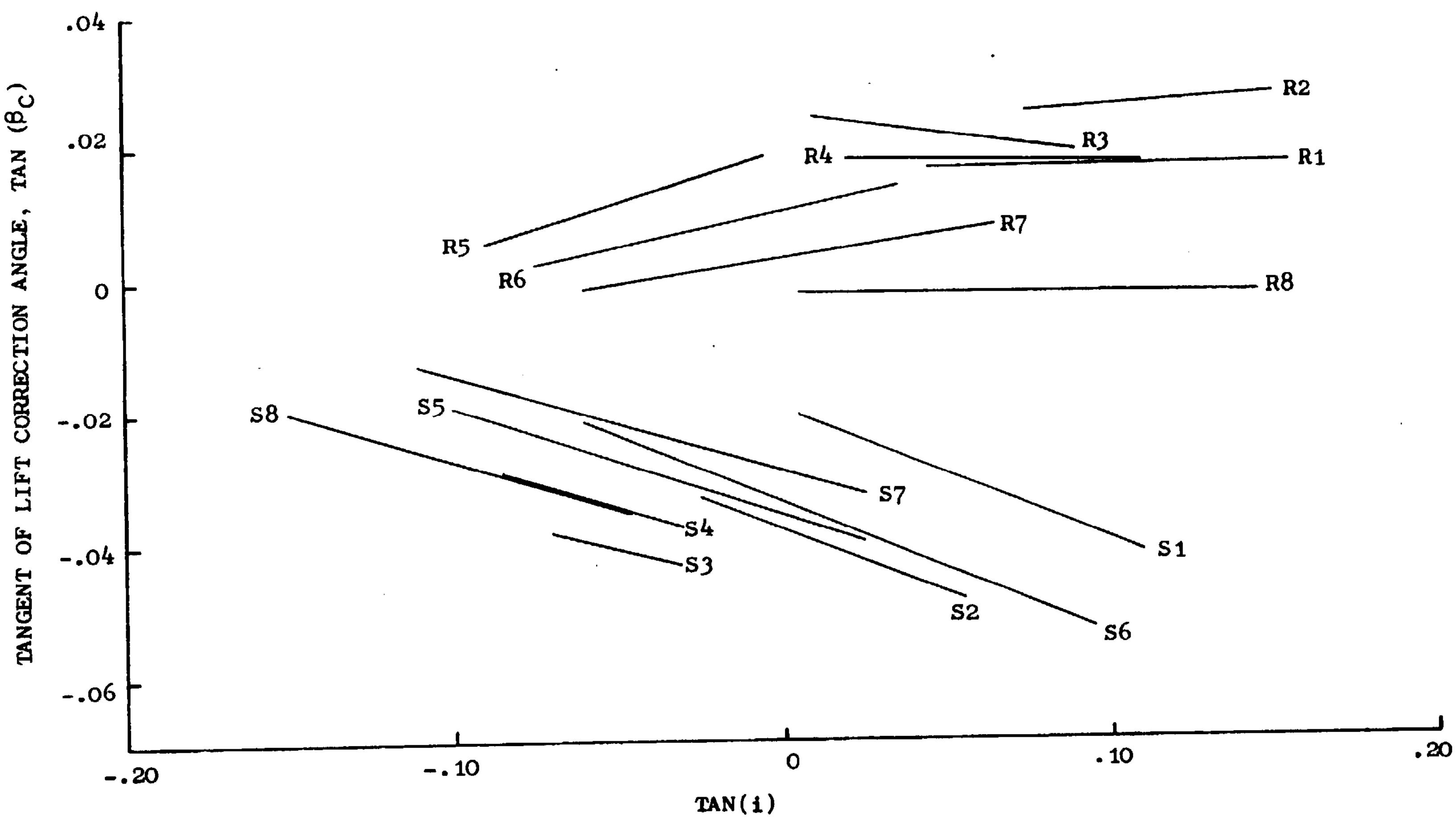

Figure 73. Lift Direction Correction Angles, "Moss" Engine 80% $N/\sqrt{\theta}$.

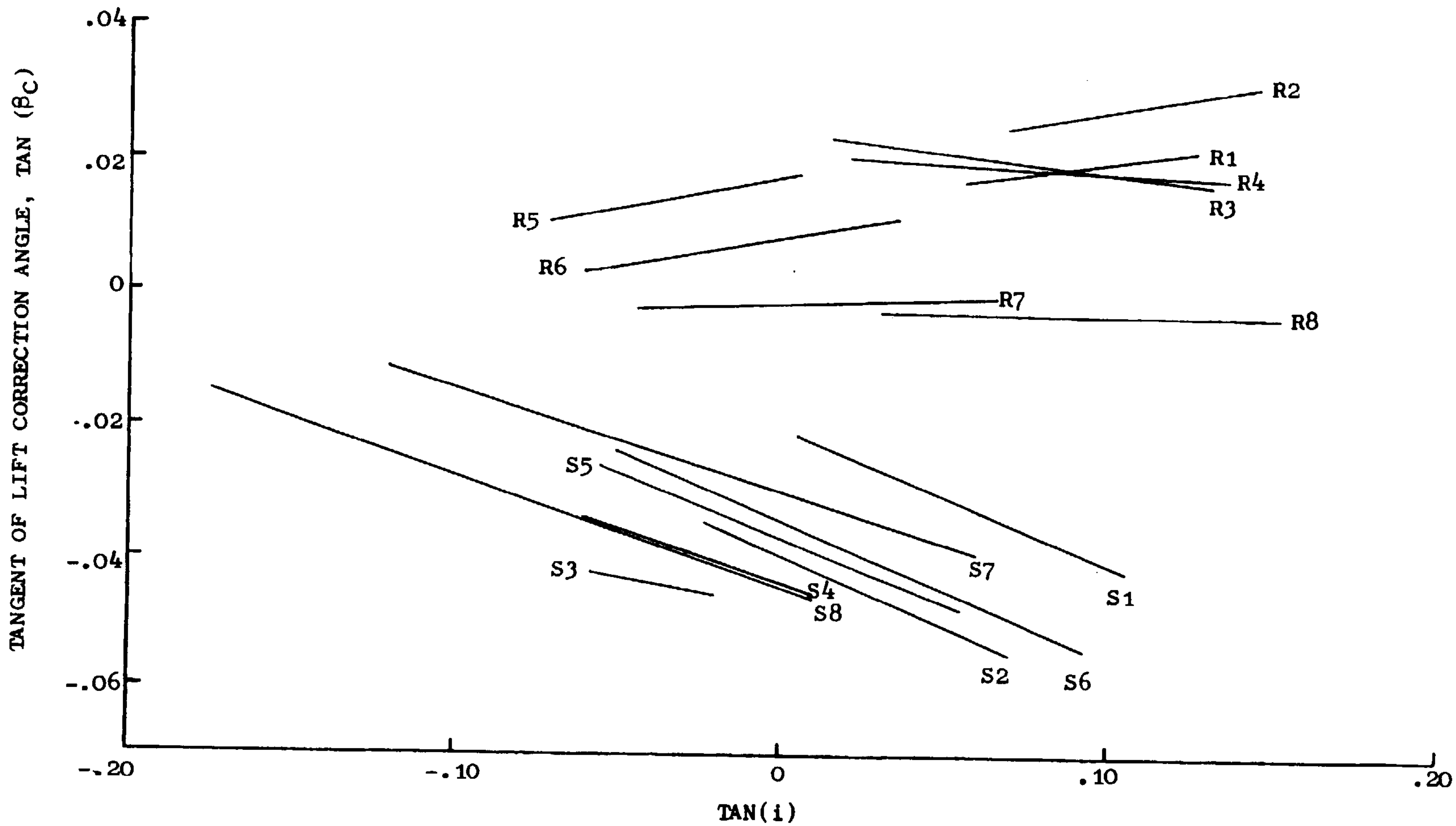

Figure 74. Lift Direction Correction Angles, "Moss" Engine 87% $N/\sqrt{\theta}$.

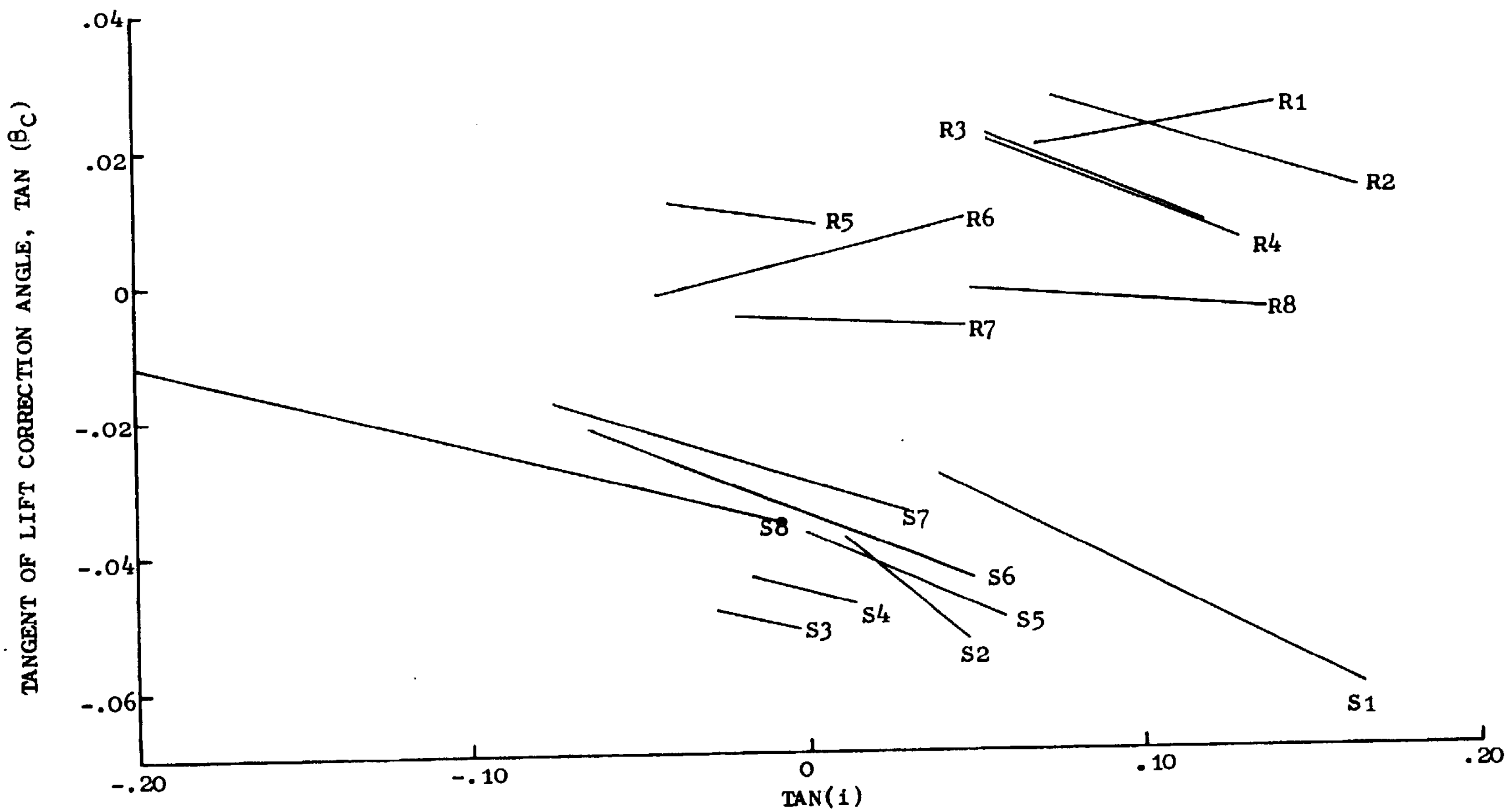

Figure 75. Lift Direction Correction Angles, "Moss" Engine 94% $N/\sqrt{\theta}$.

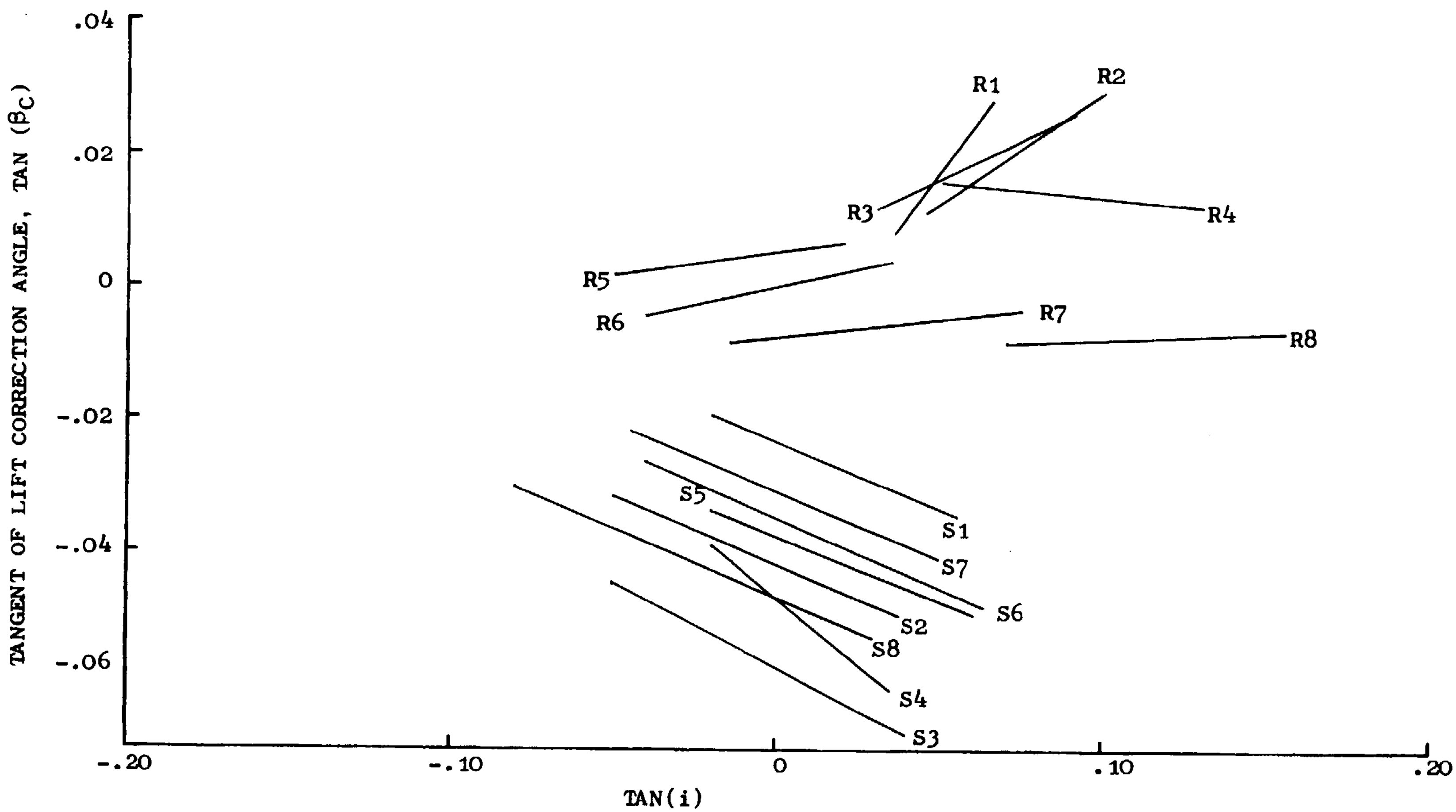

Figure 76. Lift Direction Correction Angles, "Moss" Engine 100% $N/\sqrt{\theta}$.

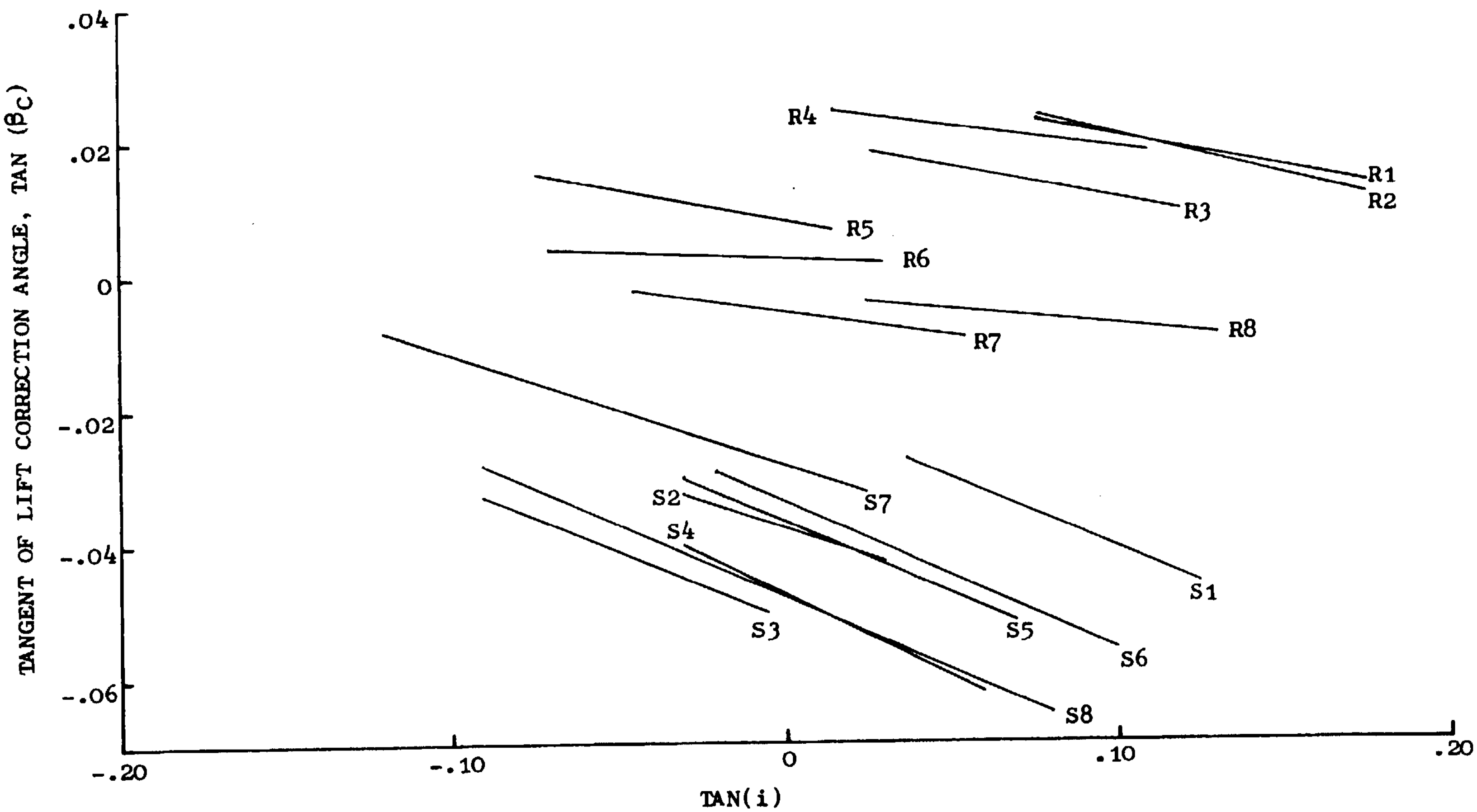

Figure 77. Lift Direction Correction Angles, "Mehalic" Engine 87% $N/\sqrt{\theta}$.

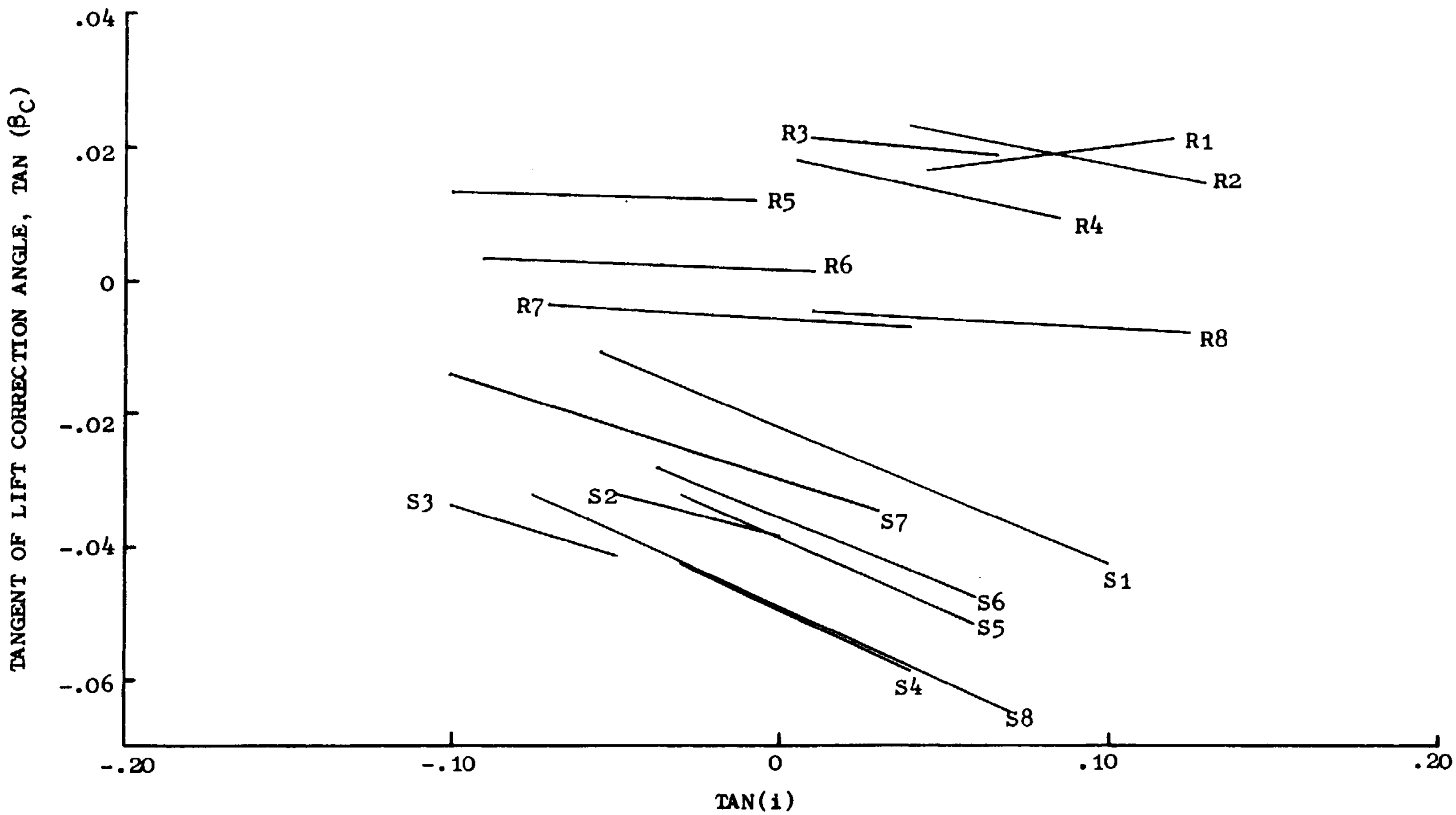

Figure 78. Lift Direction Correction Angles, "Mehalic" Engine 94% $N/\sqrt{\theta}$.

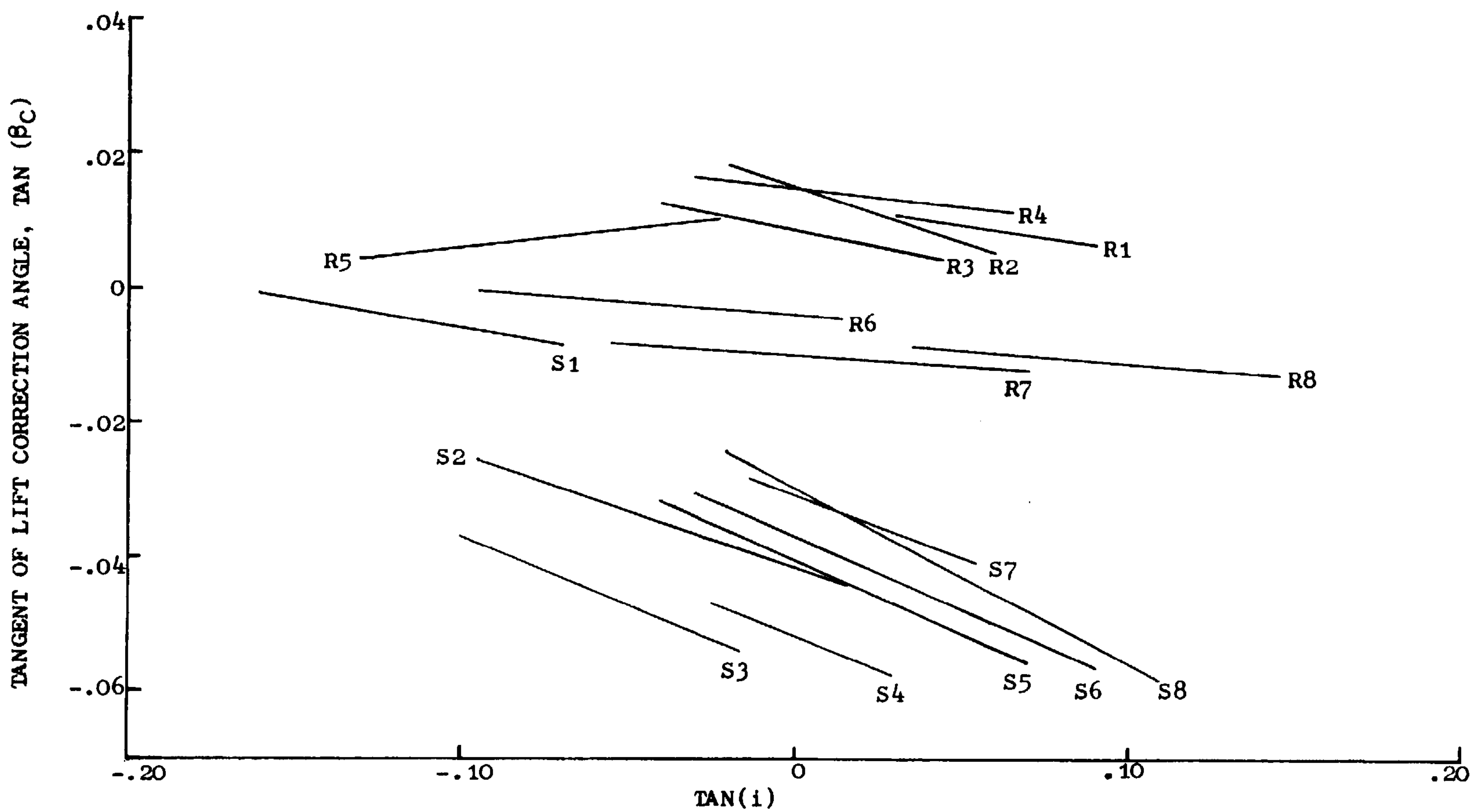

Figure 79. Lift Direction Correction Angles, "Mehalic" Engine 100% $N/\sqrt{\theta}$.

Table 16. Lift Direction Correction Angle Coefficients, "Moss" Engine, 80% $N/\sqrt{\theta}$.

$$TAN(\beta_C) = (M)(TAN(i)) + B$$

BLADE ROW	B (Y-INTERCEPT)	M (SLOPE)
R1	.016271	.0047059
S1	-.019292	-.200995
R2	.022483	.033333
S2	-.037873	-.19494
R3	.024924	-.066187
S3	-.047869	-.1375
R4	.018279	-.0085714
S4	-.041828	-.14857
R5	.019365	.1554
S5	-.03591	-.16696
R6	.010067	.10489
S6	-.03382	-.2061
R7	-.0008977	.026047
S7	-.029025	-.14517
R8	-.0019556	-.0044444
S8	-.0427	-.15269

Table 17. Lift Direction Correction Angle Coefficients, "Moss" Engine, 87% $N/\sqrt{\theta}$.

$$TAN(\beta_C) = (M)(TAN(i)) + B$$

BLADE ROW	B (Y-INTERCEPT)	M (SLOPE)
R1	.0133	.066667
S1	-.020364	-.20718
R2	.019236	.084768
S2	-.039345	-.21091
R3	.024802	-.065385
S3	-.047391	-.09375
R4	.021154	-.02766
S4	-.044667	-.17345
R5	.017569	.092517
S5	-.0368	-.19636
R6	.0083529	.087059
S6	-.034321	-.20905
R7	-.0016878	.021463
S7	-.029919	-.15563
R8	-.0025579	-.0042105
S8	-.045245	-.17283

Table 18. Lift Direction Correction Angle Coefficients, "Moss" Engine, 94% $N/\sqrt{\theta}$.

$$TAN(\beta_C) = (M)(TAN(i)) + B$$

BLADE ROW	B (Y-INTERCEPT)	M (SLOPE)
R1	.014268	.078571
S1	-.018549	-.25607
R2	.038387	-.15484
S2	-.033387	-.41935
R3	.0328	-.20333
S3	-.05186	-.104
R4	.03148	-.19813
S4	-.046207	-.12364
R5	.0086222	-.074074
S5	-.037256	-.21778
R6	.0002174	.013913
S6	-.034535	-.19434
R7	-.00559	-.030252
S7	-.029702	-.1587
R8	-.0005394	-.064789
S8	-.04536	-.1657

Table 19. Lift Direction Correction Angle Coefficients, "Moss" Engine, 100% $N/\sqrt{\theta}$.

$$TAN(\beta_C) = (M)(TAN(i)) + B$$

BLADE ROW	B (Y-INTERCEPT)	M (SLOPE)
R1	-.0148	.66667
S1	-.0234	-.20
R2	-.0035	.3333
S2	-.041916	-.20444
R3	.007	.21429
S3	-.057375	-.25
R4	.018563	-.046602
S4	-.046788	-.38824
R5	.010838	.17619
S5	-.03765	-.196
R6	.0004043	.11183
S6	-.034571	-.20779
R7	-.0083813	.06875
S7	-.03005	-.18
R8	-.0093143	.019048
S8	-.046697	-.2069

Table 20. Lift Direction Correction Angle Coefficients, "Mehalic" Engine, 87% $N/\sqrt{\theta}$.

$$TAN(\beta_C) = (M)(TAN(i)) + B$$

BLADE ROW	B (Y-INTERCEPT)	M (SLOPE)
R1	.030918	-.10256
S1	-.019775	-.21149
R2	.033216	-.12327
S2	-.037727	-.16881
R3	.020568	-.095385
S3	-.051514	-.2015
R4	.025781	-.07205
S4	-.047627	-.24545
R5	.0081652	-.093939
S5	-.036741	-.21875
R6	.0024279	-.018605
S6	-.034042	-.21953
R7	-.0055562	-.071006
S7	-.028844	-.14444
R8	-.0029805	-.04878
S8	-.04808	-.22027

Table 21. Lift Direction Correction Angle Coefficients, "Mehalic" Engine, 94% $N/\sqrt{\theta}$.

$$TAN(\beta_C) = (M)(TAN(i)) + B$$

BLADE ROW	B (Y-INTERCEPT)	M (SLOPE)
R1	.013938	.061538
S1	-.022071	-.20284
R2	.027597	-.097902
S2	-.038297	-.12571
R3	.022052	-.041121
S3	-.048343	-.145055
R4	.018734	-.10579
S4	-.049258	-.23226
R5	.012275	-.010
S5	-.038457	-.21401
R6	.0016933	-.018667
S6	-.03534	-.19762
R7	-.00563	-.028889
S7	-.029877	-.15597
R8	-.0045172	-.026263
S8	-.048774	-.22427

Table 22. Lift Direction Correction Angle Coefficients, "Mehalic" Engine, 100% $N/\sqrt{\theta}$.

$$TAN(\beta_C) = (M)(TAN(i)) + B$$

BLADE ROW	B (Y-INTERCEPT)	M (SLOPE)
R1	.01337	-.074074
S1	-.014335	-.084472
R2	.0152	-.164
S2	-.04528	-.21
R3	.01123	-.036667
S3	-.057699	-.21078
R4	.015044	-.055556
S4	-.051818	-.19273
R5	.012426	.067532
S5	-.040244	-.22095
R6	-.0036409	-.030108
S6	-.036708	-.21695
R7	-.0098435	-.034783
S7	-.030629	-.18295
R8	-.0071295	-.039306
S8	-.049386	-.2656

Table 23. Average tan (β_c) for IGV and OGV for "Moss" and "Mehalic" Engines .

$$TAN(\beta_C) = (M)(TAN(i)) + B$$

SPEED	BLADE ROW	B (Y-INTERCEPT)	M (SLOPE)
MOSS 80% $N/\sqrt{\theta}$	IGV	.000190	0.0
MOSS 80% $N/\sqrt{\theta}$	OGV	-.000645	0.0
MOSS 87% $N/\sqrt{\theta}$	IGV	.014013	0.0
MOSS 87% $N/\sqrt{\theta}$	OGV	-.000648	0.0
MOSS 94% $N/\sqrt{\theta}$	IGV	.283881	0.0
MOSS 94% $N/\sqrt{\theta}$	OGV	-.000657	0.0
MOSS 100% $N/\sqrt{\theta}$	IGV	0.0	0.0
MOSS 100% $N/\sqrt{\theta}$	OGV	-.000646	0.0
MEHALIC 87% $N/\sqrt{\theta}$	IGV	.040916	0.0
MEHALIC 87% $N/\sqrt{\theta}$	OGV	-.060647	0.0
MEHALIC 94% $N/\sqrt{\theta}$	IGV	0.0	0.0
MEHALIC 94% $N/\sqrt{\theta}$	OGV	-.000652	0.0
MEHALIC 100% $N/\sqrt{\theta}$	IGV	0.0	0.0
MEHALIC 100% $N/\sqrt{\theta}$	OGV	-.000647	0.0

APPENDIX C

CLEAN INLET DOCUMENTATION

The computer output listing including herein serves to illustrate the type of documentation available for the clean inlet modeling of both the "Moss" and "Mehalic" J85-13 engines. In order to aid in the interpretation of the output, an explanation of the parameter titles is presented in Table 24. It should be noted that output is provided only for volumes occupied by either stationary or rotating blade rows.

Table 25 provides a tabulation of the compressor performance for the high flow condition on the "Moss" engine 100 percent speed line.

Table 24. Computer Listing Output Parameters.

PCTNC	-	% Corrected Speed
WCORR	-	Corrected Inlet Flow (kg/sec)
P/P-OA	-	Overall Pressure Ratio
EXIT FF	-	Exit Flow Function
CZ1	-	Inlet Axial Velcoity (m/sec)
CU1	-	Inlet Absolute Swirl (m/sec)
WU1	-	Inlet Relative Tangential Velocity (m/sec)
CT	-	Inlet Absolute Velocity (m/sec)
WT	-	Inlet Relative Velocity (m/sec)
U1	-	Inlet Pitchline Wheel Speed (m/sec)
M-ABS	-	Inlet Absolute Mach Number
M-REL	-	Inlet Relative Mach Number
ALPHA	-	Inlet Absolute Air Angle (deg.)
BETA	-	Inlet Relative Air Angle (deg.)
PSI	-	Inlet Static Pressure (N/cm^2)
PT1	-	Inlet Total Pressure (N/cm^2)
TS1	-	Inlet Static Temperature (° K)
TT1	-	Inlet Total Temperature (° K)
TNI	-	Tangent of Incidence Angle
INC	-	Incidence Angle (deg.)
LOSS	-	Total-Pressure Loss Coefficient
TND	-	Tangent of Deviation Angle
DEV	-	Deviation Angle (deg.)
DFACT	-	Diffusion Factor
PHI	-	Flow Coefficient
PSI	-	Work Coefficient
PSI-P	-	Pressure Coefficient
PR1	-	Cumulative Pressure Ratio
PR2	-	Blade-Row Pressure Ratio
TR1	-	Cumulative Temperature Ratio
TR2	-	Blade-Row Temperature Ratio

Table 24. Computer Listing Output Parameters (Concluded).

AD-EF	-	Stage Adiabatic Efficiency
W_2/W_1	-	Ratio of Exit Flow to Inlet Flow
DWX	-	Volume Averaged Flow Time Derivative (kg/sec^2)
DW/DWEX	-	Ratio of Volume Averaged Flow Time Derivative to Exit Volume Averaged Flow Time Derivative

Table 25. Calculated Performance, Clean Inlet Flow, "Moss" Engine 100% $N/\sqrt{\theta}$.

DYNAMIC PARALLEL COMPRESSOR ANALYSIS

J85-13 NAS3-18526, MOSS 100-PCT., CLEAN INLET
THROTTLING SIMULATION

WCORR=17.591 PCTNC=100.10 P/P-OA=7.2581

SECTOR= 1	PCTNCL=100.10	ANGLE=360.00
TIME STEP= 0	TALCW=17.591	P/P-OA(L)=7.25806
TIME=0.	EXIT FF= 6.3806	T/T-OA(L)=1.94161
DPTR-IN=0.	DTTR-IN=0.	DPSR-IN=0.

ROW	CZ1	CU1	WU1	C1	W1	U1	M-ABS	M-REL	ALPHA	BETA	PS1	PT1	TS1	TT1	TNI	INC	LOSS	TND
1	145.5	0.	0.	145.5	0.	0.	0.4353	0.	0.	0.	5.90	10.13	278.2	288.7	0.	0.	0.	0.
2	178.8	0.	275.8	178.3	340.0	275.8	0.6047	1.0341	0.	54.21	7.91	10.13	269.0	288.7	0.04739	2.71	0.1149	0.05302
3	180.3	127.2	0.	220.7	0.	0.	0.6355	0.	35.21	0.	10.95	14.38	300.1	324.3	0.00640	0.37	0.	0.
4	194.9	18.4	257.6	195.3	331.1	296.0	0.5591	0.9453	5.40	53.93	11.63	14.38	335.3	324.3	0.06514	3.73	0.1254	0.12062
5	181.9	152.3	0.	237.5	0.	0.	0.6473	0.	40.03	0.	15.25	20.21	335.1	363.2	-0.00956	-0.55	0.	0.
6	136.7	40.0	255.1	190.2	316.2	295.2	0.5128	0.8490	12.10	53.80	16.89	20.21	345.1	363.2	0.04812	2.75	0.1400	0.13936
7	175.9	178.1	0.	250.4	0.	0.	0.6465	0.	45.35	0.	21.06	27.89	373.2	404.4	-0.00578	-0.33	0.	0.
8	178.8	47.2	256.0	134.2	312.3	303.3	0.4687	0.7915	14.80	55.07	23.99	27.89	387.3	404.4	0.07455	4.26	0.1441	0.17194
9	171.1	185.5	0.	251.1	0.	0.	0.6149	0.	47.01	0.	25.97	37.39	414.6	446.0	0.01069	0.61	0.	0.
10	174.6	61.6	247.7	135.5	303.1	309.2	0.4464	0.7302	19.40	54.79	32.62	37.40	425.9	446.0	-0.02025	-1.16	0.1362	0.16620
11	169.9	179.7	0.	247.2	0.	0.	0.3799	0.	46.63	0.	37.70	47.34	452.3	482.7	0.01051	0.60	0.	0.
12	171.3	73.5	239.8	136.2	295.0	313.5	0.4323	0.6822	23.20	54.38	41.64	47.34	455.4	482.7	-0.00728	-0.42	0.1219	0.11358
13	166.2	171.5	0.	239.4	0.	0.	0.5422	0.	45.79	0.	45.54	56.85	485.0	513.5	0.01549	0.89	0.	0.
14	164.6	67.2	248.8	177.3	298.5	315.9	0.3975	0.6669	22.20	56.51	50.98	56.85	497.8	513.5	0.02441	1.40	0.1067	0.10892
15	156.8	150.5	0.	217.4	0.	0.	0.4773	0.	43.82	0.	56.32	65.83	516.2	539.7	0.00059	0.03	0.	0.
16	152.0	60.2	256.5	163.4	298.1	316.6	0.3554	0.6481	21.60	59.35	60.32	65.83	526.4	539.7	0.11237	6.41	0.0874	0.13671
17	145.9	126.1	0.	192.7	0.	0.	0.4132	0.	40.85	0.	55.39	73.54	542.1	560.6	-0.02185	-1.25	0.	0.
18	140.4	23.7	0.	142.4	0.	0.	0.3027	0.	9.58	0.	59.01	73.54	550.5	560.6	-0.00000	-0.00	0.	0.

ROW	DEV	DFACT	PHI	PSI	PSI-P	PR1	PR2	TR1	TR2	AD-EF	W2/W1	DWX	DW/DWEX	ROT	DPTR2	DTTR2	DPSR2
1	0.	-0.221	0.	0.	0.	1.000	1.00000	1.000	1.00000	0.	1.000000	0.245760E 02	0.	0.	0.	0.	0.
2	3.04	0.463	0.721	0.941	0.802	1.419	1.41891	1.123	1.12337	0.852	1.000000	0.119921E 02	0.	3.4	0.	0.	0.
3	0.	0.343	0.	0.	0.	1.419	1.00000	1.123	1.00000	0.	1.000000	0.134611E 01	0.	6.8	0.	0.	0.
4	6.83	0.493	0.682	0.955	0.814	1.994	1.40560	1.258	1.11986	0.852	1.000000	0.473652E 00	0.	9.6	0.	0.	0.
5	0.	0.370	0.	0.	0.	1.994	1.00000	1.258	1.00000	0.	1.000000	0.518266E 00	0.	13.2	0.	0.	0.
6	7.73	0.472	0.633	0.949	0.808	2.752	1.38007	1.401	1.11331	0.851	1.000000	0.116056E 02	0.	15.9	0.	0.	0.
7	0.	0.452	0.	0.	0.	2.752	0.99997	1.401	0.99999	0.	1.000000	0.118531E 02	0.	19.5	0.	0.	0.
8	9.76	0.435	0.590	0.910	0.772	3.691	1.34088	1.545	1.10295	0.849	1.000000	0.427290E 01	0.	22.0	0.	0.	0.
9	0.	0.435	0.	0.	0.	3.691	1.00002	1.545	1.00001	0.	1.000000	0.171620E 02	0.	25.5	0.	0.	0.
10	9.44	0.423	0.565	0.772	0.655	4.672	1.26601	1.672	1.08242	0.846	1.000000	0.241125E 02	0.	27.8	0.	0.	0.
11	0.	0.392	0.	0.	0.	4.672	0.99998	1.672	0.99999	0.	1.000000	0.242980E 02	0.	31.3	0.	0.	0.
12	6.43	0.383	0.548	0.622	0.530	5.610	1.20078	1.779	1.06368	0.843	1.000000	0.150355E 01	0.	33.3	0.	0.	0.
13	0.	0.423	0.	0.	0.	5.610	0.99999	1.779	1.00000	0.	1.000000	0.218424E 02	0.	36.4	0.	0.	0.
14	6.22	0.341	0.521	0.529	0.442	6.496	1.15795	1.869	1.05113	0.837	1.000000	0.271591E 01	0.	38.1	0.	0.	0.
15	0.	0.405	0.	0.	0.	6.496	1.00000	1.869	1.00000	0.	1.000000	0.169452E 02	0.	41.2	0.	0.	0.
16	7.78	0.273	0.480	0.418	0.343	7.258	1.11724	1.942	1.03861	0.834	1.000000	0.545607E 01	0.	42.6	0.	0.	0.
17	0.	0.462	0.	0.	0.	7.258	0.99999	1.942	1.00000	0.	1.000000	0.114361E 02	0.	44.4	0.	0.	0.
18	0.	0.084	0.	0.	0.	7.258	1.00000	1.942	1.00000	0.	1.000000	0.704460E 00	0.	44.7	0.	0.	0.

APPENDIX D

TOTAL-PRESSURE DISTORTION DOCUMENTATION

This appendix contains information which illustrates the type of documentation available for the 180°, 1/rev distortions modeled for the "Moss" J85-13 engine. Figues 80 through 82 present the distortion profiles as deduced from the distortion instrumentation measurements for three levels of distortion at 100 percent corrected speed. Both radial and circumferential profiles are supplied. The normalizing average pressures are indicated as well as the NASA reading number from which the data was obtained. Reference 4 contains a complete description of the number, type, and location of the instrumentation probes.

Detailed compressor maps of the total-pressure distortion, dynamic parallel-compressor analyses are presented in Figures 83 through 85. Included on the figures is the performance of the individual parallel-compressor sectors and the resultant overall performance.

Documentation of the distortion cases analyzed is presented in the form of computer output listings for which the reader is referred to Table 24 and supplemental Table 26 for an explanation of the parameter titles. A tabulation of compressor performance for each of the sectors for the high level total-pressure distortion at 100 percent speed is supplied in Table 27.

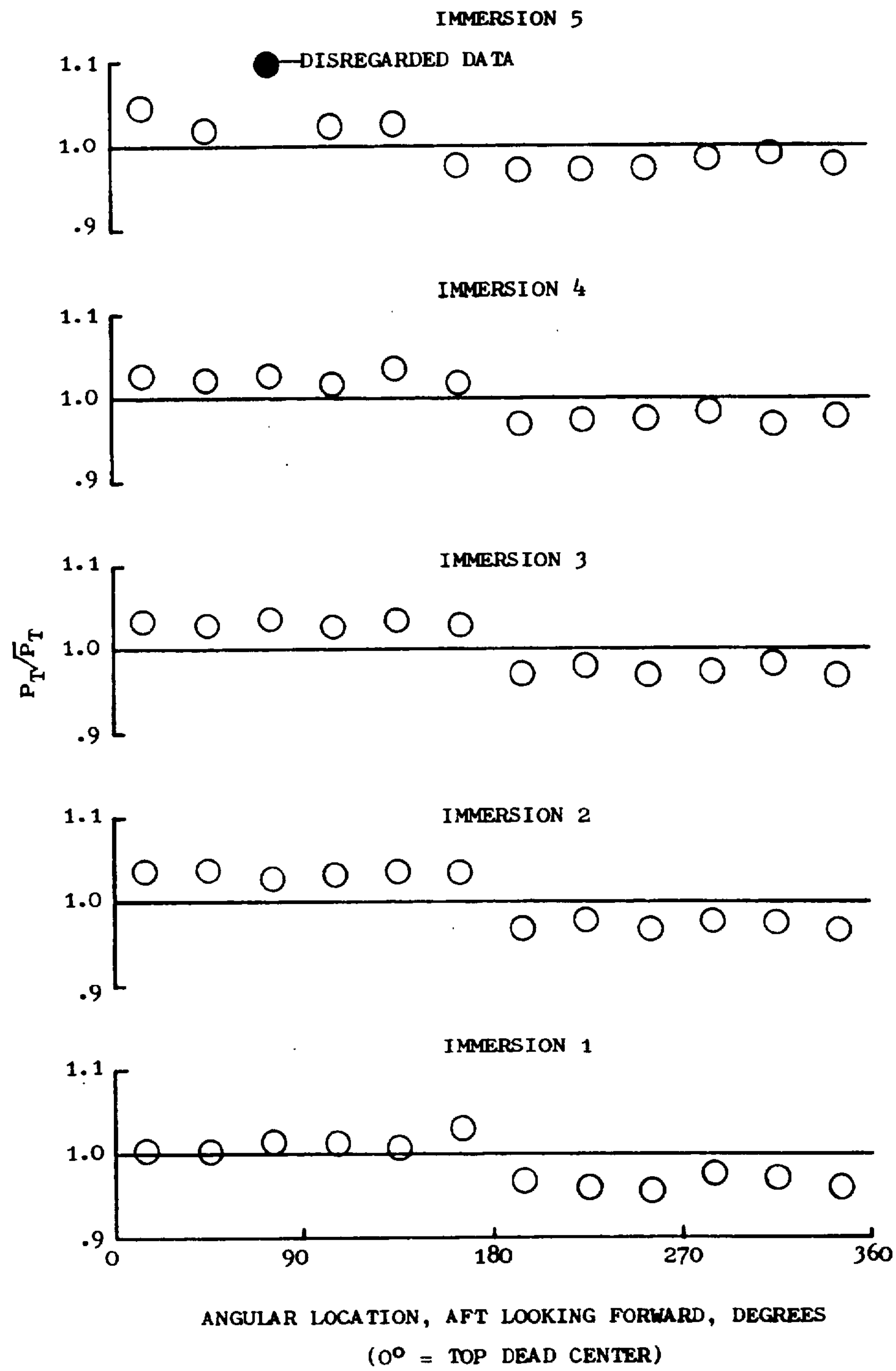

(a) Circumferential Profiles.

Figure 80. Circumferential Total-Pressure Distortion Profiles (RDG 478), "Moss" Engine 100% $N/\sqrt{\theta}$.

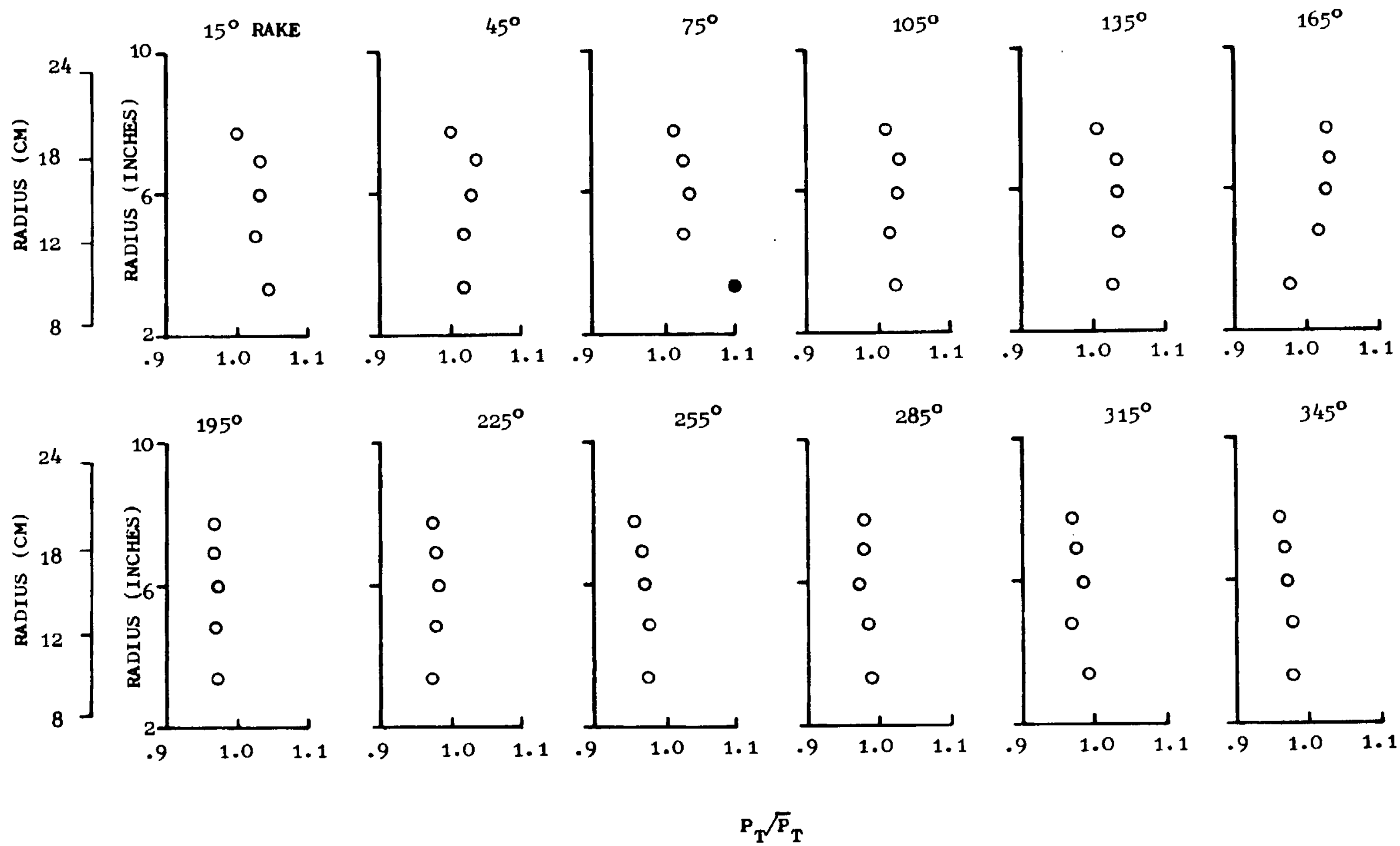

(b) Radial Profiles.
Figure 80. Circumferential Total-Pressure Distortion Profiles (RDG 478), "Moss" Engine 100% $N/\sqrt{\theta}$ (Concluded).

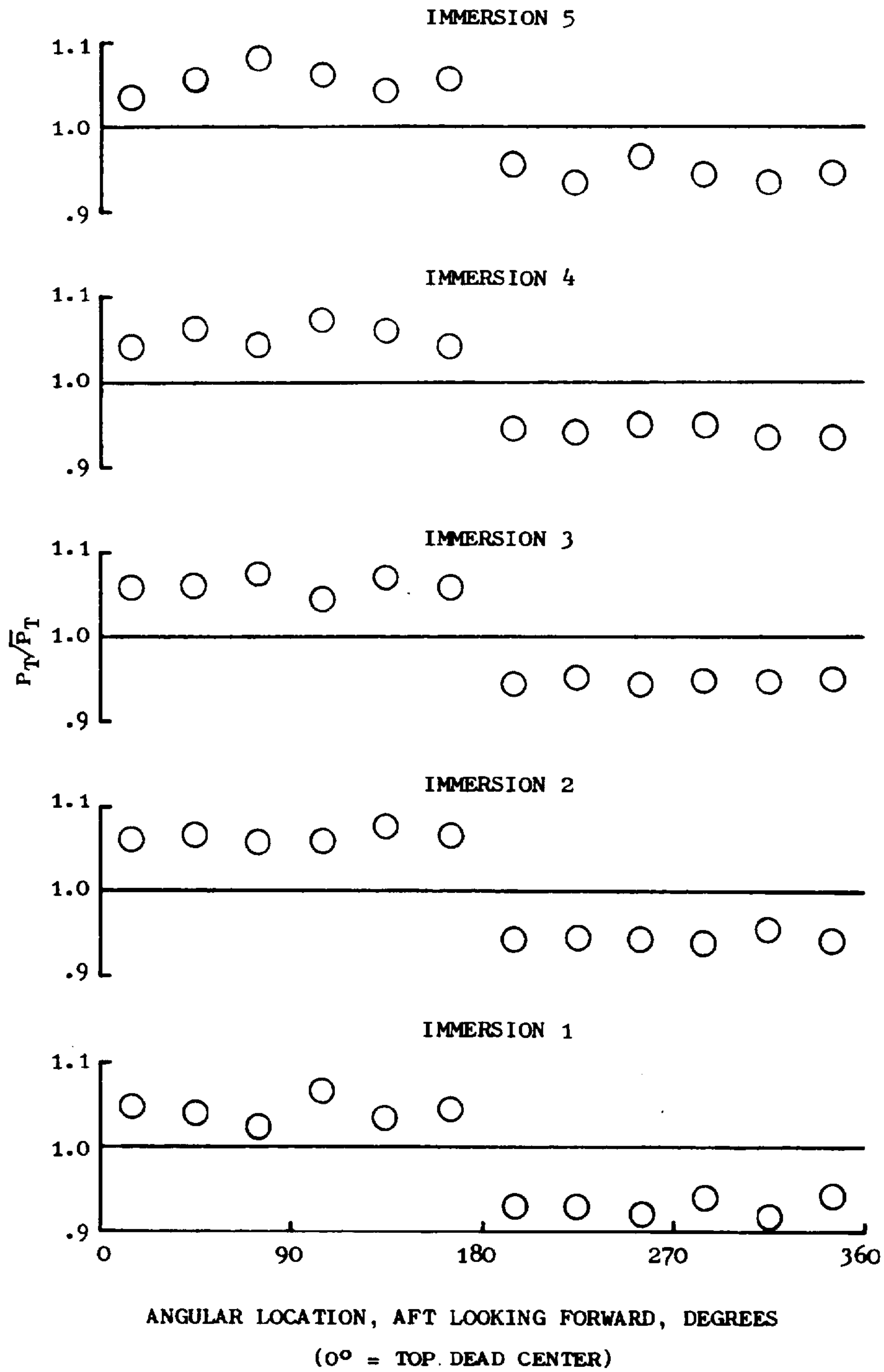

(a) Circumferential Profiles.
Figure 81. Circumferential Total-Pressure Distortion Profiles (RDG 384), "Moss" Engine 100% $N/\sqrt{\theta}$.

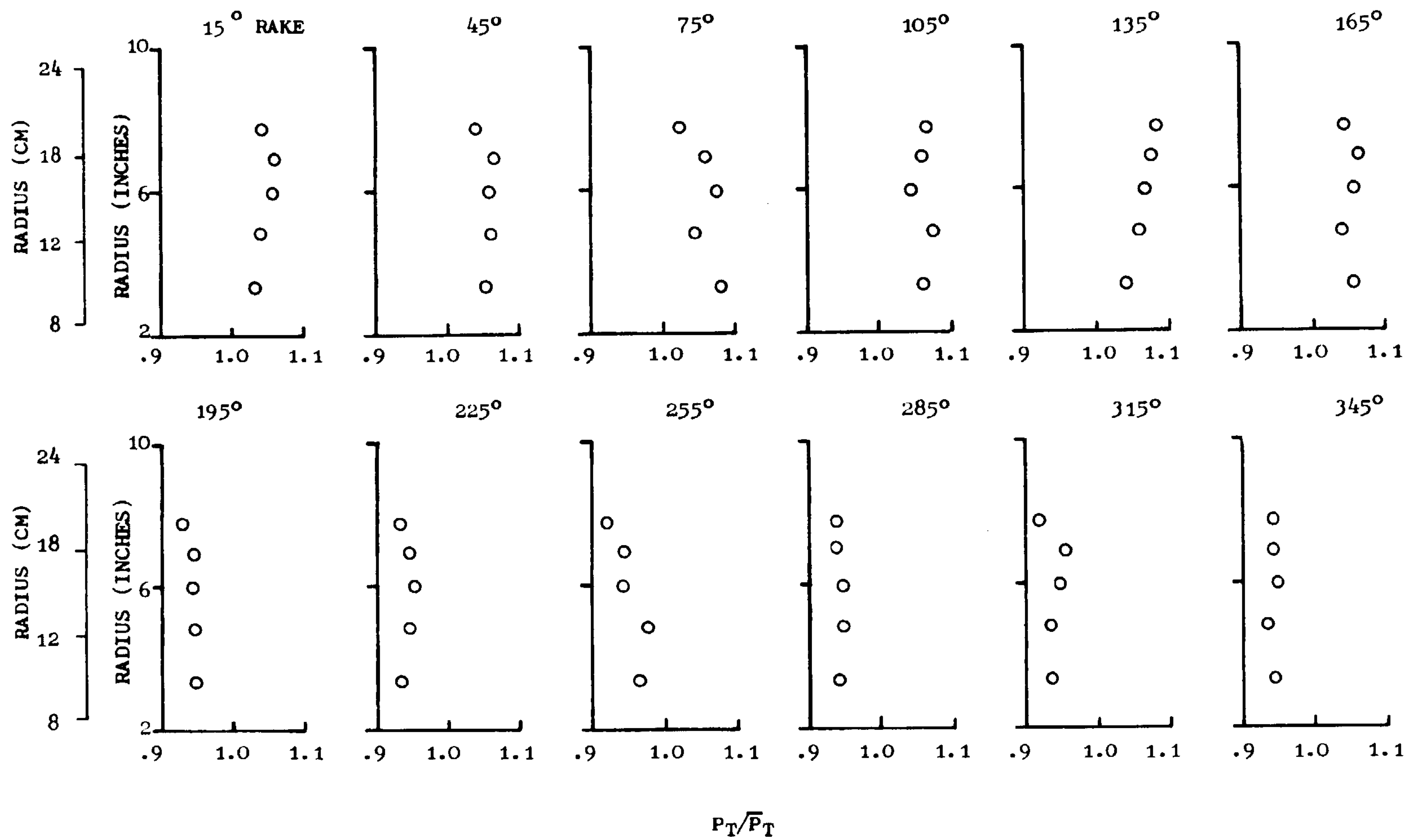

(b) Radial Profiles.

Figure 81. Circumferential Total-Pressure Distortion Profiles (RDG 384), "Moss" Engine 100% $N/\sqrt{\theta}$ (Concluded).

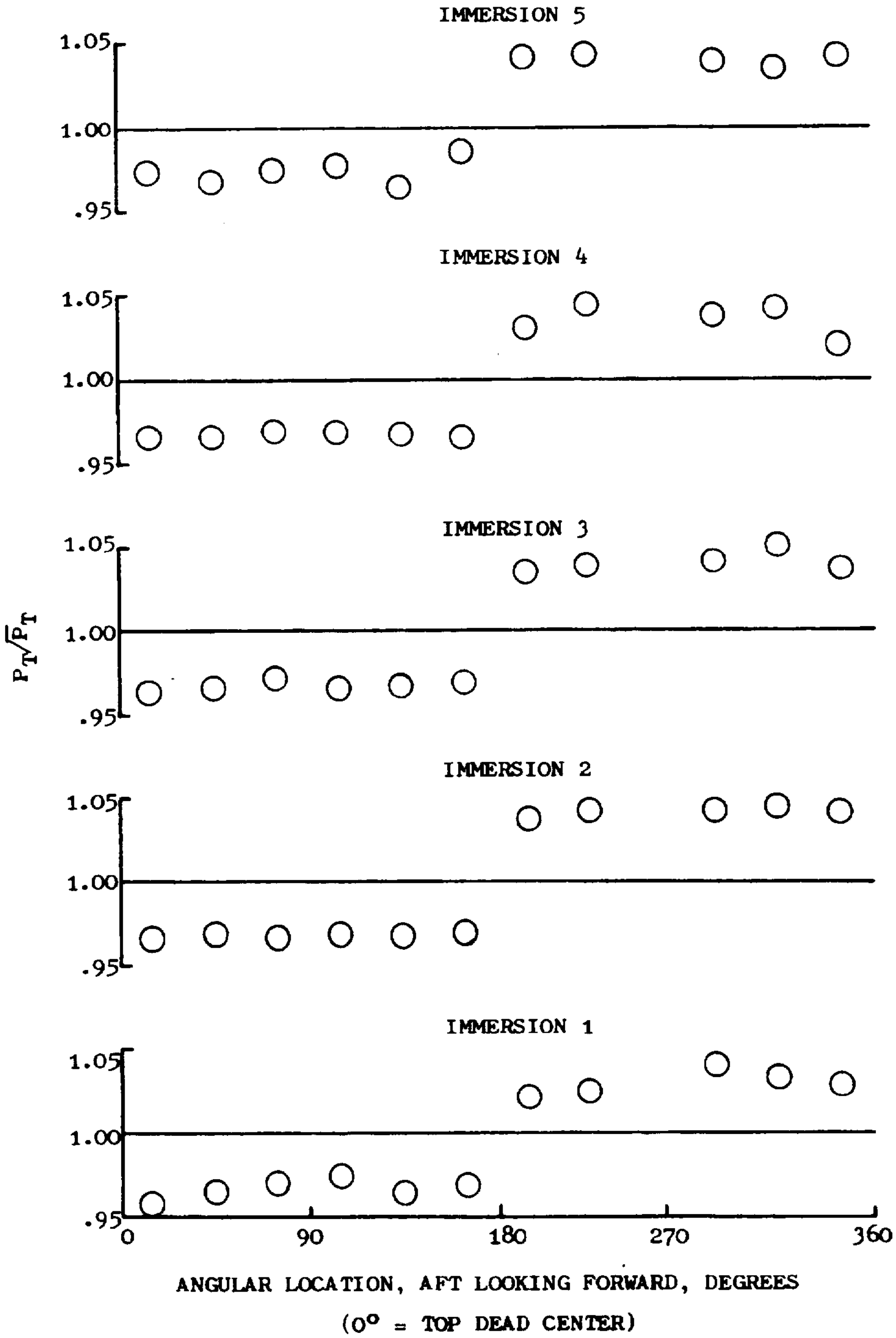

(a) Circumferential Profiles.

Figure 82. Circumferential Total-Pressure Distortion Profiles (RDG 99), "Moss" Engine 100% $N/\sqrt{\theta}$.

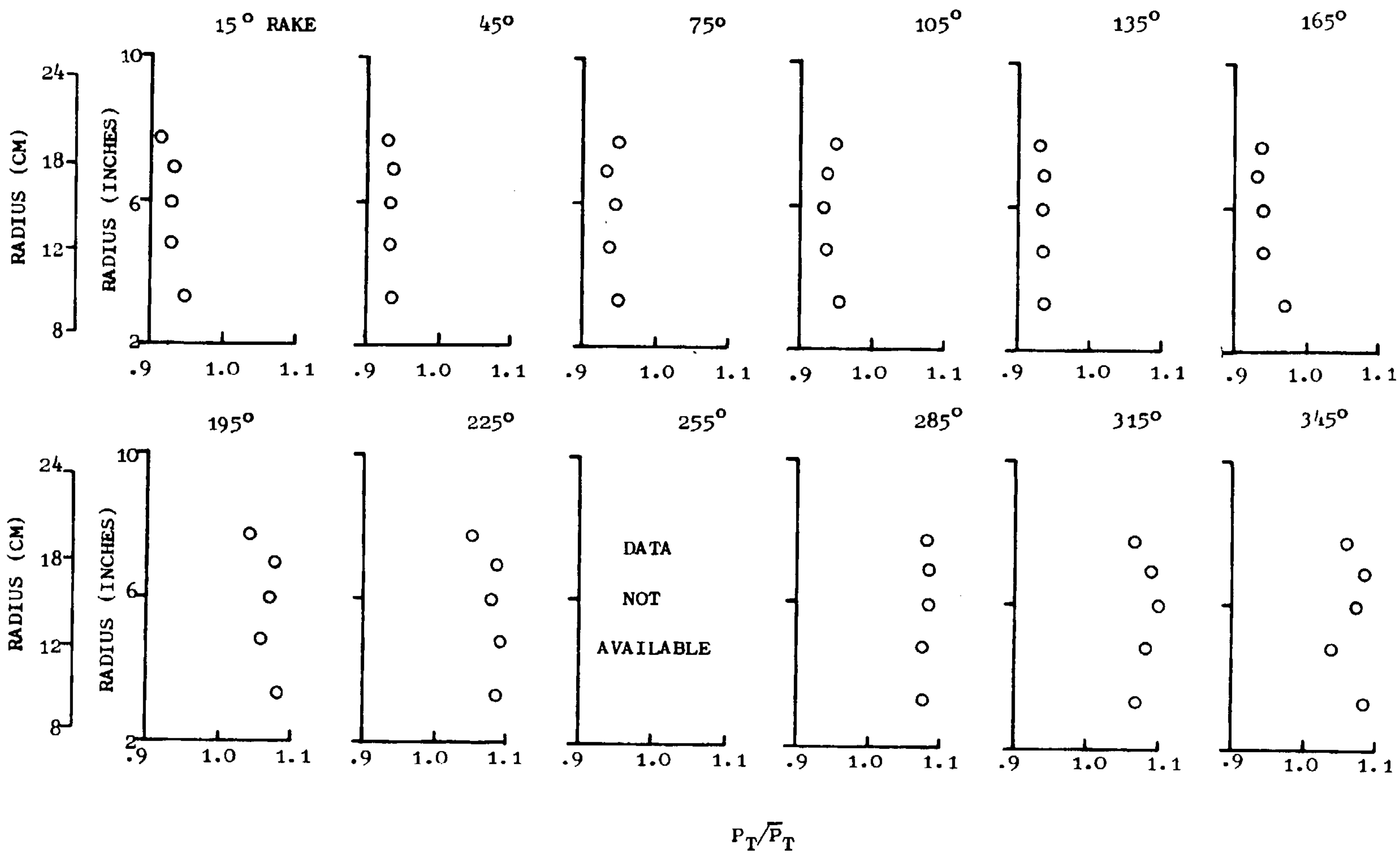

(b) Radial Profiles.

Figure 82. Circumferential Total-Pressure Distortion Profiles (RDG 99), "Moss" Engine 100% $N/\sqrt{\theta}$ (Concluded).

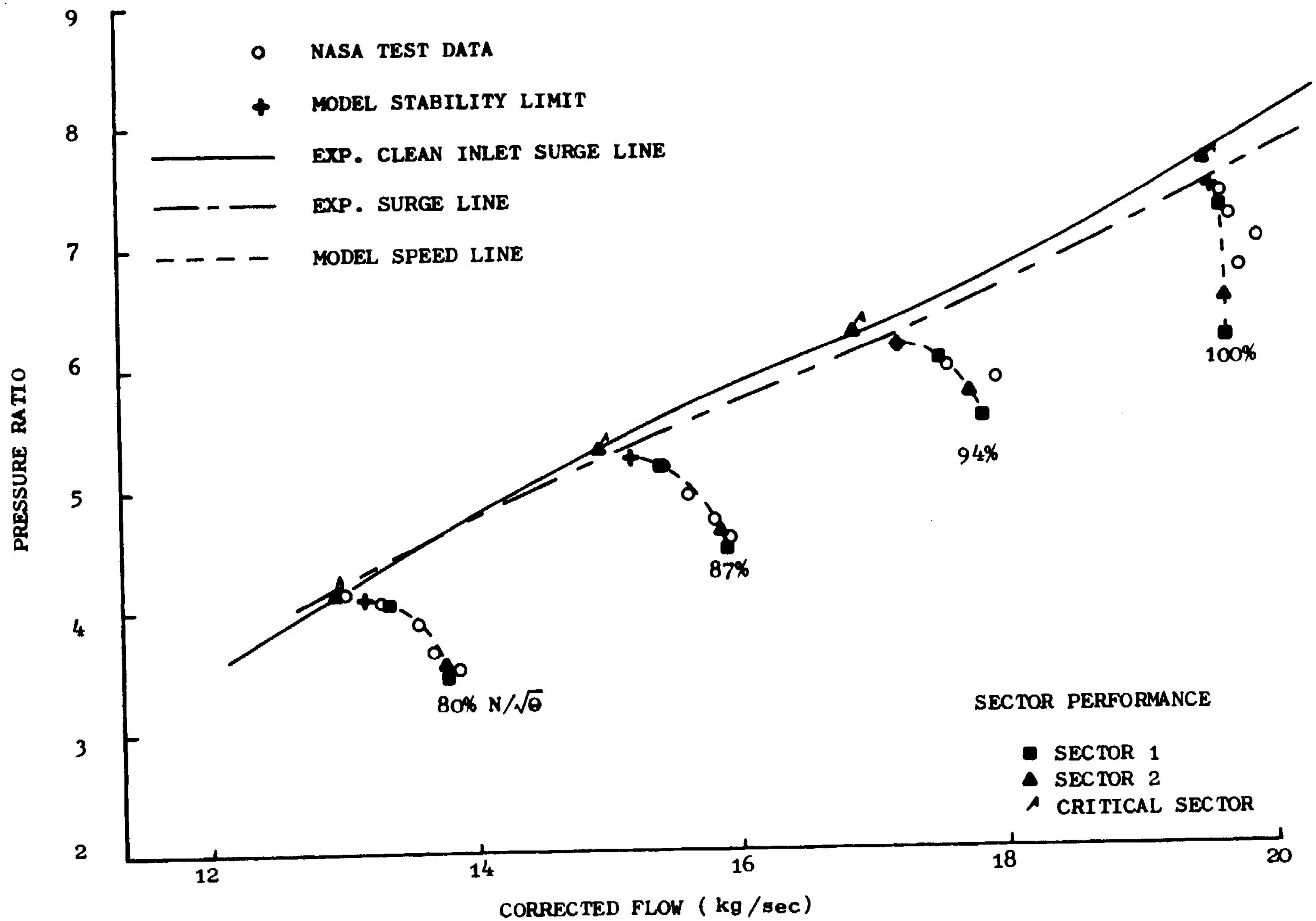

Figure 83. Effect of 180°, 1/Rev Total-Pressure Distortion (4M Screen) on Surge Line of "Moss" Engine - Sector Performance.

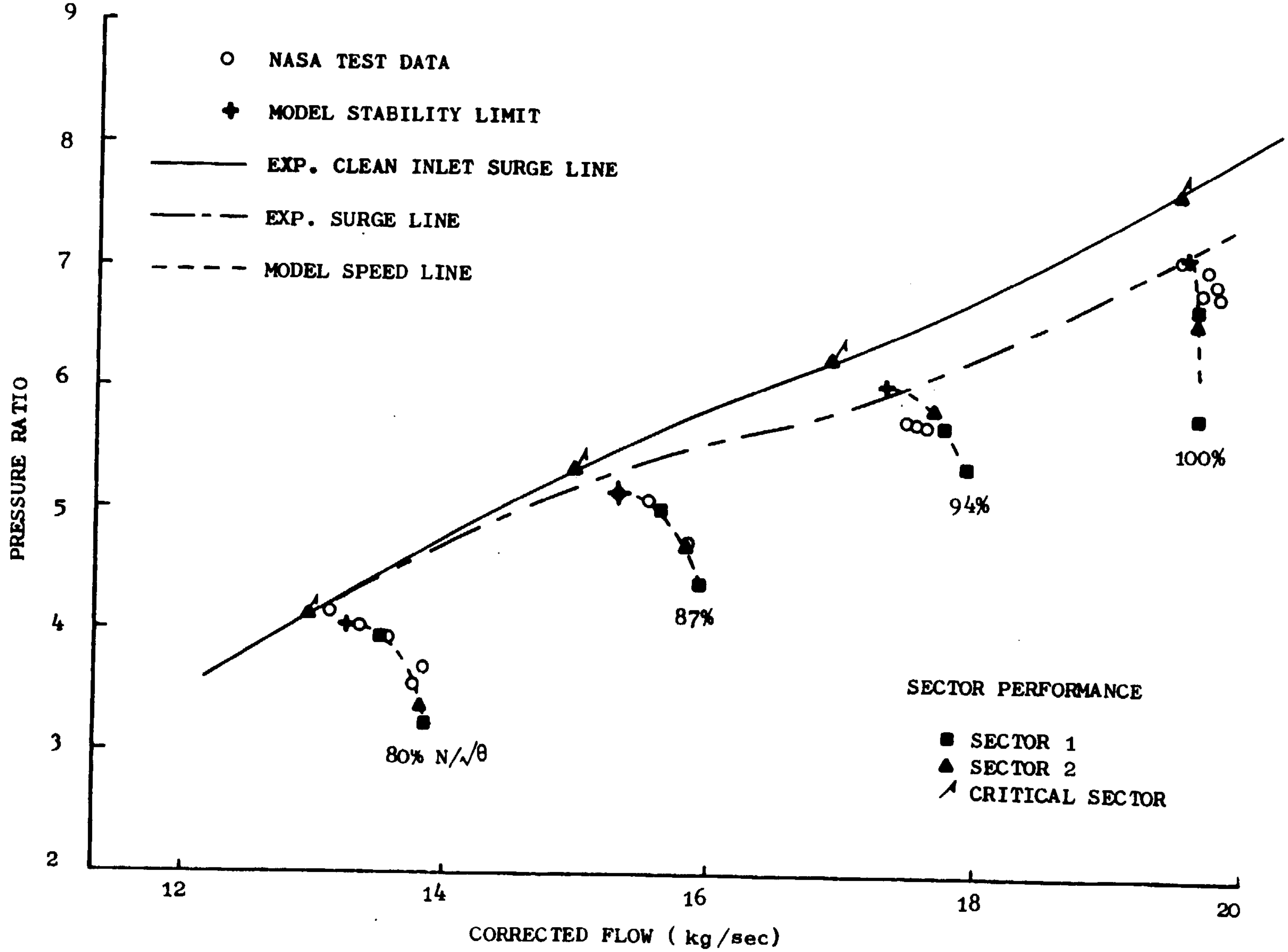

Figure 84. Effect of 180°, 1/Rev Total-Pressure Distortion (7½M Screen) on Surge Line of "Moss" Engine - Sector Performance.

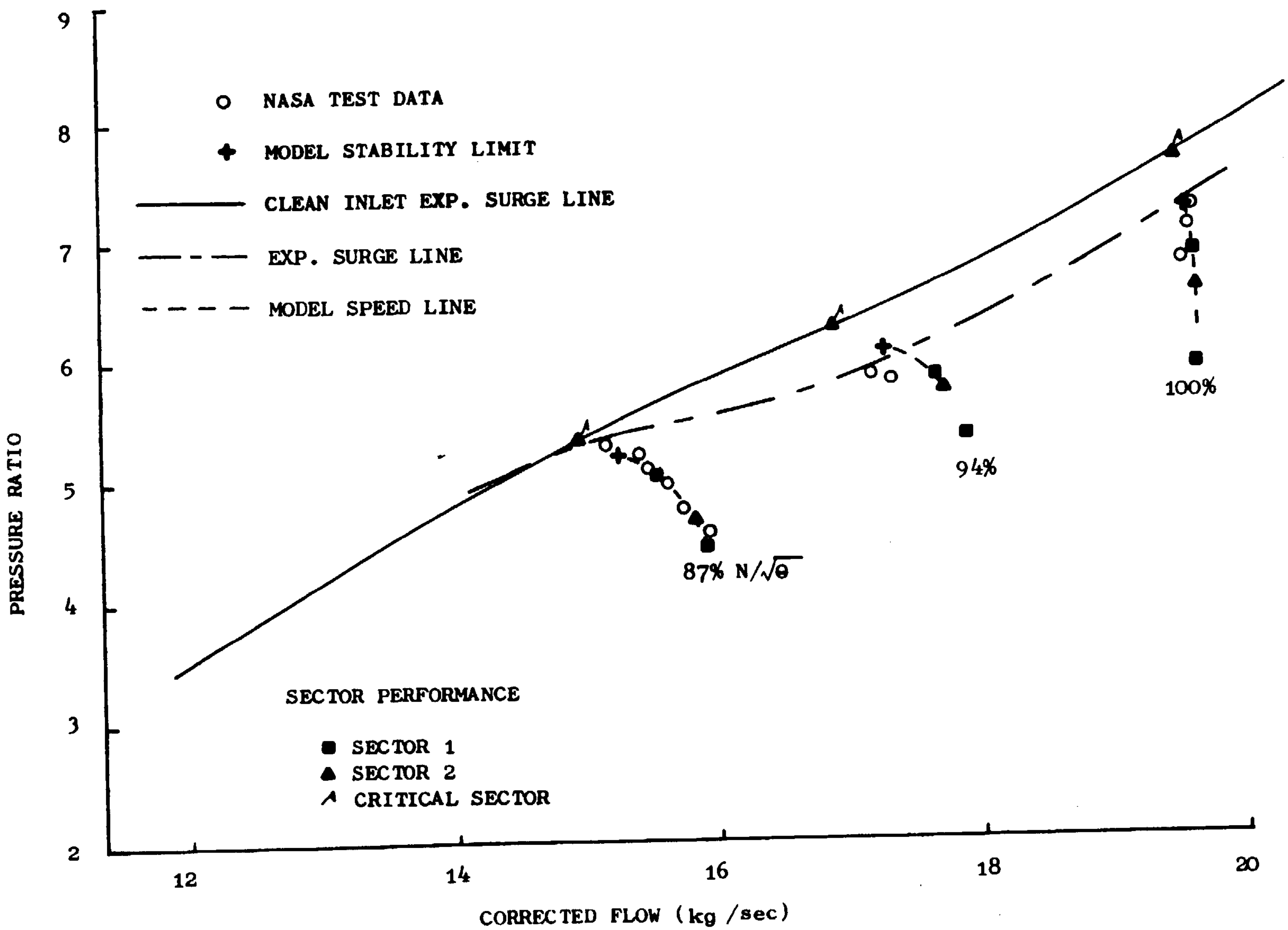

Figure 85. Effect of 180°, 1/Rev Total-Pressure Distortion (9M Screen) on Surge Line of "Moss" Engine - Sector Performance.

Table 26. Supplemental List of Computer Output Parameters.

PCTNCL	-	Sector Local Corrected Speed
ANGLE	-	Angular Extent of Sector
TALCW	-	Equivalent Total Area Sector Corrected Flow (kg/sec)
P/P-OA(L)	-	Sector Overall Pressure Ratio
T/T-OA(L)	-	Sector Overall Temperature Ratio
DPTR-IN	-	Normalized Total-Pressure Amplitude at Inlet, $\Delta P_T/\overline{P}_T$
DTTR-IN	-	Normalized Total-Temperature Amplitude at Inlet, $\Delta T_T/\overline{T}_T$
DPSR-IN	-	Normalized Static-Pressure Amplitude at Inlet, $\Delta P_S/\overline{P}_S$
ROT	-	Cumulative Sector Rotation (deg.)
DPTR2	-	Blade-Row Exit Normalized Total-Pressure Amplitude
DTTR2	-	Blade-Row Exit Normalized Total-Temperature Amplitude
DPSR2	-	Blade-Row Exit Normalized Static-Pressure Amplitude

Table 27. (a) Sector 1.
Calculated Performance, Total-Pressure Distortion (RDG 99), "Moss" Engine 100% $N/\sqrt{\theta}$.

DYNAMIC PARALLEL COMPRESSOR ANALYSIS

J85-13 NAS3-13526, MOSS 100-PCT., PT-DIST. RDG 99
THROTTLING SIMULATION

WCORR=19.604 PCTNC=100.20 P/P-OA=7.0578

SECTOR= 1 PCTNCL=100.20 ANGLE=180.00
TIME STEP= 0 TALCW=17.637 P/P-OA(L)=6.63618
TIME=0. EXIT FF= 6.5430 T/T-OA(L)=1.89693
DPTR-IN=0.13669 DTTR-IN=0. DPSR-IN=0.13550

ROW	CZ1	CU1	WU1	CT	WT	U1	M-ABS	M-REL	ALPHA	BETA	PS1	PT1	TS1	TT1	TNI	INC	LOSS	TND
1	142.5	0.	0.	142.5	0.	0.	0.4366	0.	0.	0.	5.73	6.53	265.0	275.1	0.	0.	0.	0.
2	194.8	0.	269.5	194.8	332.5	269.5	0.6071	1.0363	0.	54.14	5.09	6.53	255.2	275.1	0.04608	2.64	0.1186	0.05333
3	177.3	123.3	0.	215.9	0.	0.	0.6373	0.	34.83	0.	7.02	9.22	285.7	308.9	-0.00020	-0.01	0.	0.
4	192.0	18.1	261.3	192.9	324.3	279.5	0.5645	0.9493	5.40	55.70	7.43	9.22	293.4	308.9	0.06115	3.50	0.1274	0.12716
5	130.0	145.7	0.	231.6	0.	0.	0.6476	0.	38.99	0.	9.68	12.83	318.3	345.0	-0.02770	-1.59	0.	0.
6	185.3	39.3	248.6	170.0	310.3	288.4	0.5241	0.8561	12.10	53.23	10.64	12.83	327.1	345.0	0.03801	2.18	0.1420	0.14148
7	175.3	170.6	0.	245.1	0.	0.	0.6506	0.	44.18	0.	13.20	17.54	353.3	383.2	-0.02619	-1.50	0.	0.
8	179.4	47.4	248.9	135.6	306.8	296.3	0.4839	0.8000	14.80	54.21	14.94	17.54	366.1	383.2	0.05946	3.40	0.1531	0.14448
9	171.9	132.9	0.	251.0	0.	0.	0.6321	0.	46.77	0.	18.05	23.53	392.4	423.7	0.00643	0.37	0.	0.
10	174.3	61.5	240.5	135.3	297.4	302.2	0.4585	0.7358	19.40	54.00	20.45	23.62	406.6	423.7	-0.03406	-1.95	0.1415	0.15805
11	170.6	174.1	0.	243.4	0.	0.	0.5875	0.	45.58	0.	23.50	29.68	428.4	457.9	-0.00777	-0.45	0.	0.
12	173.0	74.2	232.1	138.5	289.5	306.3	0.4476	0.6883	23.20	53.30	25.87	29.68	440.3	457.9	-0.02627	-1.50	0.1183	0.12080
13	169.5	160.1	0.	233.1	0.	0.	0.5438	0.	43.36	0.	28.59	34.96	457.3	484.3	-0.02683	-1.54	0.	0.
14	168.5	68.8	239.7	132.0	293.2	308.7	0.4197	0.6762	22.20	54.93	30.96	34.95	467.8	484.3	-0.00323	-0.18	0.1023	0.09771
15	161.5	142.0	0.	215.1	0.	0.	0.4879	0.	41.32	0.	33.89	39.89	483.8	506.9	-0.04313	-2.47	0.	0.
16	157.2	67.2	247.2	169.0	292.9	309.4	0.3799	0.6583	21.83	57.55	35.10	39.88	492.6	506.9	0.08057	4.61	0.0778	0.13341
17	152.9	111.0	0.	139.1	0.	0.	0.4198	0.	35.99	0.	38.38	43.33	504.2	521.9	-0.10713	-6.11	0.	0.
18	148.1	25.0	0.	150.2	0.	0.	0.3315	0.	9.58	0.	40.14	43.32	510.7	521.9	-0.00000	-0.00	0.	0.

ROW	DEV	DFACT	PHI	PSI	PSI-P	PR1	PR2	TR1	TR2	AD-EF	W2/W1	D*X	DW/DWEX	ROT	DPTR2	DTTR2	DPSR2
1	0.	-0.222	0.	0.	0.	1.000	1.00000	1.000	1.00000	0.	1.000000	0.805058E 01	0.	0.	0.13669	0.00000	0.13462
2	3.05	0.462	0.723	0.934	0.790	1.413	1.41307	1.123	1.12271	0.846	1.000000	0.171543E 00	0.	3.3	0.12725	0.00164	0.12485
3	0.	0.335	0.	0.	0.	1.413	0.99999	1.123	1.00000	0.	1.000000	0.361734E 00	0.	6.7	0.12723	0.00164	0.11942
4	7.25	0.466	0.667	0.930	0.786	1.906	1.39120	1.254	1.11697	0.846	1.000000	0.618418E 00	0.	9.5	0.10852	0.00629	0.10712
5	0.	0.366	0.	0.	0.	1.956	1.00000	1.254	1.00000	0.	1.000000	0.224397E 00	0.	12.9	0.10856	0.00628	0.09418
6	8.05	0.473	0.644	0.923	0.779	2.637	1.36698	1.393	1.11074	0.844	1.000000	0.417808E 01	0.	15.6	0.09238	0.01014	0.08504
7	0.	0.427	0.	0.	0.	2.687	0.99994	1.393	0.99998	0.	1.000000	0.478561E 01	0.	19.1	0.09236	0.01015	0.07528
8	8.22	0.434	0.606	0.927	0.779	3.620	1.34707	1.540	1.10569	0.841	1.000000	0.147463E 01	0.	21.7	0.10502	0.00440	0.07749
9	0.	0.434	0.	0.	0.	3.619	0.99967	1.540	0.99991	0.	1.000000	0.526978E 01	0.	25.1	0.10461	0.00452	0.09279
10	8.98	0.412	0.579	0.754	0.629	4.548	1.25680	1.664	1.08083	0.835	1.000000	0.105613E 02	0.	27.4	0.09283	0.00693	0.08325
11	0.	0.369	0.	0.	0.	4.548	0.99996	1.664	0.99999	0.	1.000000	0.178469E 00	0.	30.7	0.09281	0.00694	0.07837
12	6.89	0.339	0.565	0.565	0.469	5.356	1.17768	1.760	1.05764	0.830	1.000000	0.931349E 00	0.	32.7	0.06388	0.01552	0.06140
13	0.	0.368	0.	0.	0.	5.355	0.99985	1.760	0.99996	0.	1.000000	0.155979E 00	0.	35.7	0.06375	0.01556	0.04509
14	5.58	0.302	0.546	0.476	0.393	6.111	1.14116	1.842	1.04659	0.825	1.000000	0.134200E 01	0.	37.3	0.04257	0.02185	0.03175
15	0.	0.354	0.	0.	0.	6.110	0.99989	1.842	0.99997	0.	1.000000	0.659480E 01	0.	40.2	0.04246	0.02188	0.02416
16	7.60	0.207	0.508	0.317	0.255	6.638	1.03637	1.897	1.02977	0.805	1.000000	0.321526E 01	0.	41.5	0.00900	0.03211	0.00101
17	0.	0.394	0.	0.	0.	6.636	0.99976	1.897	0.99993	0.	1.000000	0.447679E 01	0.	43.1	0.00877	0.03217	0.00857
18	0.	0.084	0.	0.	0.	6.636	1.00000	1.897	1.00000	0.	1.000000	0.375079E 00	0.	43.4	0.00877	0.03217	0.00798

Table 27. (b) Sector 2.
Calculated Performance, Total-Pressure Distortion (RDG 99), "Moss" Engine 100% $N/\sqrt{\theta}$ (Concluded).

```
DYNAMIC PARALLEL COMPRESSOR ANALYSIS

JT5-15 NAS3-13526, MOSS 100-PCT., PT-DIST. RDG 99
THROTTLING SIMULATION

WCORR=19.604          PCTNC=100.20    P/P-OA=7.0578

SECTOR= 2             PCTNCL=100.20   ANGLE=180.00
TIME STEP=     0      FALCW=19.566    P/P-OA(L)=7.54334
TIME=0.               EXIT FF= 0.543C T/T-OA(L)=1.95896
DPTR-IN=0.13669       DTTR-IN=0.      DPSR-IN=0.13550
```

ROW	C21	CU1	WU1	CT	WT	U1	M-ABS	M-REL	ALPHA	BETA	PS1	PT1	TS1	TT1	TNI	INC	LOSS	TND
1	141.3	0.	0.	141.8	0.	0.	0.4346	0.	0.	0.	5.00	5.69	265.1	275.1	0.	0.	0.	0.
2	193.7	0.	269.5	193.7	331.9	259.5	0.6034	1.0339	0.	54.30	5.45	5.69	255.5	275.1	0.04882	2.80	0.1117	0.05327
3	174.2	125.5	0.	215.2	0.	0.	0.6344	0.	35.62	0.	5.19	8.12	286.4	309.4	0.01363	0.78	0.	0.
4	188.7	17.8	261.6	189.6	322.6	279.5	0.5538	0.9425	5.40	54.20	5.59	8.12	291.5	309.4	0.06989	4.00	0.1231	0.11872
5	175.3	151.7	0.	231.4	0.	0.	0.6459	0.	40.87	0.	9.70	11.51	320.5	347.2	0.00501	0.29	0.	0.
6	179.2	38.4	250.0	183.3	307.6	238.4	0.5030	0.8441	12.10	54.36	9.68	11.51	330.5	347.2	0.05785	3.31	0.1380	0.14279
7	158.4	175.6	0.	243.5	0.	0.	0.6418	0.	46.21	0.	12.12	15.99	357.7	387.1	0.00927	0.53	0.	0.
8	170.7	45.1	251.2	176.5	303.7	296.3	0.4568	0.7859	14.80	55.81	13.86	15.99	371.6	387.1	0.08756	5.00	0.1361	0.20485
9	163.4	174.1	0.	236.8	0.	0.	0.5977	0.	46.81	0.	15.71	21.27	397.2	425.6	0.00718	0.41	0.	0.
10	168.0	59.2	243.0	178.1	295.4	302.2	0.4389	0.7280	19.40	55.34	18.63	21.27	409.8	425.6	-0.01060	-0.61	0.1330	0.17427
11	162.7	176.1	0.	237.7	0.	0.	0.5750	0.	47.26	0.	21.62	27.05	432.5	461.1	0.02150	1.23	0.	0.
12	164.4	70.5	235.8	178.9	287.5	306.3	0.4230	0.6797	23.20	55.11	23.92	27.05	445.2	461.1	0.00545	0.31	0.1247	0.11407
13	159.1	170.2	0.	233.5	0.	0.	0.5403	0.	47.04	0.	26.89	32.79	464.8	491.9	0.03731	2.14	0.	0.
14	156.4	63.8	244.9	158.2	290.6	308.7	0.3855	0.6632	22.20	57.44	29.60	32.79	477.7	491.9	0.04068	2.33	0.1087	0.11910
15	148.5	148.6	0.	210.3	0.	0.	0.4710	0.	45.05	0.	32.84	38.22	496.1	518.1	0.02200	1.26	0.	0.
16	143.7	56.9	252.5	154.6	290.5	309.4	0.3428	0.6442	-21.60	60.34	35.24	38.22	506.2	518.1	0.12995	7.40	0.0901	0.15016
17	137.5	134.7	0.	135.7	0.	0.	0.4055	0.	42.16	0.	38.34	42.94	521.8	539.0	0.00112	0.06	0.	0.
18	132.4	22.3	0.	134.3	0.	0.	0.2909	0.	9.58	0.	40.49	42.94	530.0	539.0	-0.00000	-0.00	0.	0.

ROW	DEV	DFACT	PHI	PSI	PSI-P	PR1	PR2	TR1	TR2	AD-EF	W2/W1	DWX	DW/DWEX	ROT	DPTR2	DTTR2	DPSR2
1	0.	-0.221	0.	0.	0.	1.000	1.00000	1.000	1.00000	0.	1.000000	0.684061E 01	0.	0.	0.13669	0.00000	0.13462
2	3.05	0.473	0.719	0.948	0.813	1.427	1.42652	1.125	1.12455	0.858	1.000000	0.294001E 01	0.	3.4	0.12725	0.00164	0.12485
3	0.	0.355	0.	0.	0.	1.427	1.00001	1.125	1.00000	0.	1.000000	0.272866E 00	0.	6.8	0.12723	0.00164	0.11942
4	6.77	0.494	0.675	0.973	0.835	2.022	1.41757	1.262	1.12217	0.858	1.000000	0.425098E 01	0.	9.8	0.10852	0.00629	0.10712
5	0.	0.409	0.	0.	0.	2.022	0.99997	1.262	0.99999	0.	1.000000	0.113145E 00	0.	13.4	0.10856	0.00628	0.09418
6	5.13	0.535	0.621	0.965	0.826	2.809	1.38933	1.407	1.11504	0.856	1.000000	0.294939E 01	0.	16.2	0.09738	0.01014	0.08504
7	0.	0.471	0.	0.	0.	2.809	0.99996	1.407	0.99999	0.	1.000000	0.276018E 01	0.	19.8	0.09236	0.01015	0.07528
8	11.54	0.477	0.575	0.880	0.752	3.737	1.33008	1.547	1.09936	0.855	1.000000	0.904047E 00	0.	22.4	0.10502	0.00440	0.07749
9	0.	0.425	0.	0.	0.	3.737	1.00008	1.547	1.00002	0.	1.000000	0.536558E 01	0.	25.8	0.10461	0.00452	0.09279
10	9.87	[illegible]	0.556	0.782	0.666	4.752	1.27174	1.676	1.08345	0.852	1.000000	0.545867E 01	0.	28.1	0.09283	0.00693	0.08325
11	0.	0.406	0.	0.	0.	4.752	0.99998	1.676	0.99999	0.	1.000000	0.624352E 01	0.	31.6	0.09281	0.00694	0.07837
12	6.51	0.405	0.537	0.657	0.559	5.761	1.21229	1.788	1.06675	0.847	1.000000	0.317680E 00	0.	33.7	0.06388	0.01552	0.06140
13	0.	0.451	0.	0.	0.	5.761	0.99999	1.788	1.00000	0.	1.000000	0.536455E 01	0.	36.9	0.06375	0.01556	0.04509
14	6.79	0.359	0.507	0.552	0.464	6.715	1.16560	1.883	1.05319	0.841	1.000000	0.596712E 00	0.	38.6	0.04257	0.02185	0.03175
15	0.	0.430	0.	0.	0.	6.715	1.00000	1.883	1.00000	0.	1.000000	0.430652E 01	0.	41.8	0.04246	0.02188	0.02416
16	8.54	0.274	0.465	0.439	0.367	7.543	1.12333	1.959	1.04035	0.837	1.000000	0.130317E 01	0.	43.3	0.00900	0.03211	0.00101
17	0.	0.505	0.	0.	0.	7.543	0.99999	1.959	1.00000	0.	1.000000	0.288340E 01	0.	45.1	0.00877	0.03217	0.00857
18	0.	0.084	0.	0.	0.	7.543	1.00000	1.959	1.00000	0.	1.000000	0.150930E 00	0.	45.3	0.00877	0.03217	0.00798

APPENDIX E

TOTAL-TEMPERATURE DISTORTION DOCUMENTATION

In the same manner as Appendix D, this appendix illustrates the detailed supplemental information that is available as model output. Figure 86 presents the circumferential and radial profiles of the temperature distortion as indicated by the NASA test data. Included on the figure are the NASA reading number and the normalizing parameters. A detailed compressor map of the temperature-distortion throttling simulations, illustrating the operating points of the parallel-compressor sectors is presented in Figure 87. Table 28 presents documentation of the compressor performance for the "Mehalic" engine 100 percent corrected flow high-flow condition.

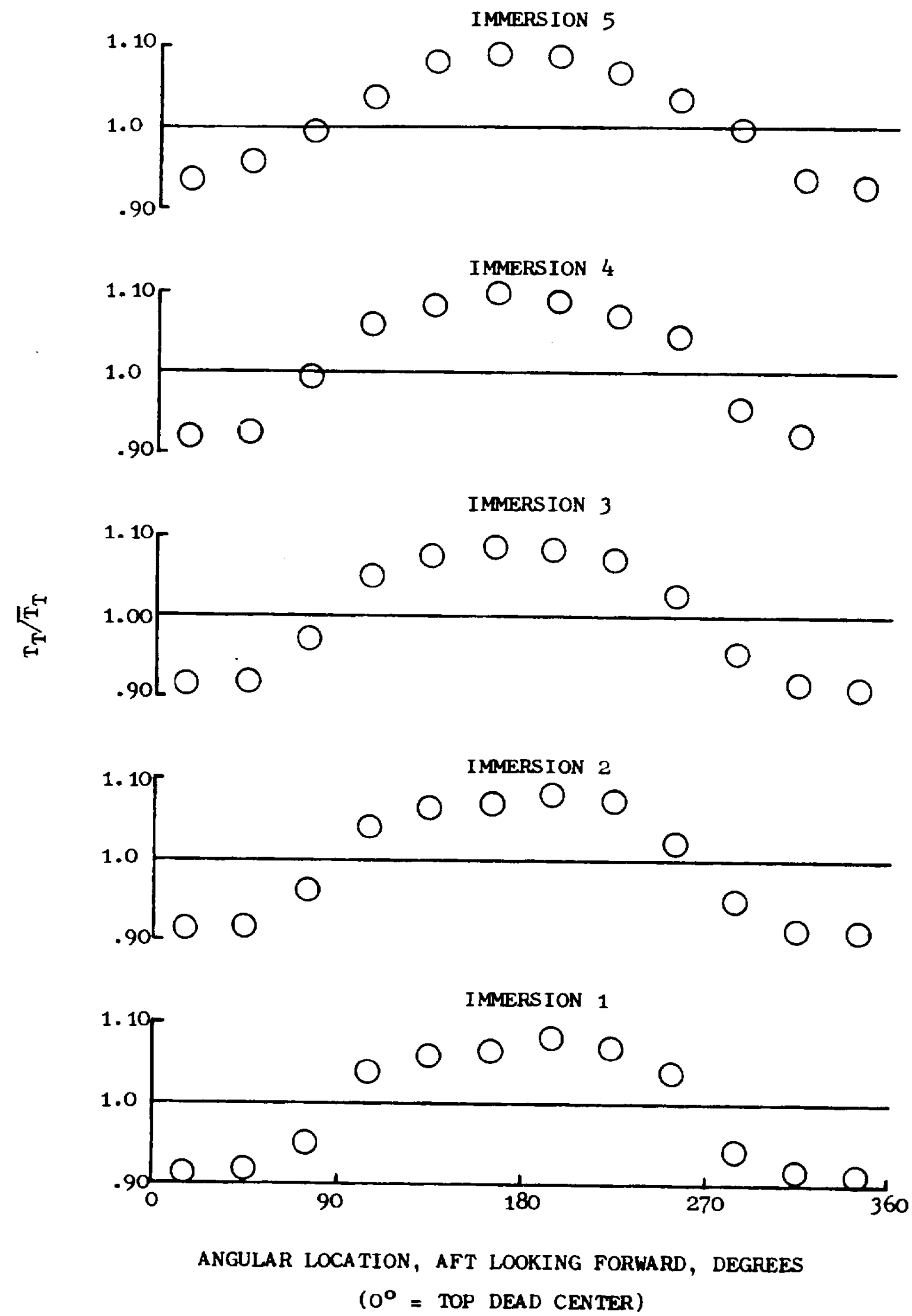

(a) Circumferential Profiles.

Figure 86. Circumferential Total-Temperature Distortion Profiles (RDG 568), "Mehalic" Engine 86.8% $N/\sqrt{\theta}$.

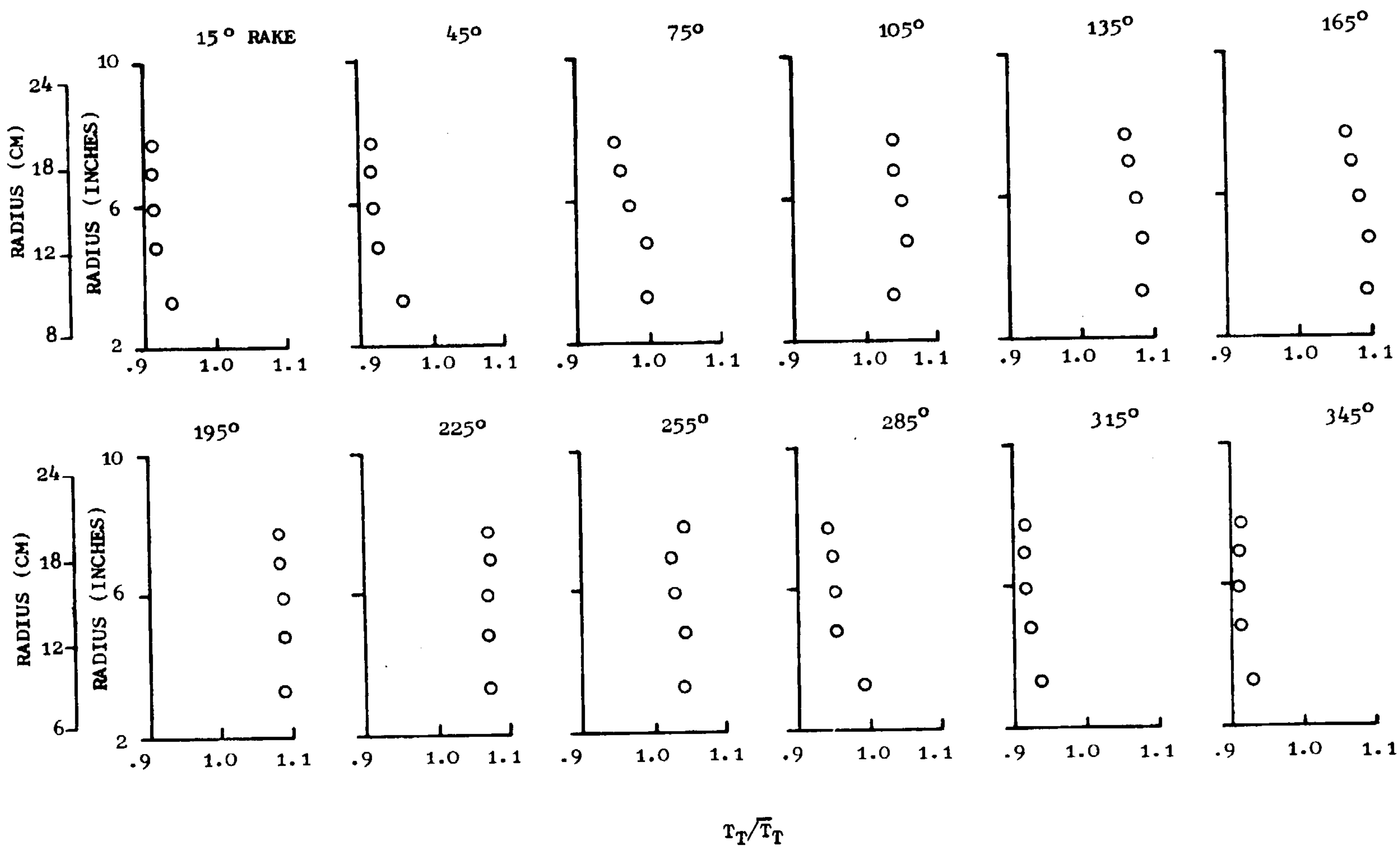

(b) Radial Profiles.

Figure 86. Circumferential Total-Temperature Distortion Profiles (RDG 568), "Mehalic" Engine 86.8% $N/\sqrt{\theta}$ (Concluded).

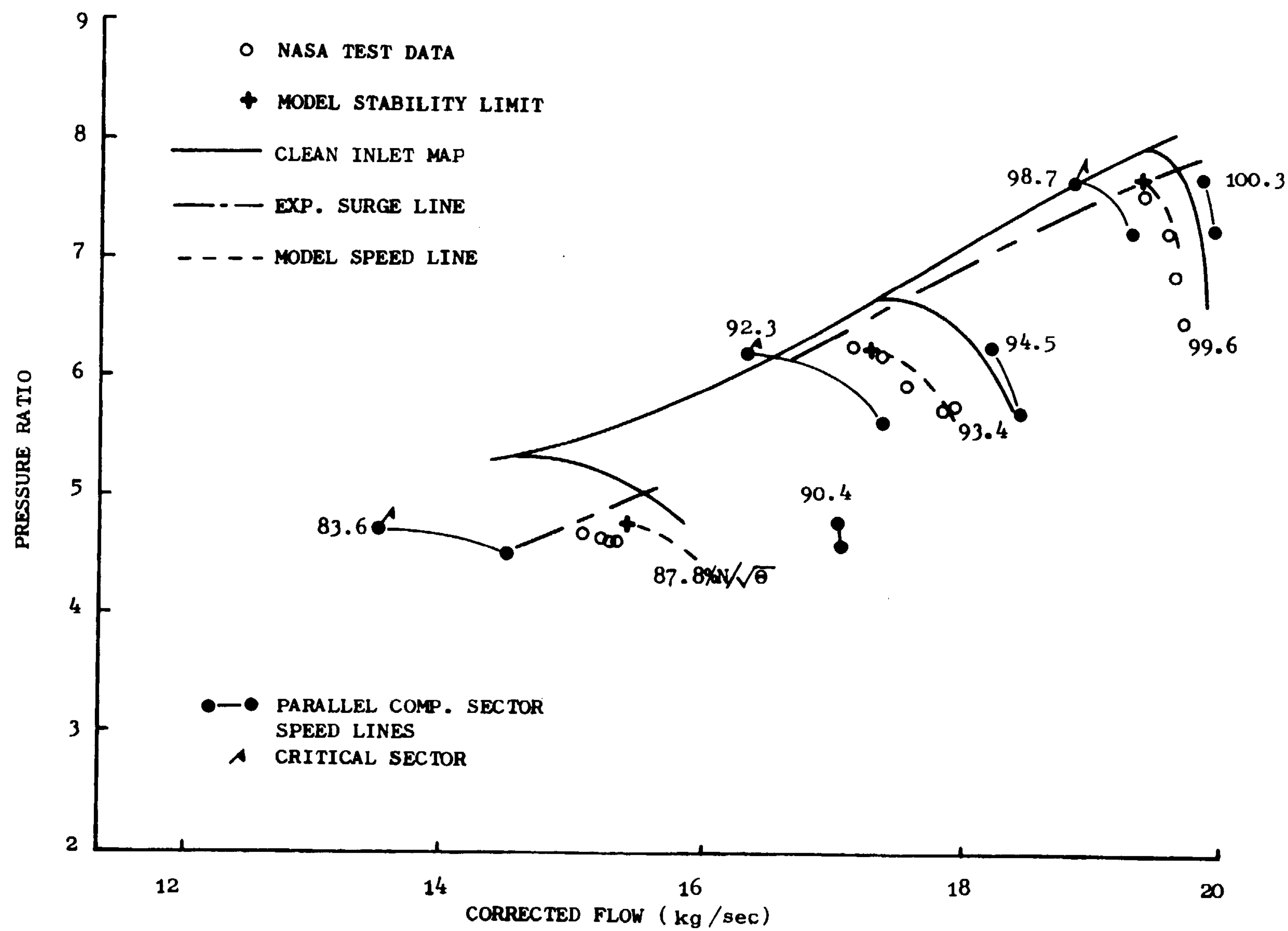

Figure 87. Effect of 180°, 1/Rev Total-Temperature Distortion on Surge Line of "Mehalic" Engine - Sector Performance.

Table 28. (a) Sector 1.
Calculated Performance, Total-Temperature Distortion (RDG 138), "Mehalic" Engine $99.6\%\ \dot{N}/\sqrt{\theta}$.

DYNAMIC PARALLEL COMPRESSOR ANALYSIS

J85-13 NAS3-18526, TT-DIST MEHALIC ENG., RDG 138
THROTTLING SIMULATION

WCORR=17.504 PCTNC= 99.56 P/P-OA=7.5610

SECTOR= 1	PCTNCL=100.49	ANGLE=180.00
TIME STEP= 0	TALCW=19.686	P/P-OA(L)=7.57022
TIME=0.	EXIT FF= 6.1703	T/T-OA(L)=1.99044
DPTR-IN=0.	DTTR-IN=0.03628	DPSR-IN=0.01278

ROW	CZ1	CU1	WU1	CT	WT	U1	M-ABS	M-REL	ALPHA	BETA	PS1	PT1	TS1	TT1	TNI	INC	LOSS	TND
1	147.5	0.	0.	147.5	0.	0.	0.4437	0.	0.	0.	5.05	5.92	274.8	285.6	0.	0.	0.	0.
2	202.5	0.	275.4	202.5	341.8	275.4	0.6204	1.0471	0.	53.66	5.34	5.92	255.2	285.6	0.03779	2.16	0.0865	0.11938
3	191.8	93.3	0.	213.5	0.	0.	0.6262	0.	26.06	0.	6.92	9.02	289.2	311.9	-0.15436	-8.78	0.	0.
4	219.0	20.7	264.9	219.7	343.6	285.6	0.6467	1.0105	5.40	50.42	6.81	9.02	297.8	311.9	0.00383	0.22	0.1289	0.06954
5	202.6	152.2	0.	253.4	0.	0.	0.7090	0.	36.91	0.	9.05	12.66	317.9	349.9	-0.06411	-3.67	0.	0.
6	207.9	44.6	250.1	212.7	325.3	294.7	0.5863	0.8968	12.10	50.26	10.03	12.66	327.4	349.9	-0.01378	-0.79	0.1376	0.09707
7	196.2	175.4	0.	263.2	0.	0.	0.6975	0.	41.90	0.	12.50	17.30	354.4	388.8	-0.06775	-3.88	0.	0.
8	199.5	52.7	250.0	206.5	319.9	302.8	0.5372	0.8324	14.60	51.40	14.22	17.30	357.6	388.8	0.01024	0.59	0.1593	0.06017
9	190.4	138.9	0.	275.3	0.	0.	0.6904	0.	46.25	0.	17.33	23.54	395.7	433.4	-0.00257	-0.15	0.	0.
10	189.8	66.6	241.2	201.2	307.5	308.7	0.4938	0.7545	19.40	51.88	20.18	23.84	413.3	433.4	-0.07112	-4.07	0.1576	0.05144
11	133.8	179.1	0.	271.0	0.	0.	0.6459	0.	47.29	0.	23.50	31.12	437.9	474.5	0.02195	1.26	0.	0.
12	131.4	77.7	235.2	177.4	297.0	312.9	0.4615	0.6946	23.20	52.36	26.89	31.12	455.1	474.5	-0.04261	-2.44	0.1554	0.01073
13	176.0	122.1	0.	260.5	0.	0.	0.5953	0.	47.50	0.	30.24	38.43	476.5	510.3	0.04535	2.60	0.	0.
14	169.6	69.2	246.2	133.2	299.0	315.4	0.4113	0.6713	22.20	55.43	34.21	38.43	493.6	510.3	0.00564	0.32	0.1257	0.06590
15	151.7	138.3	0.	226.7	0.	0.	0.4993	0.	44.48	0.	37.83	44.86	512.9	538.5	0.01200	0.69	0.	0.
16	155.6	61.6	254.5	167.4	298.3	316.1	0.3646	0.6497	21.40	58.56	40.92	44.86	524.5	538.5	0.09832	5.62	0.1380	0.04085
17	147.7	157.2	0.	215.7	0.	0.	0.4607	0.	46.78	0.	45.31	52.40	545.4	568.5	0.08190	4.68	0.	0.
18	159.1	23.5	0.	141.1	0.	0.	0.2977	0.	9.58	0.	49.28	52.41	558.7	568.6	-0.00000	-0.00	0.	0.

ROW	DEV	DFACT	PHI	PSI	PSI-P	PR1	PR2	TR1	TR2	AD-EF	W2/W1	DWK	DW/DWEN	ROT	DPTR2	DTTR2	DPSR2
1	0.	-0.225	0.	0.	0.	1.000	1.00000	1.000	1.00000	0.	1.000000	0.935095E 01	0.	0.	0.00000	0.03628	0.02208
2	5.81	0.337	0.736	0.695	0.593	1.302	1.30218	1.092	1.09184	0.853	1.000000	0.234053E 01	0.	2.5	0.02448	0.04450	0.04126
3	0.	0.130	0.	0.	0.	1.302	1.00001	1.092	1.00000	0.	1.000000	0.650556E 00	0.	5.0	0.02410	0.04439	0.07486
4	5.93	0.444	0.767	0.936	0.783	1.829	1.40427	1.225	1.12183	0.836	1.000000	0.280369E 01	0.	7.7	0.02172	0.04514	0.05024
5	0.	0.334	0.	0.	0.	1.829	1.00004	1.225	1.00001	0.	1.000000	0.435240E 00	0.	11.0	0.02180	0.04517	0.05853
6	5.54	0.442	0.716	0.902	0.756	2.500	1.36681	1.361	1.11135	0.839	1.000000	0.557462E 01	0.	13.6	0.01496	0.04257	0.04781
7	0.	0.346	0.	0.	0.	2.500	1.00002	1.361	1.00001	0.	1.000000	0.680529E 01	0.	16.9	0.01472	0.04250	0.04105
8	3.44	0.434	0.652	0.977	0.817	3.443	1.37750	1.517	1.11461	0.836	1.000000	0.327878E 01	0.	19.4	0.00358	0.03917	0.02964
9	0.	0.440	0.	0.	0.	3.443	1.00002	1.517	1.00001	0.	1.000000	0.259826E 01	0.	22.8	0.00354	0.03916	0.02107
10	2.94	0.452	0.615	0.666	0.723	4.495	1.30533	1.661	1.09480	0.834	1.000000	0.541219E 01	0.	25.1	0.00479	0.03998	0.01776
11	0.	0.425	0.	0.	0.	4.495	1.00007	1.661	1.00002	0.	1.000000	0.512933E 01	0.	28.6	0.00470	0.03995	0.01974
12	1.61	0.427	0.580	0.735	0.605	5.551	1.23494	1.787	1.07548	0.823	1.000000	0.373670E 00	0.	30.7	0.00299	0.03965	0.01710
13	0.	0.476	0.	0.	0.	5.551	1.00008	1.787	1.00002	0.	1.000000	0.524627E 01	0.	33.9	0.00286	0.03961	0.01384
14	3.77	0.360	0.538	0.569	0.466	6.479	1.16720	1.885	1.05515	0.819	1.000000	0.816423E 00	0.	35.7	0.00215	0.03954	0.01198
15	0.	0.424	0.	0.	0.	6.480	1.00000	1.885	1.00000	0.	1.000000	0.627560E 01	0.	38.8	0.00210	0.03953	0.01028
16	2.34	0.393	0.492	0.605	0.492	7.569	1.16819	1.990	1.05582	0.814	1.000000	0.653471E 00	0.	40.4	0.00222	0.03828	0.00668
17	0.	0.603	0.	0.	0.	7.570	1.00012	1.990	1.00004	0.	1.000000	0.375024E 01	0.	42.4	0.00245	0.03822	0.00230
18	0.	0.984	0.	0.	0.	7.570	1.00000	1.990	1.00000	0.	1.000000	0.233653E 00	0.	42.7	0.00243	0.03822	0.00214

(b) Sector 2.

Table 28. Calculated Performance, Total-Temperature Distortion (RDG 138), "Mehalic" Engine 99.6% $N/\sqrt{\theta}$ (Concluded).

DYNAMIC PARALLEL COMPRESSOR ANALYSIS

J85-13 NAS3-18526, TT-DIST MEHALIC ENG., RDG 138
THROTTLING SIMULATION

WCORR=19.504 PCTNC= 99.56 P/P-0A=7.5610

SECTOR= 2	PCTNCL= 98.67	ANGLE=180.00
TIME STEP= 0	TALC#=19.111	P/P-0A(L)=7.55185
TIME=0.	EXIT FF= 0.1703	T/T-0A(L)=1.99432
DPTR-IN=0.	DTTR-IN=0.03628	DPSR-IN=0.01278

ROW	CZ1	CU1	WU1	CT	WT	U1	M-ABS	M-REL	ALPHA	BETA	PS1	PT1	TS1	TT1	TNI	INC	LOSS	TND
1	143.0	0.	0.	143.0	0.	0.	0.4218	0.	0.	0.	5.13	6.92	286.0	296.2	0.	0.	0.	0.
2	193.8	0.	275.4	193.4	336.7	275.4	0.5805	1.0084	0.	54.86	5.51	6.92	277.5	296.2	0.05868	3.36	0.0995	0.10770
3	192.4	107.0	0.	211.5	0.	0.	0.6053	0.	30.38	0.	7.21	9.24	303.8	326.1	-0.07798	-4.46	0.	0.
4	203.4	19.2	266.3	204.3	335.1	285.6	0.5832	0.9568	5.40	52.63	7.33	9.23	335.3	326.0	0.04252	2.43	0.1492	0.07549
5	191.8	157.0	0.	248.4	0.	0.	0.6767	0.	39.46	0.	9.52	12.94	335.3	366.0	-0.01963	-1.12	0.	0.
6	195.7	42.0	252.7	200.1	319.6	294.7	0.5366	0.8571	12.10	52.25	10.64	12.94	346.1	366.0	0.02096	1.20	0.1412	0.12260
7	185.9	175.2	0.	255.5	0.	0.	0.6597	0.	43.30	0.	13.12	17.56	373.3	405.7	-0.04152	-2.38	0.	0.
8	190.1	50.2	252.5	196.6	316.1	302.8	0.4989	0.8021	14.80	53.03	14.82	17.56	386.5	405.7	0.03877	2.22	0.1669	0.08104
9	182.7	198.1	0.	269.3	0.	0.	0.6603	0.	47.31	0.	17.85	23.92	414.6	450.7	0.01589	0.91	0.	0.
10	183.3	64.6	244.2	194.3	305.3	308.7	0.4665	0.7329	19.40	53.10	23.61	23.92	431.9	450.7	0.04972	-2.85	0.1701	0.04866
11	178.0	203.3	0.	270.2	0.	0.	0.6302	0.	48.79	0.	23.93	31.27	457.5	493.8	0.04820	2.76	0.	0.
12	175.4	75.2	237.8	190.9	295.5	312.9	0.4386	0.6758	23.20	53.58	27.43	31.26	475.7	493.8	-0.02137	-1.22	0.1648	0.01939
13	170.5	193.6	0.	258.0	0.	0.	0.5769	0.	48.62	0.	30.76	38.54	497.8	531.0	0.06497	3.72	0.	0.
14	154.3	67.2	248.2	178.3	297.9	315.4	0.3912	0.6547	22.20	56.42	34.68	38.54	515.2	530.9	0.02278	1.31	0.1328	0.07512
15	157.3	160.2	0.	224.6	0.	0.	0.4343	0.	45.52	0.	38.29	44.75	535.1	560.2	0.03022	1.73	0.	0.
16	151.5	60.0	256.1	163.0	297.6	316.1	0.3478	0.6348	21.60	59.38	41.35	44.95	547.0	560.2	0.11285	6.44	0.1434	0.05343
17	144.2	136.9	0.	213.2	0.	0.	0.4461	0.	47.42	0.	45.61	52.29	568.1	590.7	0.09305	5.32	0.	0.
18	130.2	23.0	0.	133.2	0.	0.	0.2359	0.	9.58	0.	49.40	52.28	581.2	590.7	-0.00000	-0.00	0.	0.

ROW	DEV	DFACT	PHI	PSI	PSI-P	PR1	PR2	TR1	TR2	AD-EF	W2/W1	DWX	DW/DWEX	ROT	DPTR2	DTTR2	DPSR2
1	0.	-0.217	0.	0.	0.	1.000	1.00000	1.000	1.00000	0.	1.000000	0.707618E 01	0.	0.	0.00000	0.03628	0.02208
2	6.15	0.392	0.734	0.722	0.675	1.334	1.33446	1.101	1.10086	0.852	1.000000	0.347209E 00	0.	2.9	0.02448	0.04450	0.04126
3	0.	0.228	0.	0.	0.	1.334	0.99962	1.101	0.99989	0.	1.000000	0.457299E 01	0.	5.8	0.02410	0.04439	0.07486
4	4.32	0.479	0.712	0.986	0.813	1.869	1.40094	1.236	1.12267	0.824	1.000000	0.935896E 00	0.	8.7	0.02172	0.04514	0.05024
5	0.	0.335	0.	0.	0.	1.869	1.00012	1.236	1.00003	0.	1.000000	0.178021E 00	0.	12.2	0.02180	0.04517	0.05853
6	[illegible]	0.451	0.664	0.717	0.773	2.537	1.35750	1.370	1.10847	0.841	1.000000	0.429788E 01	0.	14.8	0.01496	0.04257	0.04781
7	0.	0.402	0.	0.	0.	2.537	0.99978	1.370	0.99994	0.	1.000000	0.597243E 01	0.	18.2	0.01472	0.04250	0.04105
8	4.63	0.500	0.628	0.966	0.821	3.456	1.36225	1.522	1.11090	0.833	1.000000	0.924990E 00	0.	20.8	0.00358	0.03917	0.02964
9	0.	0.455	0.	0.	0.	3.455	0.99998	1.522	0.99999	0.	1.000000	0.313773E 01	0.	24.3	0.00354	0.03916	0.02107
10	[illegible]	0.473	0.594	0.909	0.755	4.516	1.30696	1.667	1.09570	0.831	1.000000	0.517937E 01	0.	26.7	0.00479	0.03998	0.01776
11	0.	0.457	0.	0.	0.	4.516	0.99998	1.667	1.00000	0.	1.000000	0.387288E 01	0.	30.3	0.00470	0.03995	0.01974
12	1.11	0.447	0.561	0.762	0.625	5.568	1.23284	1.793	1.07515	0.820	1.000000	0.295750E 00	0.	32.4	0.00299	0.03965	0.01710
13	0.	0.476	0.	0.	0.	5.567	0.99994	1.793	0.99998	0.	1.000000	0.464766E 01	0.	35.7	0.00286	0.03961	0.01384
14	4.30	0.374	0.522	0.591	0.462	6.493	1.16637	1.891	1.05508	0.816	1.000000	0.658175E 00	0.	37.5	0.00215	0.03954	0.01198
15	0.	0.445	0.	0.	0.	6.493	0.99996	1.891	0.99999	0.	1.000000	0.528479E 01	0.	40.6	0.00210	0.03953	0.01028
16	5.05	0.400	0.460	0.614	0.497	7.552	1.16314	1.994	1.05451	0.810	1.000000	0.585375E 00	0.	42.3	0.00222	0.03828	0.00668
17	0.	0.612	0.	0.	0.	7.552	0.99992	1.994	0.99998	0.	1.000000	0.329637E 01	0.	44.3	0.00243	0.03822	0.00230
18	0.	0.084	0.	0.	0.	7.552	1.00000	1.994	1.00000	0.	1.000000	0.174375E 00	0.	44.6	0.00243	0.03822	0.00214

APPENDIX F

COMBINED TOTAL-PRESSURE AND TOTAL-TEMPERATURE DISTORTION DOCUMENTATION

Sample radial and circumferential profiles of the 180°, 1/rev total-pressure and total-temperature distortions as taken from the NASA data for the opposed, coincident, and 90° overlapped orientations are presented in Figures 88 through 90. The normalizing parameters and NASA test reading numbers are indicated on the plots.

Figures 91 and 92 represent the opposed orientation, Figure 93 the coincident orientation, and Figures 94 and 95 represent the 90° overlapped orientation with the operating points of each of the parallel compressor sectors shown on each figure. The local corrected speeds of each sector are also indicated on the maps.

Table 29 illustrates the type of documentation that is available as model output, in this case, for the "Mehalic" engine 100 percent corrected flow condition.

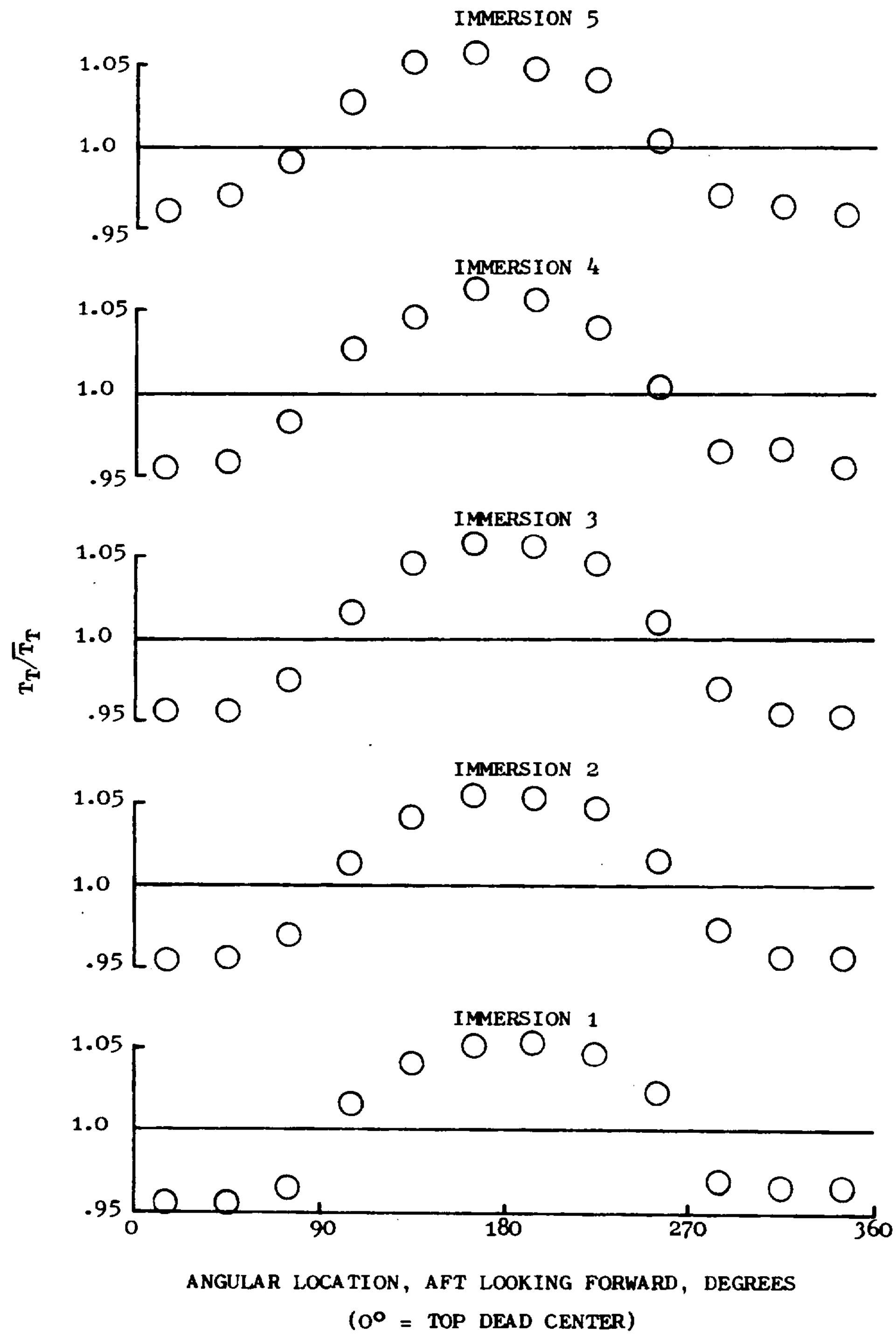

(a) Circumferential Temperature Profiles.

Figure 88. Combined Circumferential Total-Pressure and Total-Temperature Distortion Profiles, Opposed Orientation (RDG 479), "Mehalic" Engine 92.5% $N/\sqrt{\theta}$.

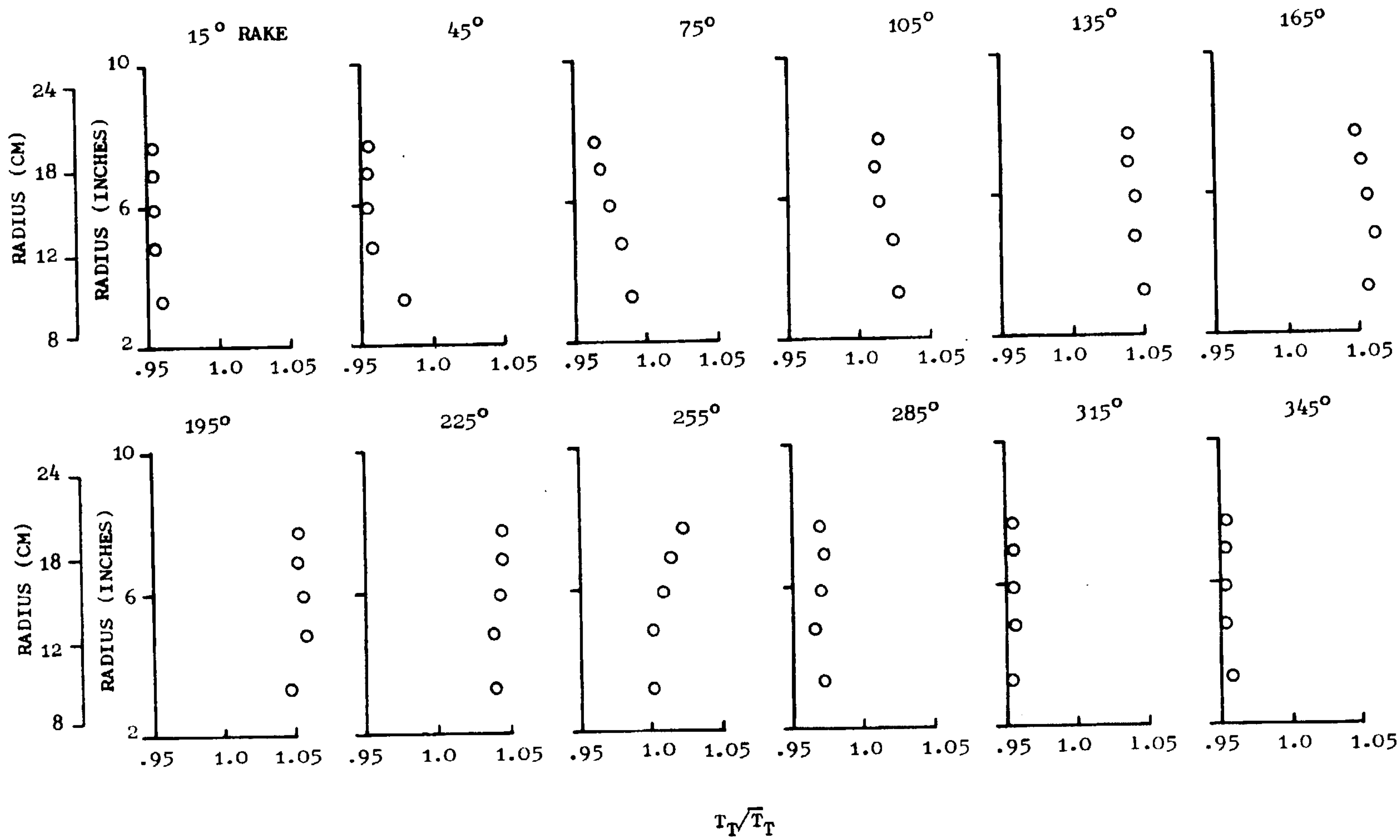

(b) Radial Temperature Profiles.

Figure 88. Combined Circumferential Total-Pressure and Total-Temperature Distortion Profiles, Opposed Orientation (RDG 479), "Mehalic" Engine 92.5% $N/\sqrt{\theta}$ (Continued).

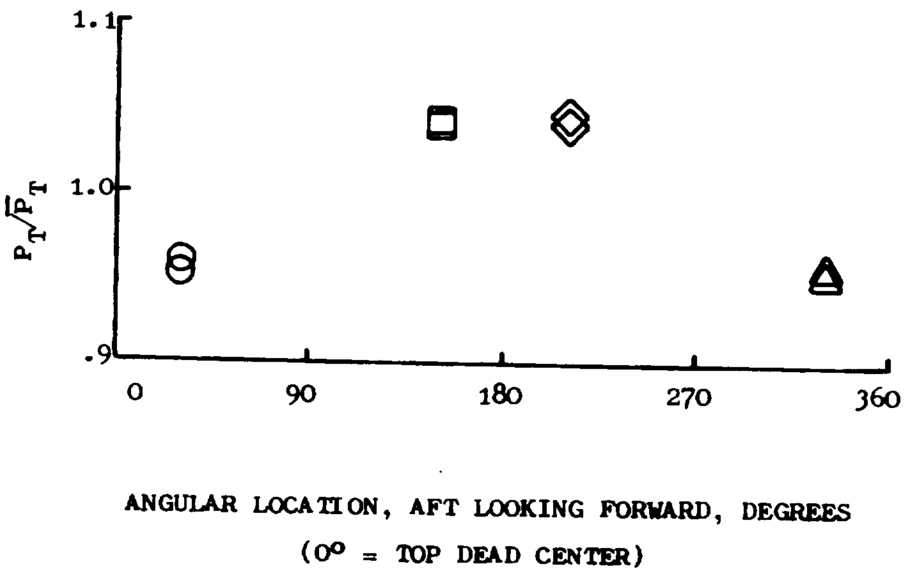

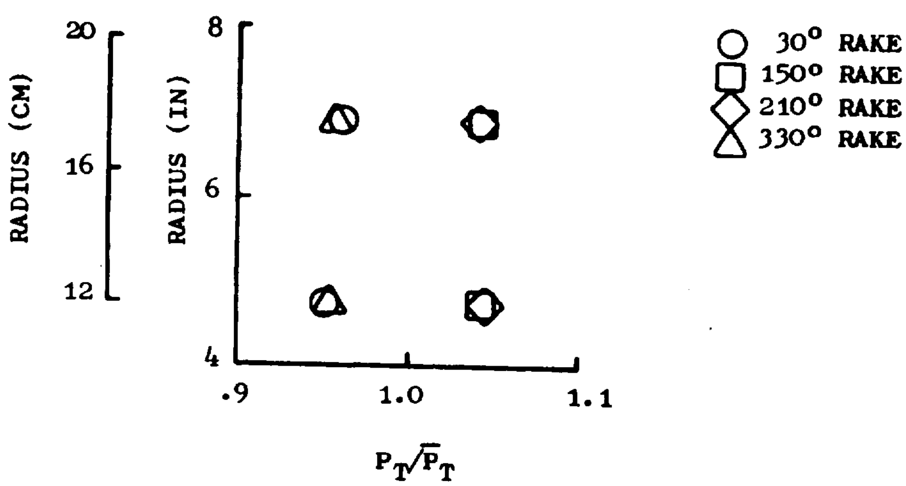

(c) Pressure Profiles.

Figure 88. Combined Circumferential Total-Pressure and Total-Temperature Distortion Profiles, Opposed Orientation (RDG 479), "Mehalic" Engine 92.5% $N/\sqrt{\theta}$ (Concluded).

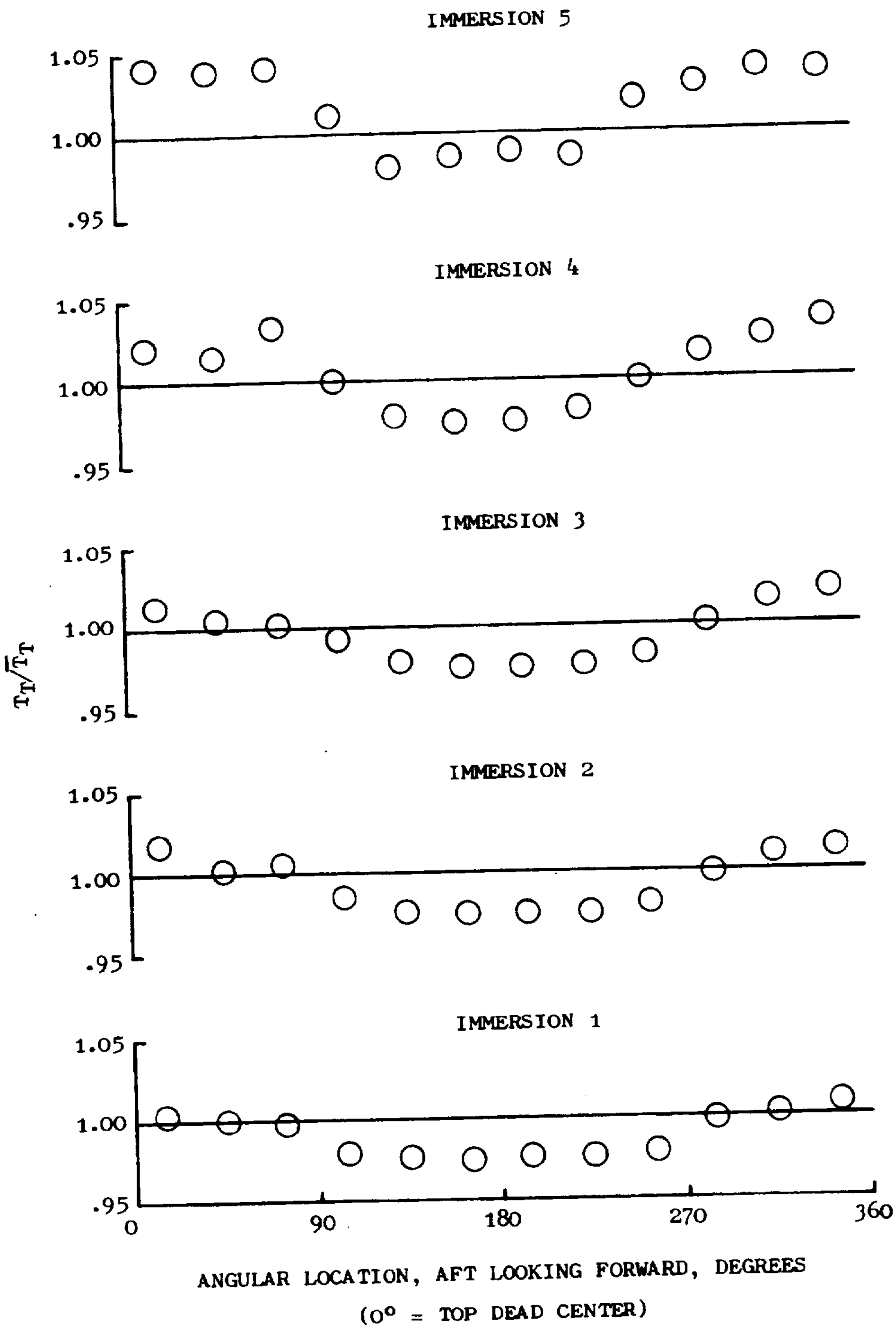

(a) Circumferential Temperature Profiles.

Figure 89. Combined Circumferential Total-Pressure and Total-Temperature Distortion Profiles, Coincident Orientation (RDG 423), "Mehalic" Engine 99.1% $N/\sqrt{\theta}$.

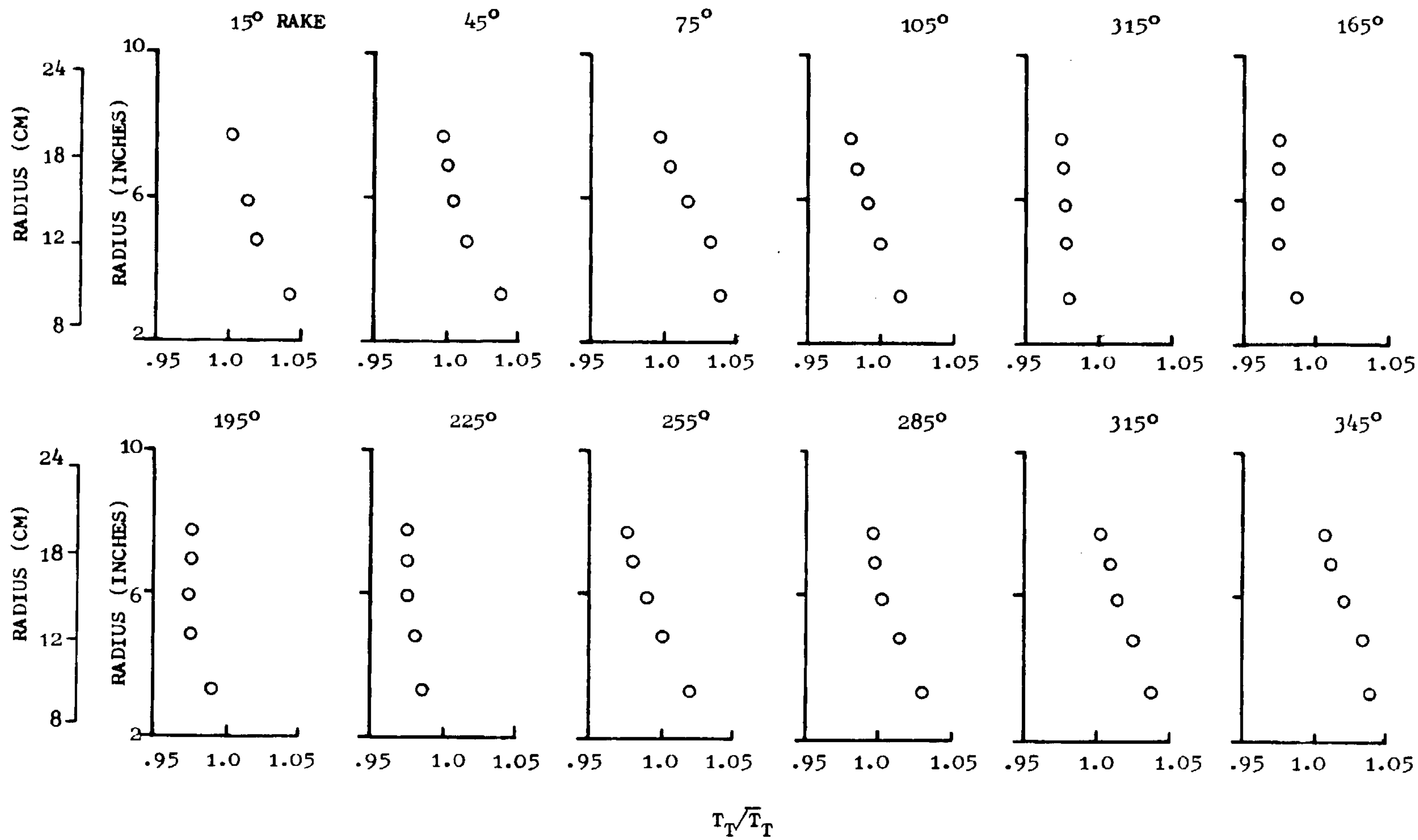

(b) Radial Temperature Profiles.

Figure 89. Combined Circumferential Total-Pressure and Total-Temperature Distortion Profiles, Coincident Orientation (RDG 423), "Mehalic" Engine 99.1% $N/\sqrt{\theta}$ (Continued).

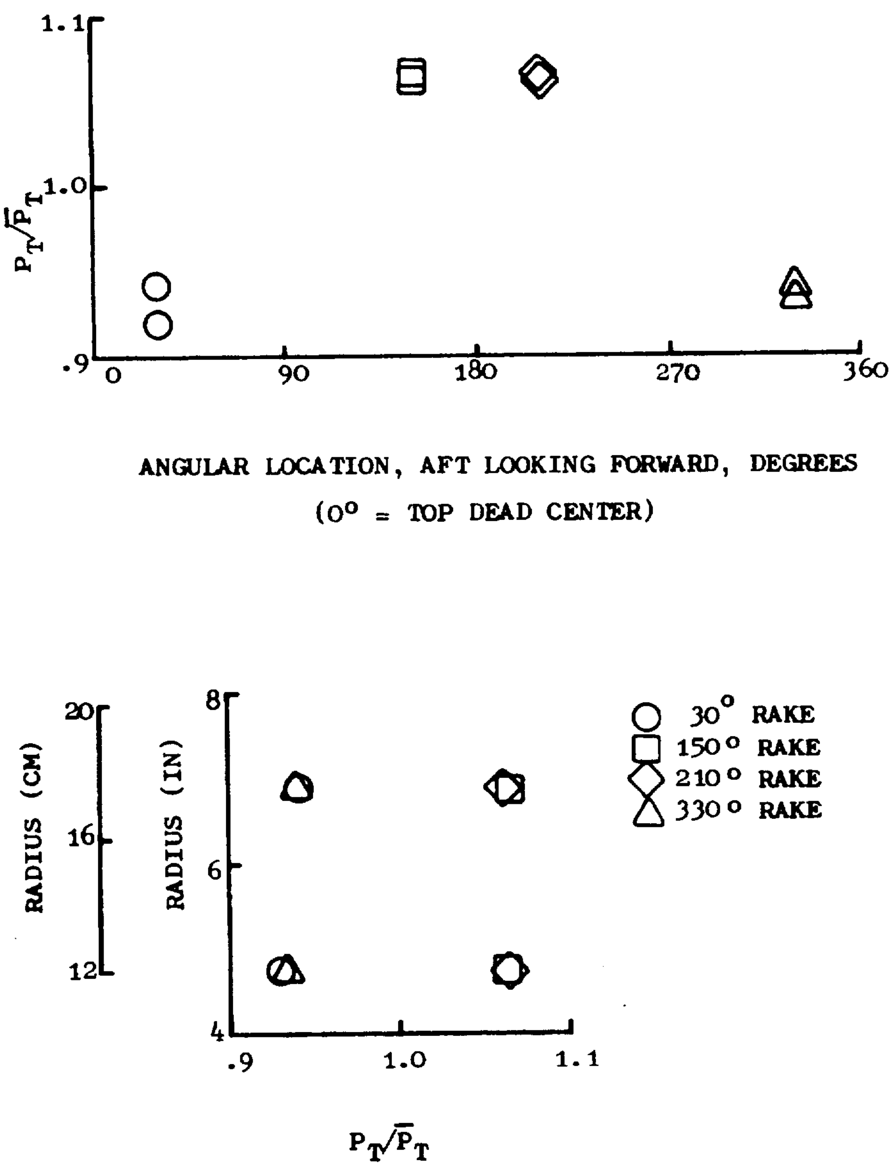

(c) Pressure Profiles.

Figure 89. Combined Circumferential Total-Pressure and Total-Temperature Distortion Profiles, Coincident Orientation (RDG 423), "Mehalic" Engine 99.1% $N/\sqrt{\theta}$ (Concluded).

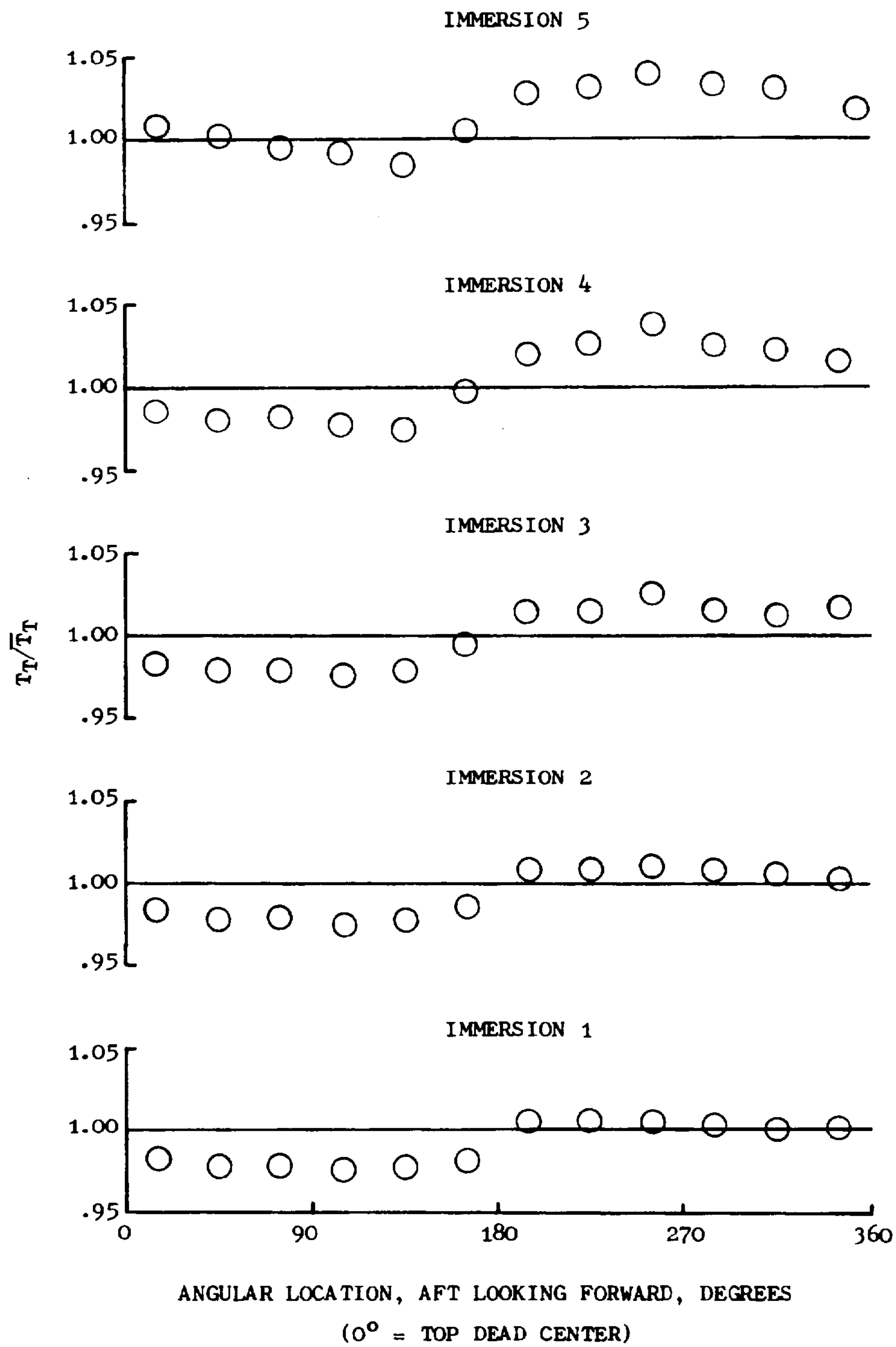

(a) Circumferential Temperature Profiles.
Figure 90. Combined Circumferential Total-Pressure and Total-Temperature Distortion Profiles, 90° Overlapped Orientation (RDG 420), "Mehalic" Engine 99.0% $N/\sqrt{\theta}$.

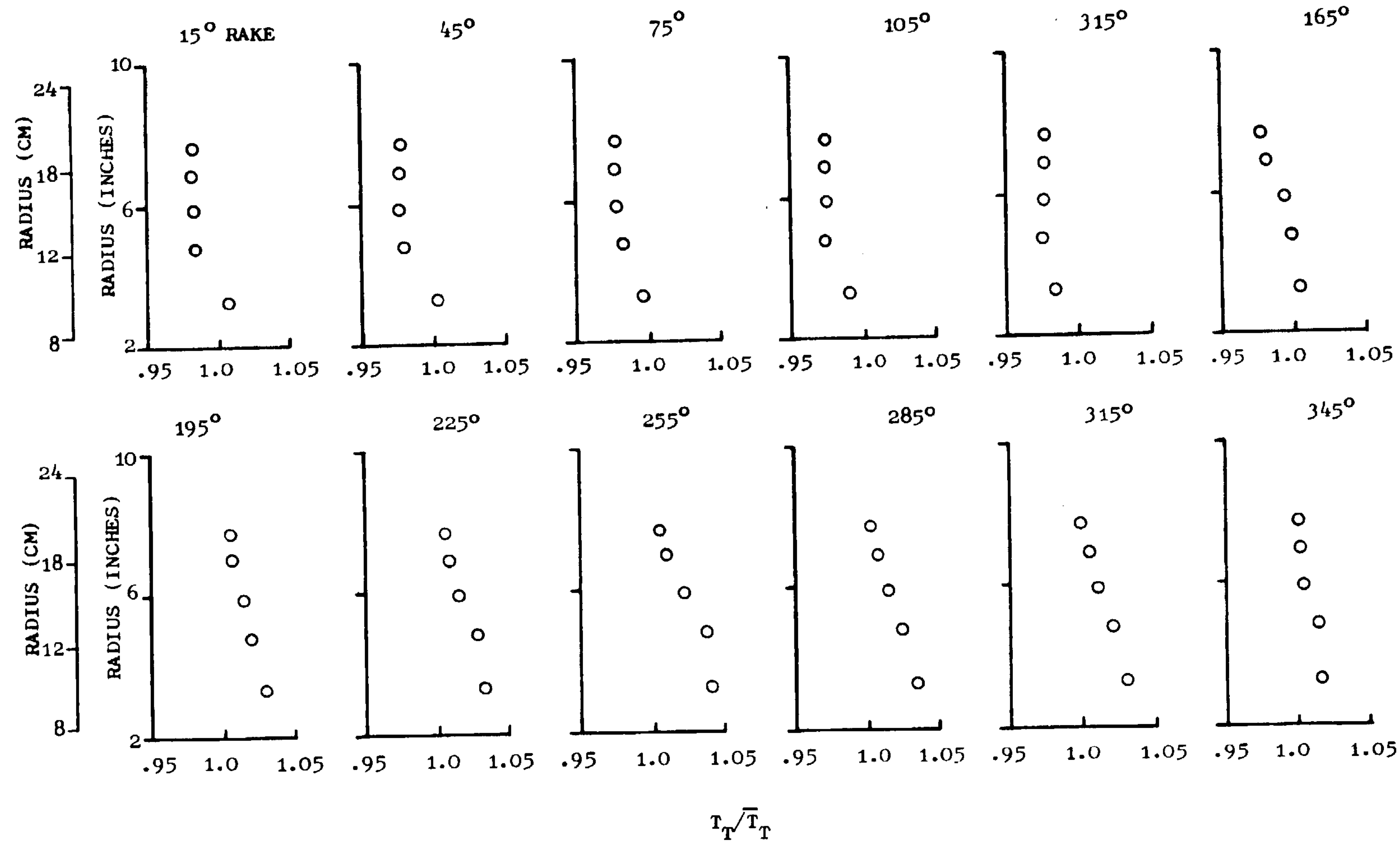

(b) Radial Temperature Profiles.

Figure 90. Combined Circumferential Total-Pressure and Total-Temperature Distortion Profiles, 90° Overlapped Orientation (RDG 420), "Mehalic" Engine 99.0% $N/\sqrt{\theta}$ (Continued).

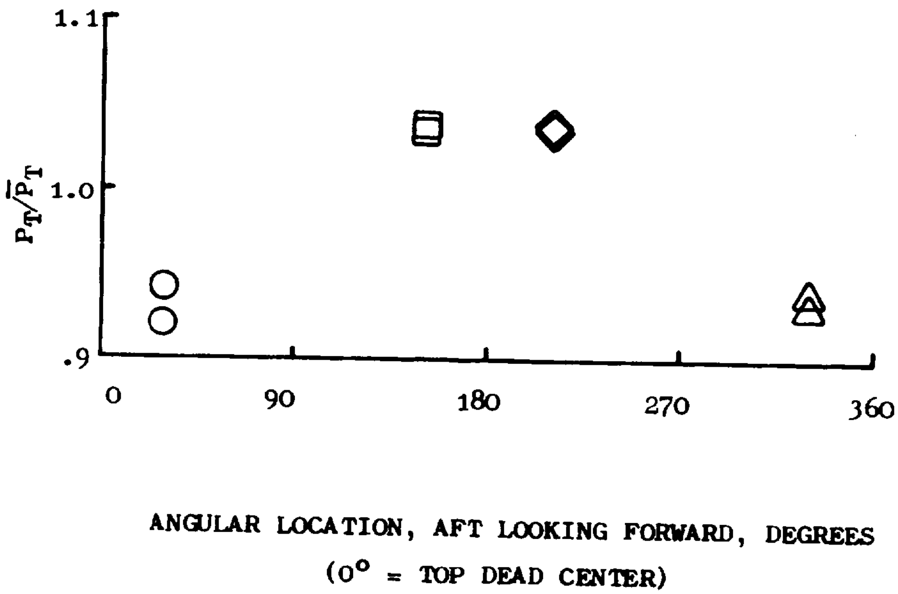

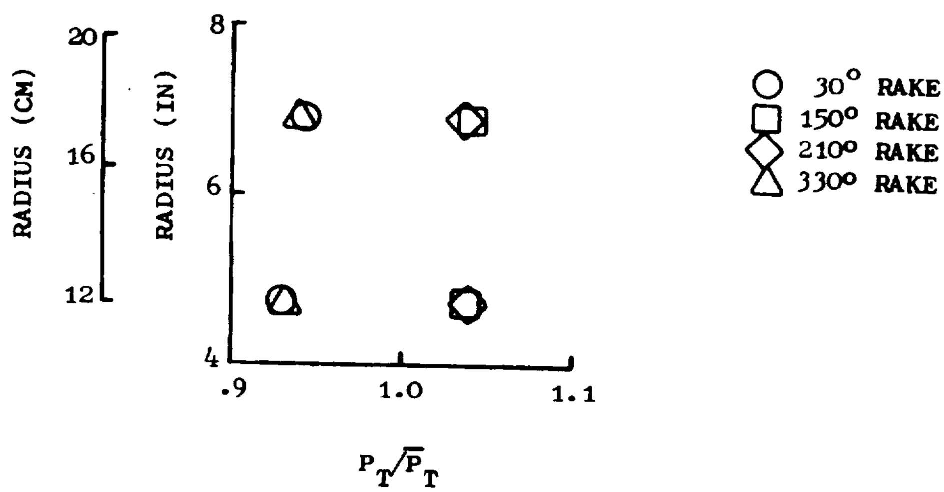

(c) Pressure Profiles.

Figure 90. Combined Circumferential Total-Pressure and Total-Temperature Distortion Profiles, 90° Overlapped Orientation (RDG 420), "Mehalic" Engine 99.0% $N/\sqrt{\theta}$ (Concluded).

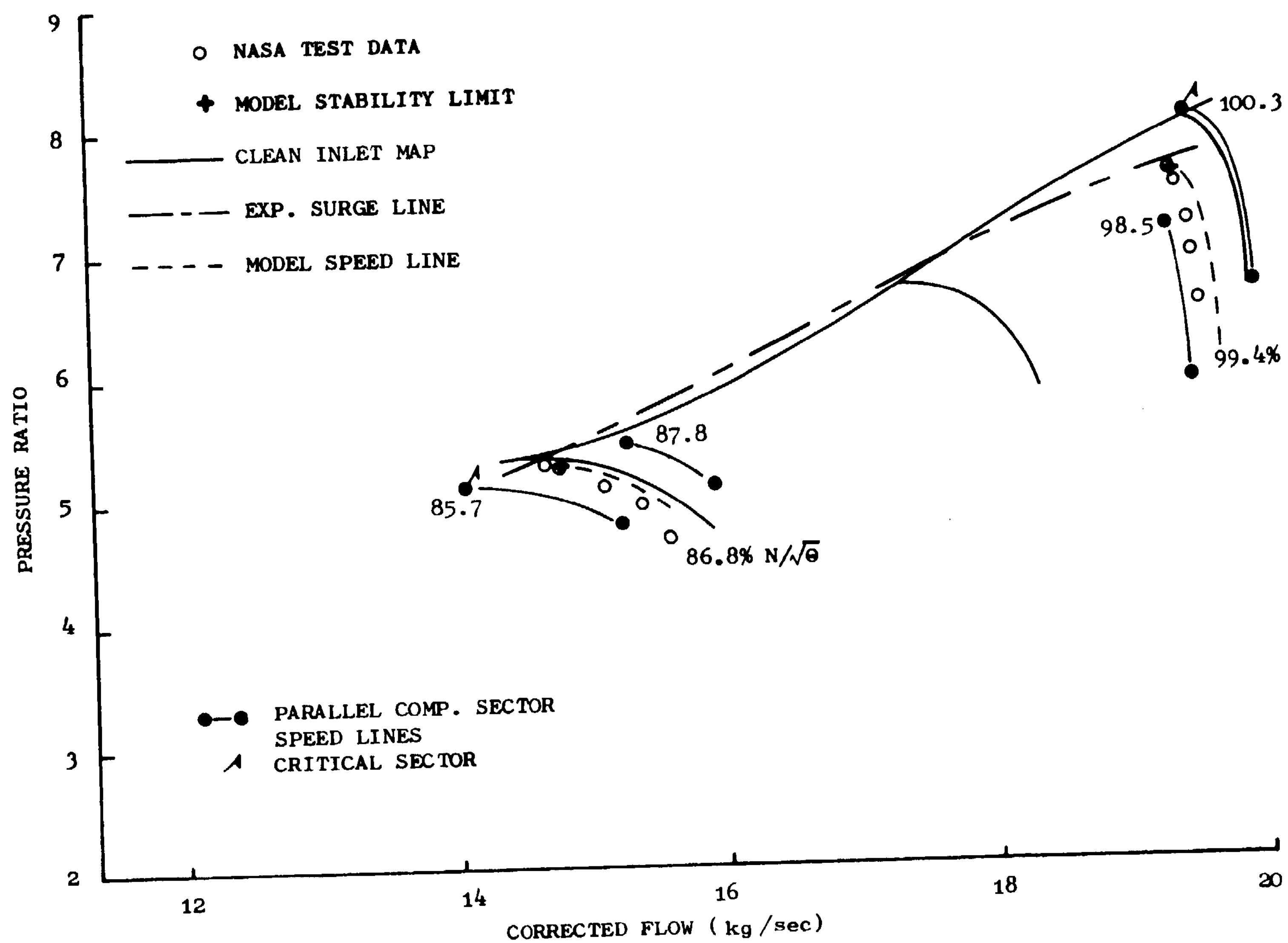

Figure 91. Effect of 180°, 1/Rev Combined Total-Pressure and Total-Temperature Distortion, Opposed Orientation Low Total-Temperature Distortion on Surge Line of "Mehalic" Engine - Sector Performance.

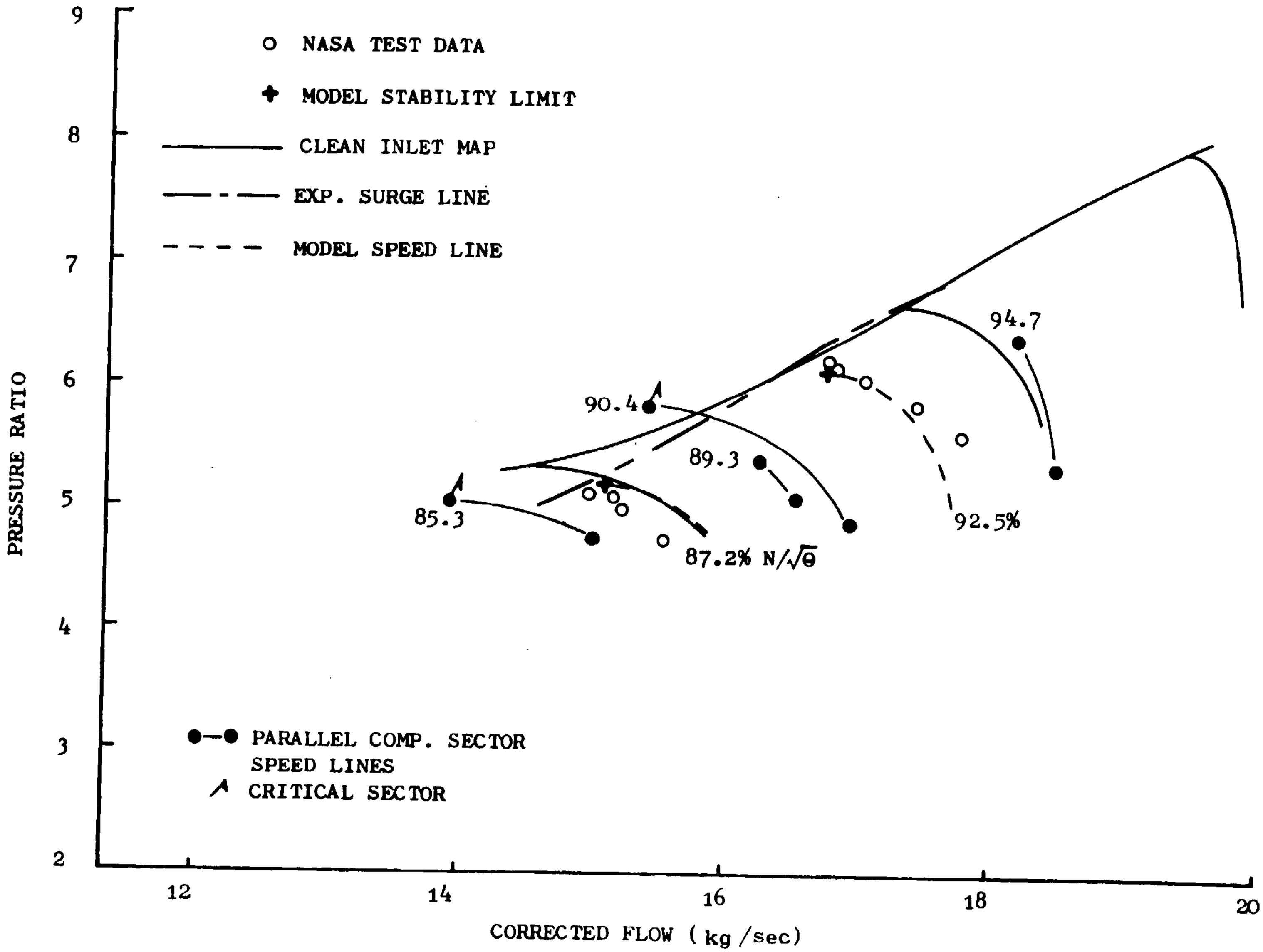

Figure 92. Effect of 180°, 1/Rev Combined Total-Pressure and Total-Temperature Distortion, Opposed Orientation Moderate Total-Temperature Distortion on Surge Line of "Mehalic" Engine - Sector Performance.

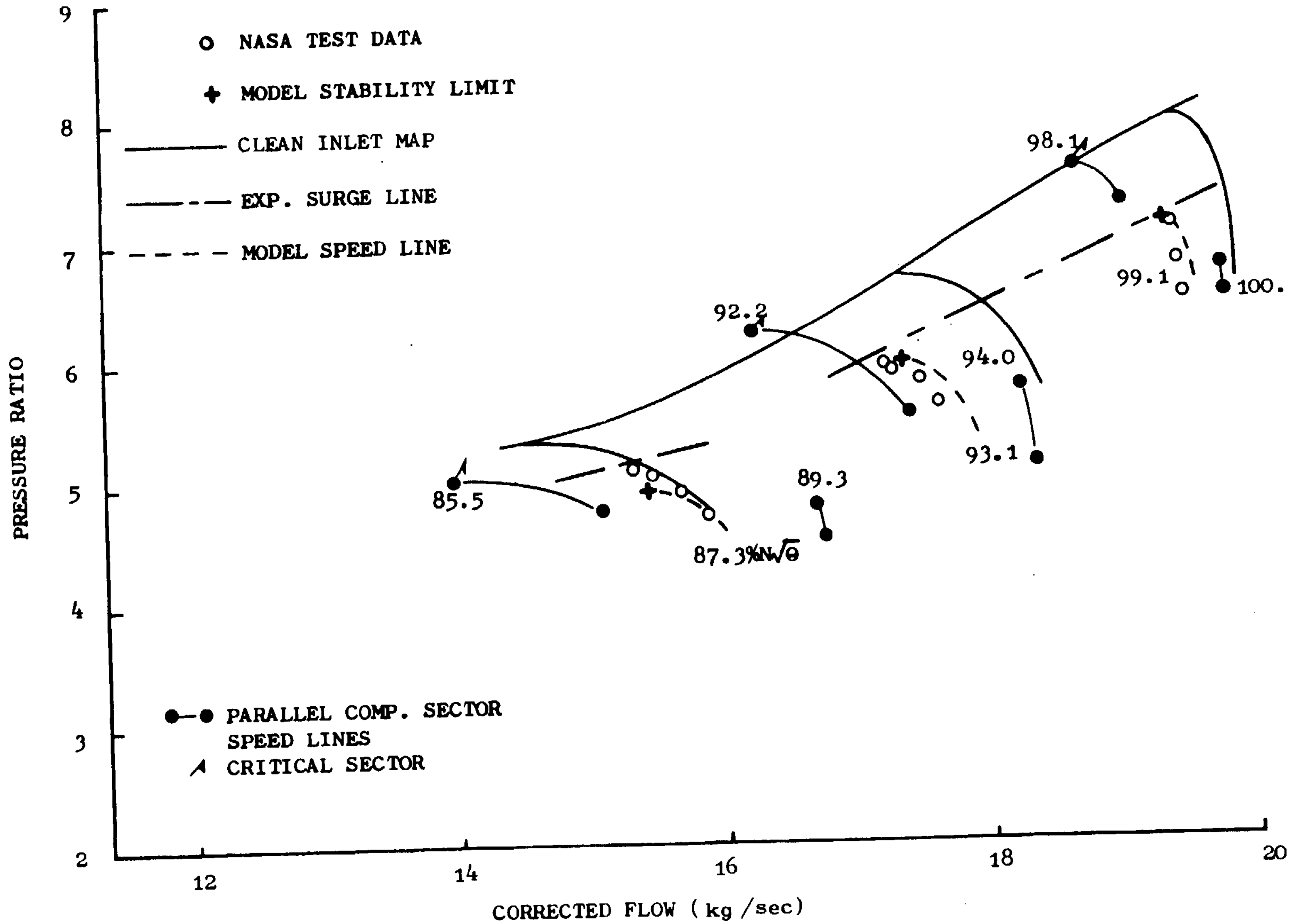

Figure 93. Effect of 180°, 1/Rev Combined Total-Pressure and Total-Temperature Distortion, Coincident Orientation on Surge Line of "Mehalic" Engine - Sector Performance.

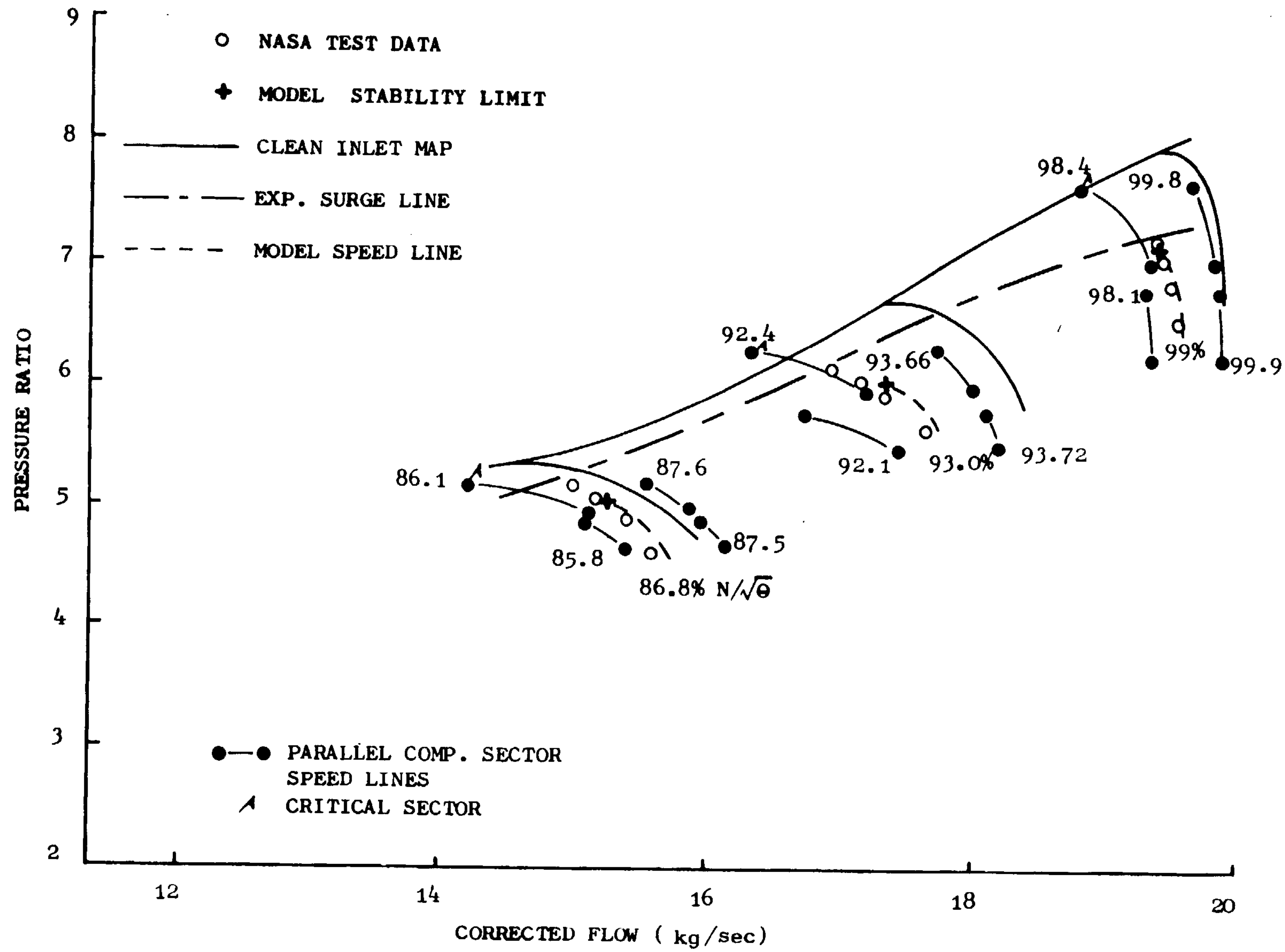

Figure 94. Effect of 180°, 1/Rev Combined Total-Pressure and Total-Temperature Distortion, 90° Overlapped Orientation Low Total-Temperature Distortion on Surge Line of "Mehalic" Engine - Sector Performance.

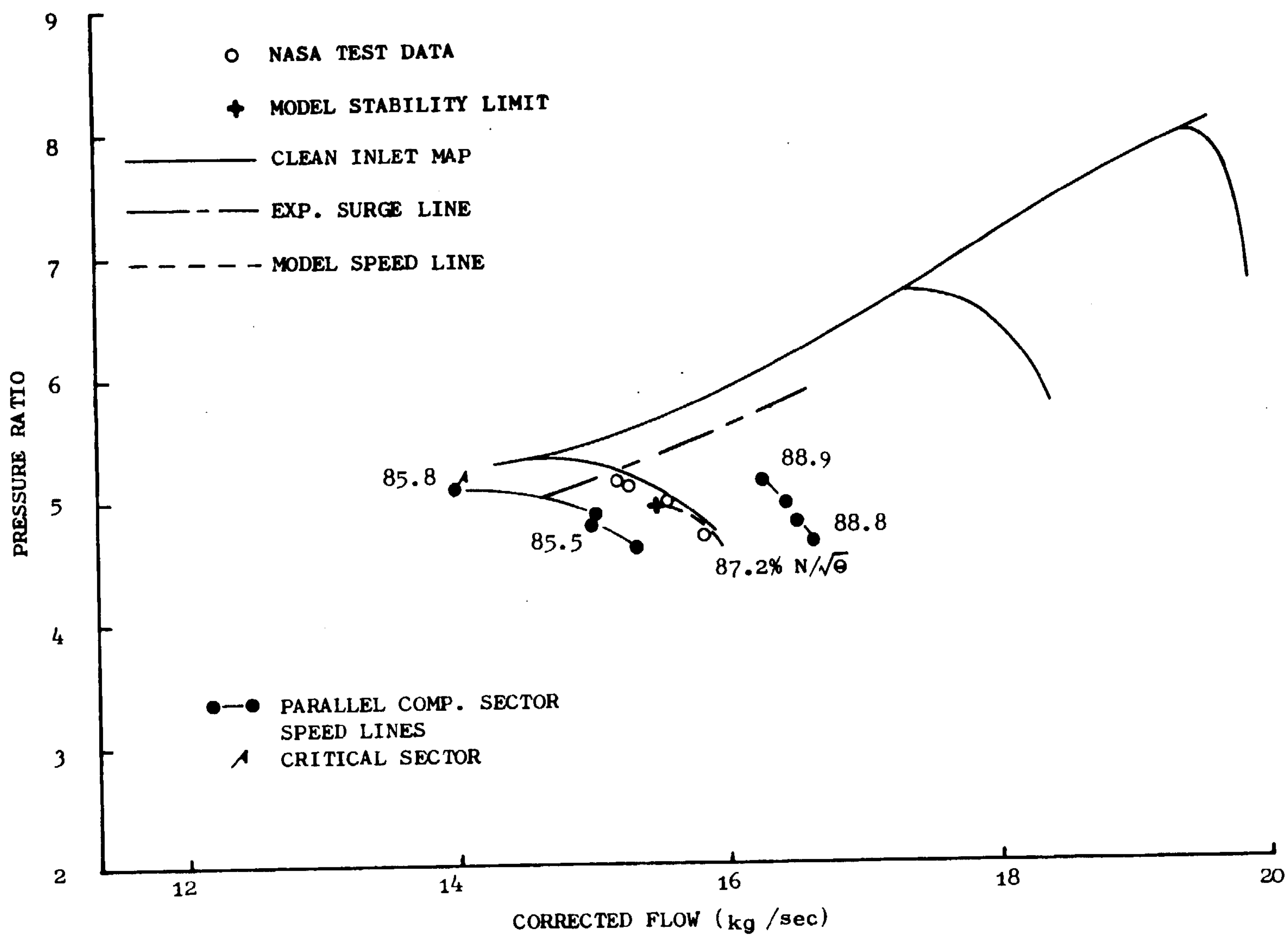

Figure 95. Effect of 180°, 1/Rev Combined Total-Pressure and Total-Temperature Distortion, 90° Overlapped Orientation Moderate Total-Temperature Distortion on Surge Line of "Mehalic" Engine - Sector Performance.

(a) Sector 1.

Table 29. Calculated Performance, Combined Total-Pressure and Total-Temperature Distortion (RDG 420), "Mehalic" Engine 99.0% $N/\sqrt{\theta}$.

DYNAMIC PARALLEL COMPRESSOR ANALYSIS

J85-13 NAS3-18528 OOMD-DIST 90 OVERLAP, MEH EQG RDG 420
THROTTLING SIMULATION

WCORR=19.391	PCTNC= 99.03	P/P-0A=7.1496
SECTOR= 1	PCTNCL= 98.62	ANGLE= 90.00
TIME STEP= 0	TALCW=19.261	R/R-3A(L)=6.74191
TIME=0.	EXIT FF= 6.4267	T/T-3A(L)=1.89836
DPTR-IN=0.12716	DTTR-IN=0.03518	DPSR-IN=0.13282

ROW	CZ1	CU1	WU1	CT	WT	U1	M-ABS	M-REL	ALPHA	BETA	PS1	PT1	TS1	TT1	TRI	INC	LOSS	TND
1	145.1	0.	0.	145.1	0.	0.	0.4260	0.	0.	0.	6.97	7.90	288.7	299.2	0.	0.	0.	0.
2	197.1	0.	275.2	197.1	338.5	275.2	0.5879	1.0095	0.	54.39	6.25	7.90	279.8	299.2	0.05041	2.59	0.0867	0.11144
3	186.1	102.0	0.	212.2	0.	0.	0.6060	0.	28.72	0.	8.13	10.41	305.2	327.6	-0.00729	-6.12	0.	0.
4	209.3	19.8	265.6	210.2	338.1	285.4	0.5999	0.9649	5.40	51.76	8.16	10.41	305.6	327.6	0.02728	1.56	0.1198	0.07801
5	196.5	147.9	0.	245.9	0.	0.	0.6707	0.	36.97	0.	10.61	14.34	334.6	364.7	-0.06306	-3.61	0.	0.
6	203.8	43.7	250.8	208.4	383.2	294.5	0.5612	0.8703	12.10	50.91	11.58	14.35	343.1	364.7	-0.00240	-0.14	0.1244	0.12344
7	193.2	170.0	0.	257.4	0.	0.	0.6679	0.	41.34	0.	14.29	19.27	369.5	402.4	-0.07589	-4.34	0.	0.
8	199.2	52.6	250.0	206.0	319.6	302.6	0.5263	0.8165	14.80	51.45	15.96	19.27	381.3	402.4	0.01116	0.64	0.1464	0.05814
9	190.3	196.7	0.	273.7	0.	0.	0.6751	0.	45.94	0.	19.35	26.25	409.0	446.3	-0.00797	-0.46	0.	0.
10	191.3	67.4	241.2	202.8	307.8	308.5	0.4902	0.7442	19.40	51.59	22.28	26.25	425.8	446.3	-0.07633	-4.36	0.1438	0.07321
11	186.0	192.0	0.	267.3	0.	0.	0.6289	0.	45.91	0.	25.74	33.61	449.5	485.1	-0.00207	-0.12	0.	0.
12	185.9	79.7	233.1	202.3	298.1	312.8	0.4681	0.6899	23.20	51.42	28.92	33.61	464.7	485.1	-0.05913	-3.38	0.1307	0.03093
13	181.0	183.0	0.	257.4	0.	0.	0.5832	0.	45.31	0.	32.28	40.64	484.5	517.5	0.00711	0.41	0.	0.
14	176.6	72.1	243.1	190.8	380.5	315.2	0.4259	0.6708	22.20	54.00	35.88	40.68	499.4	517.5	-0.01936	-1.11	0.1045	0.05576
15	169.1	151.5	0.	227.1	0.	0.	0.4982	0.	41.84	0.	39.36	46.63	516.8	542.5	-0.03398	-1.95	0.	0.
16	163.9	64.9	251.0	176.3	299.8	315.9	0.3832	0.6515	21.60	56.85	42.14	46.63	527.0	542.5	0.06834	3.91	0.1106	0.04629
17	156.5	145.6	0.	213.8	0.	0.	0.4868	0.	42.94	0.	46.14	53.24	545.2	567.9	0.01461	0.84	0.	0.
18	148.6	25.1	0.	150.7	0.	0.	0.3186	0.	9.58	0.	49.63	53.24	556.6	567.9	-0.00000	-0.00	0.	0.

ROW	DEV	DFACT	PHI	PSI	PSI-P	PR1	PR2	TR1	TR2	AD-EF	W2/W1	DWX	DW/DBEX	ROT	DPTR2	DTTR2	DPSR2
1	0.	-0.218	0.	0.	0.	1.000	1.00000	1.000	1.00000	0.	1.000000	0.425557E 01	0.	0.	0.12716	0.03518	0.13691
2	6.36	0.371	0.716	0.756	0.653	1.319	1.31864	1.095	1.09517	0.864	1.000000	0.651382E 00	0.	2.7	0.13022	0.04246	0.13960
3	0.	0.190	0.	0.	0.	1.318	0.99971	1.095	0.99992	0.	1.000000	0.874501E 00	0.	5.5	0.12992	0.04236	0.14714
4	5.60	0.442	0.733	0.914	0.275	1.816	1.37753	1.219	1.11311	0.847	1.000000	0.568682E 00	0.	8.2	0.11034	0.05030	0.13354
5	0.	0.325	0.	0.	0.	1.816	1.00026	1.219	1.00008	0.	1.000000	0.226182E 00	0.	11.5	0.11043	0.05028	0.11405
6	7.04	0.432	0.692	0.874	0.744	2.440	1.34357	1.345	1.10345	0.851	1.000000	0.288123E 01	0.	14.0	0.09483	0.05183	0.10769
7	0.	0.366	0.	0.	0.	2.440	0.99991	1.345	0.99997	0.	1.000000	0.112014E 00	0.	17.3	0.09477	0.05173	0.09115
8	3.90	0.478	0.658	0.963	0.816	3.324	1.36227	1.492	1.10899	0.847	1.000000	0.126695E 01	0.	19.8	0.09354	0.04915	0.09004
9	0.	0.427	0.	0.	0.	3.324	0.99998	1.492	0.99999	0.	1.000000	0.231901E 01	0.	23.2	0.09349	0.04914	0.08288
10	4.19	0.426	0.620	0.819	0.689	4.255	1.28005	1.621	1.08698	0.840	1.000000	0.466079E 01	0.	25.5	0.06998	0.05799	0.07585
11	0.	0.388	0.	0.	0.	4.255	1.00002	1.621	1.00001	0.	1.000000	0.457575E 01	0.	28.9	0.06991	0.05797	0.05556
12	1.77	0.384	0.595	0.668	0.556	5.146	1.20941	1.730	1.06680	0.856	1.000000	0.310974E 00	0.	31.9	0.04755	0.06595	0.04982
13	0.	0.422	0.	0.	0.	5.147	1.00003	1.730	1.00001	0.	1.000000	0.435988E 01	0.	34.0	0.04749	0.06591	0.03166
14	3.76	0.316	0.560	0.705	0.419	5.904	1.14726	1.813	1.04826	0.830	1.000000	0.661219E 00	0.	36.6	0.02906	0.07261	0.02389
15	0.	0.367	0.	0.	0.	5.904	0.99996	1.813	0.99999	0.	1.000000	0.401018E 01	0.	38.6	0.02893	0.07263	0.01409
16	2.65	0.329	0.519	0.712	0.422	6.741	1.14175	1.898	1.04689	0.823	1.000000	0.634120E 00	0.	41.1	0.01008	0.07906	0.00716
17	0.	0.528	0.	0.	0.	6.742	1.00011	1.898	1.00003	0.	1.000000	0.261119E 01	0.	43.9	0.01030	0.07900	0.00999
18	0.	0.084	0.	0.	0.	6.742	1.00000	1.898	1.00000	0.	1.000000	0.168969E 00	0.	48.2	0.01030	0.07900	0.00930

(b) Sector 2.

Table 29. Calculated Performance, Combined Total-Pressure and Total-Temperature Distortion (RDG 420), "Mehalic" Engine 99.0% $N/\sqrt{\theta}$ (Continued).

DYNAMIC PARALLEL COMPRESSOR ANALYSIS

J85-13 NAS3-18526 COMB-DIST 90 OVERLAP, MEM ENG RDG 420
THROTTLING SIMULATION

WCORR=19.391   PCTNC= 99.03   P/P-OA=7.1496

SECTOR= 2   PCTNCL= 98.39   ANGLE= 90.00
TIME STEP= 0   TALCH=18.844   P/P-OA(L)=7.59703
TIME=0.   EXIT FF= 6.4267   T/T-OA(L)=2.01054
DPTR-IN=0.12718   DTTR-IN=0.03518   DPSR-IQ=0.13282

ROW	CZ1	CU1	WU1	CT	WT	U1	M-ABS	M-REL	ALPHA	BETA	PS1	PT1	TS1	TTS	TRI	INC	LOSS	TVD
1	140.9	0.	0.	140.9	0.	0.	0.4144	0.	0.	0.	6.18	6.95	287.6	297.5	0.	0.	0.	0.
2	190.2	0.	275.2	190.2	334.5	275.2	0.5676	0.9982	0.	55.35	5.59	6.95	279.5	297.5	0.06723	3.85	0.1095	0.10209
3	178.9	112.0	0.	211.1	0.	0.	0.6014	0.	32.05	0.	7.34	9.37	306.6	328.8	-0.04866	-2.79	0.	0.
4	197.8	15.7	266.7	198.7	332.0	285.4	0.5638	0.9421	5.40	53.43	7.54	9.36	309.1	328.8	0.05648	3.23	0.1655	0.07131
5	187.9	161.5	0.	247.8	0.	0.	0.6710	0.	40.67	0.	9.72	13.14	339.4	369.9	0.00155	0.09	0.	0.
6	190.8	40.9	253.6	195.2	317.4	294.5	0.5197	0.8451	12.10	53.04	10.93	13.14	350.9	369.9	0.03471	1.99	0.1517	0.12790
7	182.1	176.2	0.	253.4	0.	0.	0.6500	0.	44.05	0.	13.41	17.81	378.3	410.2	-0.02845	-1.53	0.	0.
8	186.1	49.2	253.4	192.5	314.4	302.6	0.4852	0.7925	14.80	53.70	15.16	17.80	391.7	410.2	0.05055	2.59	0.1784	0.08599
9	179.8	198.5	0.	267.8	0.	0.	0.6519	0.	47.83	0.	18.16	24.17	419.9	455.6	0.02498	1.43	0.	0.
10	180.4	63.5	245.0	191.3	304.3	308.5	0.4563	0.7258	19.40	53.63	20.95	24.18	437.4	455.6	-0.04055	-2.32	0.1804	0.04597
11	175.6	205.2	0.	270.1	0.	0.	0.6260	0.	49.44	0.	24.27	31.61	463.3	499.6	0.05967	3.41	0.	0.
12	172.8	74.1	238.7	188.0	294.7	312.8	0.4272	0.6696	23.20	54.09	27.88	31.61	482.0	499.6	-0.01236	-0.71	0.1737	0.02000
13	168.3	194.9	0.	257.5	0.	0.	0.5719	0.	49.19	0.	31.22	38.98	504.5	537.5	0.07499	4.29	0.	0.
14	162.5	66.3	240.9	175.5	297.3	315.2	0.3832	0.6490	22.20	56.85	35.22	38.97	522.1	537.5	0.03046	1.74	0.1392	0.07795
15	155.3	161.2	0.	223.8	0.	0.	0.4995	0.	46.08	0.	38.85	45.47	542.4	567.3	0.03957	2.27	0.	0.
16	149.6	59.2	256.7	160.9	297.1	315.9	0.3410	0.6295	21.60	59.76	41.95	45.46	554.4	567.3	0.11956	6.52	0.1488	0.05743
17	142.6	157.4	0.	212.3	0.	0.	0.4414	0.	47.83	0.	46.22	52.83	575.8	598.2	0.10026	5.73	0.	0.
18	134.7	22.7	0.	136.7	0.	0.	0.2809	0.	9.58	0.	50.81	52.82	588.9	598.2	-0.00000	-0.00	0.	0.

ROW	DEV	DFACT	PHI	PSI	PSI-P	PR1	PR2	TR1	TR2	AD-EF	W2/W1	DWX	DWZDFEX	RBT	DSTR2	DTTR2	DPSR2
1	0.	-0.214	0.	0.	0.	1.000	1.00000	1.000	1.00000	0.	1.000000	0.323552E-01	0.	0.	0.12716	0.03518	0.13591
2	5.83	0.413	0.691	0.938	0.701	1.347	1.34704	1.105	1.10516	0.845	1.000000	0.691190E-01	0.	3.0	0.13022	0.04246	0.13960
3	0.	0.266	0.	0.	0.	1.346	0.99945	1.105	0.99984	0.	1.000000	0.151712E 00	0.	6.2	0.12992	0.04236	0.14714
4	4.08	0.495	0.693	1.016	0.825	1.890	1.40350	1.243	1.12522	0.812	1.000000	0.781680E 00	0.	9.1	0.11034	0.05030	0.13354
5	0.	0.411	0.	0.	0.	1.889	0.99990	1.243	0.99997	0.	1.000000	0.584756E-01	0.	12.7	0.11043	0.05028	0.11405
6	7.29	0.472	0.648	0.934	0.778	2.561	1.35565	1.379	1.10898	0.833	1.000000	0.183623E 01	0.	15.4	0.09483	0.05183	0.10769
7	0.	0.423	0.	0.	0.	2.560	0.99962	1.379	0.99989	0.	1.000000	0.266072E-01	0.	18.8	0.09477	0.05173	0.09115
8	4.91	0.508	0.615	0.997	0.821	3.475	1.35742	1.531	1.11073	0.824	1.000000	0.394920E-02	0.	21.4	0.09354	0.04915	0.09004
9	0.	0.465	0.	0.	0.	3.475	0.99994	1.531	0.99998	0.	1.000000	0.150741E 01	0.	25.0	0.09349	0.04914	0.08289
10	2.63	0.490	0.585	0.930	0.767	4.546	1.30804	1.679	1.09670	0.825	1.000000	0.264407E 01	0.	27.3	0.06995	0.05799	0.07585
11	0.	0.472	0.	0.	0.	4.545	0.99991	1.679	0.99998	0.	1.000000	0.168606E 01	0.	30.0	0.06991	0.05797	0.05556
12	1.15	0.458	0.553	0.778	0.434	5.605	1.23322	1.807	1.07578	0.814	1.000000	0.140870E 00	0.	33.1	0.04755	0.06595	0.04582
13	0.	0.508	0.	0.	0.	5.605	0.99986	1.807	0.99996	0.	1.000000	0.215961E 01	0.	36.5	0.04749	0.06591	0.03166
14	4.46	0.384	0.516	0.603	0.489	6.539	1.16667	1.907	1.05550	0.811	1.000000	0.310293E 00	0.	38.3	0.02906	0.07261	0.02389
15	0.	0.453	0.	0.	0.	6.538	0.99993	1.907	0.99998	0.	1.000000	0.248207E 01	0.	41.4	0.02893	0.07263	0.01409
16	3.29	0.406	0.474	0.622	0.501	7.598	1.16210	2.011	1.05449	0.805	1.000000	0.274638E 00	0.	43.1	0.01008	0.07906	0.00716
17	0.	0.619	0.	0.	0.	7.597	0.99985	2.011	0.99996	0.	1.000000	0.155572E 01	0.	45.1	0.01030	0.07900	0.00999
18	0.	0.084	0.	0.	0.	7.597	1.00000	2.011	1.00000	0.	1.000000	0.862037E-01	0.	48.4	0.01030	0.07900	0.00930

Table 29. (c) Sector 3.
Calculated Performance, Combined Total-Pressure and Total-Temperature Distortion (RDG 420), "Mehalic" Engine 99.0% $N/\sqrt{\theta}$ (Continued).

DYNAMIC PARALLEL COMPRESSOR ANALYSIS

J85-13 NAS3-18526 COMB-DIST 90 OVERLAP, MEH ENG RDG 420
THROTTLING SIMULATION

WCORR=19.391 PCTNC= 99.03 P/P-OA=7.1496

SECTOR= 3	PCTNCL= 99.80	ANGLE= 90.00
TIME STEP= 0	TALCN=19.612	R/P-OA(L)=7.61373
TIME=0.	EXIT FF= 6.4267	T/T-OA(L)=1.99575
DPTR-IN=0.12718	DTTR-IN=0.03518	DPSR-IN=0.13282

ROW	CZ1	CU1	WU1	CT	WT	U1	M-ABS	M-REL	ALPHA	BETA	PS1	PT1	TS1	TT1	PHI	INC	LOSS	TVD
1	145.8	0.	0.	145.8	0.	0.	0.4359	0.	0.	0.	6.10	6.95	278.6	289.2	0.	0.	0.	0.
2	199.3	0.	275.2	199.3	339.8	275.2	0.6058	1.0328	0.	54.88	5.43	6.95	269.4	289.2	0.04515	2.58	0.0905	0.11550
3	188.2	98.5	0.	212.4	0.	0.	0.6177	0.	27.62	0.	7.06	9.14	294.2	316.7	-0.02661	-7.22	0.	0.
4	212.8	20.1	265.3	213.8	340.1	285.4	0.6220	0.9895	5.40	51.26	7.84	9.14	293.9	316.7	0.01851	1.06	0.1366	0.07027
5	198.4	154.7	0.	251.5	0.	0.	0.6971	0.	37.95	0.	9.28	12.84	324.0	355.5	-0.04600	-2.63	0.	0.
6	202.9	43.5	251.0	207.5	382.8	294.5	0.5664	0.8809	12.10	51.85	10.33	12.84	334.1	355.5	-0.00001	-0.00	0.1386	0.10592
7	191.9	175.6	0.	260.1	0.	0.	0.6828	0.	42.47	0.	12.83	17.52	361.1	394.8	-0.05616	-3.21	0.	0.
8	195.5	51.6	258.9	202.2	318.1	302.6	0.5212	0.8200	14.80	52.08	14.56	17.52	374.5	394.8	0.02217	1.27	0.1610	0.05997
9	186.9	198.2	0.	272.4	0.	0.	0.6774	0.	46.67	0.	17.67	24.03	402.5	439.4	0.00477	0.27	0.	0.
10	186.9	65.8	242.7	198.2	388.3	308.5	0.4824	0.7459	19.40	52.40	20.50	24.03	419.9	439.4	-0.06200	-3.55	0.1629	0.04861
11	181.1	201.2	0.	270.8	0.	0.	0.6403	0.	48.01	0.	23.86	31.44	445.0	481.5	0.03454	1.98	0.	0.
12	178.5	76.5	236.3	194.2	296.1	312.8	0.4504	0.6867	23.20	52.93	27.35	31.44	462.7	481.5	-0.03268	-1.97	0.1601	0.01317
13	173.3	193.1	0.	259.5	0.	0.	0.5881	0.	48.18	0.	30.74	38.85	484.5	518.0	0.05584	3.20	0.	0.
14	167.1	68.2	247.0	180.4	290.2	315.2	0.4018	0.6641	22.20	55.93	34.76	38.85	501.8	518.0	0.01434	0.52	0.1296	0.07042
15	159.4	159.5	0.	225.5	0.	0.	0.4926	0.	45.03	0.	38.43	45.36	521.4	546.7	0.02161	1.24	0.	0.
16	153.4	60.7	255.2	165.0	297.7	315.9	0.3564	0.6433	21.68	58.99	41.55	45.36	533.1	546.7	0.10601	6.05	0.1417	0.04616
17	145.7	157.5	0.	214.5	0.	0.	0.4546	0.	47.22	0.	45.94	52.94	554.2	577.1	0.08955	5.12	0.	0.
18	137.4	23.2	0.	139.3	0.	0.	0.2917	0.	9.50	0.	49.90	52.94	567.5	577.1	-0.00000	-0.00	0.	0.

ROW	DEV	DFACT	PHI	PSI	PSI-P	PR1	PR2	TR1	TR2	ABLEF	W2/W1	DWK	DW/DWEX	ROT	DPTR2	DTTR2	DPSR2
1	0.	-0.222	0.	0.	0.	1.000	1.00000	1.000	1.00000	0.	1.000000	0.424954E 01	0.	0.	0.12716	0.03518	0.13891
2	6.59	0.357	0.724	0.730	0.623	1.314	1.31423	1.095	1.09511	0.854	1.000000	0.601739E 00	0.	2.6	0.13022	0.04246	0.13960
3	0.	0.166	0.	0.	0.	1.314	1.00003	1.095	1.00001	0.	1.000000	0.590849E 00	0.	5.3	0.12992	0.04236	0.14714
4	4.02	0.460	0.746	0.958	0.797	1.846	1.40475	1.229	1.12258	0.882	1.000000	0.531646E-02	0.	8.1	0.11034	0.05030	0.13354
5	0.	0.355	0.	0.	0.	1.847	1.00019	1.229	1.00005	0.	1.000000	0.142701E 00	0.	11.4	0.11043	0.05028	0.11405
6	6.04	0.451	0.689	0.911	0.765	2.520	1.36481	1.365	1.11056	0.841	1.000000	0.255948E 01	0.	14.0	0.09483	0.05183	0.10769
7	0.	0.397	0.	0.	0.	2.520	0.99995	1.365	0.99999	0.	1.000000	0.318346E 01	0.	17.4	0.09477	0.05173	0.09115
8	4.00	0.490	0.646	0.979	0.819	3.457	1.37155	1.520	1.11300	0.836	1.000000	0.122408E 01	0.	19.9	0.09354	0.04915	0.09004
9	0.	0.446	0.	0.	0.	3.457	1.00001	1.520	1.00000	0.	1.000000	0.146896E 01	0.	23.4	0.09349	0.04914	0.08289
10	2.78	0.465	0.606	0.883	0.740	4.521	1.30795	1.665	1.09569	0.833	1.000000	0.256453E 01	0.	26.7	0.06998	0.05799	0.07585
11	0.	0.442	0.	0.	0.	4.521	1.00005	1.665	1.00001	0.	1.000000	0.219205E 01	0.	29.3	0.06991	0.05797	0.05556
12	0.75	0.438	0.571	0.750	0.617	5.587	1.23569	1.791	1.07583	0.822	1.000000	0.162699E 00	0.	33.4	0.04755	0.06595	0.04982
13	0.	0.487	0.	0.	0.	5.587	1.00002	1.791	1.00001	0.	1.000000	0.244252E 01	0.	34.6	0.04749	0.06591	0.03164
14	4.03	0.369	0.530	0.580	0.474	6.524	1.16760	1.891	1.05539	0.817	1.000000	0.373292E 00	0.	36.4	0.02906	0.07261	0.02389
15	0.	0.434	0.	0.	0.	6.523	1.00000	1.891	1.00000	0.	1.000000	0.291629E 01	0.	39.5	0.02893	0.07263	0.01408
16	2.64	0.399	0.486	0.613	0.497	7.613	1.16709	1.996	1.05564	0.811	1.000000	0.309938E 00	0.	45.2	0.01005	0.07908	0.00716
17	0.	0.610	0.	0.	0.	7.614	1.00003	1.996	1.00001	0.	1.000000	0.177283E 01	0.	45.2	0.01030	0.07900	0.00399
18	0.	0.084	0.	0.	0.	7.614	1.00000	1.996	1.00000	0.	1.000000	0.104521E 00	0.	45.4	0.01030	0.07900	0.00930

(d) Sector 4.

Table 29. Calculated Performance, Combined Total-Pressure and Total-Temperature Distortion (RDG 420), "Mehalic" Engine 99.0% $N/\sqrt{\theta}$ (Concluded).

DYNAMIC PARALLEL COMPRESSOR ANALYSIS

J85-13 NAS3-18526 COMP-DIST 90 OVERLAP, MEH ENG RDG 420
THROTTLING SIMULATION

WCORR=19.391 PCTNC= 99.03 P/P-0A=7.1496

SECTOR= 4 PCTNCL= 99.80 ANGLE= 90.00
TIME STEP= 0 TALCW=19.793 P/P-0A(L)=6.75799
TIME=0. EXIT FF= 6.4267 T/T-0A(L)=1.91392
DPTR-IN=0.12718 DTTR-IN=0.03516 DPSR-IN=0.13282

ROW	CZ1	CU1	WU1	CT	WT	U1	M-ABS	M-REL	ALPHA	BETA	PS1	PT1	TS1	TT1	TRI	INC	LOSS	TVD
1	147.4	0.	0.	147.4	0.	0.	0.4411	0.	0.	0.	6.91	7.90	278.0	288.8	0.	0.	0.	0.
2	202.1	0.	275.2	202.1	341.5	275.2	0.6154	1.0395	0.	53.70	6.12	7.90	268.5	288.8	0.03843	2.20	0.0847	0.11851
3	191.7	94.0	0.	213.5	0.	0.	0.6228	0.	26.13	0.	7.91	10.27	292.4	345.1	-0.05324	-8.71	0.	0.
4	218.8	20.7	264.7	219.8	343.4	285.4	0.6426	1.0042	5.40	50.42	7.78	10.27	291.1	345.1	0.00388	0.22	0.1251	0.03274
5	203.9	147.2	0.	251.5	0.	0.	0.7009	0.	35.83	0.	10.24	14.21	320.3	351.8	-0.08313	-4.75	0.	0.
6	211.3	45.3	249.2	216.1	326.7	294.5	0.5948	0.8993	12.10	49.70	11.19	14.21	328.5	351.8	-0.02354	-1.35	0.1328	0.10147
7	200.0	171.7	0.	263.6	0.	0.	0.6978	0.	40.65	0.	13.88	19.21	355.0	389.5	-0.08804	-5.03	0.	0.
8	205.0	54.2	248.4	212.0	322.1	302.6	0.5519	0.8385	14.80	50.48	15.62	19.21	367.2	389.5	-0.00583	-0.33	0.1563	0.04741
9	195.5	199.0	0.	279.0	0.	0.	0.7003	0.	45.51	0.	19.02	26.39	395.0	433.8	-0.01555	-0.39	0.	0.
10	195.0	68.7	239.9	206.8	309.2	308.5	0.5079	0.7593	19.40	50.88	22.13	26.39	412.5	433.8	-0.08868	-5.07	0.1460	0.07170
11	189.9	189.9	0.	268.6	0.	0.	0.6419	0.	45.00	0.	25.56	33.72	435.7	471.6	-0.01793	-1.03	0.	0.
12	189.9	81.4	231.3	206.7	299.3	312.8	0.4858	0.7037	23.20	50.61	28.69	33.72	450.3	471.5	-0.07320	-4.19	0.1348	0.02239
13	185.2	182.3	0.	259.8	0.	0.	0.5981	0.	44.55	0.	31.99	40.74	469.7	503.3	-0.00606	-0.35	0.	0.
14	180.4	73.6	241.6	194.9	301.5	315.2	0.4417	0.6835	22.20	53.25	35.63	40.74	484.4	503.3	-0.03253	-1.56	0.1072	0.03576
15	172.9	151.1	0.	229.6	0.	0.	0.5116	0.	41.15	0.	39.06	46.70	501.4	527.7	-0.04611	-2.64	0.	0.
16	187.4	66.3	249.6	190.1	300.6	315.9	0.3972	0.6630	21.80	56.15	41.88	46.69	511.5	527.6	0.05607	3.21	0.1140	0.03424
17	159.9	146.1	0.	216.6	0.	0.	0.4696	0.	42.43	0.	45.89	53.37	529.5	552.8	0.00582	0.33	0.	0.
18	151.4	25.6	0.	153.6	0.	0.	0.3293	0.	9.55	0.	49.51	53.37	541.1	552.8	-0.00000	-0.00	0.	0.

ROW	DEV	DFACT	RHI	PSI	PSI-P	PR1	PR2	TR1	TR2	ADEF	W2/W1	DWX	DW/DBEX	RBT	DPTR2	DTTR2	DPSR2
1	0.	-0.224	0.	0.	0.	1.000	1.00000	1.000	1.00000	0.	1.000000	0.915544E 01	0.	0.	0.12716	0.03518	0.13591
2	6.76	0.338	0.735	0.697	0.597	1.300	1.30034	1.091	1.09099	0.856	1.000000	0.159372E 01	0.	2.5	0.13022	0.04246	0.13960
3	0.	0.131	0.	0.	0.	1.300	0.99979	1.091	0.99994	0.	1.000000	0.373669E 00	0.	5.1	0.12992	0.04236	0.14714
4	4.73	0.430	0.767	0.705	0.756	1.799	1.38396	1.218	1.11639	0.836	1.000000	0.307253E-01	0.	7.6	0.11034	0.05030	0.13354
5	0.	0.306	0.	0.	0.	1.799	0.99995	1.218	0.99999	0.	1.000000	0.333769E 00	0.	10.8	0.11043	0.05028	0.11405
6	5.79	0.423	0.718	0.875	0.733	2.432	1.35190	1.349	1.10730	0.838	1.000000	0.346479E 01	0.	13.4	0.09483	0.05183	0.10769
7	0.	0.358	0.	0.	0.	2.432	0.99994	1.349	0.99998	0.	1.000000	0.116872E 00	0.	16.6	0.09477	0.05173	0.09115
8	2.71	0.473	0.677	0.972	0.813	3.342	1.37401	1.502	1.11363	0.836	1.000000	0.190526E 01	0.	19.1	0.09354	0.04915	0.09004
9	0.	0.425	0.	0.	0.	3.342	0.99996	1.502	0.99999	0.	1.000000	0.168148E 01	0.	22.4	0.07349	0.04914	0.08289
10	4.10	0.410	0.632	0.797	0.864	4.269	1.27759	1.633	1.08707	0.833	1.000000	0.562064E-01	0.	24.6	0.05795	0.05799	0.07585
11	0.	0.370	0.	0.	0.	4.269	0.99998	1.633	1.00000	0.	1.000000	0.923671E-01	0.	28.0	0.06991	0.05797	0.05556
12	1.28	0.371	0.607	0.652	0.538	5.159	1.20831	1.742	1.06726	0.826	1.000000	0.394445E 00	0.	30.0	0.04755	0.06595	0.04582
13	0.	0.409	0.	0.	0.	5.158	0.99997	1.742	0.99999	0.	1.000000	0.488563E 01	0.	33.0	0.04749	0.06591	0.03166
14	3.19	0.306	0.572	0.493	0.405	5.913	1.14627	1.827	1.04848	0.820	1.000000	0.804533E 00	0.	34.7	0.02905	0.07261	0.02389
15	0.	0.355	0.	0.	0.	5.912	0.99986	1.827	0.99996	0.	1.000000	0.460817E 01	0.	36.6	0.02593	0.07263	0.01409
16	1.96	0.324	0.530	0.207	0.414	6.758	1.14299	1.914	1.04772	0.816	1.000000	0.730154E 00	0.	39.1	0.01005	0.07906	0.00716
17	0.	0.521	0.	0.	0.	6.758	1.00007	1.914	1.00002	0.	1.000000	0.295771E 01	0.	41.9	0.01030	0.07900	0.00999
18	0.	0.084	0.	0.	0.	6.758	1.00000	1.914	1.00000	0.	1.000000	0.209638E 00	0.	43.1	0.01030	0.07900	0.00930

APPENDIX G

DISTORTION TRANSMISSION DOCUMENTATION

As an aid in identifying regions of amplification and attenuation of distortion in the compressor, the distortion amplitudes at the exit of each blade row have been calculated as shown in the listings presented in Appendices B - F. This appendix is a compilation of the amplification results established in the distortion analysis performed at the intermediate flow condition. The normalized distortion amplitudes are formulated as the difference in the sector blade row exit maximum and minimum values normalized by the average of the parameter values. Plots are provided for normalized total-pressure, total-temperature, and static-pressure amplitudes.

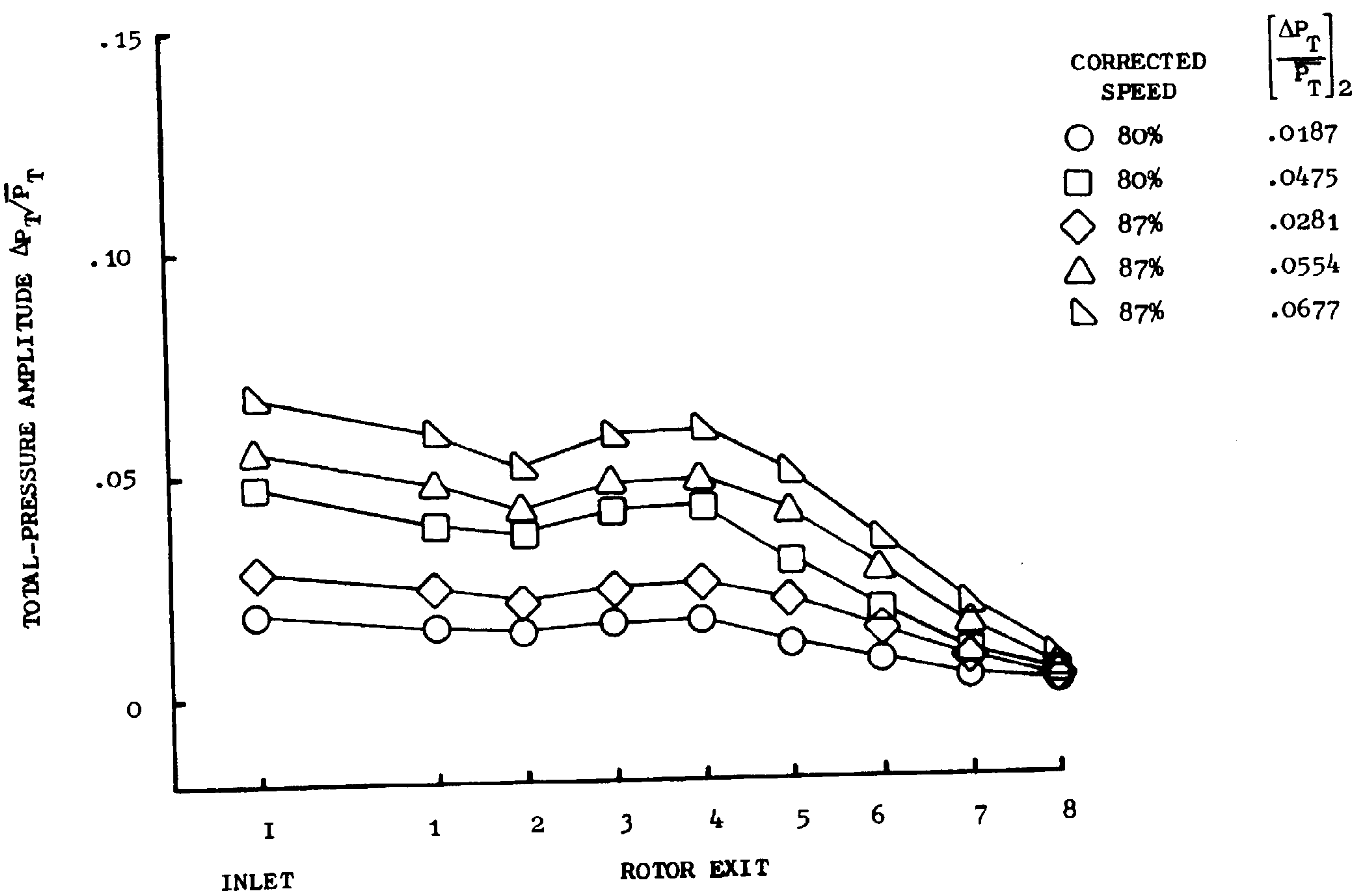

Figure 96. Predicted Total-Pressure Amplification For Inlet Total-Pressure Distortion at 80% and 87% $N/\sqrt{\theta}$.

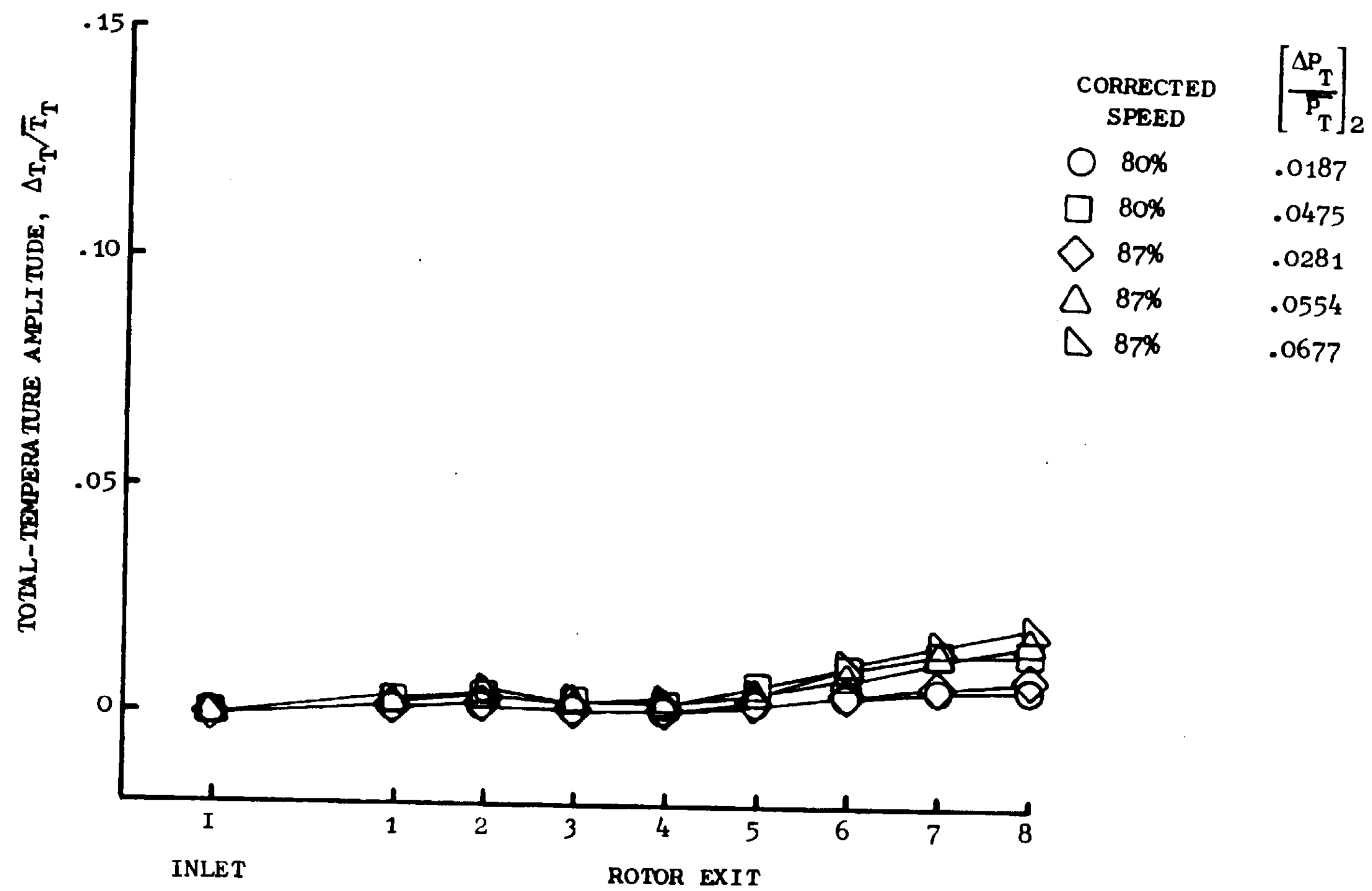

Figure 97. Predicted Total-Temperature Amplification For Inlet Total-Pressure Distortion at 80% and 87% $N/\sqrt{\theta}$.

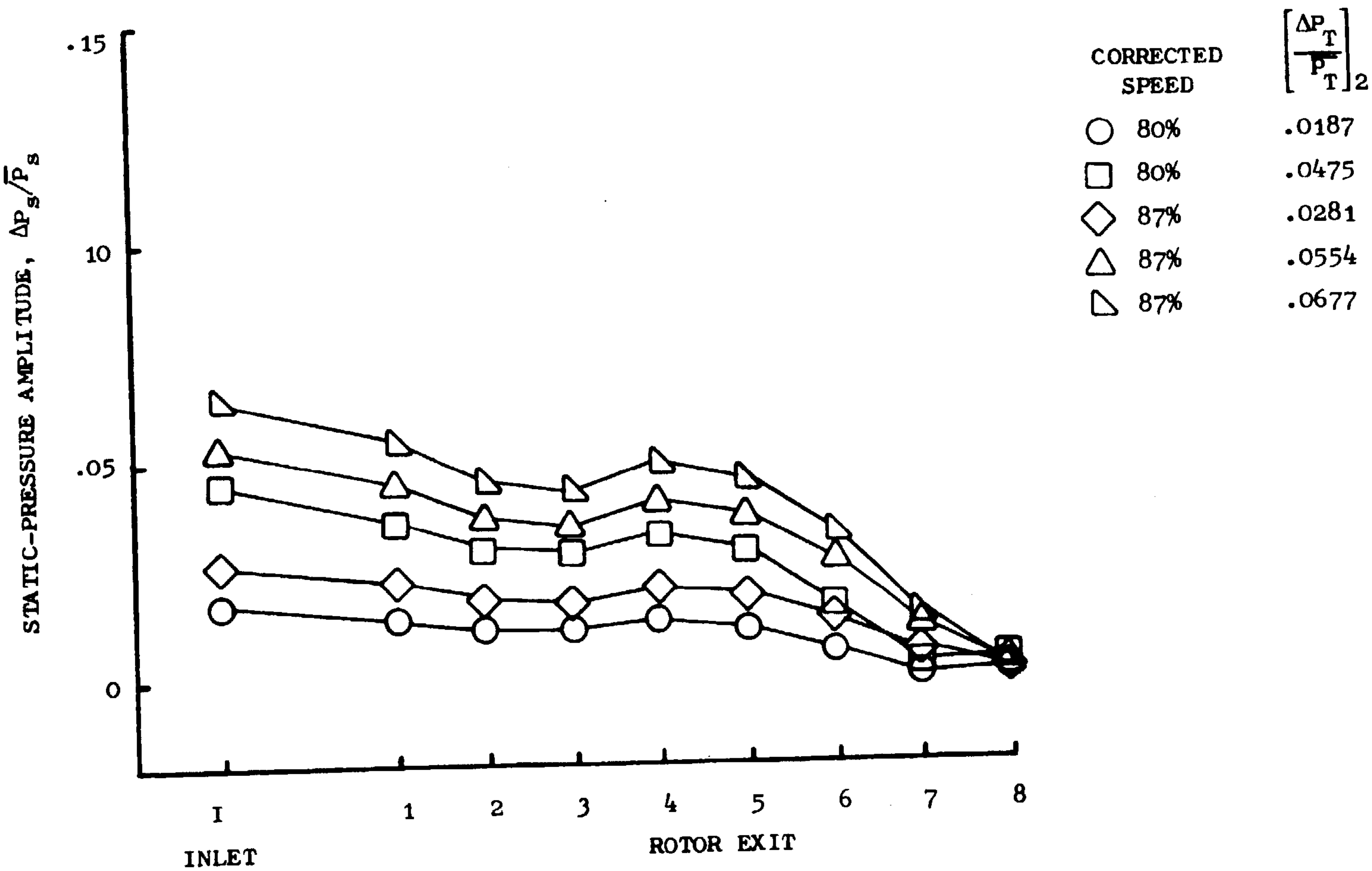

Figure 98. Predicted Static-Pressure Amplification For Inlet Total-Pressure Distortion at 80% and 87% $N/\sqrt{\theta}$.

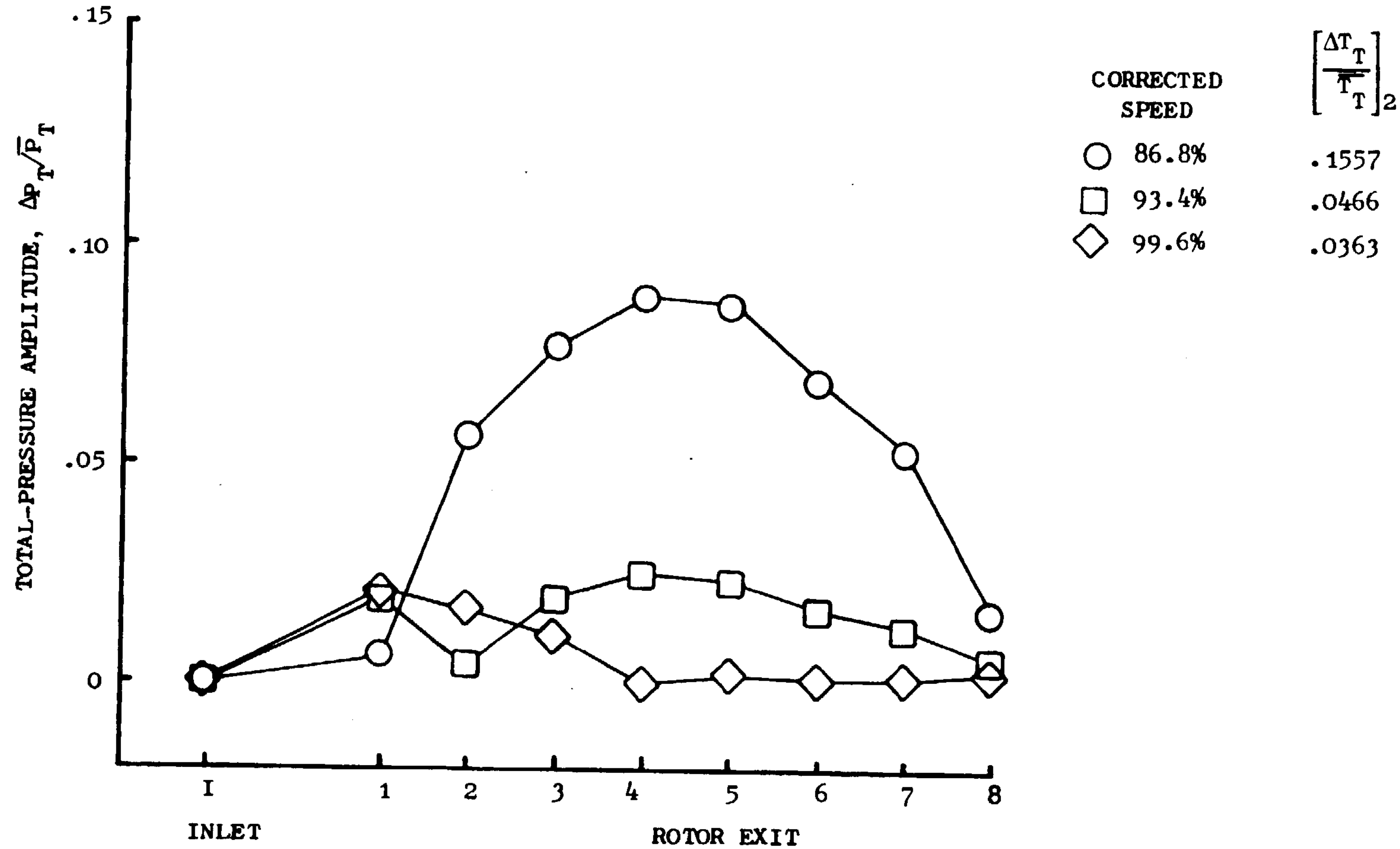

Figure 99. Predicted Total-Pressure Amplification For Inlet Total-Temperature Distortion.

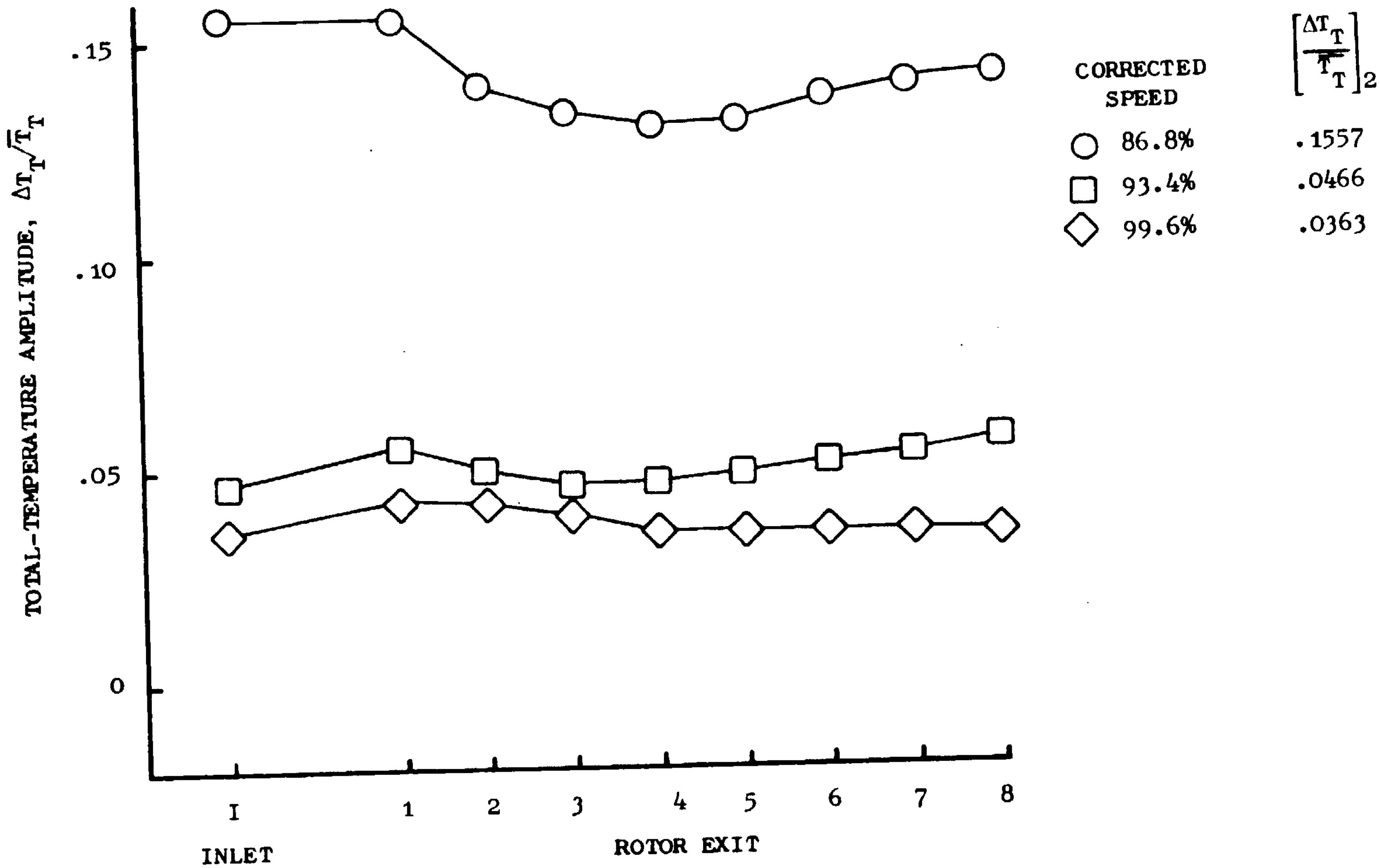

Figure 100. Predicted Total-Temperature Amplification For Inlet Total-Temperature Distortion.

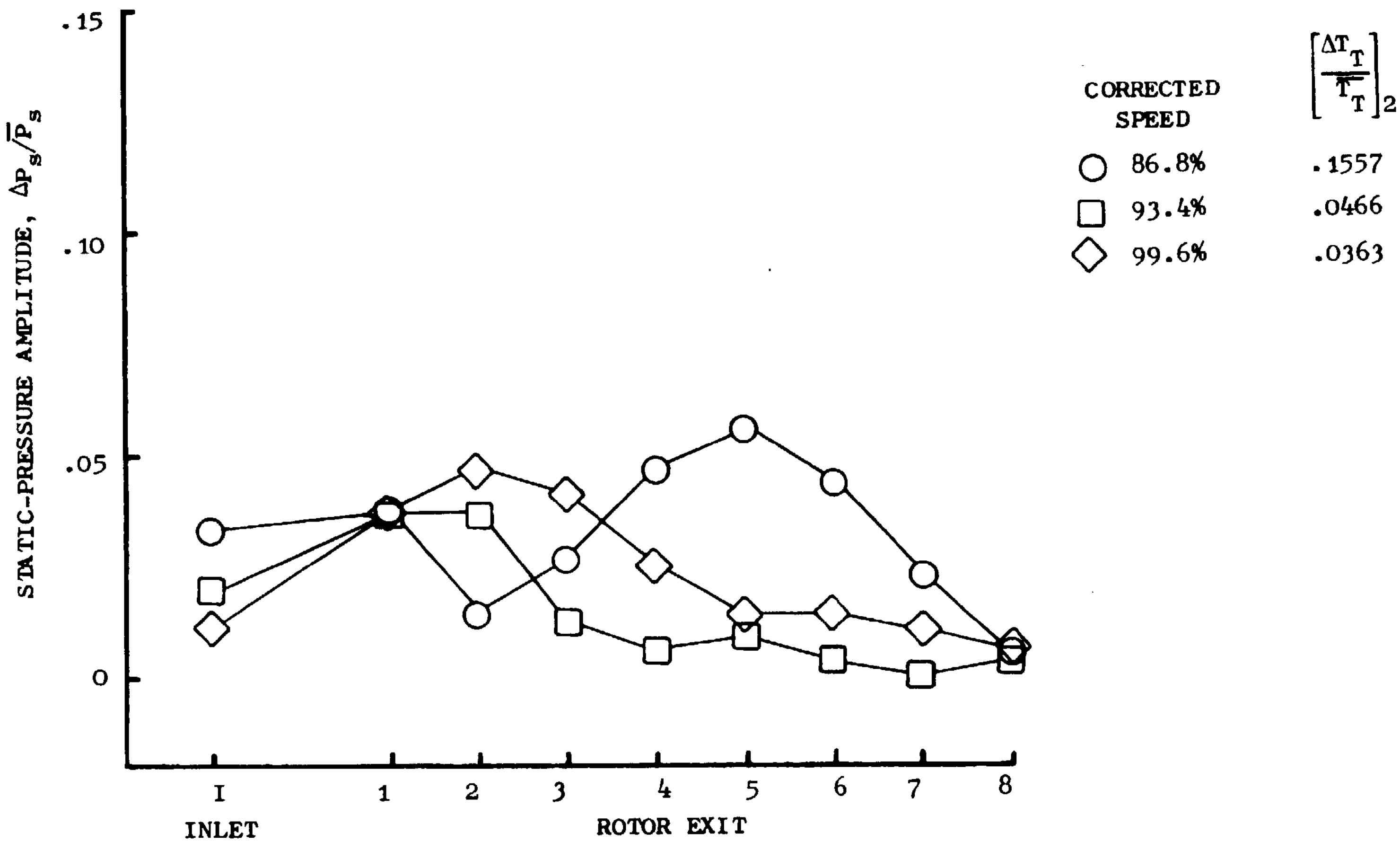

Figure 101. Predicted Static-Pressure Amplification For Inlet Total-Temperature Distortion.

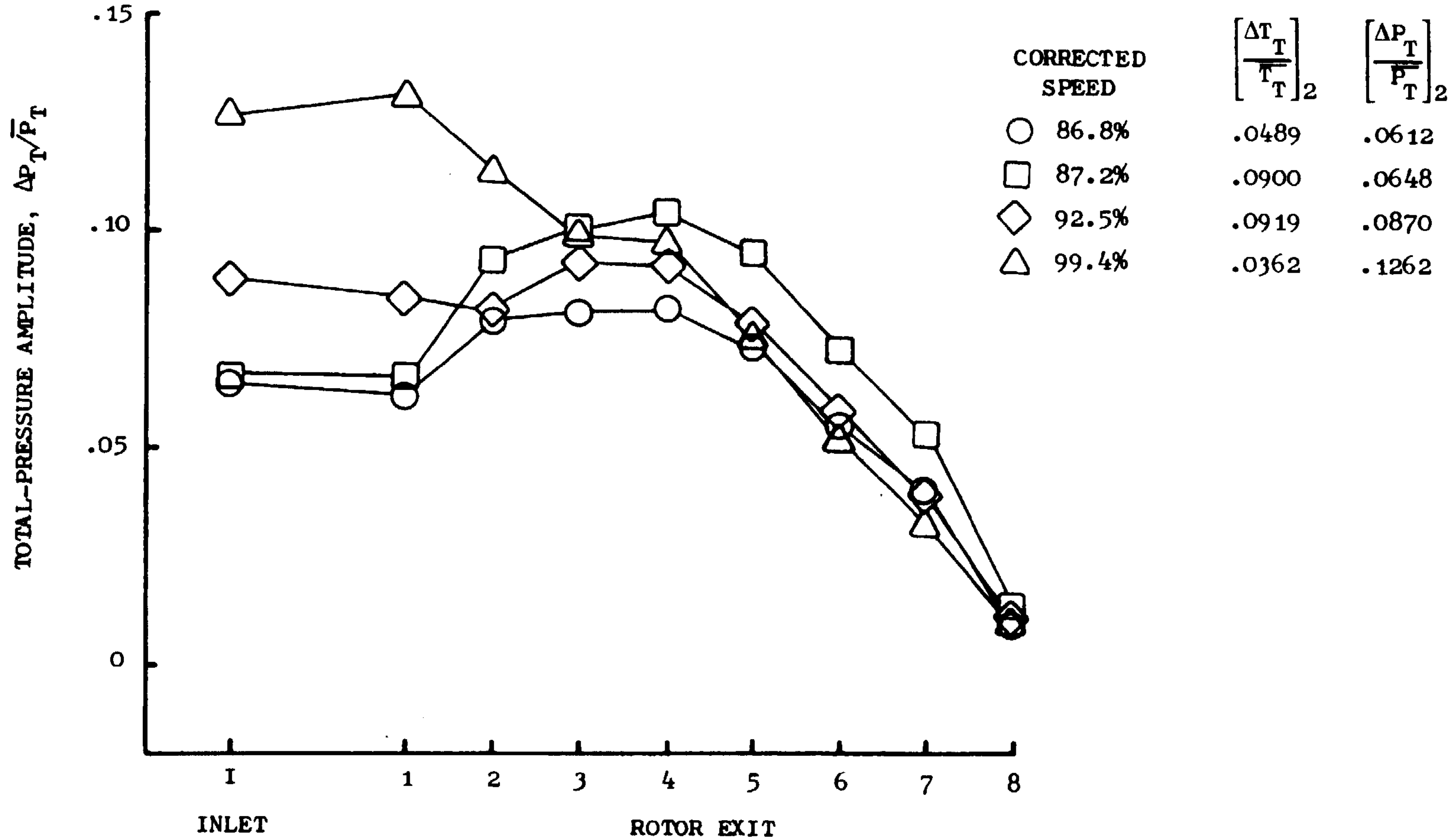

Figure 102. Predicted Total-Pressure Amplification For Combined Inlet Total-Pressure and Total-Temperature Distortion, Opposed Orientation.

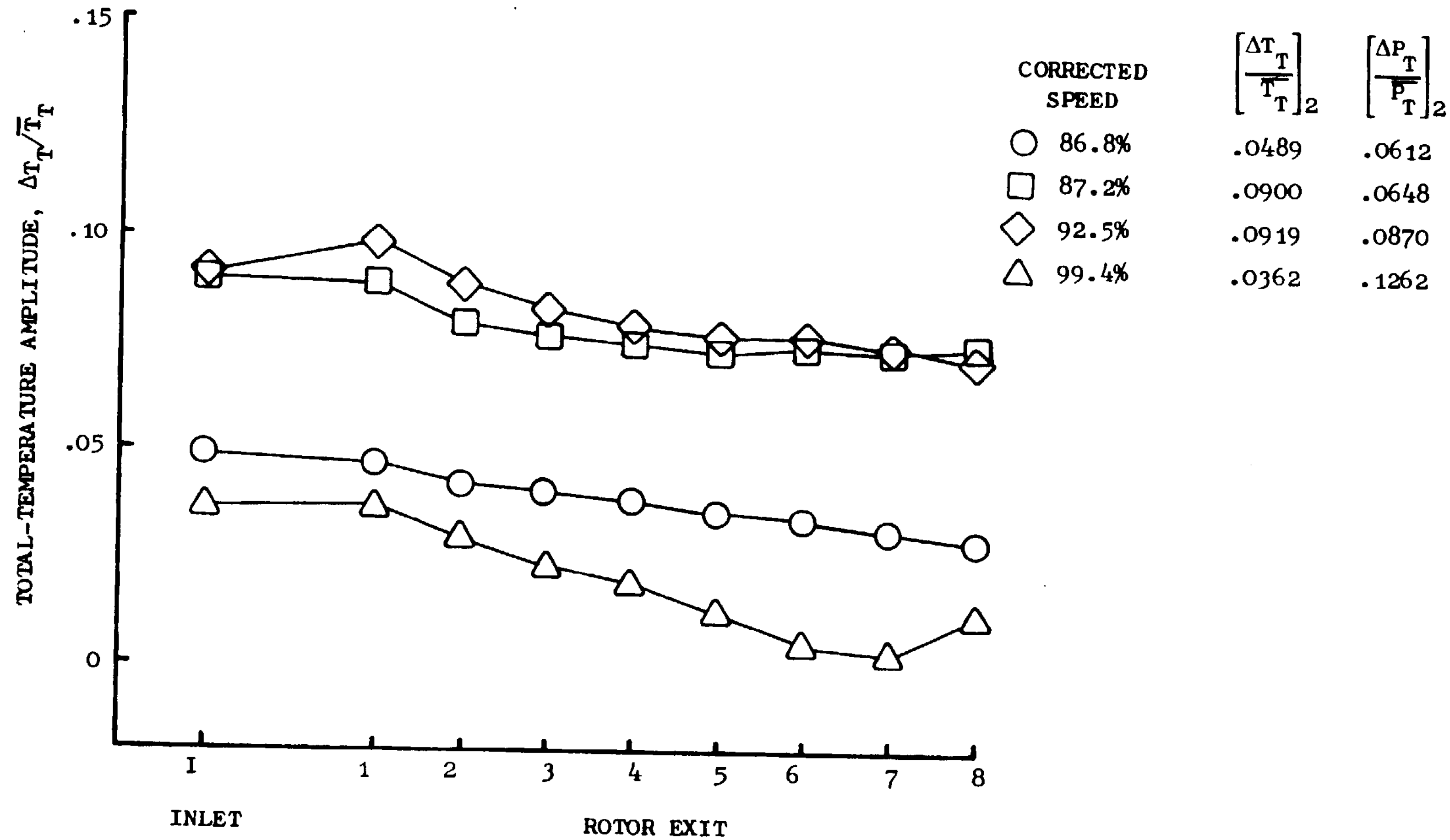

Figure 103. Predicted Total-Temperature Amplification for Combined Inlet Total-Pressure and Total-Temperature Distortion, Opposed Orientation.

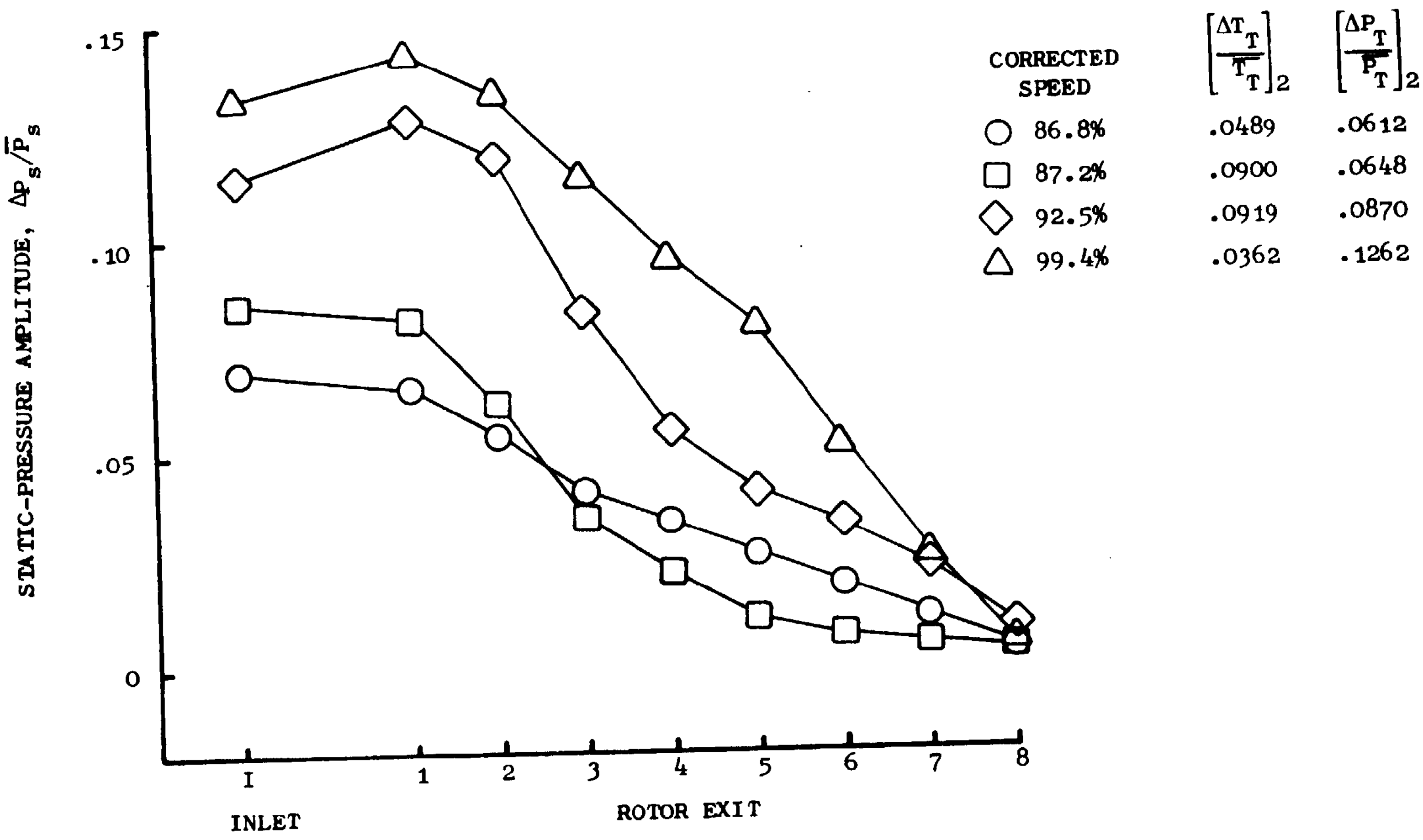

Figure 104. Predicted Static-Pressure Amplification for Combined Inlet Total-Pressure and Total-Temperature Distortion, Opposed Oreintation.

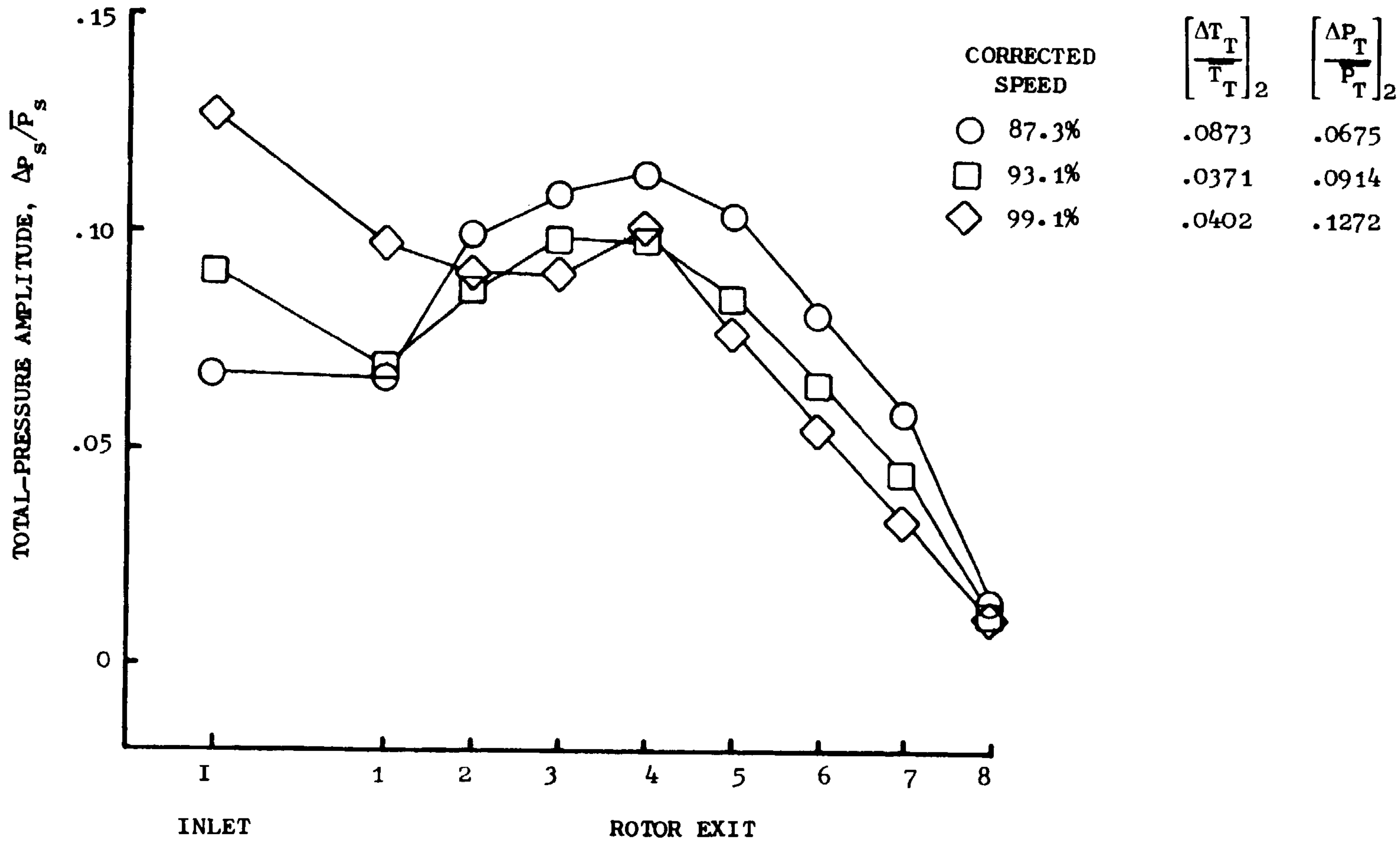

Figure 105. Predicted Total-Pressure Amplification for Combined Inlet Total-Pressure and Total-Temperature Distortion, Coincident Orientation.

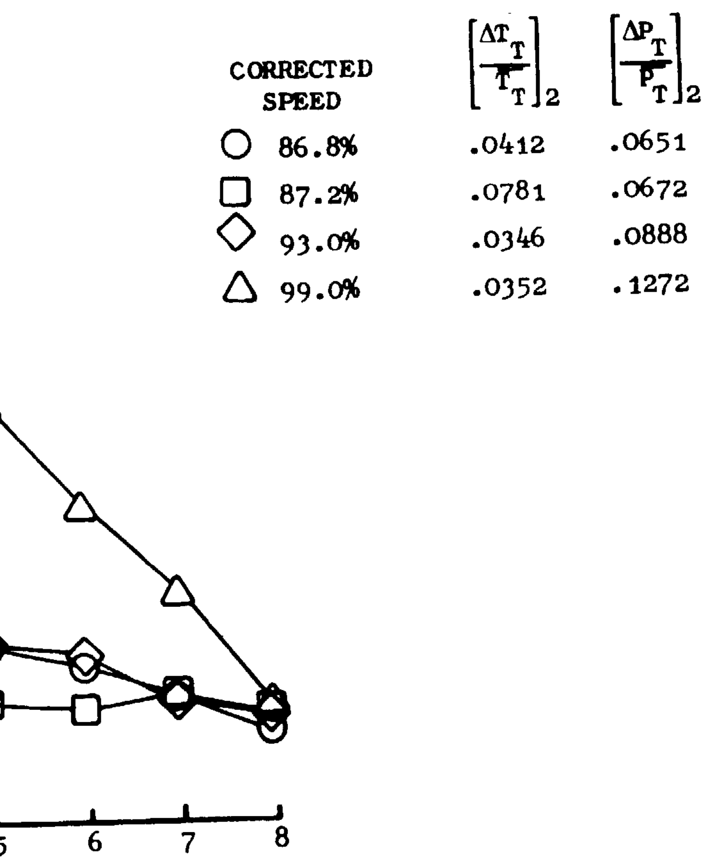

ation for Combined Inlet Total-Pressure
90° Overlapped Orientation.

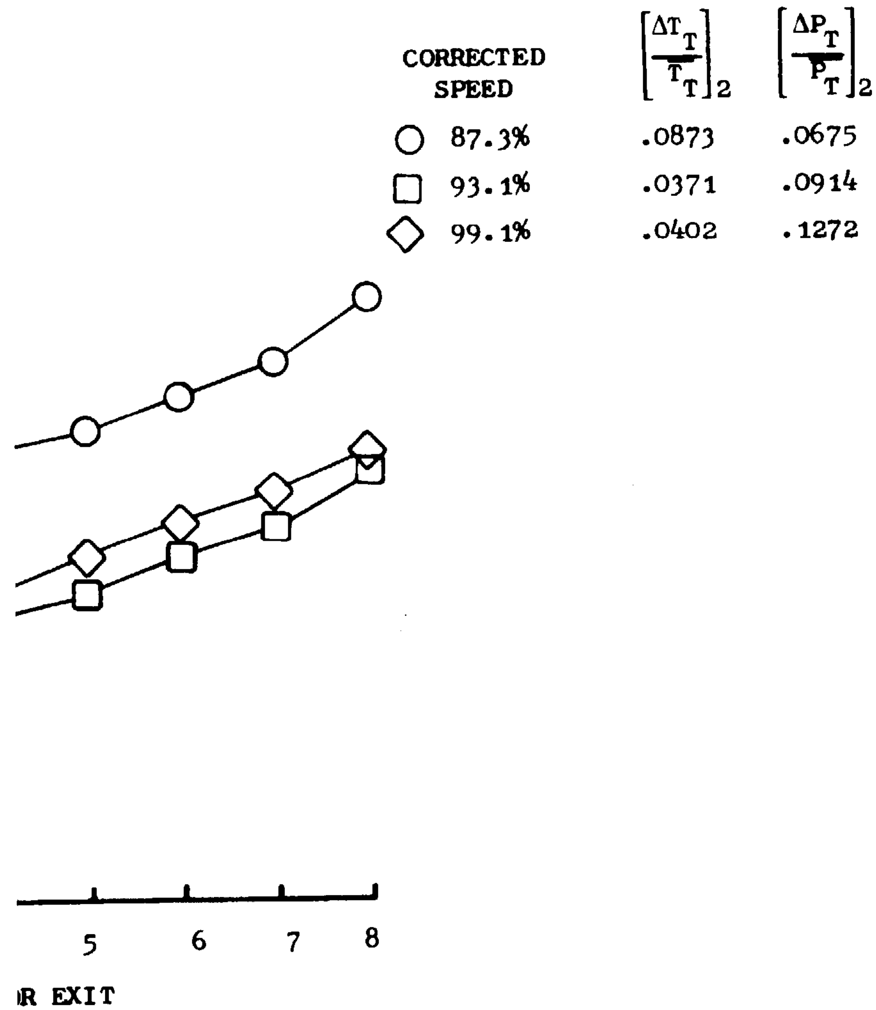

e Amplification for Combined Inlet Total-Pressure
ortion, Coincident Orientation.

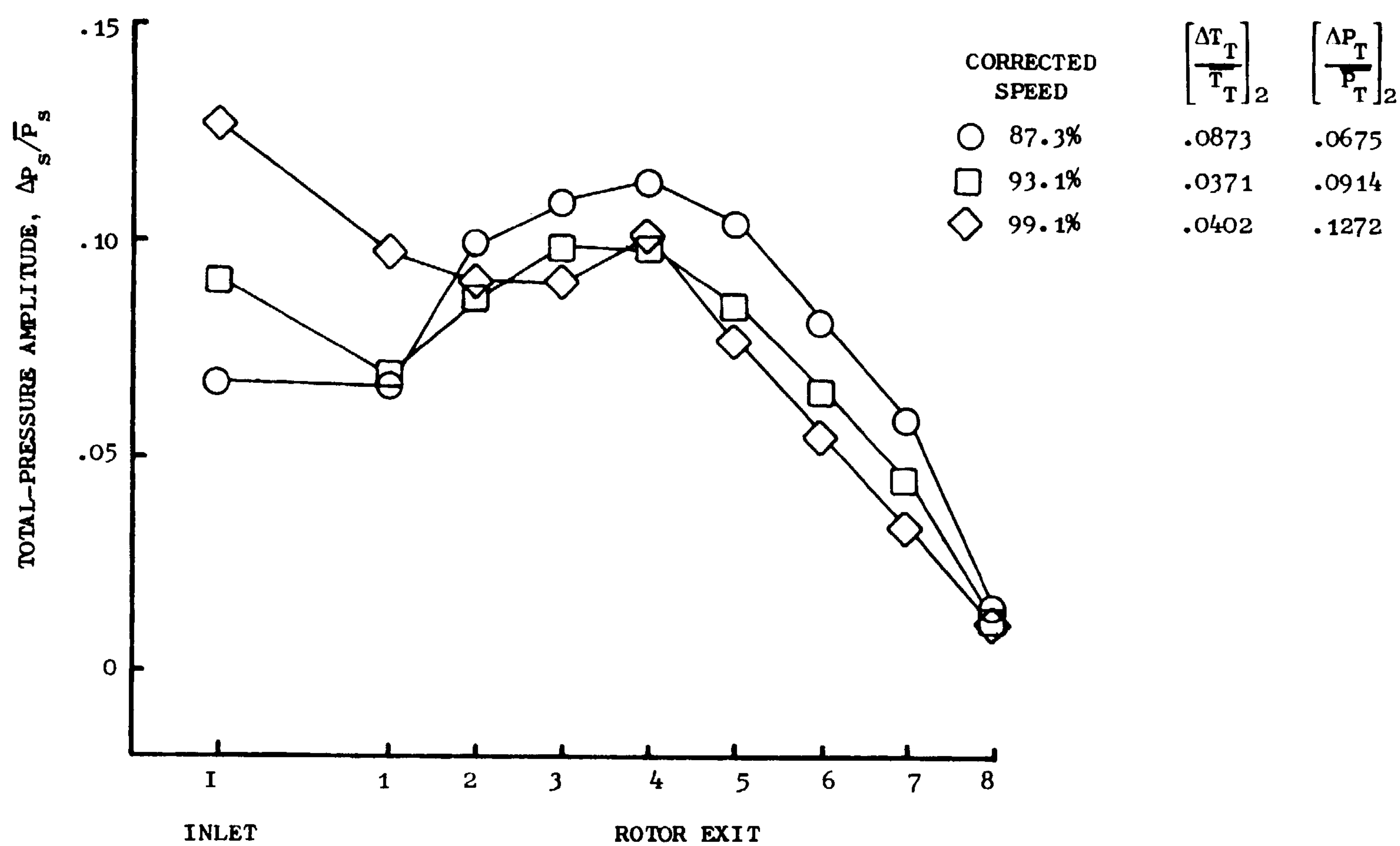

Figure 105. Predicted Total-Pressure Amplification for Combined Inlet Total-Pressure and Total-Temperature Distortion, Coincident Orientation.

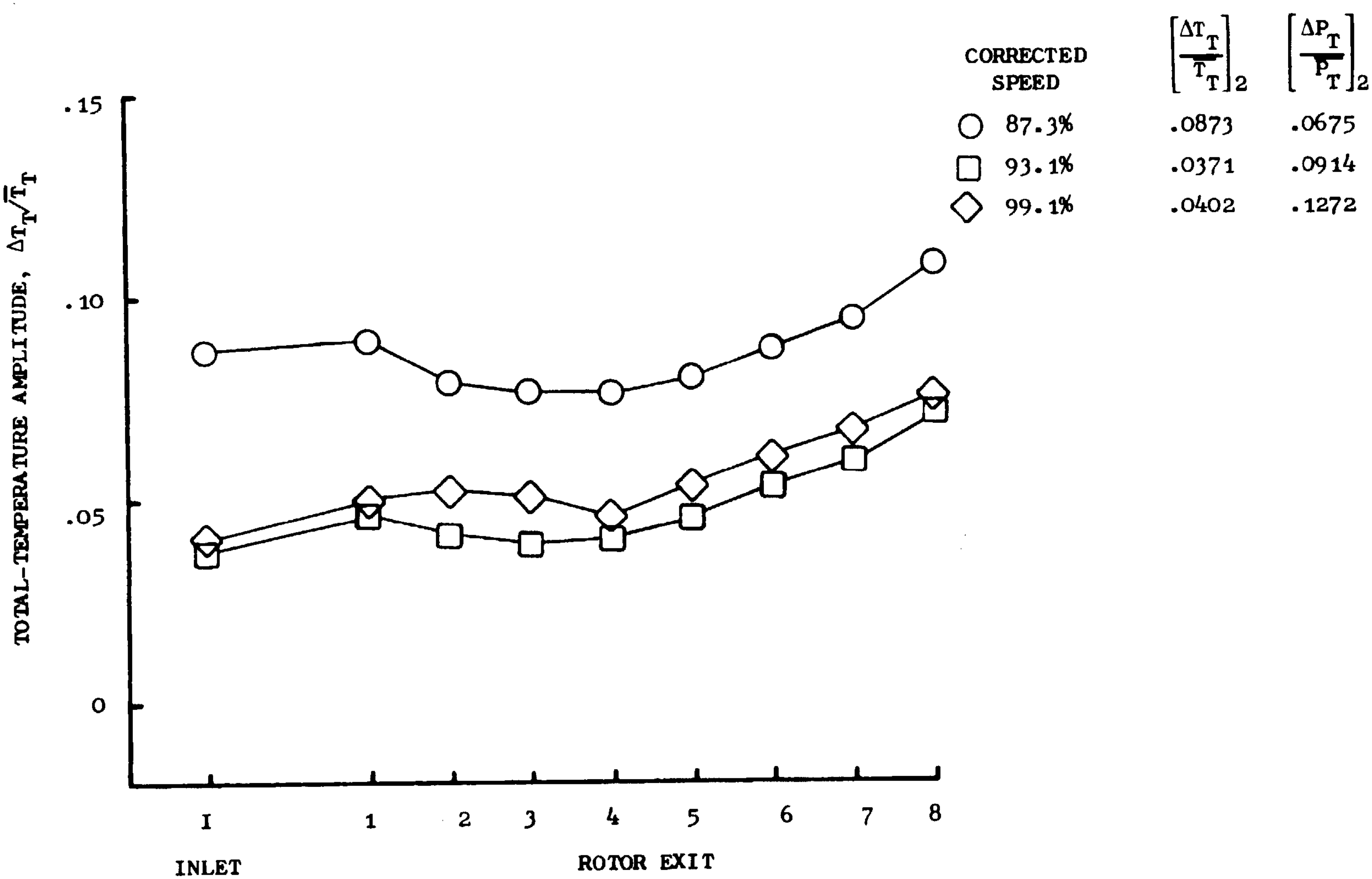

Figure 106. Predicted Total-Temperature Amplification for Combined Inlet Total-Pressure and Total-Temperature Distortion, Coincident Orientation.

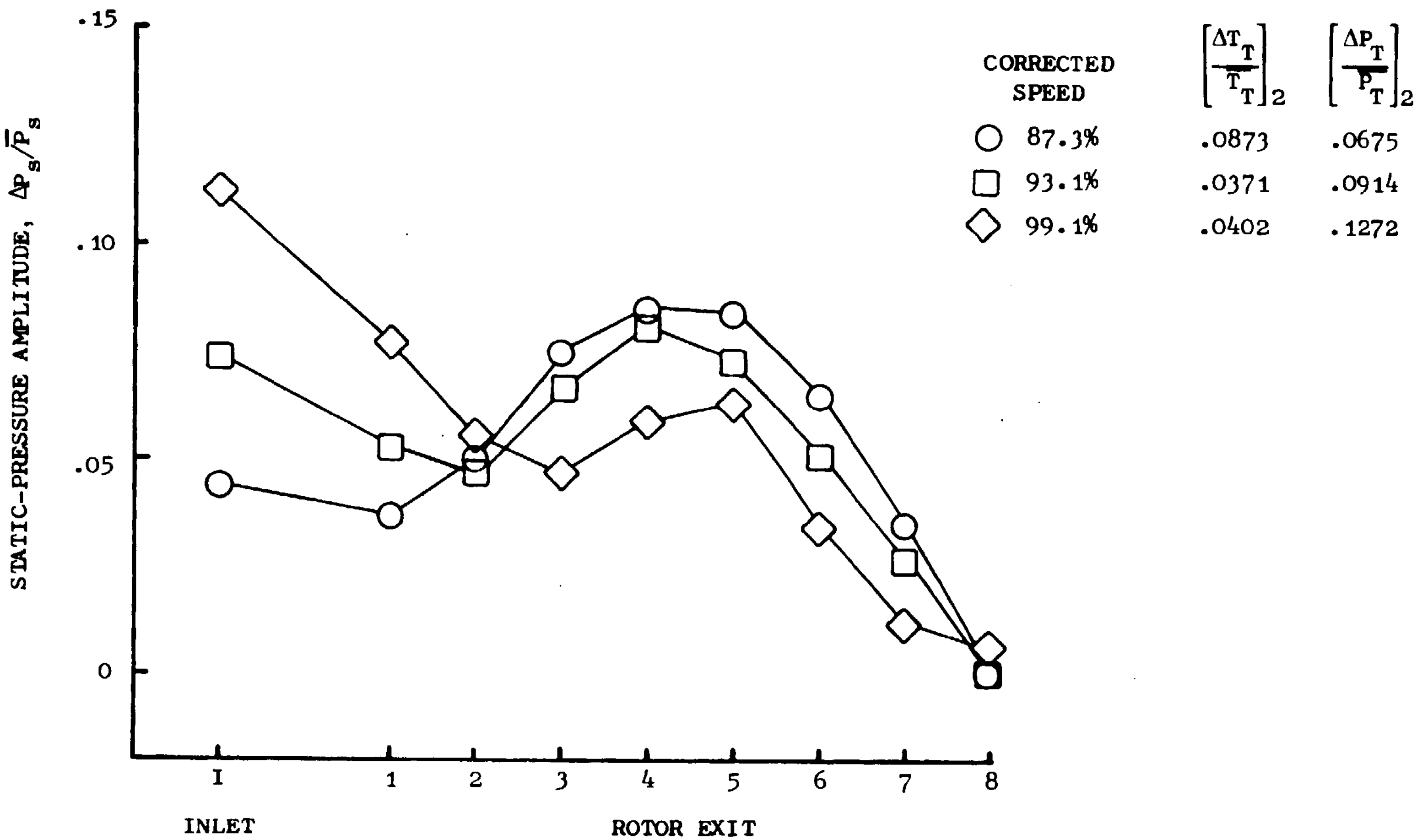

Figure 107. Predicted Static-Pressure Amplification for Combined Inlet Total-Pressure and Total-Temperature Distortion, Coincident Orientation.

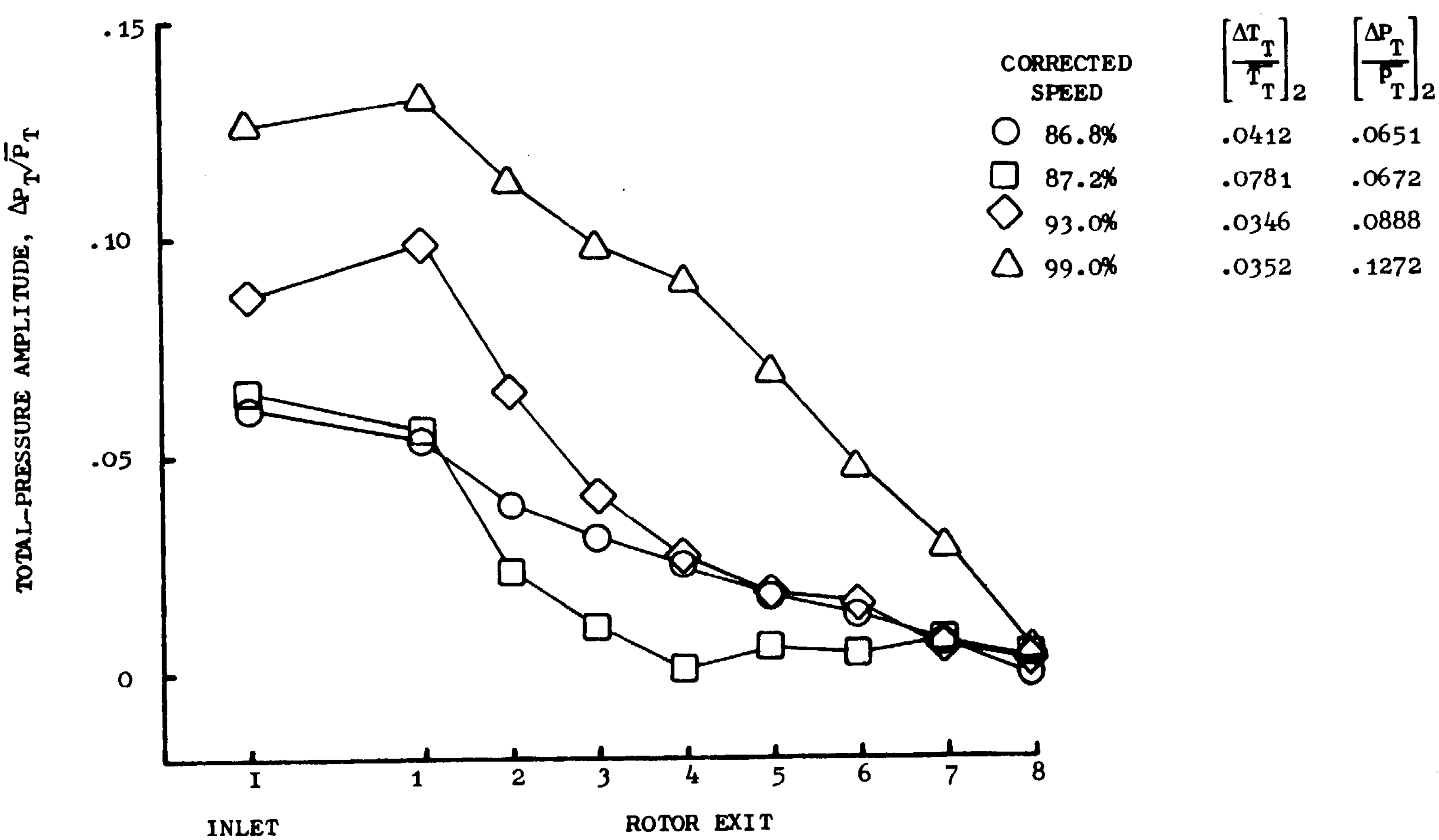

Figure 108. Predicted Total-Pressure Amplification for Combined Inlet Total-Pressure and Total-Temperature Distortion, 90° Overlapped Orientation.

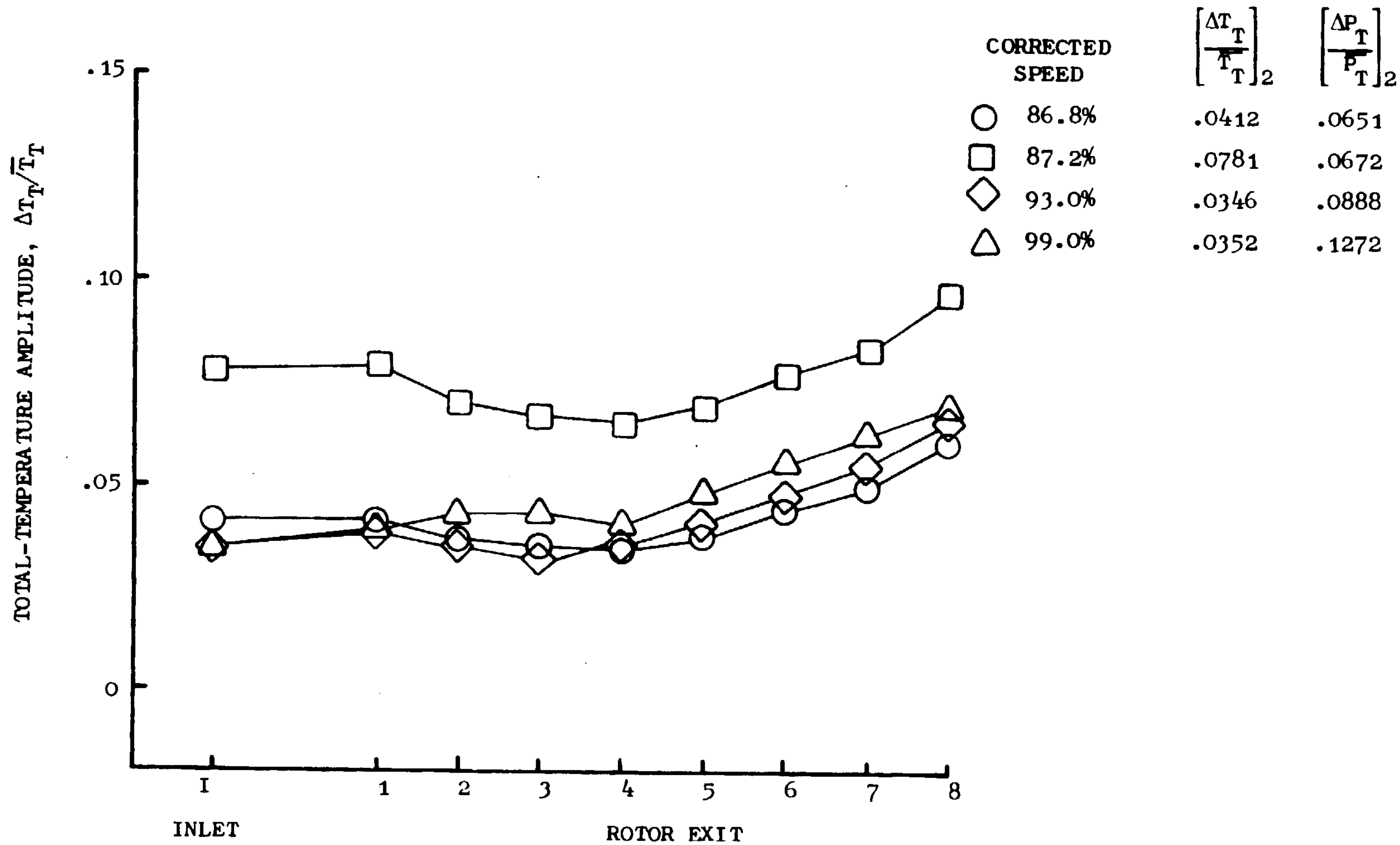

Figure 109. Predicted Total-Temperature Amplification for Combined Inlet Total-Pressure and Total-Temperature Distortion, 90° Overlapped Orientation.

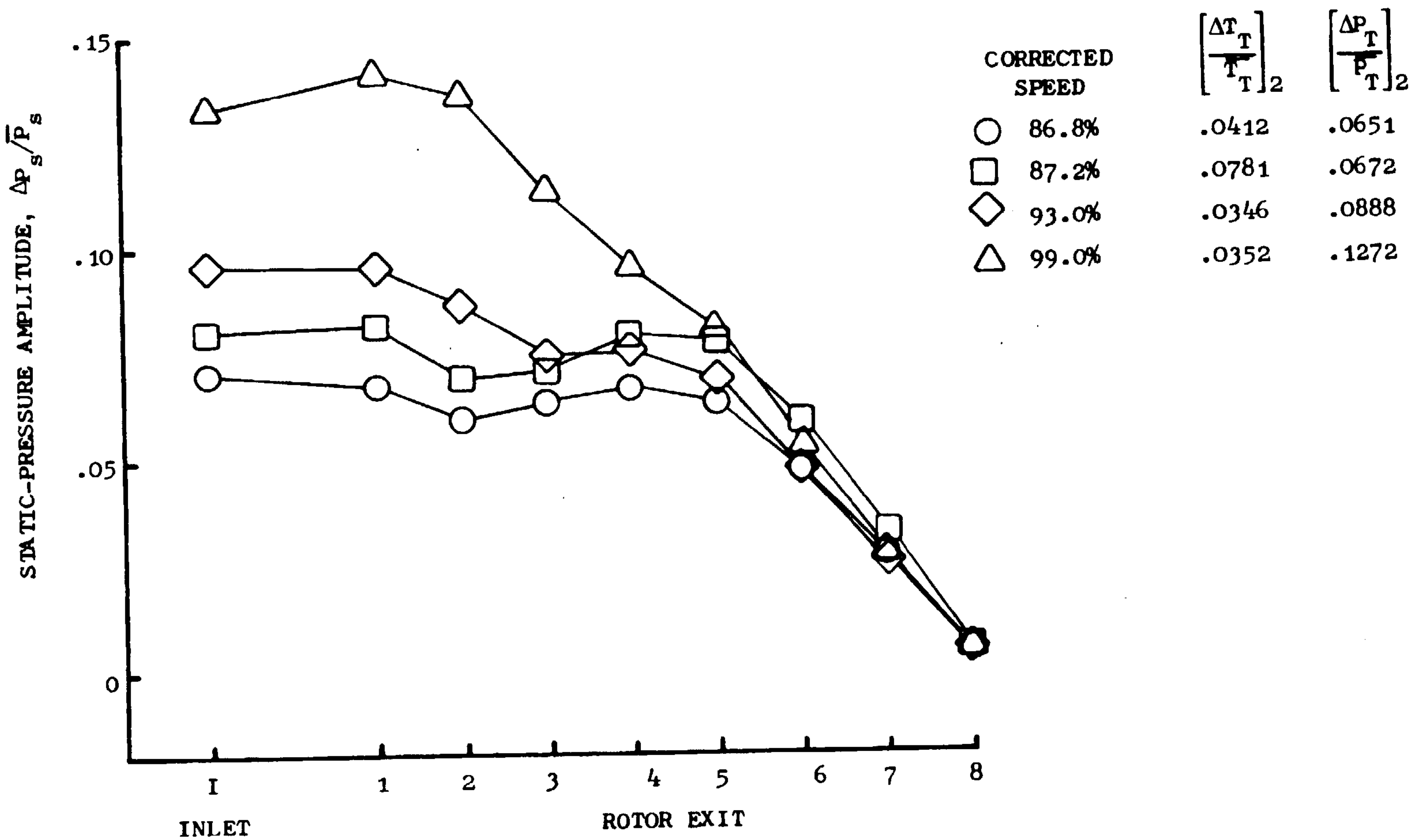

Figure 110. Predicted Static-Pressure Amplification for Combined Inlet Total-Pressure and Total-Temperature Distortion, 90° Overlapped Orientation.

REFERENCES

1. Jansen, W., and Smith, G.E., "Propulsion System Flow Stability Program (Dynamic) Phase I Final Technical Report Part X. Explicit Stall Prediction Model - Theory and Comparison of Computed and Experimental Results," Air Force Aero Propulsion Laboratory Technical Report AFAPL-TR-68-142, Part X, December 1968.

2. Daniele, C.J., Blaha, R.J., and Seldner, K., "Prediction of Axial Flow Instabilities in a Turbojet Engine by Use of a Multistage Compressor Simulation on a Digital Computer," National Aeronautics and Space Administration Technical Memorandum TM X-3134, 1974.

3. Ruegg, R.G., "A Numerical Technique for Analyzing One-Dimensional, Unsteady, Compressible Flow Problems," University of Cincinnati Master of Science Thesis, 1975.

4. Wenzel, L.M., Moss, J.E. Jr., and Mehalic, C.M., "Effect of Casing Treatment on Performance of a Multistage Compressor," National Aeronautics and Space Administration Technical Memorandum TM X-3175, 1975.

5. Mehalic, C.M., and Lottig, R.A., "Steady-State Inlet Temperature Distortion Effects on the Stall Limits of a J85-GE-13 Turbojet Engine," National Aeronautic and Space Administration Memorandum TM X-2990, 1974.

6. Schorr, B., and Reddy, K.C., "Inviscid Flow Through Cascades in Oscillatory and Distorted Flow," AIAA 8th Aerospace Science Meeting, AIAA Paper No. 70-131, January, 1970.

7. Reid, C., "The Response of Axial Flow Compressors to Intake Distortion," ASME Gas Turbine Conference and Products Show, ASME Paper No. 69-GT-29, March, 1969.

8. Plourde, G.A., and Stenning, A.H., "Attenuation of Circumferential Inlet Distortion in Multistage Axial Compressors," J. of Aircraft v5, n3, pp 236-242.

9. Bird, R.B., Stewart, W.E., and Lightfoot, E.N., Transport Phenomena, Wiley, New York, 1960.

10. Johnsen, I.A., and Bullock, R.D., (Editors), "Aerodynamic Design of Axial-Flow Compressors," National Aeronautics and Space Administration Report NASA SP-36, Revised 1965.

11. Goethert, B.H., and Staff of University of ennessee Space Institute, "Research and Engineering Studies and Analysis of Fan Engine Stall, Dynamic Interaction with other Subsystems, and Systems Performance," Air Force Aero Propulsion Laboratory Technical Report AFAPL TR-70-51, July 1970.

REFERENCES (Concluded)

12. Spring, A.H., "Upstream Influence of an Axial Compressor on Circumferentially Distorted Flow, "Proceedings of the Air Force Airframe-Propulsion Compatibility Symposium, Air Force Aero Propulsion Laboratory Technical Report AFAPL-TR-69-103, June 1970.

13. Adamczyk, J.J., "Unsteady Fluid Dynamic Response of an Isolated Rotor With Distorted Inflow," AIAA 12th Aerospace Sciences Meeting, AIAA Paper No. 74-49, January-February 1974.

14. Braithwaite, W.M., Graber, E.J. Jr., and Mehalic, C.M., "The Effect of Inlet Temperature and Pressure Distortion on Turbojet Performance," AIAA/SAE 9th Propulsion Conference, Paper No. 73-1316, November, 1973.